Exploration of Wavelet-Based Feature Spaces in Medical Image Analysis

Dissertation
zur Erlangung des Doktorgrades
an der Fakultät für Physik
der Universität Bielefeld
vorgelegt von

BIRGIT LESSMANN

März 2007

Gedruckt auf alterungsbeständigem Papier gemäß ISO 9706.

Acknowledegments

At this point, I would like to thank all those who supported me in this project. Many thanks to my supervisors Prof. Dr. Philippe Blanchard, Junior-Prof. Tim W. Nattkemper and PD. Dr. Andreas Degenhard for giving me the opportunity to participate in this fascinating project and for fruitful discussions.

Furthermore I would like to thank the University of Bielefeld and the federal state Nordrhein-Westfalen for the funding of my scholarship.

The data processed in this work were provided by the Institute of Neuropathology (Evangelisches Krankenhaus Bielefeld) and the MR Research Group at the Institute of Cancer Research, (Royal Marsden Hospital, Sutton, Surrey). Many thanks to PD. Dr. Volkmar Hans, Prof. Dr. Martin O. Leach, Dr. Preminda Kessar, Linda Pointon and Dr. Michael Khazen.

A special thank goes to to Prof. Dr. Friederike Schmid for her support, to my colleagues for training my physical as well as my humorous fitness and to Beate and Hanne for their constant backup in the everday life.

Thanks to Oliver for the discussions regarding my work and to Thorsten, Martin and Jens for the proof-reading of my thesis.

Finally I have to mention those, who gave me the strength and the endurance to finish my project. Oliver, my family, Steffie and Daniel, thank you for your patience and affection.

Publications

Parts of this thesis were published as follows.

[1] B. Lessmann, T. Twellmann, A. Degenhard, T. Nattkemper and M. O. Leach. **Wavelet features for improved tumour detection in DCE-MRI**. In *Proceedings of Medical Image Understanding and Analysis (MIUA)*, pp. 93–96. BMVA, London, UK, 2004.

[2] B. Lessmann, T. Nattkemper, A. Degenhard, L. Pointon, P. Kessar, M. Khazen and M. Leach. **Clustering approach for wavelet transformed MR image data**. In *Proceedings of the 14th International Conference of Medical Physics*, pp. 1412–1413. 2005.

[3] B. Lessmann, T. Nattkemper, A. Degenhard, L. Pointon, P. Kessar, M. Khazen and M. O. Leach. **SOM-based wavelet filtering for the exploration of medical images**. In *Proceedings of the 15th International Conference on Artificial Neural Networks*, volume 3696 of *Lecture Notes in Computer Science*, pp 671–678. Springer Verlag, Warsaw, Sep 2005.

[4] B. Lessmann, V. Hans, A. Degenhard and T. Nattkemper. **Feature-space exploration of pathology images using content-based database visualization**. In J. Reinhardt and J. Pluim (editors), *Proceedings of SPIE Medical Imaging*, volume 6144, 61445Z. San Diego, California, USA, 2006.

[5] B. Lessmann, T. W. Nattkemper, J. Huth, C. Loyek, P. Kessar, M. Khazen, L. Pointon, M. O. Leach and A. Degenhard. **Content-based image retrieval for dynamic time series data**. In *Proceedings of Bildverarbeitung für die Medizin (BVM) 06*, pp. 61–65. Springer Verlag, 2006.

[6] C. Varini, B. Lessmann, A. Degenhard, V. Hans and T. W. Nattkemper. **Visual exploration of pathology images by a discrete wavelet transform preprocessed locally linear embedding**. In *Proceedings of Bildverarbeitung für die Medizin (BVM) 06*, pp. 66–70. Springer Verlag, 2006.

[7] B. Lessmann, T. W. Nattkemper, P. Kessar, L. Pointon, M. Khazen, M. O. Leach and A. Degenhard. **Multiscale analysis of MR mammography data**. *Zeitschrift für Medizinische Physik*, **2**, 2007. Accepted.

[8] B. Lessmann, T. W. Nattkemper, V. Hans, and A. Degenhard. **A method for linking computed image features to histological semantics in neuropathology**. Submitted to: *Journal of Biomedical Informatics - Special Issue on Intelligent Data Analysis*.

Abstract

In medical image processing a wide amount of different tasks is currently under consideration. The principle in most of the developed technical solutions is the numerical representation of an image. The numerical description of the image by so called feature vectors then allows to analyse or classify the images or to process them in any different way. The important challenge here is to find numerical features, which are particularly appropriate to represent the image and its clinical characteristics. In this work a methodology is presented allowing to develop and analyse those features in order to obtain a numerical representation especially well adapted to the clinical context. The features are obtained from a Discrete Wavelet Transform and analysed and optimized by methods of dimension reduction. The methodology is demonstrated on two highly different types of datasets acquired for the purpose of tumour diagnostics. For both databases numerical features are defined suitable to represent the particular dataset in various applications.

Les problémes liés au traitement d'images médicales sont au centre de la recherche actuelle. Dans de nombreuses applications on s'intéresse à la représentation numérique de l'image. Cette description numérique est effectuée à l'aide de vecteurs caractéristiques. En conséquence la chose la plus importante est de trouver une description numérique effective, qui assure une représentation bien adaptée aux caractéristiques médicales de chaque image. Dans cette thèse de doctorat on présent une méthode pour développer et analyser des descriptions numériques d'images, qui sont particulièrement adaptées au contexte clinique. Ces descriptions numériques sont obtenues par une transformée en ondelette discrète et elles sont étudiées et optimisées par des formules de réduction dimensionnelle. La méthode est appliquée à deux types d'images très différentes, utilisées pour le diagnostic des tumeurs. Dans les deux cas des description numériques sont définies, qui sont bien appropriées à la représentation de l'image en fonction des différentes applications médicales.

Die medizinische Bildanalyse beinhaltet eine Vielzahl unterschiedlicher Fragestellungen und Anforderungen. Grundprinzip für viele Anwendungen ist es hier, den Bilddatensatz numerisch zu repräsentieren. Diese numerische Beschreibung in Form sogenannter Merkmalsvektoren kann dann dazu genutz werden, Bilddatensätze zu analysieren, zu klassifizieren oder anderweitig zu verarbeiten. Die Herausforderung ist es demnach, geeignete numerische Merkmale zu finden, die das zu analysierede Bild und seine medizinischen Charakteristiken optimal repräsentieren. In dieser Arbeit wird eine Methodik vorgestellt, die es erlaubt, solche spezifischen Merkmale zu entwickeln, zu analysieren und an den jeweiligen medizinischen Kontext anzupassen. Die Merkmale werden mittels einer Diskreten Wavelet-Transformation erzeugt und mittels Methoden der Dimensions-Reduktion analysiert und optimiert. Die Methodik wird an zwei sehr unterschiedlichen Bildatensätzen aus der klinischen Tumordiagnostik demonstriert. Für beide Datensätze werden numerische Merkmale entwickelt, die dazu geeignet sind, den Datensatz im Rahmen unterschiedlicher Anwendungen zu repräsentieren.

Contents

List of Figures

List of Tables

1. Introduction

In the current clinical practice a multitude of imaging techniques are applied for a wide spectrum of diagnostic tasks. These techniques are e.g. magnetic resonance imaging, computer tomography, X-Ray imaging, ultrasound, positron emission tomography or the acquisition of photomicrographs of microscopy images.

The amount of acquired images therefore increases significantly. Furthermore, increasing resolution or simultaneous monitoring of time and space-dependent characteristics leads to a growing complexity of the considered datasets. In this way the diagnostic process in clinical practice becomes more and more difficult and especially time-consuming for the medical expert, since the expert has to take into account a huge amount of image information. At this point it becomes obvious that the development of methods to assist the medical expert in the diagnostic process is highly desirable. In fact, nowadays the amount of such tools currently developed in medical image analysis is very high. These tools are supposed to perform tasks such as segmentation of image structures, denoising, compression and enhancement of particular characteristics, registration of different images, classification of image characteristics into healthy and pathological or retrieval of particular images from medical databases for diagnostic support. As wide as the spectrum of required tasks is the range of image domains and diagnostic processes.

In the last years many different approaches have been pursued in order to provide diagnostic aid for the medical expert. In a review of medical image analysis Duncan and Ayache describe these approaches and note future challenges and perspectives in this field of research [1]. One major challenge is that the tasks of medical image analysis are usually *taken in isolation, rather than considered together*, although they might be closely related [1]. For instance, the image characteristics utilised to classify images or image regions into different categories (e.g. healthy and pathological) can also be utilised for purposes of image retrieval. Denoising, compression and enhancement are closely related since both tasks require the image information to be categorised into a significant and a non-significant part. Regarding segmentation various techniques

exist. However, they can be interpreted as a classification of image information into two categories, either within or outside of the image part considered. In general, it can be expected that the solution of one particular image processing task might bear potential regarding further applications. It is therefore highly desirable to develop methodologies for a general analysis of images that naturally provides solutions for a broad spectrum of tasks. However, as pointed out by Duncan and Ayache, this is still an open question in medical image analysis.

The basic idea in such general approaches is to represent the image content by numerical features, i.e. numerical vectors that encode the clinically important image characteristics. These numerical features, which can represent either total images or only particular parts of a large dataset, can then be compared or clustered in order to obtain classification results, retrieval results, segmentation of structures and so on.

At this point it is extremely important to adapt these features very carefully to the underlying medical context. Duncan and Ayache note as a future key challenge that *the work in general must be developed and clearly motivated from the underlying biological problems that are being addressed* [1]. The better the numerical features are specialised to the particular diagnostic process, the easier the particular task of medical image analysis can be fulfilled. Here, the major requirement is to define a numerical representation of the image encoding the biologically and clinically significant image characteristics appropriately.

In this thesis a study project is described to analyse images regarding the clinical context. Numerical features are defined and evaluated in order to find a discriminative set of numerical features for a specific purpose.

For a high generalisability of this framework it must be able to handle special issues arising in the daily clinical practice. Due to the increasing size and complexity of datasets in medical imaging, the framework has to be able to provide concepts for the handling of a huge amount of image information. Furthermore, regarding the varying appearance of medical images, the method has to be able to describe both global and local characteristics. Global image characteristics such as texture are important in the diagnosis of entire images or large regions, e.g. microscopy images in neuropathology. In contrast to this, other applications require the detection or classification of a very small and localised part of the image, e.g. benign or malignant tumours.

Yet another extremely important aspect is the need for appropriate visualisation interfaces for the exploration of the designed features. Especially regarding the fact that the design of those features should include the knowledge of

both image processing and medical experts an intuitive visualisation is absolutely essential as an appropriate communication environment. This additionally provides the potential of a detailed evaluation of single features concerning the clinical semantics. Finally, it is desirable to devise solutions in medical image processing that are applicable in clinical practice. For instance solutions requiring time-consuming or even human-based pre-processing steps such as a detailed manual segmentation of lesions are not suited for the daily work of a clinician.

The framework described in the following provides solutions regarding the noted issues. Its potential is demonstrated on two databases. Both databases require solutions for very different applications and diagnostic processes.

For the definition of features principles of Wavelet Analysis are applied. Wavelet Analysis is a young mathematical theory, developed mainly in the 1980s. It has many applications in mathematics, theoretical physics and signal or image processing. Wavelet theory has influenced an extremely wide range of scientific disciplines and was developed by experts from quite different fields of research. Jean Morlet, a geophysicist, included basic principles of wavelet theory into the analysis of geophysical experiments. He started a cooperation with Alex Grossman, a theoretical physicist from Marseille, to formulate the mathematical background of his work. Ingrid Daubechies, a belgian physicist and mathematician, was responsible for the formulation of orthogonal wavelet bases with compact support. Yves Meyer and Stéphane Mallat, both french mathematicians, developed the so called Multiresolution Analysis in wavelet theory.

Nowadays, wavelet theory is extremely important for signal and image processing, but also for areas of research like quantum mechanics and hydrodynamics. As Ingrid Daubechies noted:

Wavelets are a fairly simple mathematical tool, with a great variety of applications.

Especially the principle of multiresolution analysis, i.e. the potential to decompose signals into the information at different levels of details, has become enormously interesting in various applications. Yves Meyer used the following metaphor to explain principle and meaning of multiresolution analysis:

Maps contain different information at different scales. For example, it is impossible to plan a trip to visit the Roman churches at Charente and Poitou using the map of

France found on a globe of the earth.

Multiresolution analysis is a very general principle, applicable in a wide range of scientific problems in physics and computer science. Hence, the entire wavelet theory is a framework generated and applied in an interdisciplinary environment with significant contributions from mathematics, physics and computer science.

In image processing techniques of wavelet theory are utilised in an enormously large field of applications. Wavelet Analysis allows to decompose signals and images into scale-dependent and localised image information. First, in this way images can be studied at different levels of detail. This allows to identify relevant scales in the image and thus the extraction of the relevant image information. Second, due to the localisation properties of the Wavelet Transform, both features describing localised image information as well as global features such as texture can be defined.

It is thus a very powerful and general framework for image processing tasks of various applications.

When representing images or image characteristics utilising a wavelet transform it is quite common not to use the raw wavelet coefficients but to compute particular numerical features from the coefficients to reduce the amount of data to be processed. These features are often based on heuristic considerations but are however still rather abstract.

Here, the question arises how to evaluate the potential of these features with respect to the diagnostic process. This can for instance be done by interpreting the numerical features in the image domain. In fact, we consider a detailed understanding of features in medical image analysis as essential, since this enables a definition of numerical features encoding especially the clinically relevant image characteristics.

However, it is not easy to interpret features which are based on a wavelet transform and hence of a quite abstract nature. This phenomenon of missing interpretability is also termed the *semantic gap*. Thus, this project study concentrates on the exploration of the wavelet-based feature spaces. To link numerical and clinical characteristics appropriate visualisation methods are necessary. In this work methods from the field of dimension reduction, especially Self Organizing Maps, are used to accomplish this task. The Self Organizing Map is an unsupervised machine learning algorithm. It allows to project the feature space on a two-dimensional grid providing an interface for visual inspection. This visualisation enables to evaluate and optimise the features according to

the desired purpose.

The exploration of the feature space allows a step-wise optimisation and selection of the features resulting in newly defined feature vectors adapted to the specific purpose. The focus of this thesis lies especially on the interpretation and thus detailed analysis of the image domain and therefore a definition of features very close to clinical semantics.

Our methodology is applied on two databases acquired for quite different diagnostic tasks.

The first database contains microscopy images of benign brain tumours, so called meningioma WHO Grade I. These are two-dimensional RGB images of tumour tissue. Four different types of meningiomas are classified by a human expert due to varying texture appearance of the microscopy images taken.

The texture-related image characteristics can be divided into two types, characteristics distinguishing the four classes (interclass differences) and thus clinically relevant and characteristics introducing differences within a particular class (innerclass differences). The latter ones are usually ignored in the diagnostic process by the human expert but can still be very noticeable.

The analysis of this database starts with the definition of wavelet-based texture features derived from heuristic considerations. These features are then analysed within our framework. The main focus of this analysis is the interpretation of the single features regarding the clinical semantics. The exploration procedure especially aims at a detailed understanding of the feature space and thus provides a link of single numerical features to histological characteristics in the image. Particularly important is to distinguish between numerical features encoding clinically relevant image differences and the clinically irrelevant ones.

The second database contains three-dimensional time series of magnetic resonance images of the female breast. These images or volumes have been acquired for the diagnostics of breast cancer, the most common cancer of women in the western countries. In our case a contrast agent is applied to detect lesions, a method termed as dynamic contrast enhanced magnetic resonance imaging (DCE-MRI). The principle of DCE-MRI is the monitoring of breast tissue after the injection of the contrast agent. The tissue of breast tumours differs from healthy tissue regarding the vascularity and permeability. Thus monitoring of contrast agent uptake in the breast tissue provides valuable information for the detection and classification of lesions. Both the dynamical properties

of tumour tissue - e.g. speed of enhancement - and the tumour morphology - e.g. the margin of the tumour - are important for the diagnosis.

One main property of this type of diagnostics is that not only tumour tissue provides the ability of contrast agent uptake. Further types of tissue or body regions such as veins or the chest (including the heart) also show a significant uptake. Again the question arises how to distinguish between the clinically important features - enhancement in the tumour - and other types of enhancement - for instance enhancement in the heart.

The datasets are grey value images, which are both time and space-dependent, hence large and complex. One major requirement is here to handle the huge amount of image information and to find features representing localised and time-dependent image information.

A further step is the search for new features to encode morphological criteria. As described above the tumour morphology is supposed to be a very important aspect in tumour diagnostics. However, the challenge is to find a numerical representation of the tumour properties that can be utilised in applications such as classification, retrieval or visualisation purposes. Here it is desirable to be able to describe both margin and texture of the tumour as a time-dependent variable.

The two types of databases and the related diagnostic processes are very different. However, it will be shown that our framework is suitable for the analysis of both.

Outline of the thesis This thesis is organised as follows. In chapter 2 current challenges in medical image processing are described.

In chapter 3 the datasets analysed are described. It is presented, how the images are acquired and how the medical expert diagnoses the images based on specific characteristics of the tissue examined.

The methods applied for the derivation and exploration of features are explained in chapter 4. The multiscale features are computed based on the results of a Discrete Wavelet Transform, a method for the scale-wise decomposition of signals and images. The computed features are then explored using methods from the field of dimension reduction such as the Principal Component Analysis and Self Organizing Maps.

In chapter 5 the analysis of pathology images is described. Based on the Discrete Wavelet Transform texture features are derived describing typical image characteristics at different levels of detail. The exploration procedure applied allows a selection of a subset of features, especially appropriate to characterise

tissue details chosen to be particularly important in the clinical diagnostic process.

Chapter 6 describes the application of our framework to the analysis of MR volume time series. The exploration of multiscale features can be utilised to derive features characterising dynamical and morphological patterns typical for tumour tissue. The benefits of these features are a robust segmentation procedure and a robust numerical description of the time-dependent tumour morphology.

The results presented in this work are finally summarised in chapter 7. In this chapter the benefits and limitations regarding the databases and diagnostic tasks processed in this work are described. Furthermore the potential of our framework concerning further diagnostic tasks is discussed.

2. Current Challenges in Medical Image Processing

2.1. Increasing Size and Complexity of Datasets

As described in the introduction the increasing amount of data is currently one of the most important challenges in medical image processing. An increasing number of images and the related patient information is stored in clinical practice and then used not only for the specific diagnosis, but also in the development of clinical databases and tools for diagnostic support. The datasets stored and analysed can be very large and high-dimensional depending on the application [2]. This may be due to different imaging modalities, which are combined for one clinical task. In other applications the datasets are both space- and time-dependent and therefore difficult to evaluate and analyse [2]. Thus, the determination of specific numerical features appropriate for the representation of the complex image domain becomes more and more difficult. In contrast to the handling of general image databases, the applications related to medical images are usually quite specialised and the features have to be adapted to clinical semantics. The development of a general framework for feature generation and evaluation is therefore highly desirable.

2.2. Curse of Dimensionality

In diagnostic applications the image content is characterised by numerical image features. These numerical features are vectors utilised e.g. for the training of classificators or performing retrieval tasks. It might be expected that the performance of a system for classification or retrieval increases with the number of computed features, i.e. with the length of the feature vectors. But in fact it is desirable to keep the feature vector as short as possible. This reduces computational costs and avoids the effects of a phenomenon termed as *curse of*

dimensionality. As described in [3] this term is related to the effect that in high-dimensional feature spaces it becomes more and more difficult to compare two feature vectors reliably.

2.3. Semantic Gap

In applications of image analysis the image content is characterised by numerical features. While more simple and direct features such as colour histograms are easy to interpret in the image domain, features based on transforms such as Fourier or Wavelet Transform are much more difficult to understand. This phenomenon is termed the *semantic gap* and is defined according to [4] in the following way: *The semantic gap is the lack of coincidence between the information that one can extract from the visual data and the interpretation that the same data have for a user in a given situation.* The width of the semantic gap strongly depends on the domain described. In a narrow image domain providing *limited and predictable variability in all relevant aspects of its appearance* the gap between *features and semantic interpretation is usually smaller* [4]. However, the problem is still unsolved in medical image analysis. One possible solution is the annotation of images by an expert. Since the labelling of images is *cumbersome and expensive* [4] several approaches exist focusing on an automatic solution of this problem. In [5] it is noted that most of the approaches for deriving semantic features come down to attaching textual labels to the images. In [6] images are annotated using medical key words in order to improve retrieval performance. In [7] semantic metadata is extracted from visual descriptors by classifying images into semantic categories and organising a database based on certain concepts.

2.4. Applicability in Clinical Practice

Current applications of diagnostic tools in clinical practice often suffer from a high necessary amount of human interaction that is often undesirable. For instance, in some works tumours are characterised according to their shape. The features for shape characterisation usually require an exact determination of the tumour boundary, which is in most cases hand-drawn [8, 9]. However, this is not only a very time-consuming task, it additionally introduces a certain variability into the entire diagnostic process. Thus it is desirable to obtain

methods not relying on such a huge amount of human-based pre-processing.

2.5. Wavelet Analysis in Medical Image Processing

Wavelet Analysis has often been used in medical image processing. Some reviews describing current applications are [10, 11]. Wavelet Analysis is a very powerful tool and thus applicable for many different purposes. The most frequent application is the compression of images, see e.g. [12]. Also quite common are approaches for denoising images [13]. Both compression and denoising are also very common in the processing of other image domains. Closely related to the field of denoising is the enhancement of image structures considered to be of clinical importance [10].

Some wavelet research is very close to the imaging process such as wavelet-encoded magnetic resonance imaging [14] or the wavelet-based image reconstruction from tomography data [15].

Of special interest in this work is the field of feature extraction. The term *feature extraction* is quite general and can include various applications. In [16] features are extracted from digital mammograms to detect and enhance microcalcifications. There, the algorithm starts with compression and denoising. Other works focus on the computation of features, i.e. numerical representation of images for the purpose of classification or image retrieval [17].

Overall these different applications are somehow related. This corresponds to the observation of Duncan and Ayache [1] that has already been noted in the introduction (1).

Since wavelet analysis is a very general framework, it can help to integrate the different fields in image analysis. It is therefore expected that the definition of wavelet-based image features to represent particular significant image characteristics is suitable for various purposes relevant for the specific image domain.

3. Materials

In this chapter the medical databases analysed in this work are presented. Two types of medical images have been investigated, both acquired for the diagnosis of tumours. The first database contains microscopy images of meningiomas Grade I, a benign brain tumour. The second database provides magnetic resonance images acquired for the detection of breast cancer. To facilitate the understanding of the medical background a short overview of tumours including development, diagnostics and treatment is provided in the beginning of this chapter. Then the two databases and their diagnostic characteristics are described in detail.

3.1. Medical Background: Tumours

3.1.1. Tumours and Tumour Development

Tumour Classification The medical term *tumour* denotes a distinct mass in a tissue or organ, formed by abnormal or disorganised growth. This abnormal growth is referred to as *neoplasia*, therefore a tumour might also be termed a *neoplasm* [18, chapter 7.2]. Several types of tumours can be distinguished. *Malignant tumours*, also known as "cancer", show an increased growth potential. They can become invasive i.e. can penetrate and destroy the surrounding tissue. In this state the tumour can create metastases. The tumour tissue strongly differs from the normal tissue regarding histological characteristics. After patient's treatment, a relapse is possible. *Benign tumours* usually show a moderate growth. They do not penetrate the surrounding tissue which means, that they do not metastasise. The histological characteristics of benign tumour tissue are quite similar to those of the normal tissue. The occurrence of relapses is rare. However, some benign tumours can change and become malignant [18, chapter 7.2]. *Semimalignant tumours* invade the neighbouring tissue but metastasise only rarely [18, chapter 7.2].

Tumour Development Tumour growth is caused by genetical mutations in the cell, leading to uncontrolled and possibly rapid proliferation. These genetical mutations include e.g. the deactivation or activation of specific genes for growth control. Especially the risk factors of developing cancer are intensely investigated. Some genetical mutations can be passed from one generation to another, leading to a higher risk for developing some specific type of cancer. Besides an inherited predeposition there are several more factors considered to influence the risk of developing cancer, e.g. tobacco, diet and physical examination. Environmental impacts such as radioactive radiation, ultraviolet radiation, viruses or some toxic substances are also known to increase the risk of cancer [18, chapter 7.2].

3.1.2. Diagnostic Methods

Depending on type and localisation of the tumour, several diagnostic methods are common to make a clear diagnosis. The most important ones are described as follows.

Palpation An experienced physician can detect lesions or tumours by palpation [19]. The palpation of the breast is e.g. part of each preventive medical checkup regarding breast cancer.

Blood Tests Some types of cancer can be diagnosed by a blood test due to an abnormal concentration of some specific proteins or other substances, so called *tumour markers*. One example is the so called PSA (prostate specific antigen). An increased concentration of PSA is often associated with prostate cancer [20].

Histological Methods Abnormal cells can be diagnosed by histological methods. To this end, a removal of cells is necessary. This can be done by a smear or several biopsy techniques. During fine needle aspiration biopsy a piece of tissue is obtained using a thin, hollow needle. Core (needle) biopsy includes the removal of multiple pieces of tissue. In case of contradictory results a surgical biopsy may be necessary including the removal of a tissue sample (incisional biopsy) or of the complete suspicious area (excisional biopsy) [19]. Furthermore excised tissue can regularly be examined during or after surgery. The tissue is prepared, stained and examined by microscopy. The preparation procedure for the diagnosis of meningiomas is detailed in section 3.2.

Imaging Techniques Most existing medical imaging techniques are applied for the detection of tumours. The most common ones in tumour diagnostics are described in this paragraph. For further imaging techniques not described here, please refer to [21].

Medical Sonography is an imaging technique based on ultrasound, i.e. sound with a frequency above the bandwidth of human hearing. Frequencies appropriate for medical diagnosis range from 0.8 to 15 MHz. Strong pulses of sound are transmitted into the tissue to be examined. At the interface of different tissues the sound waves are partially reflected. A detector receives the echoes and creates a real time image depending on intensity and transit time of the echoes. Especially muscles and soft tissue can be imaged very efficiently. Medical sonography e.g. is used during breast examination allowing to detect and to distinguish different types of masses [22].

In *X-Ray Radiology* the attenuation of X-Rays, i.e. photons with a frequency of $10^{16} - 10^{20}$ Hz [23] is monitored. The energy spectrum for medical applications is usually 17-150 keV [24] corresponding to a frequency range of approximately $4 \cdot 10^{18} - 4 \cdot 10^{19}$ Hz. Attenuation in tissue can be due to several physical processes including scattering and photoelectric absorption. The attenuation differs strongly regarding different types of tissue e.g. bones and soft tissue [24].

Standard X-Ray radiology is a very common method in breast examinations (X-Ray Mammography). However, the resulting image is a two-dimensional projection of the attenuation in a tissue volume. To preserve the depth information, X-Ray *Computed Tomography (CT)* has been developed. The principle of CT is to image slices of the part of the body examined. Two-dimensional X-Ray images are taken around an axis of rotation. From these images the three-dimensional image information is reconstructed. In the fourth generation of CT scanners, the detectors are arranged in a stationary ring, while the source rotates during image acquisition [25].

Another imaging technique to obtain three-dimensional images of the human body is *Magnetic Resonance Imaging* (MRI). The principle of MRI is to monitor the behaviour of protons - nuclei of the hydrogen contained in water. In this way images of the soft tissue can be obtained. Due to a strong magnetic field, the spins of the nuclei are aligned parallel or antiparallel to the field direction. At room temperature and equilibrium the protons are more often aligned parallel. With an electromagnetic pulse transitions between the two states are caused. After the disturbance of the equilibrium, relaxation processes can be measured by signals from induction currents. The tissue dependence of these

relaxation processes allows to reconstruct images that provide tissue dependent contrast [26]. MRI is further detailed in section 3.3.

3.1.3. Treatment

The choice of treatment strongly depends on the type and localisation of the tumour and the patient's general condition. Benign tumours may not require any treatment, due to their low growth potential and their non-invasive behaviour. However, they have to be removed by *surgery*, if they start to compress adjacent structures or possibly can become malignant. Most of the malignant tumours have to be treated. A removal of the tumour by *surgery* may prevent the creation of metastases [27]. Furthermore it allows to determine the extent of the disease. In *radiation therapy* the patient is locally treated with ionising radiation to kill cancer cells and decrease the size of tumours [28]. It may be applied as primary therapy or combined with surgery or medical treatment. A medical treatment of cancer can include a wide range of substances. The treatment with cytostatic drugs, substances inhibiting cell growth, is usually termed *chemotherapy* [29]. Some types of cancer can be inhibited by influencing the hormone balance. This *endocrine therapy* is e.g. appropriate for some types of prostate and breast cancer [30]. Specific types of cancer are treated by *immunotherapy*, i.e. a stimulation of the immune system [31] or administration of specialised antibodies to destroy cancer cells [32]. In some cases bone marrow transplantation is chosen as treatment [33, 34].

3.2. Database I: Microscopy Images of Meningiomas

3.2.1. Tumours of the Central Nervous System

Regarding brain tumours the common histological classification of tumours is not appropriate. Brain tumours in general rarely metastasise, even if they are highly malignant. Furthermore even benign tumours can be highly dangerous to the patient, if the tumour is located in a sensitive area inside the brain and its growth causes compression of adjacent structures [18, chapter 19.1]. Due to these aspects, brain tumours are classified into four grades, strongly varying regarding the patient's prognosis (Table 3.1).

WHO Grade	Characteristics
Grade I	slowly growing, benign, good patients prognosis
Grade II	increased growth potential, may become malignant, relapse possible
Grade III	fast growing, features of malignancy, unfavourable clinical outcome
Grade IV	very fast growing and highly malignant, highly unfavourable prognosis

Table 3.1.: The WHO classification of brain tumours.

In [35] brain tumours are further classified according to the tissue of origin:

- Tumours of neuroepithelial tissue, i.e epithelial, excitable cells
- Tumours of peripheral nerves. These tumours arise from nerves of the peripheral nervous system, but may effect the central nervous system
- Tumours of the meninges, i.e. the coverings of the brain
- Lymphoma and haemopoietic neoplasms, i.e. malignant tumours of the lymph tissue or cells pertaining blood formation
- Germ cell tumours. These tumours are morphological homologues of neoplasms arising in testicles and ovaries
- Tumours of the sellar region, i.e. near to and including the hypophysis
- Metastatic tumours

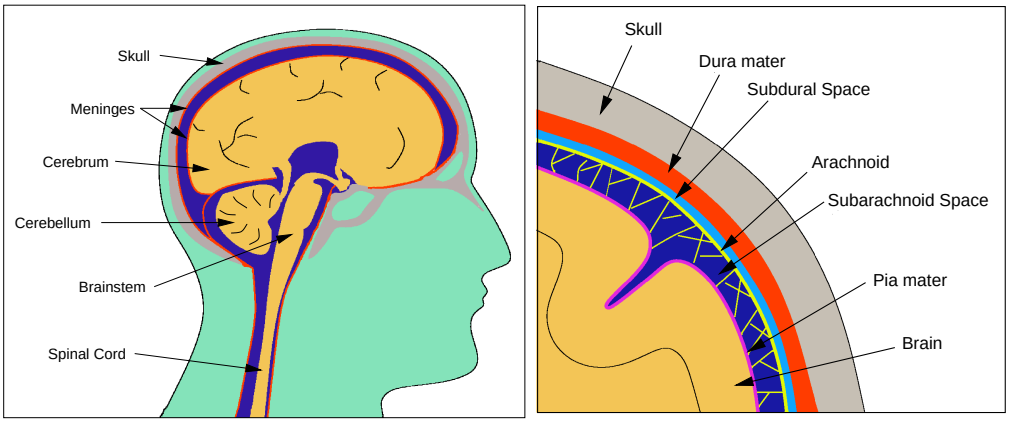

Figure 3.1.: Location and anatomy of the meninges. Left: The meninges encloses the brain and the spinal cord and is attached to the skull. Right: The meninges is composed of three different membranes.

3.2.2. Meningiomas

Meningiomas are mostly slowly growing, benign brain tumours of the meninges [36], which is the covering of the brain. The meninges encloses the brain and the spinal cord (Figure 3.1). The meninges is composed of three different connective tissue membranes. The innermost is the *pia mater* following the surface of the brain and spinal cord closely. The second membrane, the *arachnoid* does not follow the surface of the brain. Between pia mater and arachnoid there is the so called *subarachnoid space* filled with cerebrospinal fluid. Thin threads of connective tissue span the subarachnoid space connecting the pia mater and the arachnoid. The outermost, thick and dense membrane is the *dura mater*. It covers the inside of the skull and contains larger blood vessels. The very narrow space between dura mater and the arachnoid is the subdural space. The dura serves to restrict the movements of the brain in the skull [37].

Meningiomas are attached to the dura mater and composed of arachnoidal cells. Approximately 85 % of meningiomas are of WHO grade I [18, chapter 19.1]. However, they may have to be treated by surgery, due to compression of adjacent structures inside the brain. Besides the WHO grade I meningiomas also Grade II and III meningiomas may occur with a correspondingly less favourable clinical outcome [36]. A histological examination of resected tissue allows a detailed classification into a large number of distinguishable subtypes (Table 3.2) [36]. The by far most common subtypes of meningiomas

meningioma	WHO grade
meningotheliomatous meningiomas	Grade I
fibroblastic meningiomas	Grade I
transitional meningiomas	Grade I
psammomatous meningiomas	Grade I
angiomatous meningiomas	Grade I
microcystic meningiomas	Grade I
secretory meningiomas	Grade I
lymphoplasmacyte-rich meningiomas	Grade I
metaplastic meningiomas	Grade I
chordoid meningiomas	Grade II
clear cell meningiomas	Grade II
atypical meningiomas	Grade II
rhaboid meningiomas	Grade III
papillary meningiomas	Grade III
anaplastic meningiomas	Grade III

Table 3.2.: Histological classification of meningiomas.

are the meningotheliomatous, the fibroblastic, the transitional and the psammomatous subtype [18, chapter 19.1].

3.2.3. Acquisition of Microscopy Images

Histological Tissue Preparation

The diagnostic tumour samples analysed were derived from neurosurgical resections at the Bethel Department of Neurosurgery, Bielefeld, Germany for therapeutic purpose and have been prepared postoperatively. The preparation is shown in Figure 3.2 and includes four steps.

Fixation Fixation means an interruption of all biological processes in the cell to prevent decay. The most common fixation technique uses formalin, an aqueous solution of Formaldehyde (HCHO). The formalin stabilises the tissue by interlacing processes [38].

Embedding To obtain a sample providing homogeneous conditions during sectioning, the sample is embedded into an appropriate substance, in most

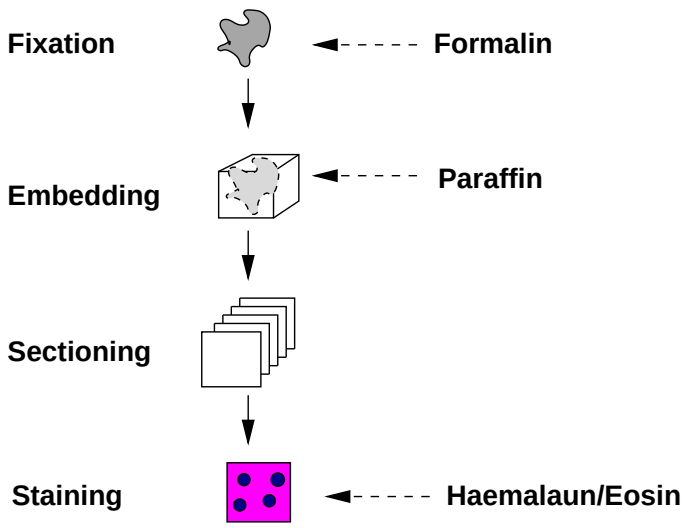

Figure 3.2.: The procedure of histological tissue preparation.

cases paraffin. The embedding process requires a prior dehydration of the tissue [38].

Sectioning After fixation and embedding sections of approximately four μm thickness are taken out using a microtome. The sections are then placed on glass slides for further processing.

Staining In histology several different staining techniques exist [38]. The most common standard staining method is the so called H&E staining. The used pigments are haemalaun or hematoxylin and eosin. The positively charged pigment haemalaun attaches at the negatively charged phosphate group of the nucleic acid in the cell nuclei, resulting in a blue colouration of the nuclei [39]. In contrast to this, the eosin colours cytoplasm and collagen in red or pink [38].

Image Acquisition

For the database analysed archive cases from 2004 and 2005 were selected to represent typical features of the four most common meningioma subtypes. Slides were analyzed on a *Zeiss Axioskop 2 plus* microscope with a Zeiss Achroplan 40x/0,65 lens. After manually focusing and automated background correction, 1300x1030 pixels, 24 bit, true color RGB pictures were taken at standardised 3200 K light temperature in TIF format using Zeiss AxioVision 3.1

software and a Zeiss AxioCam HRc digital color camera (Carl Zeiss AG, Oberkochen, Germany). Five cases were selected for each diagnostic group and four different photomicrographs were taken of each case, resulting in a set of 80 pictures (Table 3.3).

Subtype	No. of patients	No. of. images per patient	total No. of pictures
meningotheliomatous	5	4	20
fibroblastic	5	4	20
psammomatous	5	4	20
transitional	5	4	20

Table 3.3.: Database of microscopy images of meningiomas.

3.2.4. Database Characteristics

Our database contains microscopic images of the most frequent subtypes, i.e. the *meningotheliomatous, fibroblastic, transitional* and *psammomatous* meningiomas. Histological features can be described to distinguish the four subtypes (interclass differences). However, in each class innerclass differences can be observed.

Interclass Differences

The four subtypes are characterised by distinct features allowing a trained investigator to make an unequivocal diagnosis in most cases. Table 3.4 gives an overview of these features [36, 40].

Meningotheliomatous meningiomas provide a quite isotropic structure. The cells, which form a syncytium, provide round, blue stained cell nuclei on a background of red to pink cytoplasm. An example image is presented in Figure 3.3.

The fibroblastic subtype provides a quite anisotropic structure. The cells and cell nuclei are spindle-shaped and a fascicular structure is visible, containing fibres of collagen (Figure 3.4).

The most important histological features of the psammomatous subtype are the so called psammoma bodies, calcifications embedded in the tissue. The psammoma bodies are often surrounded by white artefacts (Figure 3.5). These

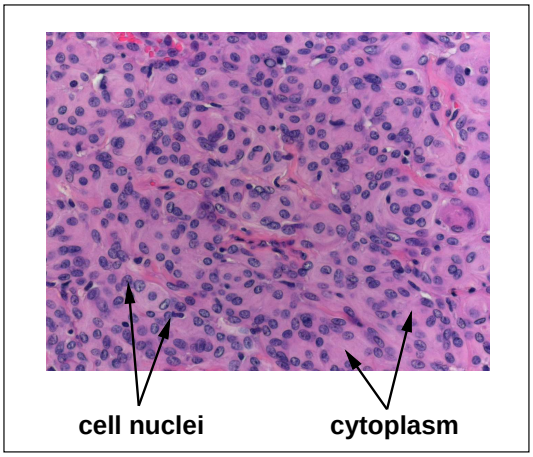

Figure 3.3.: Example image of the meningotheliomatous subtype.

Subtype	Characteristics
Meningotheliomatous	Lobulated, cells forming a syncytium
Fibroblastic	Spindle-shaped cells, matrix abundant in collagen
Transitional	Whorls, few psammoma bodies, features of fibroblastic
Psammomatous	Transitional appearance, abundant psammoma bodies

Table 3.4.: An overview of the histological features of the four tumour classes.

artefacts are cracks in the tissue occurring during sectioning due to the hard calcifications.

The transitional subtype is named according to the intermediate features provided. Transitional meningiomas may contain a few psammoma bodies (not in the database at hand) or features of fibroblastic, i.e. spindle-shaped cells and bunches of collagen. Furthermore whorls are typical for this subtype. Figure 3.6 shows the features by an example image.

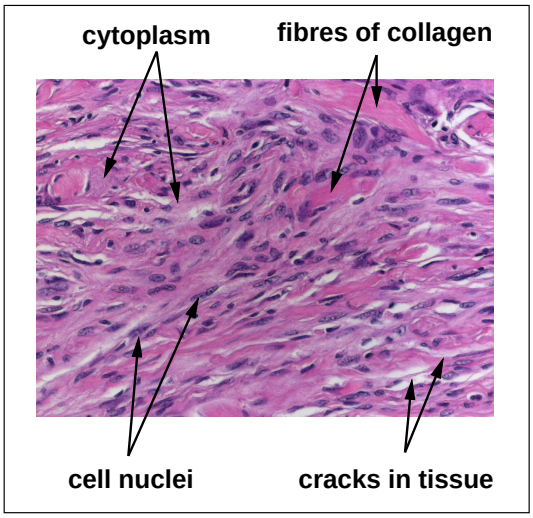

Figure 3.4.: Example image of the fibroblastic subtype.

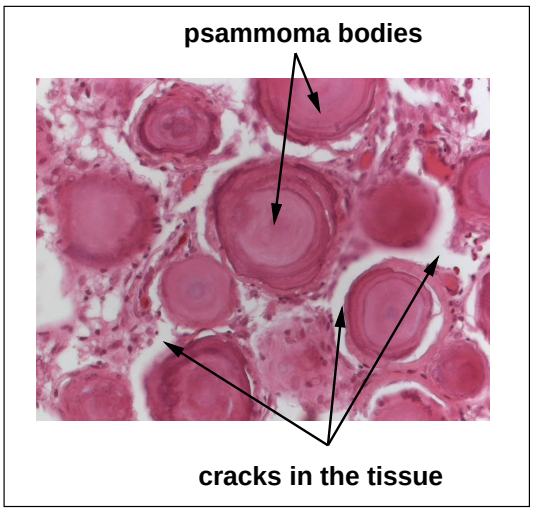

Figure 3.5.: Example image of the psammomatous subtype.

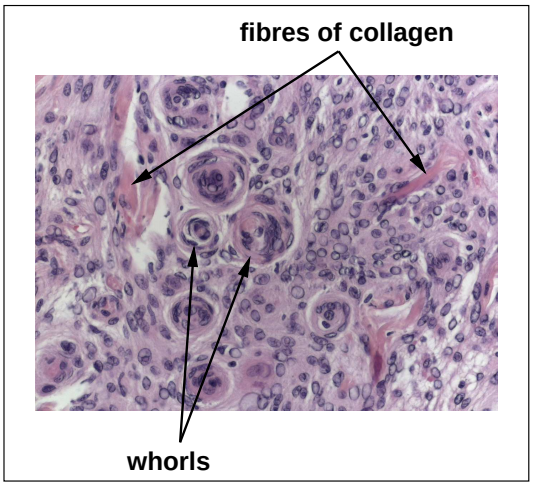

Figure 3.6.: Example image of the transitional subtype.

Innerclass Differences

An important aspect producing innerclass differences is the colouration of the images. The staining process is influenced by variations in the preparation procedure of the microscopic images regarding the duration and the temperature. Furthermore, the thickness of the sections may slightly vary. Besides technical aspects the colouration can vary due to physiological variation from patient to patient. Especially the colouration of the cytoplasm shows clear differences between different patients even for meningiomas of the same subtype. In Figure 3.7 two example images of the meningotheliomatous subtype are shown. The cytoplasm in the image at the right-hand side has a much more intense staining than the cytoplasm of the left image. Besides a variation in the colouration there are more innerclass variation. In the following these variations are described with respect to one particular meningioma subtype. However, they may also somewhat occur in other subtypes.

Meningotheliomatous Meningioma The most important innerclass variation for the meningotheliomatous subtype beside the tissue colouration is the density of cell nuclei. In Figure 3.8 two example images are presented. The image at the left hand clearly features a higher density of cell nuclei compared to the image at the right hand side.

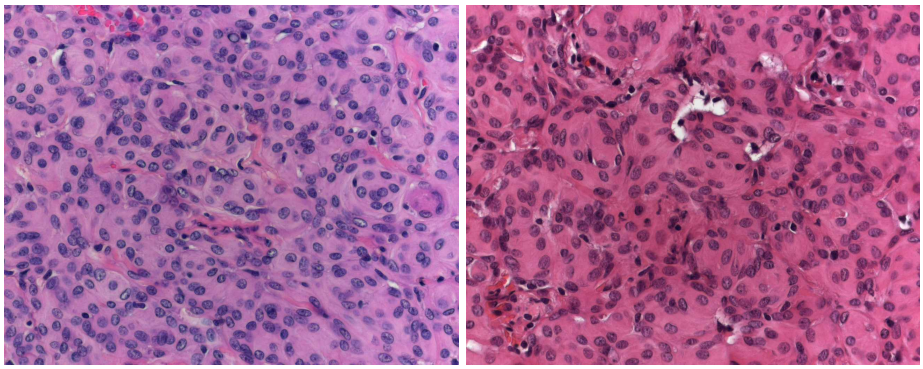

Figure 3.7.: Two images of the meningotheliomatous subtype showing strong differences in colouration.

Fibroblastic Meningioma Fibroblastic tissue can show very strong innerclass differences due to the fascicular structure. This fascicular architecture forwards the rupture of the tissue during preparation. Hence, an increased amount of image inhomogeneities created by cracks in the tissue can occur. In Figure 3.9 two images of different patients belonging to the fibroblastic subtype are presented. The image at the right hand side depicts an increased amount of inhomogeneities due to tissue cracking compared to the image on the left.

Psammomatous Meningioma Where the psammomatous subtype is concerned, the ratio of psammoma bodies and syncytium may differ strongly. Figure 3.10 shows two images with clearly varying amount of calcifications embedded into the syncytium. The higher the amount of psammoma bodies the higher most often the amount of very large cracks in the tissue.

Transitional Meningioma As a subtype providing intermediate features the transitional subtype can show several types of innerclass differences. Here, the amount of collagen can vary strongly as shown in Figure 3.11. Besides the amount of collagen also that of whorls, as well as the staining, the density of cell nuclei or the number of cracks can differ strongly from patient to patient.

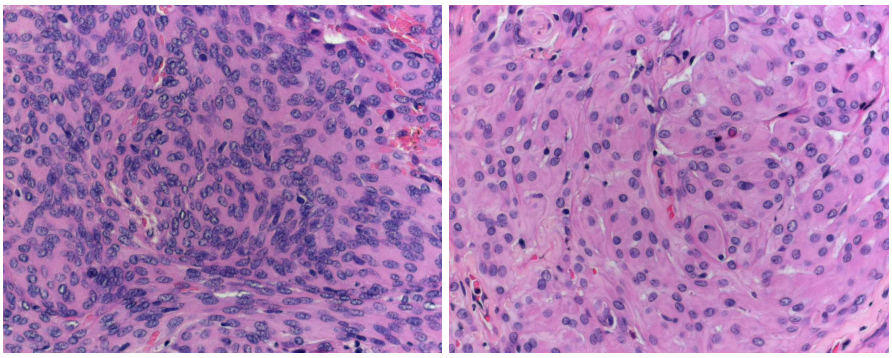

Figure 3.8.: Two images of the meningotheliomatous subtype showing strong differences regarding the density of cell nuclei.

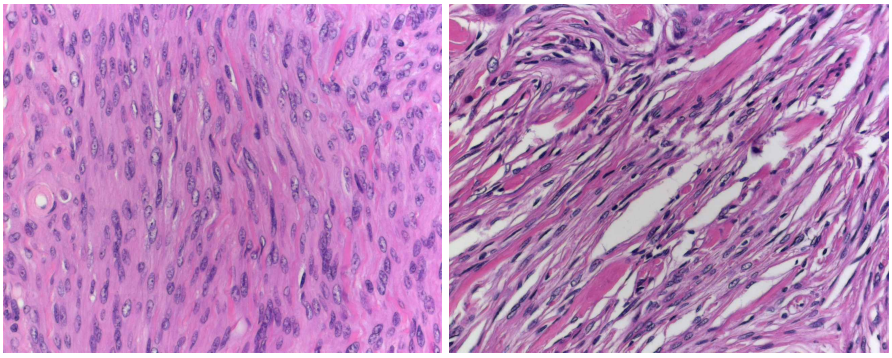

Figure 3.9.: Two images of the fibroblastic subtype with strongly varying amount of tissue cracking.

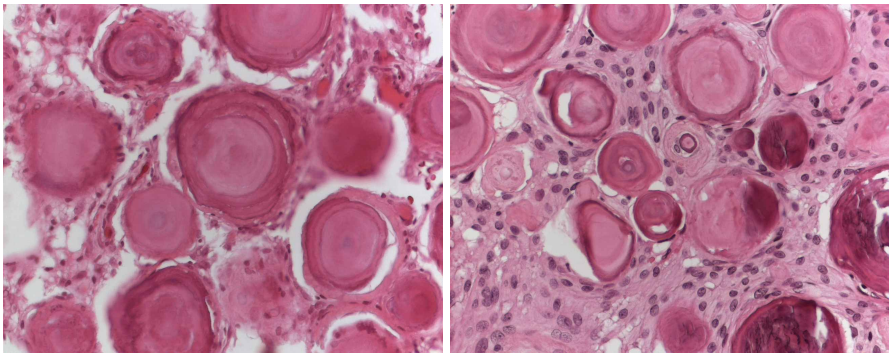

Figure 3.10.: Two images of the psammomatous subtype with strongly different amount of psammoma bodies.

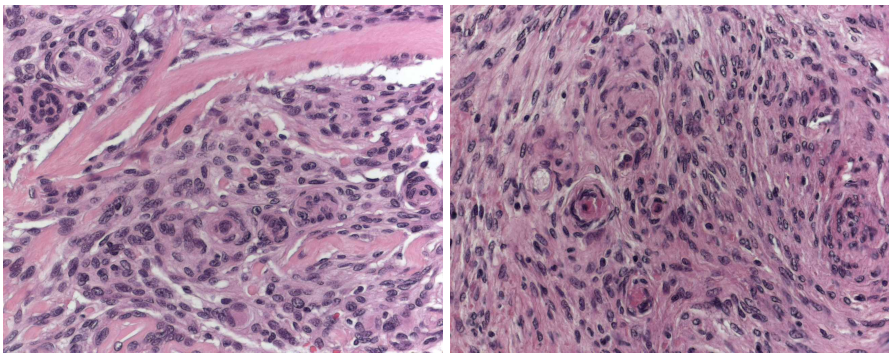

Figure 3.11.: Two images of the transitional subtype providing a significantly varying amount of collagen.

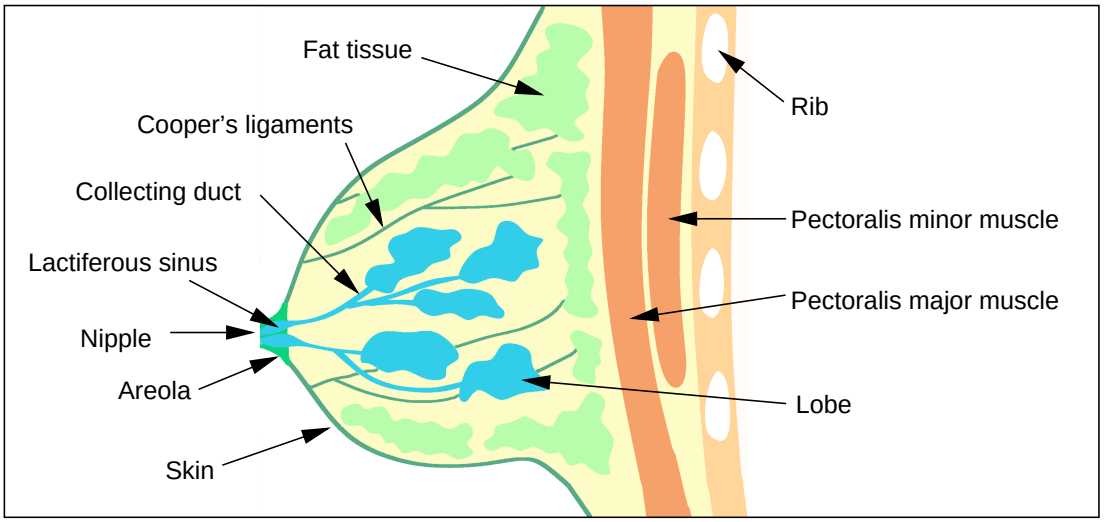

Figure 3.12.: Anatomy of the female breast.

3.3. Database II: MR Images of Breast Lesions

3.3.1. Anatomy of the Female Breast

The female breast is composed of approximately 80% connective tissue and 20% glandular tissue [19]. Figure 3.12 illustrates the anatomy of the female breast by showing a cross-section. The breast is located over the pectoralis muscles and covered by skin. The connective tissue includes fat tissue and Cooper's ligaments, which maintain the structural integrity. A number of 15-20 glandular nodes or lobes is arranged in a radial fashion. Each single lobe is composed of 20-40 lobules, each one containing 10-100 alveoli or acinii, the secretory element of the breast. The secretion or milk is transported by the ducts to the nipple. Each lobe has one collecting duct converging into a lactiferous sinus directly connected to the nipple. The nipple is surrounded by the areolar and contains sweat glands and nerve endings [19].

3.3.2. Lesions of the Breast

In [41] breast tumours are histologically divided into eight major categories depending on their origin (Table 3.5). Each of the categories can be subdivided into further subcategories. However, in clinical practice some lesions commonly occur, which do not belong to any of these categories, e.g. inflam-

Epithelial Tumours	Tumours arising from the epithelium, i.e. the covering of organs or bodies
Myoepithelial Tumours	Tumours of myoepithelial cells, i.e. special type of epithelial cells with contractile qualities
Mesenchymal Tumours	Tumours of the mesenchyma, a special type of connective tissue
Fibroepithelial Tumours	Tumours with components of epithelial and connective tissue
Tumours of the nipple	Tumours restricted to the nipple and areola
Malignant lymphoma	a malignant tumour of lymph tissue
Metastatic Tumours	metastasis from other malignant tumours
Tumours of the male breast	very rare

Table 3.5.: WHO categories of breast tumours.

mations and solitary cysts. Other tumours of the breast mentioned in [41] occur only very rarely.

In the following the most frequently diagnosed breast lesions will be described. For a more detailed description the reader is referred to [41].

Benign Lesions

A very common lesion regarding the female breast is a *cyst*. Cysts are benign, fluid-filled lesions, which occur quite frequently and are harmless in nature. The most important method for the diagnosis of cysts is ultrasound [19].

Most of the women examined in clinical practice are considered to have *fibrocystic changes*, also termed *fibrocystic disease* or *fibrocystic conditions* [19]. This includes a broad spectrum of patterns, e.g. formation of *cysts*, formation of excess fibrous connective tissue (*fibrosis*) and increase of the number of epithelial cells (*epithelial hyperplasia*).

Further benign diseases of the breast are the *periductal mastitis* and the *duct ectasia*. *Mastitis* is an infection of the breast, which may lead to a blocked duct. It often appears during time of breast-feeding. *Periductal mastitis* is an infection of the ducts around the nipple. A *duct ectasia* is a dilation of a duct behind the nipple. If the dilation is filled with fluid, the duct can be blocked. Inflammations are also possible [19]. *Sclerosing lymphocytic lobulitis*, also termed *diabetic mastopathy* and *lymphocytic mastitis* are benign, inflammatory breast diseases often associated with diabetes [42, 43].

There are several benign lesions categorised as epithelial tumours or proliferations. The *papilloma* is a benign tumour of the major duct, which in rare cases can show malignant degeneration [41]. The *adenosis* is a benign, epithelial proliferative process affecting mainly the lobular components of the breast parenchyma [41]. In case of a accompanying fibrosis it is called a *sclerosing adenosis*. The *complex sclerosing lesion* or *radial scar* are complex epithelial lesions incorporating several benign changes including adenosis. These lesions differing in size are characterised by architectural distortions of the breast parenchyma [41].

The most common benign breast tumour is the *fibroadenoma*, which belongs to the benign fibroepithelial tumours. Fibroadenomas can vary strongly according to their histological appearance. Most of them can be correctly diagnosed using fine needle aspiration biopsy. The occurrence is most frequent in women under the age of 30 [41].

Malignant Lesions

Breast cancer is the most common cancer in women [41]. However, the risk of developing breast cancer varies strongly depending on the area of living. The areas of high risk are North America, Europe and Australia, where 6% of women develop breast cancer before age 75. In general, the risk increases rapidly with age [41]. In young women most tumours are benign ones, whereas cancer is the most frequent tumour in woman at age 60 or above. Nearly all malignant lesions occurring in the breast are carcinomas, i.e. epithelial tumours. For information regarding other rarely occurring types of malignant tumours in the breast the reader may refer to [41].

Non-invasive Carcinomas

Non-invasive carcinomas do not invade the basal membrane. There is a risk that they become invasive, but they do not need to. The non-invasive carcinomas include the *lobular carcinoma in situ* (LCIS) and the *ductal carcinoma in situ* (DCIS), depending on their origin. If the DCIS grows into the duct with a papillary configuration it is termed a *papillary carcinoma*, which very rarely becomes invasive. DCIS are usually classified depending on their histological characteristics. The most frequent histological patterns are *comedo, cribriform, solid, papillary* and *micropapillary* [41].

Invasive Carcinomas

If a lobular carcinoma extends beyond the boundary of the lobule of origin, it is called an *invasive lobular carcinoma*. A DCIS becoming invasive is termed a *invasive* or *infiltrating ductal carcinoma*. Most of these carcinomas do not provide a clearly recognisable histological structure and are therefore classified as NOS (not other specified). The *infiltrating ductal carcinoma NOS* accounts for nearly 80 % of breast cancers [44]. Besides these there exist some much rarer ductal carcinomas. One of these is the *tubular carcinoma*, which is very well differentiated and provides a particularly favourable prognosis. The *medullary carcinoma* is well circumscribed and contains cells arranged in sheets. It has a better prognosis than the invasive ductal carcinoma NOS [41]. The *mucinous carcinoma* is very rare. It is formed by cells producing mucus. The so called *Paget's Disease of the nipple* is a carcinoma located at the nipple and areola which may show eczematous appearance [45]. Other very rarely occurring carcinomas are described in [41]. In some cases invasive carcinomas are classified as combinations of the ones previously described [44].

Carcinomas are classified into three categories (Grade I - III) according their biological aggressiveness. Grade I includes the non-metastasising carcinomas, Grade II the uncommonly metastasising carcinomas and Grade III all other types [46].

3.3.3. Diagnostic Methods for the Detection of Breast Cancer

Due to the fact that breast cancer is one of the most frequent types of cancer in western countries [47] a yearly medical prevent checkup is quite common. The usual methods during checkup are palpation by the medical expert, medical sonography and X-Ray mammography. In cases of doubt also a biopsy may be used. A regular screening of woman older than 40 years using X-Ray mammography is usually recommended [48, chapter 1]. The strengths of X-Ray mammography are the high sensitivity in fatty areas and the demonstration of microcalcifications, often a sign of malignancy [48, chapter 1]. However, the benefit of this imaging technique for younger woman is limited, since the younger breast is more radiographically dense and the interpretation of mammograms therefore more difficult [19]. Sonography is very useful for distinguishing solid masses from cysts or imaging masses in dense breast tissue. However, some malignant lesions are not visible sonographically [48, chapter 1]. Most of the masses detected by palpation provide a diameter of more

than 1 *cm*, i.e. small masses tend to be missed. Fine needle aspiration and core biopsy have gained increasing importance as they provide high specificity values. The accuracy depends on technical and biological factors, e.g. small tumours are more likely to be missed [48, chapter 1].

Considering the described strengths and limitations of the standard diagnostic methods, in a certain percentage of cases a clear diagnosis remains difficult. In some of these cases the method of choice for an accurate diagnostic result is dynamic contrast enhanced magnetic resonance imaging (DCE-MRI), i.e MRI involving the administration of a contrast agent [48, chapter 1]. The administration of a paramagnetic contrast agent can provide additional useful information on the vascularity and permeability of the tissue examined. DCE-MRI is especially interesting in the following cases [48, chapter 1]. Severe scars after surgery can mimic or obscure malignancy in conventional imaging, demanding additional information. Silicone implants tend to mammographically obscure the surrounding tissue. MRI is useful to evaluate the implant integrity and to detect or exclude the existence of malignant lesions next to the implant. The additional information of MR images is mostly desirable in case of dense breast tissue, especially regarding patients with a high risk of developing breast cancer and for the preoperative diagnosis of multifocality (existence of two or more lesions). Furthermore DCE-MRI can be applied in cases with contradictory results from other diagnostic methods [48, chapter 1]. The principles of MR imaging of the female breast are detailed in the next subsections.

3.3.4. Principle of MR Imaging

Magnetic resonance, also termed Nuclear Magnetic Resonance (NMR) as a medical imaging technique is still in an early stage [26]. It can provide three-dimensional images of the patient's anatomy. The contrast of tissues varies depending on the particular settings of the imaging process.

Physical Basics

The Nuclear Spin In MR imaging the principle of nuclear magnetic resonance is used to create images of living tissue. Each nucleus is associated with a spin providing a spin angular momentum **I** and a magnetic moment μ. In an external magnetic field **B** the magnetic quantum number can take values in the range $-I, -(I-1)...(I-1), I$. Due to the fact that living tissue is examined, the observed nucleus is usually the nucleus of the hydrogen atom contained in

water. Therefore the following explanations will be discussed with focus on the proton spin, though some MR techniques exist aiming at different nuclei [26]. For the following description the magnetic field is set parallel to the z-axes of the coordinate system regarded, i.e. $\mathbf{B}_0 = (0, 0, B_0)$. The proton has a spin angular momentum of $\frac{1}{2}$, thus the magnetic spin quantum number can take the values $\pm\frac{1}{2}$, i.e the spin is aligned parallel or antiparallel to the external magnetic field. As a consequence the energy of the two states is given by

$$E = \mu\mathbf{B} \tag{3.1}$$

$$= \pm\frac{1}{2}\gamma\hbar B_0 \tag{3.2}$$

with the gyromagnetic ratio of the proton γ and $\hbar \approx 1.0546 \cdot 10^{-34}\frac{m^2kg}{s}$.

Due to the large number of protons examined, statistical descriptions have to be taken into account [26]. The two possible states are occupied depending on the temperature. According to the Boltzmann distribution the difference regarding the population of the two states is described by

$$\frac{n(+\frac{1}{2})}{n(-\frac{1}{2})} = e^{\frac{\Delta E}{kT}} \tag{3.3}$$

with the Boltzmann constant $k \approx 1.38 \cdot 10^{-23}\frac{m^2kgK}{s^2}$, the temperature T and the energy difference between the two states

$$\Delta E = \gamma\hbar B_0. \tag{3.4}$$

The state providing a lower energy, associated with an alignment parallel to the external field, is usually preferred, leading to a net-magnetisation of the probe. The behaviour of this net-magnetisation $\mathbf{M}$ can be sufficiently described classically due to the large number of nuclei. Therefore the classical description will be further detailed. For the quantum-mechanical description of the process the reader may refer to appendix A.

The Magnetisation A constant external magnetic field $\mathbf{B}_0$ exerts a couple on the magnetisation according to

$$\frac{\mathrm{d}\mathbf{M}}{\mathrm{d}t} = \gamma\mathbf{M} \times \mathbf{B}_0. \tag{3.5}$$

This equation describes a precession of the magnetisation vector with angular velocity

$$\omega_0 = -\gamma \mathbf{B}_0. \tag{3.6}$$

Equation 3.5 is called *Larmor Equation* and ω_0 the *Larmor Frequency* [26].

The principle of MR imaging is to change the magnetisation by applying an additional external magnetic field. This field is oriented in the xy-plane, provides the flux density $\mathbf{B}_1$ and rotates at the Larmor frequency. For an efficient description of this process, we consider a reference frame rotating in the xy-plane with angular velocity ω. In this reference frame the magnetisation is described by

$$\frac{\mathrm{d}\mathbf{M}}{\mathrm{d}t} = \gamma \mathbf{M} \times (\mathbf{B}_0 + \frac{\omega}{\gamma} + \mathbf{B}_1). \tag{3.7}$$

If $\mathbf{B}_0$ is chosen such that $B_0 = -\frac{\omega}{\gamma}$ equation 3.7 becomes

$$\frac{\mathrm{d}\mathbf{M}}{\mathrm{d}t} = \gamma \mathbf{M} \times \mathbf{B}_1 \tag{3.8}$$

meaning that the magnetisation vector $\mathbf{M}$ rotates about the direction of $\mathbf{B}_1$ [26]. If the pulse is applied for a specific time t the magnetisation vector is tilted about

$$\alpha = \gamma B_1 t. \tag{3.9}$$

By controlling the time t it is possible to rotate the magnetisation vector through particular angles, e.g. 90° or 180° [26].

Relaxation Processes After tilting the magnetisation vector out of its original position, the magnetisation relaxes back into its initial position. In most cases this can be described by the Bloch equations [26]

$$\frac{\mathrm{d}M_z}{\mathrm{d}t} = -\frac{(M_z - M_0)}{T_1} \tag{3.10}$$

$$\frac{\mathrm{d}M_x}{\mathrm{d}t} = \gamma M_y B - \frac{M_x}{T_2} \tag{3.11}$$

$$\frac{\mathrm{d}M_y}{\mathrm{d}t} = -\gamma M_x B - \frac{M_y}{T_2} \tag{3.12}$$

with the longitudinal relaxation time T_1, the transverse relaxation time T_2 and the fully relaxed magnetisation M_0. B represents the total magnetic field experienced by the spins. Detailed properties of this field in case of image acquisition are explained in the next paragraph.

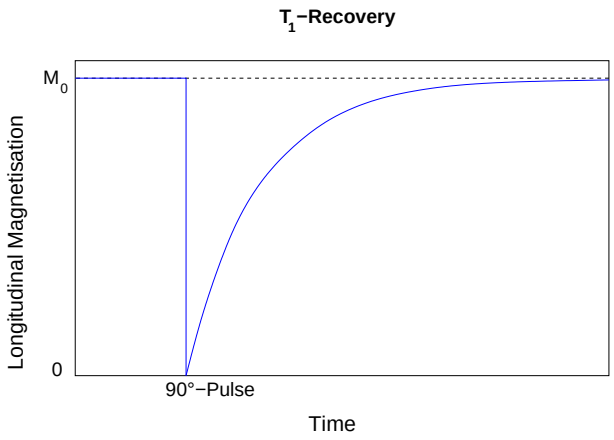

Figure 3.13.: Recovery of the longitudinal magnetisation after tilting the magnetisation vector about 90°.

Quantum-mechanically the relaxation is a process of stimulated emission, caused by different physical effects contributing to the relaxation of the magnetisation [26]. The emitted signal can be measured using a receiver coil and is called *free induction decay - FID* [49].

The first-order ordinary differential equation 3.10 can easily be solved resulting in a solution for the longitudinal magnetisation M_z.

$$M_z = M_0(1 - e^{\frac{-t}{T_1}}) \tag{3.13}$$

This equation describes the recovery of the longitudinal magnetisation (so called T_1-recovery) and is schematically shown in Figure 3.13 for a tilting angle of 90°. The solution for the transverse components of the magnetisation with the initial magnetisation $\mathbf{M} = (-M_0, 0)$ is given by

$$M_x = (-M_0 \cos \omega t) e^{\frac{-t}{T_2}} \tag{3.14}$$

$$M_y = (M_0 \sin \omega t) e^{\frac{-t}{T_2}} \tag{3.15}$$

with $\omega = \gamma B$ [50, chapter 4].

A combination of the x- and y-components yields a generalised transverse magnetisation traditionally represented by a complex number M^c_{xy} according to [50, chapter 4]

$$M^c_{xy} = M_x + iM_y \tag{3.16}$$

$$= M_{xy0}\, e^{\frac{-t}{T_2}} e^{-i\omega t} \tag{3.17}$$

with $M_{xy0} = -M_0$. The change of the transverse magnetisation in the xy-plane over time is shown at the top of Figure 3.14. The vector of the transverse magnetisation describes a spiralling path in the complex plane. The absolute value of M_{xy}^c - further denoted as M_{xy} - decays with time constant T_2 and is presented at the bottom of Figure 3.14.

Only the rotation of the transverse magnetisation produces a measurable signal, which is the basis for tissue characterisation. T_1 is termed the longitudinal relaxation time since it describes the relaxation of M_z. It is sometimes also termed spin-lattice relaxation time since the process of emission is here caused by interaction with the lattice, in living tissue this refers to the water. T_2 describes the relaxation of the magnetisation in the xy-plane. In tissue T_2 is usually considerably shorter than T_1. T_2 is also termed spin-spin-relaxation time since it results from a loss of phase coherence in the xy-plane due to spin-spin-interaction. In practice the decay of the transverse magnetisation is even faster than the processes described by T_2. Besides spin-spin relaxation also inhomogeneities in the magnetic field lead to a dephasing of spins and thus to a decay of M_{xy}. The latter one is described by a characteristic time T_2' [50, chapter 3]. The total decay of the transverse magnetisation is then described by the time constant T_2^*, with

$$\frac{1}{T_2^*} = \frac{1}{T_2} + \frac{1}{T_2'}. \tag{3.18}$$

Image Acquisition

The signal acquired in MR imaging is produced by the change of the time-dependent transversal magnetisation. This change of magnetisation results in a change of magnetic flux $\mathrm{d}\Phi/\mathrm{d}t$, which induces a signal in the receiver coil [50, chapter 3]. The specific properties of M_{xy} as noted in equation 3.17 yield $M_{xy} \sim \mathrm{d}M_{xy}/\mathrm{d}t$. The signal $S(t)$ is proportional to $\mathrm{d}M_{xy}/\mathrm{d}t$ and thus proportional to M_{xy}.

It is not possible to measure the magnetisation at each voxel, instead the acquired signal covers the magnetisation of a large region. Mathematically the total signal equation is therefore given by a spatial integral [50, chapter 4] over M_{xy}

$$S(t) \sim \int_x \int_y \int_z M_{xy}(x, y, z, t)\, \mathrm{d}x\, \mathrm{d}y\, \mathrm{d}z. \tag{3.19}$$

The spatial localisation during image acquisition is achieved by applying mag-

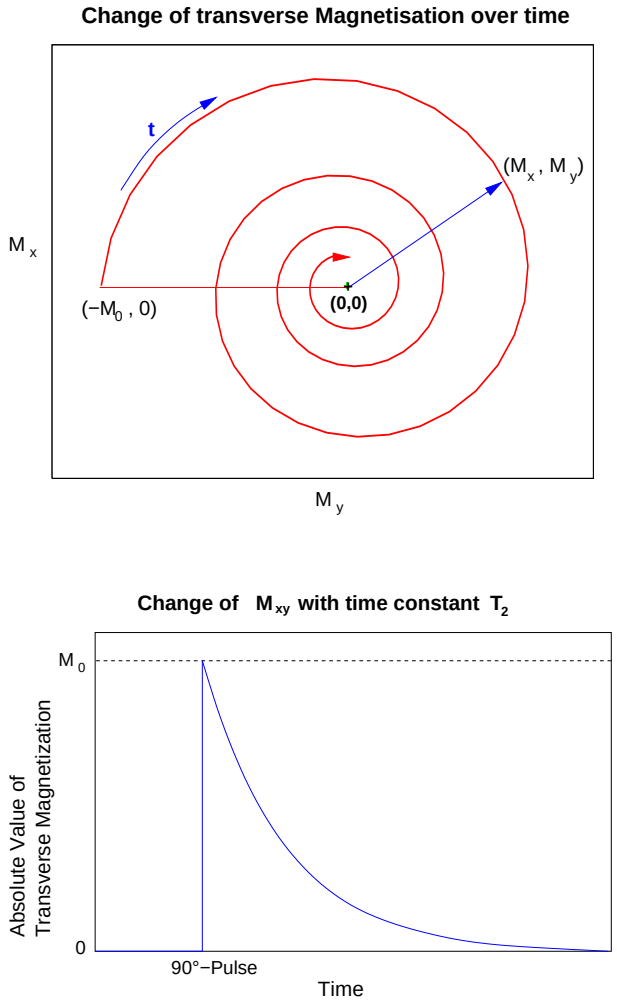

Figure 3.14.: Top: Change of the transverse magnetisation in the complex plane over time. Bottom: The absolute value of M^c_{xy} decays with time constant T_2.

netic field gradients, i.e. the magnetic field can in general be written as

$$B(t) = B_0 + G_x(t)x + G_y(t)y + G_z(t)z. \tag{3.20}$$

With a magnetic field, which is not constant in space and time, equation (eq. 3.17) for the transverse magnetisation changes slightly. The frequency $\omega = \gamma B$ now becomes a function of x, y, z and t [50, chapter 4].

$$M_{xy}(x,y,z,t) = M_{xy0}(x,y,z)\, e^{\frac{-t}{T_2}}\, e^{-i\gamma B_0 t}\, e^{-i\gamma \int_0^t (G_x(t)x + G_y(t)y + G_z(t)z)} \tag{3.21}$$

2D-Imaging In 2D-MR Imaging the object is imaged slice-wise. The selection of a slice of the z-axes can be achieved by first applying a gradient in z-direction. The Larmor frequency is then a function of z. The spins of a single slice can be excited by applying a pulse providing a restricted bandwidth [50, chapter 4].

By integrating over the z-axes in equation 3.19 the magnetisation becomes a function of x and y given by

$$S(t) \sim \int_x \int_y M_{xy0}(x,y)\, e^{\frac{-t}{T_2}}\, e^{-i\gamma B_0 t}\, e^{-i\gamma \int_0^t (G_x(t)x + G_y(t)y)}\, \mathrm{d}x\, \mathrm{d}y \tag{3.22}$$

or

$$S(k_x(t), k_y(t)) \sim \int_x \int_y M_{xy0}(x,y)\, e^{\frac{-t}{T_2}}\, e^{-i\gamma B_0 t}\, e^{-i2\pi k_x(t)x}\, e^{-i2\pi k_y(t)y}\, \mathrm{d}x\, \mathrm{d}y \tag{3.23}$$

with

$$k_i(t) = \frac{\gamma}{2\pi} \int_0^t G_i(\tau)\, \mathrm{d}\tau \qquad i = x, y. \tag{3.24}$$

The equation 3.23 reveals that the measured signal $S(t)$ is the 2D Fourier Transform of the transverse magnetisation. Corresponding to the image space given by the x- and y-axis the space of the measured signal is termed the *k-space*. The k-vector is determined by the gradients applied in x- and y-direction. First of all for image acquisition the gradient in z-direction is applied to select a slice combined with an RF pulse that excites the spins in that slice. Then a gradient in y-direction is applied followed by a gradient in x-direction. The first one changes the phase of the spins depending on their position at the y-axes. The second one is applied during signal acquisition and directly influences the frequency in the reading-out process. The two processes described are termed *phase encoding* and *frequency encoding*. By varying the gradients G_x and G_y the signal depending on different k-values can be measured, i.e. $S(k_x, k_y)$ is acquired. The signal is given in Fourier space or k-space. An inverse 2D Fourier Transform then produces the two-dimensional image of M_{xy0} [50, chapter 4].

3D-Imaging In 3D MR Imaging the electromagnetic pulse does not excite a single slice but the entire probe, i.e. it is non-selective. The spatial encoding is achieved by applying three spatial gradients. Here, both x- and y-direction are phase-encoded while frequency-encoding is applied in z-direction [49]. The acquired signal now depends on k_x, k_y and k_z according to

$$S(t) \sim S(k_x(t), k_y(t), k_z(t)) \tag{3.25}$$

$$\sim \int_x \int_y \int_z M_{xy0}(x,y,z) e^{\frac{-t}{T_2}} e^{-i\gamma B_0 t} e^{-i2\pi k_x(t)x} e^{-i2\pi k_y(t)y} e^{-i2\pi k_z(t)z} \,\mathrm{d}x\,\mathrm{d}y\,\mathrm{d}z \tag{3.26}$$

and has to be Fourier-transformed in three dimensions to obtain the 3D MR image [50, chapter 4].

Pulse Sequences and Contrast Mechanisms

Principle to Achieve Static Contrasts In 2D-imaging the image is acquired slicewise. However, the entire slice cannot be imaged with one single excitation pulse. During one excitation only one line of the 2D k-space is acquired. Thus, several repeated excitation pulses are necessary to fill the k-space, i.e. to image the whole slice.

By repeating the excitation pulse in different ways several types of contrast mechanisms can be achieved. A sequence of excitation pulses is termed *pulse sequence*. Various pulse sequences can be applied to assess particular tissue properties such as T_1, T_2, T_2^* or the proton density.

To explain the principles of contrast mechanisms let us consider a very simple sequence consisting of repeated 90°-pulses. More sophisticated sequences are described in the next paragraph. Two basic factors describing the simple sequence are the time interval between successive excitation pulses T_R and the time interval between excitation and data acquisition T_E. Let T_R be chosen in a way that the transverse magnetisation is fully recovered before the next excitation pulse is applied. After the time interval T_E the transverse magnetisation is then given by

$$M_{xy} = M_{xy0}\, e^{\frac{-T_E}{T_2}}. \tag{3.27}$$

Since the recovery of the longitudinal magnetisation is considerably longer, the value M_{xy0} depends on the T_1-recovery of the prior pulse. Thus equation 3.27 becomes

$$M_{xy} = M_0\,(1 - e^{\frac{-T_R}{T_1}})\, e^{\frac{-T_E}{T_2}} \tag{3.28}$$

or including also the field inhomogeneities

$$M_{xy} = M_0 \left(1 - e^{\frac{-T_R}{T_1}}\right) e^{\frac{-T_E}{T_2^*}}. \tag{3.29}$$

In MR imaging the contrast C_{AB} between two different types of tissue A and B is important and can be described by the difference in magnetisation [50, chapter 5]

$$C_{AB} = M_{0A} \left(1 - e^{\frac{-T_R}{T_{1A}}}\right) e^{\frac{-T_E}{T_{2A}^*}} - M_{0B} \left(1 - e^{\frac{-T_R}{T_{1B}}}\right) e^{\frac{-T_E}{T_{2B}^*}}. \tag{3.30}$$

By controlling the parameters T_R and T_E it is possible to vary the influence of T_1 or T_2^* onto C_{AB}. Choosing a very short or very long T_R leads to comparable factors $e^{\frac{-T_R}{T_{1A}}}$ and $e^{\frac{-T_R}{T_{1B}}}$ and thus a minimised T_1-contrast. Accordingly, the T_2^*-contrast is minimised using very short or very long values for T_E. The acquired images showing a specific type of contrast are termed *T_1-weighted* or *T_2^*-weighted*. If both T_1- and T_2^*-contrast are minimised, the obtained contrast is based on the sheer number of protons contained in the tissue examined. This form of contrast is termed *proton density*. In practice it is usually obtained with extremely short T_E-intervals and very long T_R-intervals [50, chapter 5].

Pulse Sequences As described above several variations in the imaging parameters can be utilised to maximize T_1-, T_2- or T_2^*-contrast. In the following some particular pulse sequences are described, which differ slightly from the simple sequence already presented.

A special sequence to increase the T_1-contrast is the so called *inversion recovery sequence*. It is characterised by a 180° pulse and a followed 90° pulse. The 180° pulse flips the magnetisation vector into the negative z-direction, hence the transverse magnetisation is zero and no signal can be measured. After a specific time T_I, the remaining longitudinal component of the magnetisation is flipped into the xy-plane due to the 90°-pulse, generating a measurable signal. This doubles the dynamic range of the signal [50, chapter 5].

Another sequence - the so called *spin echo sequence* - is very common in MR imaging. If applying this sequence, a 90° pulse is applied rotating the magnetisation into the xy-plane. Now the signal decreases mainly due to the field inhomogeneities, i.e. the spins dephase with the time constant T_2^*. After a time $\frac{T_E}{2}$ a 180° pulse is applied, rotating the magnetisation vector along the x-axes. Due to this pulse the spins rephase after the time $\frac{T_E}{2}$. Therefore an additional

signal, a spin echo, can be observed after the time T_E, the echo time. Due to the rephasing effect, the amplitude of the echo is characterised by the time-constant T_2 and not by T_2^*. In fact, a spin echo sequence is the only method to assess T_2, i.e. the raw spin-spin-interaction effect without any field inhomogeneities. To maximize the T_2-contrast one has to choose a long value for T_R and an intermediate value for T_E. If the repitition time T_R is chosen as intermediate and the echo time T_E as short, the T_1-contrast is maximized [50, chapter 5].

Yet another sequence based on echos is the *gradient echo sequence*. Based on this pulse sequence, T_2^**-weighted* images are acquired if T_R is long and T_E provides an intermediate value. It is not possible to measure T_2^* with a refocusing spin-echo sequence since then all effects due to field inhomogeneities would be removed and only T_2 could be measured. Thus, the gradient field applied for spatial localisation is utilised to produce an echo: As a side-effect the gradient applied along the z-axes introduces an additional dephasing effect. Therefore the gradient in z-direction is switched at the beginning of the phase-encoding period. Due to the switched gradient the previously introduced dephasing processes are inverted and a gradient echo occurs. Also T_1-weighted images can be acquired by choosing an intermediate value for T_R and a short value for T_E [50, chapter 5].

The dominating time in the sequences above is the repitition time T_R, which is usually of the order of magnitude of T_1 or longer. Due to this fact, the acquisition times of the images can be undesirably long. Therefore *fast imaging techniques* have been developed. One of these is called *Fast Low Angle Shot* (FLASH), since the magnetisation vector is tilted about an angle $\theta \leq 90^\circ$. Due to the low angle, the relaxation processes are much shorter. In FLASH image acquisition a *gradient echo* is used to produce a measurable signal. The measurable signal is in this case both T_1 and T_2^*-dependent. A variation of the repetition time T_R, echo time T_E and the flip angle θ influences the contrast of the images. The image can provide T_1-weighted or T_2^*-weighted contrast or show the proton density [49].

Figure 3.15 shows example images of tissue imaged with varying contrast mechanisms. At the top T_1- and T_2-weighted images of the brain are presented. At the bottom a T_1-weighted image and a proton-density image of the female breast are shown.

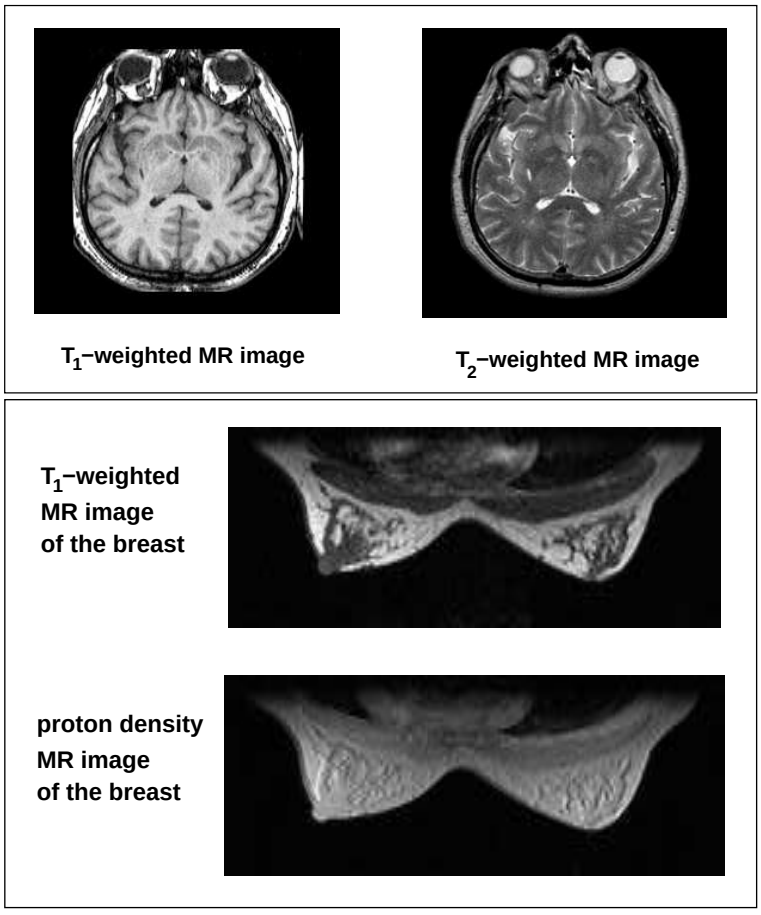

Figure 3.15.: Top: T_1 and T_2-weighted MR images of the brain. Courtesy of the *Whole brain atlas* by Keith A. Johnson, M.D. and J. Alex Becker, Ph.D. [51]. Bottom: T_1-weighted and proton-density MR image of the female breast. Acquired in the UK Breast screening study [52].

3.3.5. DCE-MRI for the Detection of Breast Lesions

The static contrast mechanisms described above are useful to reveal characteristic properties of the female breast. T_2-weighted images e.g. show the content of fibrous tissue, cells and water, while fat tissue is clearly visible at T_1-weighted images. Especially acquisition of the same lesion with different pulse sequences can be quite useful for lesion detection [48, chapter 1]. However, for tumour detection further tissue properties are important such as the vascularity and the permeability. To assess these characteristics the injection of a contrast agent is required. The contrast agent Gd-DTPA[1] is a paramagnetic substance strongly influencing the measured relaxation times. Tissue showing an uptake of the contrast agent therefore provides a significantly increased signal intensity. The monitoring of a contrast agent injected prior to image acquisition is called Dynamic Contrast Enhanced Magnetic Resonance Imaging (DCE-MRI). After injection of Gd-DTPA T_1-weighted images are acquired. According to [48, chapter 2] 3D-FLASH imaging is the most appropriate imaging method for DCE-MRI, since Gd-DTPA provides very high signal intensities in images acquired using a FLASH sequence. The short imaging time is a further advantage since it decreases the amount of the patient's movement during image acquisition. The major advantages of 3D imaging are the simultaneous acquisition of the information of all voxels and the higher Signal-to-Noise-Ratio.

In T_1-weighted images fat and glandular tissue can be clearly distinguished. Figure 3.16 shows as an example a single slice of a three-dimensional, T_1-weighted image of the female breast, acquired using a FLASH-sequence. A slice of the 3D pre-contrast image (prior to Gd-DTPA administration) and the same slice of the 3D first post-contrast image (after Gd-DTPA administration) are shown. As marked in the image, fat tissue provides a very high signal intensity in contrast to glandular tissue. The signal intensity of tumour tissue in the pre-contrast image is quite similar to the signal intensity of glandular tissue. However, after injection of the contrast agent the tumour is characterised by a very high signal intensity due to its high vascularity. The tumour tissue has absorbed the contrast agent and is now clearly visible. In DCE-MRI time series of MR images are acquired. This allows a monitoring of the contrast agent uptake characteristics of tissue over time, thereby providing additional information.

[1] Gadolinium (III) diethyltriaminepentaacetic acid

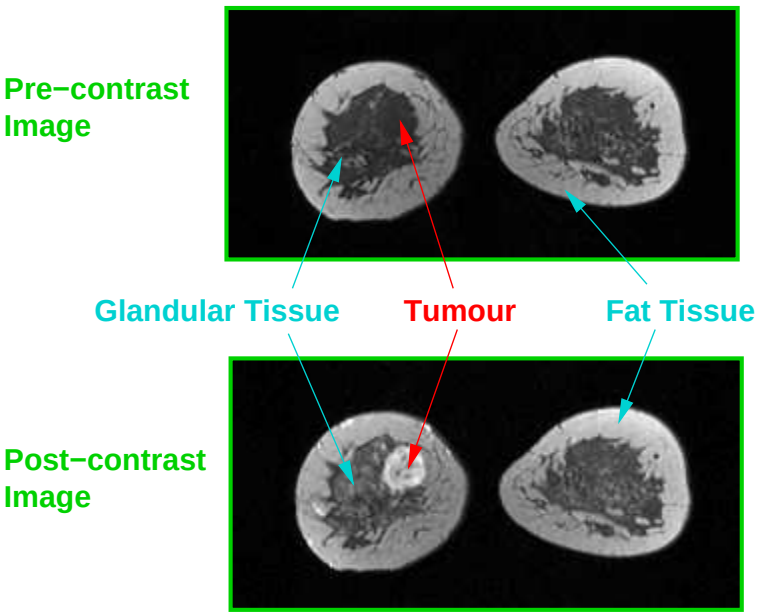

Figure 3.16.: T_1-weighted MR images of the female breast. Top: MR image prior to contrast agent injection. The signal intensity of tumour and glandular tissue is quite similar. Bottom: Same image after injection of the contrast agent. The tumour shows a strong uptake of Gd-DTPA and is now clearly visible.

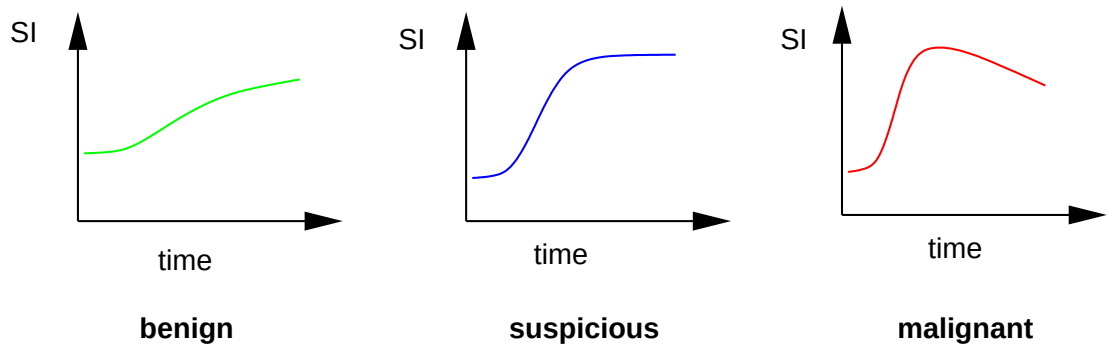

Figure 3.17.: Typical patterns of contrast enhancement. The time-dependent signal intensity (SI) of different types of tissue is shown.

Diagnostic Properties

Both the dynamics and the morphology of the enhanced tissue are considered to provide information on the malignancy of the tumour tissue.

Enhancement Dynamics According to [52] benign tumours usually show a delayed uptake, while malignant tumours are characterised by a fast and high uptake and a washout of the contrast agent afterwards due to their higher vascularity. In Figure 3.17 the typical patterns of contrast enhancement are presented. Signal curves with a fast uptake but without washout are classified as suspicious [52].

According to [48, chapter 3] some more detailed enhancement characteristics of different lesions can be described. Cysts usually do not enhance at all. Fibrosis cannot be seen on DCE-MR images, since this process does not lead to an increase in enhancement. Proliferative dysplasias such as adenosis result in significant but mostly low and delayed enhancement patterns. Inflammatory diseases of the breast can provide a contrast agent uptake usually also with a dynamically delayed characteristic. The enhancement patterns of papillomas can vary. Non-sclerosed papillomas show a variable amount of enhancement, whereas sclerosed papillomas do not enhance [48, chapter 3]. The enhancement patterns of fibroadenomas vary strongly depending on their histological appearance. Fibrous Fibroadenomas containing high amounts of fibrous tissue show only little enhancement. Fibroadenomas with a high amount of glandular tissue enhance significantly. Especially the so called myoxid fibroadenomas enhance very strongly and can therefore be hardly distinguishable from car-

cinomas. Invasive carcinomas are normally characterised by strong and fast enhancement, often followed by a washout. However, the enhancement characteristics can vary slightly depending on the histological appearance. Most of in situ carcinomas enhance, but in approximately 50 % of the cases the enhancement does not show the typical signs of malignancy [48, chapter 3].

Enhancement Morphology In [52] several examples of typical enhancement patterns are presented and described. The classification of the morphology of lesions includes two aspects, the classification of the edge and contour of a lesion and the classification of the pattern of contrast enhancement. The contour of a lesion can be described as well defined, which is usually a sign of benign lesions, poorly defined, which characterises suspicious lesions, and spiculated or focal branching. The latter one is most often a sign of malignancy. The pattern of the contrast enhancement is characterised as centrifugal, homogeneous, heterogeneous, ring-like or not present [52]. These terms describe, which parts of the lesion enhance and how the dynamical enhancement characteristics spatially differ. Benign lesions are usually associated with no or minimal enhancement, centrifugal or homogeneous enhancement. Heterogeneous enhancement is classified as suspicious and ring-like enhancement as malignant [52].

3.3.6. Database Characteristics

Imaging Details The database analysed contains images acquired within the UK breast screening study. Women with an increased genetic risk of developing breast cancer have been screened regularly using DCE-MRI and X-Ray mammography [52]. The database analysed contains T_1-weighted MR images acquired using a 3D FLASH sequence with a flip angle of 35°, repetition time $T_R = 10 - 14\ ms$ and echo time $T_E = 4.2 - 5\ ms$ on 1.5-Tesla systems and $T_E = 7\ ms$ on 1-Tesla systems. Usually two images are acquired before injection of the contrast agent and four or five images afterwards. Thus a time series of MR images is available for monitoring the contrast agent uptake. The acquisition time for each single MR image is approximately 90 s and the spatial resolution is 1.33 mm in both coordinates of the frontal plane and 2.5 mm in the direction orthogonal to the frontal plane as visualised in Figure 3.18 [52].

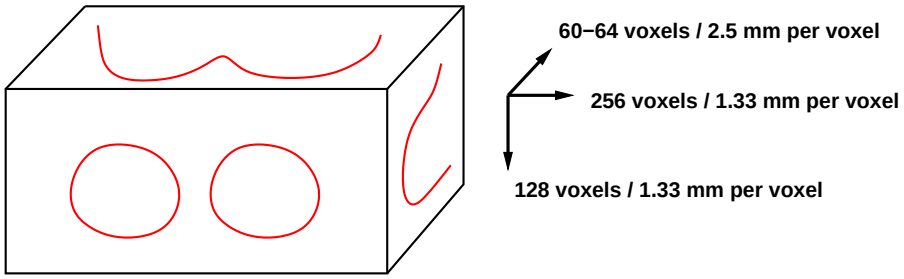

Figure 3.18.: Spatial resolution of the 3D DCE-MR image volumes analysed.

Expert Labels For each lesion analysed an expert label is available, i.e. a medical expert has marked the voxels in the image belonging to the respective lesion. This label is stored as a binary image, i.e. all voxels with the value set to 1 mark the tumour region, all voxels with the value set to 0 the non-tumour region. The labels were generated by Dr. Premina Kessar[1].

Included Lesions Table 3.6 presents an overview of the database analysed and the lesions included. In some cases several lesions have been diagnosed using different diagnostic methods including some types of lesions, which are not visible on MR images. However, usually only a selected number of these lesions is marked by an expert label and therefore relevant in the further analysis. The lesions considered are noted in Table 3.6. Red colour indicates malignant and green colour benign lesions.

[1]Now at: Bromley Hospitals NHS Trust, UK

Collection	Patient	No. of volumes		Diagnosis
		pre	post	
C_1	1	2	5	invasive ductal/NST/lobular carcinoma, Grade 2, vascular invasion
	2	2	5	Sclerosing lymphocytic lobulitis
	3	2	5	invasive tubular carcinoma, Grade 1
	4	2	5	invasive ductal carcinoma - NST, Grade 2 two lesions
	5	2	5	Fibroadenoma, Fibrocystic change
	6	2	5	Fibroadenoma
	7	2	5	invasive ductal carcinoma - NST, Grade 3
	8	2	5	invasive carcinoma, type not assessable, Grade 3
C_2	9	2	5	benign - no additional information
	10	2	4	invasive lobular carcinoma, Grade 2
	11	2	4	invasive ductal carcinoma - NST, Grade 2 two lesions
	12	2	4	Multiple papilloma Fibroadenoma
	13	2	4	invasive ductal carcinoma - NST, Grade 3 two lesions vascular invasion
	14	2	4	benign - no additional information two lesions
	15	2	4	invasive ductal carcinoma, Grade 3 - NST vascular invasion
	16	2	4	invasive ductal carcinoma, Grade 3 - NST malignant - no additional information three lesions
	17	2	4	invasive ductal carcinoma - NST, Grade 2 malignant - no additional information two lesions
	18	2	4	benign lesion - no additional information

Table 3.6.: Content of collections 1 and 2.

4. Methods

L'imagination d'un mathématicien qui crée n'est pas différente de celle d'un poète qui invente.

The imagination of a creative mathematician does not differ from the one of a creative poet.

JEAN-BAPTIST LE ROND D'ALEMBERT

In this chapter the methods utilised in this work are described. As mentioned in the introduction, these are the Discrete Wavelet Transform (DWT) - providing scale-dependent and localised image analysis - as well as methods of dimension reduction. In this way wavelet-based feature spaces can be analysed and new features derived. In the following, the principles of wavelet analysis are presented. Afterwards the methods of dimension reduction utilised for feature space exploration are described.

4.1. Wavelet Analysis

Wavelet Analysis is a powerful mathematical framework applied in the analysis of signals and images [53]. The most important aspect of Wavelet Analysis is that it provides simultaneous time- and frequency analysis. In this section the basic principles of wavelet analysis will be described including its advantages over the more classical Fourier Analysis. For a more detailed description especially with respect to further methods of time-frequency analysis the reader may refer to [53, chapter 4].

4.1.1. From Fourier to Wavelet Analysis

An essential part in signal processing is to extract information from the signal by analysing its frequency contents. The mathematical method to perform

this task is the *Fourier Analysis*. However, the *Fourier Analysis* extracts only global frequency information and one is often interested in the analysis of localised phenomena, i.e. the frequency characteristics of a signal within a specific interval of time. For this purpose the *Windowed Fourier Transform* has been developed, providing Fourier Analysis applied piecewise to the signal, i.e. to intervals. Although the *Windowed Fourier Transform* allows a time-frequency analysis it still has some disadvantages. The most important aspect here is, that the size of the window, i.e. the part of the signal the Fourier Transform is applied to, has to be chosen a priori and may not be suited for the specific purpose. *Wavelet Analysis* is a method which overcomes this disadvantage by adapting the length of the analysed signal to the frequency content.

In this section, the principles of time-frequency analysis and its development will be detailed starting from the *Fourier Transform*. From there, the *Windowed Fourier Transform* will be described and finally the basics of *Wavelet Analysis* are presented.

Fourier Analysis

As mentioned above Fourier Analysis provides the analysis of signals regarding the frequency content. Two types of analysis methods exist, the expansion into a *Fourier Series*, which is appropriate for periodic functions and the *Fourier Transform* applied to non-periodic functions.

Fourier Series A *Fourier Series* is the expansion of a periodic function into a trigonometric polynomial, i.e. a polynomial of cosine and sine functions [54, chapter 2]. For the mathematical description of periodic functions the following definitions are utilised

$$\mathbf{L}^1_{2\pi}(\mathbb{R}) = \left\{ f : \mathbb{R} \to \mathbb{C} : f \; 2\pi-\text{periodic}, \int_{-\pi}^{\pi} |f(t)| \mathrm{d}t < \infty \right\}, \tag{4.1}$$

$$\mathbf{L}^2_{2\pi}(\mathbb{R}) = \left\{ f : \mathbb{R} \to \mathbb{C} : f \; 2\pi-\text{periodic}, \int_{-\pi}^{\pi} |f(t)|^2 \mathrm{d}t < \infty \right\}. \tag{4.2}$$

It can be shown [54, chapter 3] that the trigonometric system $\left\{ \frac{1}{\sqrt{2\pi}} e^{ikt} \right\}_{k=-\infty}^{\infty}$ defines an orthonormal basis in $\mathbf{L}^2_{2\pi}(\mathbb{R})$, which is a Hilbert space with the scalar product

$$\langle f, g \rangle = \int_{-\pi}^{\pi} f(t) \overline{g(t)} \, \mathrm{d}t \tag{4.3}$$

for $f, g \in \mathbf{L}^2_{2\pi}(\mathbb{R})$ and the norm

$$||f|| = \sqrt{\int_{-\pi}^{\pi} |f(t)|^2} \, \mathrm{d}t. \tag{4.4}$$

Please note, that the interval for integration can be replaced by an arbitrary interval of length 2π, due to the periodicity of the function f and g.

Using the relation $e^{ix} = \cos x + i \sin x$ the Fourier Series of a function f can be written as a series of complex exponential functions [54, chapter 2]. If $f(t) \in \mathbf{L}^1_{2\pi}(\mathbb{R})$ the Fourier Series of $f(t)$ is defined as

$$f^{FS}(t) = \sum_{k=-\infty}^{+\infty} c_k e^{ikt} \tag{4.5}$$

with the Fourier coefficients

$$c_k = \frac{1}{2\pi} \int_0^{2\pi} f(t) e^{-ikt} \, \mathrm{d}t. \tag{4.6}$$

The Fourier coefficients $c_{\pm k}$ can be interpreted as the contribution of the frequency $|k|$ to f^{FS}.

The answer to the question, whether the partial sum $f_n^{FS} = \sum_{k=-n}^{+n} c_k e^{ikt}$ of the Fourier Series converges to f for $n \to \infty$ is not obvious. However, the convergence can be proven under certain conditions. For a detailed discussion on the convergence of f_n^{FS} to f the reader may refer to [54, chapter 2]. Here we restrict our considerations to the case $f \in \mathbf{L}^2_{2\pi}(\mathbb{R})$. Due to the property of the set $\left\{ \frac{1}{\sqrt{2\pi}} e^{ikt} \right\}_{k=-\infty}^{\infty}$ to constitute an orthonormal bases in $\mathbf{L}^2_{2\pi}(\mathbb{R})$ it can be shown that f_n^{FS} converges to f in norm, which is defined by

$$f_n^{FS} \underset{\text{in norm}}{\longrightarrow} f \;\Leftrightarrow \int_{-\pi}^{\pi} |f_n^{FS}(t) - f(t)|^2 \mathrm{d}t \underset{n\to\infty}{\to} 0. \tag{4.7}$$

The Fourier Series $f^{FS}(t)$ is the expansion of f in $\mathbf{L}^2_{2\pi}(\mathbb{R})$ and the Fourier coefficients are unique [54, chapter 2].

Fourier Transform Let us now consider non-periodic functions $f : \mathbb{R} \to \mathbb{C}$ and define $\mathbf{L}^1(\mathbb{R})$ and $\mathbf{L}^2(\mathbb{R})$ as

$$\mathbf{L}^1(\mathbb{R}) = \left\{ f : \mathbb{R} \to \mathbb{C} : \int_{-\infty}^{\infty} |f(t)| \mathrm{d}t < \infty \right\}. \tag{4.8}$$

$$\mathbf{L}^2(\mathbb{R}) = \left\{ f : \mathbb{R} \to \mathbb{C} : \int_{-\infty}^{\infty} |f(t)|^2 \mathrm{d}t < \infty \right\}. \tag{4.9}$$

The Fourier Transform measures the content of frequencies in a signal or function $f \in \mathbf{L}^1(\mathbb{R})$ by [54, chapter 7]

$$\tilde{f}(\omega) = \int_{-\infty}^{+\infty} f(t) e^{-i\omega t} \mathrm{d}t. \tag{4.10}$$

If $\tilde{f} \in \mathbf{L}^1(R)$ as well the Inverse Fourier Transform is given by

$$f(t) = \frac{1}{2\pi} \int_{-\infty}^{+\infty} \tilde{f}(\omega) e^{i\omega t} \mathrm{d}\omega. \tag{4.11}$$

and holds for almost every $t \in \mathbb{R}$ in the sense of the Lebesgue measure [54, chapter 7]. As described in [54, chapter 7] the Fourier Transform originally defined on $\mathbf{L}^1(\mathbb{R})$ can be extended to the Hilbert space $\mathbf{L}^2(\mathbb{R})$ if interpreted by a limiting process.

Heisenberg Uncertainty

In the analysis of a signal there is always a trade-off between the resolution in time and frequency. To be more explicit, let us define for a function $f \in \mathbf{L}^2(\mathbb{R})$ the temporal variance σ_t and the frequency variance σ_ω by

$$\sigma_t^2 = \frac{1}{\|f\|^2} \int_{-\infty}^{\infty} (t-u)^2 |f(t)|^2 \mathrm{d}t \tag{4.12}$$

$$\sigma_\omega^2 = \frac{1}{2\pi\|f\|^2} \int_{-\infty}^{\infty} (\omega-\xi)^2 |\hat{f}(\omega)|^2 \mathrm{d}\omega \tag{4.13}$$

with the average values u and ξ given by [53, chapter 2]

$$u = \frac{1}{\|f\|^2} \int_{-\infty}^{\infty} t |f(t)|^2 \mathrm{d}t \tag{4.14}$$

$$\xi = \frac{1}{2\pi\|f\|^2} \int_{-\infty}^{\infty} \omega |\hat{f}(\omega)|^2 \mathrm{d}\omega. \tag{4.15}$$

The temporal and frequency variances measure the energy concentration around the average values, where the energy of a function is given by the $\mathbf{L}^2$-norm. The *Heisenberg Uncertainty Principle* describes the fact that the energy of a function f cannot be arbitrarily well localised in both time and frequency domain. According to this principle the temporal and frequency variances satisfy [53, chapter 2]

$$\sigma_t^2 \sigma_\omega^2 \geq \frac{1}{4} \tag{4.16}$$

where the equality is given only if the function f is a modulated Gaussian, i.e. $f = a \exp[i\xi t - b(t-u)^2]$ [53, chapter 2]. Thus a smaller temporal variance is always associated with a higher frequency variance and vice versa.

Windowed Fourier Transform

The Fourier Analysis described above only measures the global frequency spectrum of functions and signals and thus does not provide any information regarding the time axis. For a simultaneous analysis of time and frequency content of a signal, some modifications are required. One possible solution is the *Windowed Fourier Transform* [53, chapter 4], i.e. a Fourier Transform applied only with respect to finite intervals on the time axis. For $f \in \mathbf{L}^2(\mathbb{R})$

$$WF[f(u,\xi)] = \langle f, g_{u,\xi} \rangle = \int_{-\infty}^{\infty} f(t) g(t-u) e^{-i\xi t} \mathrm{d}t \tag{4.17}$$

Here, $g(t)$ is a real and symmetric window function. It is normalised such that $\|g\| = 1$. The transform given in equation 4.17 is also termed *Short Time Fourier Transform* [53, chapter 4]. With the Fourier Transform of $\hat{g}_{u,\xi}(\omega)$

$$\hat{g}_{u,\xi}(\omega) = \hat{g}(\omega - \xi) e^{-iu(\omega-\xi)} \tag{4.18}$$

the temporal variance σ_t and frequency variance σ_ω of the function $g_{u,\xi}$ are given by

$$\sigma_t^2 = \int_{-\infty}^{\infty} (t-u)^2 |g_{u,\xi}(t)|^2 \mathrm{d}t = \int_{-\infty}^{\infty} t^2 |g(t)|^2 \mathrm{d}t \tag{4.19}$$

$$\sigma_\omega^2 = \frac{1}{2\pi} \int_{-\infty}^{\infty} (\omega - \xi)^2 |\hat{g}_{u,\xi}(\omega)|^2 \mathrm{d}\omega = \frac{1}{2\pi} \int_{-\infty}^{\infty} \omega^2 |\hat{g}(\omega)|^2 \mathrm{d}\omega \tag{4.20}$$

These two values are measures for the resolution of the Windowed Fourier Transform in time and frequency. Both are independent of the average values u and ξ respectively meaning that the resolution of the Windowed Fourier Transform is constant across time and frequency [53, chapter 4]. The resolution depends on the choice of the window function and is best if $g_{u,\xi}$ is a Gaussian [53, chapter 4]. In this case it is called a *Gabor-Transform*. The resolution of a Windowed Fourier Transform can be visualised by plotting boxes with length σ_t and σ_ω - so called Heisenberg Boxes - in the time-frequency plane (Figure 4.1). By scaling the window function in time such that σ_t increases by a factor s the frequency variance decreases by a factor $\frac{1}{s}$ due to equation (4.16). In this way a

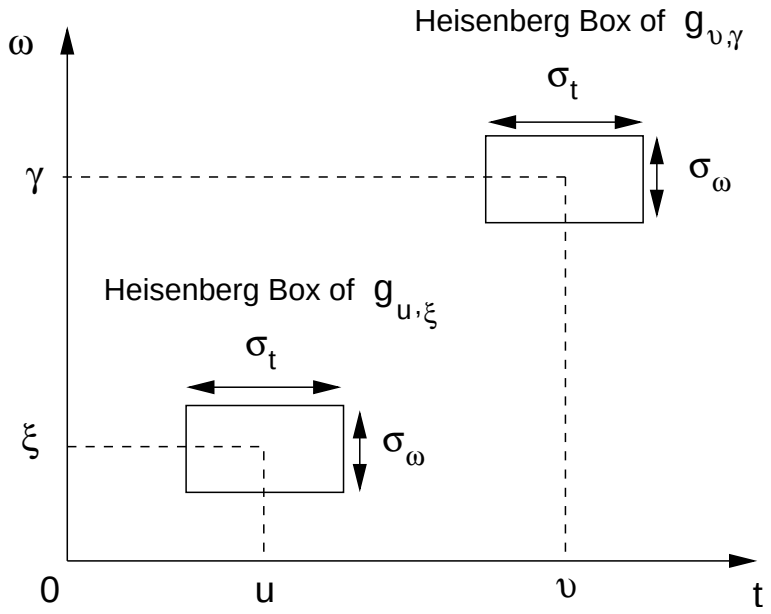

Figure 4.1.: Heisenberg Boxes of the functions $\hat{g}_{u,\xi}(\omega)$ and $\hat{g}_{\nu,\gamma}(\omega)$. The average values in time and frequency differ, but the length of the boxes in time and frequency is the same.

trade-off between time and frequency localisation can be achieved [53, chapter 4]. However, as can be seen in Figure 4.1 the size and shape of the Heisenberg Boxes and thus the resolution is constant in the time-frequency-plane. This is an important limitation of the Windowed Fourier Transform. For the analysis of signals comprising structures of different size it is desirable to perform a transform that adapts to structures with different types of support.

Wavelet Transform

The limitations of the Windowed Fourier Transform can be overcome if the function $g_{u,\xi}$ is replaced by $\psi_{a,b}(t)$ which is defined by

$$\psi_{a,b} : \mathbb{R} \to \mathbb{C} \qquad \psi_{a,b}(t) = \frac{1}{\sqrt{|a|}}\psi(\frac{t-b}{a}) \tag{4.21}$$

with the scaling parameter a and the shifting parameter b [53, chapter 4]. Jean Morlet introduced this type of analysis and termed the function "ondelette" or in english "wavelet". Here the function $\psi(t)$ is the so-called *mother wavelet* and the $\psi_{a,b}(t)$ are shifted and dilated versions of the mother wavelet (Figure 4.2).

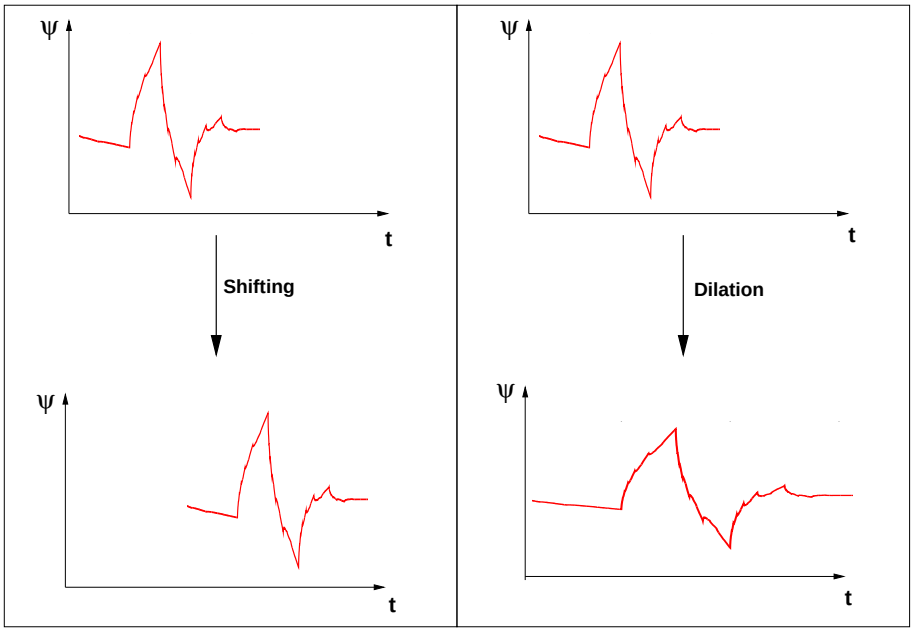

Figure 4.2.: The shifting and dilation of a wavelet. Note, that the wavelet function shown here is just an example. The general construction of such functions is explained in one of the following paragraphs.

Thus the most important difference of a wavelet in comparison to the function $g_{u,\xi}$ in the Windowed Fourier Transform is the localisation across the time-frequency plane. It can be shown [53, chapter 4] that the time- and frequency variation of a wavelet $\psi_{a,b}$ depends on the scaling parameter a in the following way.

$$\sigma_t^2(\psi_{a,b}) = a^2\sigma_t^2 \tag{4.22}$$

$$\sigma_\omega^2(\psi_{a,b}) = \frac{1}{a^2}\sigma_\omega^2 \tag{4.23}$$

with $\sigma_t = \int_{-\infty}^{\infty} t^2|\psi(t)|^2 \mathrm{d}t$ and $\sigma_\omega = \int_{-\infty}^{\infty} \omega^2|\psi(\hat{\omega})|^2 \mathrm{d}\omega$. Thus the area of a Heisenberg Box is constant across the time frequency plane but the shape of the Heisenberg Box varies. This means that the resolution in time and frequency is not constant but depends on the parameter a (Figure 4.3). In this way the scaling parameter a controls the resolution of the signal structures analysed. The parameter η in Figure 4.3 is the average value of the Fourier transformed

mother wavelet $\hat{\psi}(\omega)$

$$\eta = \frac{1}{2\pi} \int_0^\infty \omega |\hat{\psi}(\omega)|^2 \mathrm{d}\omega. \tag{4.24}$$

As can be seen in Figure 4.3 higher frequencies are associated to Heisenberg Boxes which are smaller in the time domain and thus provide a higher resolution in time. This adaption of high frequencies to a small scale time resolution and low frequencies to large scale time resolution constitutes the adaptivity we have missed regarding the Windowed Fourier Transform.

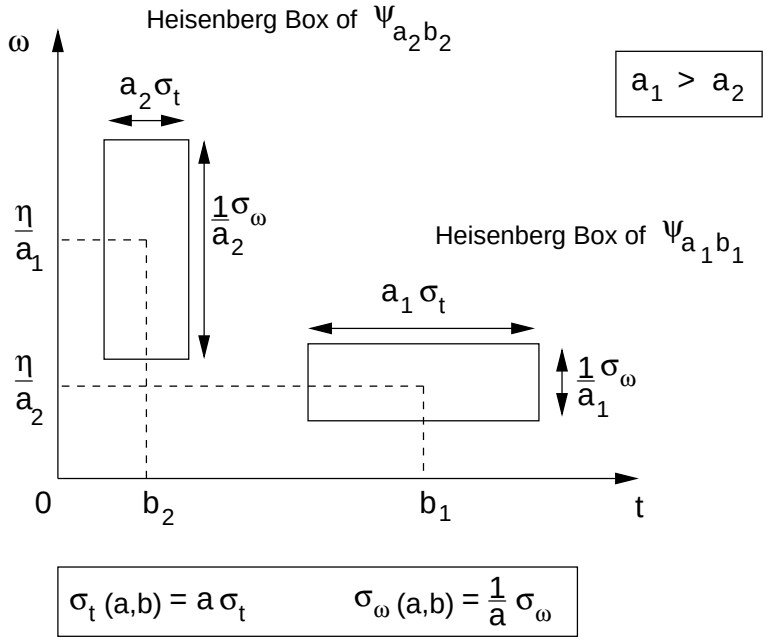

Figure 4.3.: Heisenberg Boxes of the wavelets ψ_{a_1,b_1} and ψ_{a_2,b_2}. The length of the boxes in time and frequency varies while the area of the boxes is constant.

4.1.2. Continuous and Discrete Wavelet Transform

A function $f(t)$ has to fulfil certain conditions to serve as a wavelet. These conditions depend on the type of the Wavelet Transform. For the Continuous Wavelet Transform this is the so called *admissibility condition*. For the Discrete Wavelet Transform further properties are required. The Discrete Wavelet Transform is usually discussed using the formalism of *frames*.

The Continuous Wavelet Transform The *admissibility condition* [55, chapter 2] for a wavelet $\psi(t) \in \mathbf{L}^2(\mathbb{R})$ is given by

$$C_\psi = \int_{-\infty}^{\infty} \frac{|\hat{\psi}(\omega)|^2}{\omega} \mathrm{d}\omega < \infty. \tag{4.25}$$

From equation (4.25) one can easily derive the condition $\int \psi(t)dt = 0$ [55, chapter 2], which means that wavelets have a zero average, i.e. wavelets are oscillating functions. For a wavelet $\psi(t) \in \mathbf{L}^2(\mathbb{R})$ holding the admissibility condition the *Continuous Wavelet Transform* is defined by [55, chapter 2]

$$W[f(a,b)] = \int_{-\infty}^{\infty} f(t) \frac{1}{\sqrt{a}} \psi^*(\frac{t-b}{a}) \mathrm{d}t. \tag{4.26}$$

The Continuous Wavelet Transform $W[f(a,b)]$ of a signal f describes how far the details of the scale a contribute to the signal around the time point b. The exact properties strongly depend on the chosen mother wavelet.

In [53, chapter 4] reconstruction of the signal $f(t)$ in case of a real wavelet $\psi \in \mathbf{L}^2(\mathbb{R})$ holding the slightly modified admissibility condition

$$C_\psi = \int_{0}^{\infty} \frac{|\hat{\psi}(\omega)|^2}{\omega} \mathrm{d}\omega < \infty \tag{4.27}$$

is defined by

$$f(t) = \frac{1}{C_\psi} \int_0^\infty \int_{-\infty}^{\infty} W[f(a,b)] \psi_{a,b} \frac{\mathrm{d}a\ \mathrm{d}b}{a^2}. \tag{4.28}$$

Discrete Wavelet Transform The Continuous Wavelet Transform provides a highly redundant description of a signal or function $f(t)$. This can intuitively be seen by the following observation. If scaling parameter a and shifting parameter b are continuous variables, independent of each other, the corresponding Heisenberg boxes strongly overlap in the time-frequency-plane. To reduce the redundancy, we discretise the parameters a and b. This results in a set of function $\psi_{a_{j,k},b_{j,k}}$, which under certain conditions is sufficient to reconstruct the signal f in a stable manner. The transform based on this set of functions is termed *Discrete Wavelet Transform*.

To describe the requirements on the set of wavelet functions we will refer to the formalism of frames. According to [53, chapter 5] a frame is a family of vectors $\{\varphi_n\}_{n\in\Gamma}$ that characterises a signal f by its inner products $\{\langle f, \varphi_n \rangle\}_{n\in\Gamma}$.

Here, Γ is a infinite or finite set of indices. Given a Hilbert space $\mathbf{H}$ and a sequence $\{\varphi_n\}_{n\in\Gamma}$ in $\mathbf{H}$, the sequence $\{\varphi_n\}_{n\in\Gamma}$ is a frame of $\mathbf{H}$ if there exist two constants $A > 0$ and $B > 0$ such that for any $f \in \mathbf{H}$

$$A\|f\|^2 \leq \sum_{n\in\Gamma} |\langle f, \varphi_n\rangle|^2 \leq B\|f\|^2. \tag{4.29}$$

In the case that $A = B$ the frame is said to be tight [53, chapter 5]. The linear operator U from $\mathbf{H}$ to $\mathbf{l}^2(\Gamma) = \{x : ||x||^2 = \sum_{n\in\Gamma} |x_n|^2 < \infty\}$ given by

$$(Uf)_n = \langle f, \varphi_n\rangle \tag{4.30}$$

is called *frame operator*. The dual frame $\tilde{\varphi}_n$ defined by

$$\tilde{\varphi_n} = (U^*U)^{-1}\varphi_n \tag{4.31}$$

with the adjoint operator U^* satisfies

$$\forall f \in \mathbf{H}, \quad \frac{1}{B}\|f\|^2 \leq \sum_{n\in\Gamma} |\langle f, \tilde{\varphi_n}\rangle|^2 \leq \frac{1}{A}\|f\|^2, \tag{4.32}$$

and

$$f = \tilde{U}^{-1}Uf = \sum_{n\in\Gamma} \langle f, \varphi_n\rangle \tilde{\varphi_n} = \sum_{n\in\Gamma} \langle f, \tilde{\varphi_n}\rangle \varphi_n \tag{4.33}$$

with $\tilde{U}^{-1} = (U^*U)^{-1}U^*$. The proof is given in [53, chapter 5]. If a frame $\{\varphi_n\}_{n\in\Gamma}$ is linearly independent (i.e. a Riesz basis), the dual frame $\{\tilde{\varphi_n}\}_{n\in\Gamma}$ is also linearly independent and called the dual Riesz basis [53, chapter 5]. Dual Riesz bases are so called biorthogonal families of vectors, which means that $\langle \varphi_p, \tilde{\varphi}_n\rangle = \delta_{p,n}$. *Orthonormal bases* are also special frames, i.e. they are tight frames with normalised $\{\varphi_n\}_{n\in\Gamma}$ and $A = B = 1$.

Using the definitions above, we can describe the requirements for the Discrete Wavelet Transform. A discretisation of the parameters a and b leads to a set of wavelet function $\psi_{j,k} = \psi_{a_j,b_{j,k}}, j, k \in \mathbb{Z}$ obtained from the $\psi_{a,b}$ by

$$a_j = \sigma^j \qquad b_{j,k} = k\sigma^j\tau \tag{4.34}$$

$$\psi_{j,k} = \frac{1}{\sigma^{j/2}}\psi\left(\frac{t - k\sigma^j\tau}{\sigma^j}\right) \tag{4.35}$$

with the constants $\sigma > 1$ and $\tau > 0$. The inner products of $\psi_{j,k}$ with the signal or function $f(t)$

$$\langle f, \psi_{j,k}\rangle = Wf(k\sigma^j\tau, \sigma_j) \tag{4.36}$$

sample the Continuous Wavelet Transform at time intervals $\sigma^{-j}\tau$. If the $\psi_{j,k}$ constitute a frame, then the inner products are sufficient to reconstruct the signal $f(t)$ in a complete and stable manner, i.e. the inner products are sufficient to characterise $f(t)$. In this case $f(t)$ is given by

$$f = \sum_{j,k} \langle f, \psi_{j,k} \rangle \tilde{\psi}_{j,k}. \tag{4.37}$$

The necessary and sufficient conditions on ψ, σ and τ to obtain $\psi_{j,k}$ constituting a frame are given in [53, chapter 5], [55, chapter 3].

A very common choice for the scaling parameter σ also used in the following paragraphs is $\sigma = 2$, the so called *dyadic* case.

It is not only possible to construct general wavelet frames but also to construct biorthogonal and orthonormal wavelet bases. The framework for this construction is the multiresolution analysis described in the next section.

4.1.3. Multiresolution Analysis

As described in the previous paragraph, it is possible to construct wavelets ψ such that the dilated and translated family of functions

$$\left\{ \psi_{j,k}(t) = \frac{1}{\sqrt{2^j}} \psi \left(\frac{t - 2^j k}{2^j} \right) \right\}_{(j,k) \in \mathbb{Z}^2} \tag{4.38}$$

is an orthonormal basis of $\mathbf{L}^2(\mathbb{R})$ [53, chapter 7]. In that case any function $f(t) \in \mathbf{L}^2(\mathbb{R})$ is given by

$$f(t) = \sum_{j=-\infty}^{+\infty} \sum_{k=-\infty}^{+\infty} \langle f, \psi_{j,k} \rangle \psi_{j,k} \tag{4.39}$$

with the *wavelet coefficients* $d_{j,k} = \langle f, \psi_{j,k} \rangle$. Scaling or dilation is indicated by j while k is the translation index. In this section, it is described how these orthonormal bases are constructed. For this purpose the principle of *multiresolution approximation* or *multiresolution analysis* is essential. According to [53, chapter 7] a sequence of closed subspaces $\{\mathbf{V}_j\}_{j \in \mathbb{Z}}$ of $\mathbf{L}^2(\mathbb{R})$ is a multiresolution approximation if the following statements are satisfied:

$$\forall (j,k) \in \mathbb{Z}^2, \quad f(t) \in \mathbf{V}_j \Leftrightarrow f(t - 2^j k) \in \mathbf{V}_j, \tag{4.40}$$

$$\forall j \in \mathbb{Z}, \quad \mathbf{V}_{j+1} \subset \mathbf{V}_j, \tag{4.41}$$

$$\forall j \in \mathbb{Z}, \quad f(t) \in \mathbf{V}_j \Leftrightarrow f(\frac{t}{2}) \in \mathbf{V}_{j+1}, \tag{4.42}$$

$$\lim_{j \to +\infty} \mathbf{V}_j = \bigcap_{j=-\infty}^{+\infty} \mathbf{V}_j = \{0\}, \tag{4.43}$$

$$\lim_{j \to -\infty} \mathbf{V}_j = \text{Closure} \left(\bigcup_{j=-\infty}^{+\infty} \mathbf{V}_j \right) = \mathbf{L}^2(\mathbb{R}). \tag{4.44}$$

$$\text{There exists such } \theta \text{ that } \{\theta(t-n)\}_{n \in \mathbb{Z}} \text{ is a Riesz basis of } \mathbf{V}_0. \tag{4.45}$$

Equation (4.40) describes the invariance of $\mathbf{V}_j$ by translations proportional to 2^j. Due to equation (4.41) an approximation at a specific level of resolution contains the necessary information to describe the function at a coarser level of resolution. According to equation (4.42) the dilation of a function $f(t)$ by a factor of 2 defines an approximation at a coarser resolution. With increasing scale j more and more details are lost, this results in equation (4.43). Equation (4.44) implies that with increasing resolution, i.e. decreasing scale j, the approximation converges to the original signal. The approximation of a signal $f(t)$ corresponding to a resolution of scale j is the orthogonal projection of $f(t)$ onto the subspace $\mathbf{V}_j$.

By orthogonalising the Riesz basis θ of equation (4.45) it is possible to obtain orthonormal bases of the subspaces $\mathbf{V}_j$ further denoted with $\{\phi_{j,k}\}_{k \in \mathbb{Z}}$ [53, chapter 7]. To assure that the set of functions $\{\phi_{j,k}\}_{k \in \mathbb{Z}}$ is an orthonormal basis of $\mathbf{V}_j$ for all $j \in \mathbb{Z}$ the Fourier Transform of ϕ has to hold the condition

$$\hat{\phi}(\omega) = \frac{\hat{\theta}(\omega)}{(\sum_{k=-\infty}^{+\infty} |\hat{\theta}(\omega + 2k\pi)|^2)^{\frac{1}{2}}}. \tag{4.46}$$

The function ϕ is called the "scaling function" of the multiresolution analysis. Since the $\mathbf{V}_j$ are closed subspaces of $\mathbf{L}^2(\mathbb{R})$, they are Hilbert spaces. Therefore we can define the orthogonal complement of a subspace $\mathbf{V}_j$ in $\mathbf{V}_{j-1}$ according to

$$\mathbf{V}_{j-1} = \mathbf{V}_j \oplus \mathbf{W}_j \tag{4.47}$$

with

$$\mathbf{W}_j \perp \mathbf{W}_{j'} \quad \text{if } j \neq j' \tag{4.48}$$

and

$$\mathbf{L}^2(\mathbb{R}) = \bigoplus_{j \in \mathbb{Z}} \mathbf{W}_j. \tag{4.49}$$

Let $P_{\mathbf{V}_j}$ denote the operator of the orthogonal projection of the function $f(t)$ onto the subspace $\mathbf{V}_j$. Then equation 4.47 is equivalent to

$$P_{\mathbf{V}_{j-1}} f = P_{\mathbf{V}_j} f + P_{\mathbf{W_j}} f. \tag{4.50}$$

According to [55, chapter 5] it can be shown that if a scaling function ϕ and a multiresolution approximation according to equations 4.40-4.44 exist, then an orthonormal wavelet basis $\{\psi_{j,k}\}_{(j,k)\in\mathbb{Z}^2}$ of $\mathbf{L}^2(\mathbb{R})$ exists, such that

$$P_{\mathbf{V}_{j-1}} f = P_{\mathbf{V}_j} f + \sum_{k=-\infty}^{+\infty} \langle f, \psi_{j,k} \rangle \psi_{j,k}. \tag{4.51}$$

In the following we will construct the wavelet basis $\{\psi_{j,k}\}_{(j,k)\in\mathbb{Z}^2}$ using the scaling function ϕ. Due to the multiresolution properties described $\{\phi(t-k)\}_{k\in\mathbb{Z}}$ is a orthonormal basis of $\mathbf{V}_0$. Therefore the scaling function $\frac{1}{\sqrt{2}}\phi(\frac{t}{2}) \in \mathbf{V}_1 \subset \mathbf{V}_0$ can be decomposed as

$$\frac{1}{\sqrt{2}}\phi\left(\frac{t}{2}\right) = \sum_{k=-\infty}^{+\infty} h_k \phi(t-k) \tag{4.52}$$

or

$$\phi(t) = \sqrt{2} \sum_{k=-\infty}^{+\infty} h_k \phi(2t-k) \tag{4.53}$$

with

$$h_k = \left\langle \frac{1}{\sqrt{2}}\phi(\frac{t}{2}), \phi(t-k) \right\rangle \tag{4.54}$$

$$\sum_{k=-\infty}^{+\infty} h_k \overline{h_{k+2n}} = \delta_{0,n} \tag{4.55}$$

The h_k can be interpreted as a discrete filter and are therefore termed *filter coefficients*. The corresponding wavelets constituting a basis of $\mathbf{L}^2(\mathbb{R})$ can be constructed as [55, chapter 5]

$$\psi(t) = \sqrt{2} \sum_{k=-\infty}^{+\infty} g_k \phi(2t-k) \tag{4.56}$$

with

$$g_k = (-1)^k \overline{h_{1-k}}. \tag{4.57}$$

4.1.4. The Fast Wavelet Transform

The principles of Multiresolution Analysis lead to an efficient algorithm for the computation of wavelet coefficients, the so called *Fast Wavelet Transform*. Given the orthonormal bases $\{\phi_{j,k}\}_{k\in\mathbb{Z}}$ of $\mathbf{V}_j$ and $\{\psi_{j,k}\}_{k\in\mathbf{Z}}$ of $\mathbf{W}_j$. The projections in these spaces are

$$a_{j,k} = \langle f, \phi_{j,k}\rangle \quad \text{and} \quad d_{j,k} = \langle f, \psi_{j,k}\rangle. \tag{4.58}$$

The $d_{j,k}$ are the wavelet coefficients as defined above. The $a_{j,k}$ are the projections of the signal onto the shifted and dilated versions of the scaling function and therefore often termed as "scaling function coefficients". According to [53, chapter 7] these coefficients can be computed successively with a cascade of discrete convolutions and subsamplings according to the decomposition scheme

$$a_{j+1,p} = \sum_{k=-\infty}^{+\infty} h_{k-2p} a_{j,k} \tag{4.59}$$

$$d_{j+1,p} = \sum_{k=-\infty}^{+\infty} g_{k-2p} a_{j,k}. \tag{4.60}$$

The reconstruction is computed as follows.

$$a_{j,p} = \sum_{k=-\infty}^{+\infty} h_{p-2k} a_{j+1,k} + \sum_{k=-\infty}^{+\infty} g_{p-2k} d_{j+1,k} \tag{4.61}$$

This algorithm of equations (4.59) and (4.60) is called "Mallat-Algorithm" or "pyramid algorithm" [53, chapter 7]. The wavelet coefficients are often indicated as "details" since they encode the scale-dependent details of the signal. In contrast to this, the scaling function coefficients are usually denoted as "approximation" or "approximation coefficients" since they represent a coarser version of the original signal. (This of course explains the variable names, $a_{j,k}$ for approximation and $d_{j,k}$ for details.) In Figure 4.4 the principle of the algorithm is demonstrated. Please note the subsampling or downsampling by 2 of the coefficients as indicated in Figure 4.4 using up- or down-pointing arrows. Applying this decomposition iteratively leads to the scale-wise computation of all wavelet coefficients, the *Fast Wavelet Transform*. The scale-wise reconstruction of the original signal is the *Fast Inverse Wavelet Transform* [53, chapter 7]. Both transforms are shown in Figure 4.5. The Wavelet Transform described is a non-redundant transform, i.e. a signal providing n samples is transformed

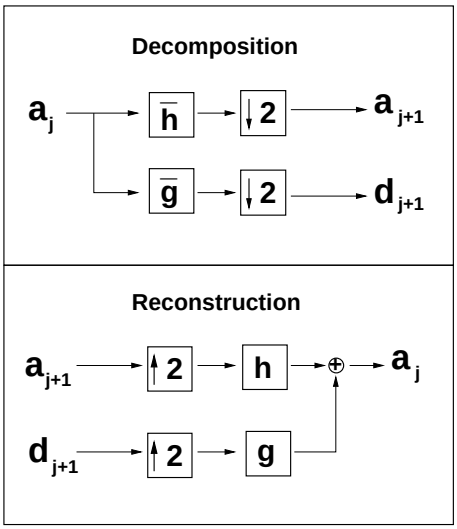

Figure 4.4.: The Mallat-Algorithm as described in equations 4.59 and 4.60.

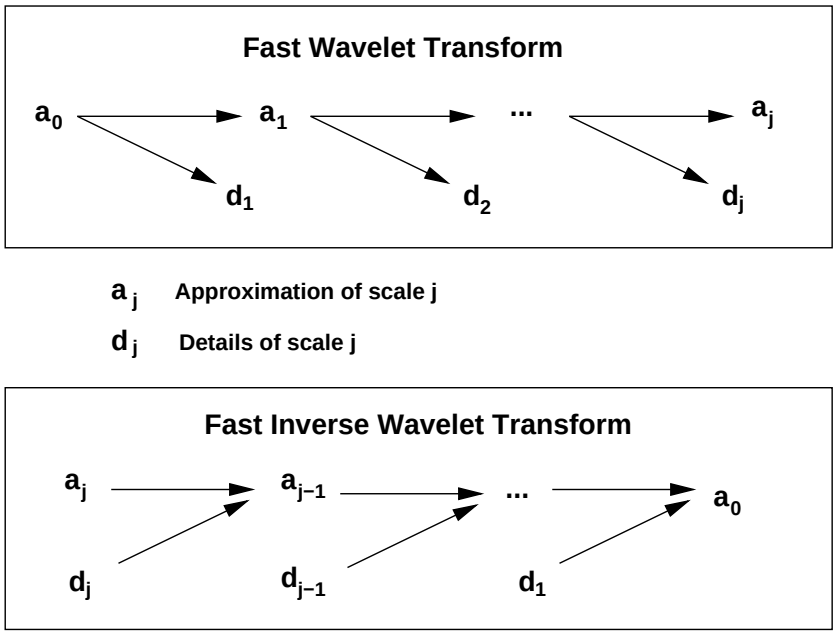

Figure 4.5.: The Fast Wavelet Transform and the Fast Inverse Wavelet Transform. The arrows indicate the decomposition or reconstruction step.

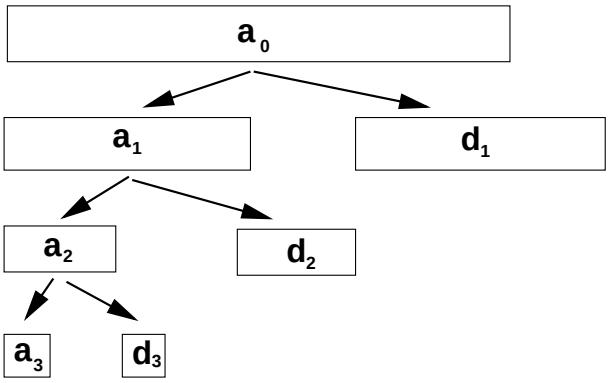

Figure 4.6.: During a Fast Wavelet Transform the number of coefficients is halved at each level of the transform.

into n coefficients. Due to the subsampling by 2 already indicated in Figure 4.4 the number of coefficients decreases with a factor 2 at each scale. This fact is shown in Figure 4.6, where the coefficients at each scale are indicated by bars. The length of the bars show the number of coefficients at the different scales.

Practical Considerations One particular aspect has to be mentioned to clarify the relation between the FWT (Figure 4.6) producing wavelet coefficients of a finite number of scales and the multiresolution approximation (equations 4.40-4.44) defined for an infinite number of scales j. The multiresolution approximation has been discussed with respect to continuous functions defined on $\mathbf{L}^2$. On the other hand, real-world signals provide a limited resolution and a limited length, i.e. they are composed of a finite number of samples. Consequently, the number of scales considered in the analysis of such a signal is also finite. The finest scale, relevant for the signal characteristics, is determined by the resolution of the signal. The coarsest relevant scale is determined by its length.

A simple and usual way to start a FWT in practice is the following. The samples of the signal are considered as the scaling function coefficients a_j of the finest relevant scale (aside from a normalisation) [53, chapter 7]. These coefficients are then decomposed into the wavelet and scaling function coefficients of the next coarser scale. By iterating this decomposition scheme all required wavelet coefficients can be computed.

Furthermore, as demonstrated above, the filter coefficients h_k and g_k are sufficient to compute all desired wavelet coefficients. The functions ϕ and ψ are

not required in the pyramid algorithm - a very important aspect for the applicability of this decomposition scheme.

4.1.5. Wavelet Transform in Higher Dimensions

There are several methods for defining wavelet functions in higher dimensions. In case of so called separable wavelets, the wavelet functions in higher dimensions are products of the one-dimensional wavelet or scaling functions. We can distinguish two types of those separable wavelet bases. In the following the principles are explained in two dimensions and then extended to higher dimensions. One possibility of basis construction is to start with a one-dimensional wavelet basis $\{\psi_{j,k}\}_{(j,k)\in\mathbb{Z}^2}$ of $\mathbf{L}^2(\mathbb{R})$ and define the two-dimensional wavelet basis of $\mathbf{L}^2(\mathbb{R}^2)$ according to

$$\left\{\psi_{j_1,k_1}(x_1)\psi_{j_2,k_2}(x_2)\right\}_{(j_1,j_2,k_1,k_2)\in\mathbb{Z}^4}. \tag{4.62}$$

This is termed the *standard construction scheme* in [56, chapter 3] and leads to a *standard decomposition* of the two-dimensional signal. One major disadvantage is, that due two different scale indices j_1 and j_2, the detail information of different scales is mixed in the transform. This effect is often undesirable [53, chapter 7]. Therefore, in this work a different type of basis construction in higher dimensions is applied.

It is possible to define a (separable) multiresolution approximation in $\mathbf{L}^2(\mathbb{R}^2)$. Let $\{\mathbf{V}_j\}_{j\in\mathbb{Z}}$ be a multiresolution of $\mathbf{L}^2(\mathbb{R})$ with the scaling function ϕ such that $\{\phi_{j,m}\}_{m\in\mathbb{Z}}$ is an orthonormal basis of $\mathbf{V}_j$. A separable multiresolution of $\mathbf{L}^2(\mathbb{R}^2)$ is then given by $\{\mathbf{V_j}^2\}_{j\in\mathbb{Z}}$ with

$$\mathbf{V}_j^2 = \mathbf{V}_j \otimes \mathbf{V}_j. \tag{4.63}$$

In that case the two-dimensional scaling function is given by

$$\phi^2(\mathbf{x}) = \phi(x_1)\phi(x_2) \tag{4.64}$$

and the orthonormal basis of $\mathbf{V}_j^2$ by [53, chapter 7]

$$\left\{\phi_{j,k}^2(\mathbf{x}) = \phi_{j,k_1}(x_1)\phi_{j,k_2}(x_2) = \frac{1}{2^j}\phi\left(\frac{x_1 - 2^j k_1}{2^j}\right)\phi\left(\frac{x_2 - 2^j k_2}{2^j}\right)\right\}. \tag{4.65}$$

Let ψ be the wavelet corresponding to the scaling function ϕ and $\mathbf{W}_j^2$ the orthogonal complement of $\mathbf{V}_j^2$ in $\mathbf{V}_{j-1}^2$

$$\mathbf{V}_{j-1}^2 = \mathbf{V}_j^2 \oplus \mathbf{W}_j^2. \tag{4.66}$$

The two-dimensional wavelet functions are defined as

$$\psi^1(\mathbf{x}) = \phi(x_1)\psi(x_2) \quad \psi^2(\mathbf{x}) = \psi(x_1)\phi(x_2) \quad \psi^3(\mathbf{x}) = \psi(x_1)\psi(x_2) \tag{4.67}$$

with

$$\psi^n_{j,k_1,k_2}(\mathbf{x}) = \frac{1}{2^j}\psi^n\left(\frac{x_1 - 2^j k_1}{2^j}, \frac{x_2 - 2^j k_2}{2^j}\right). \tag{4.68}$$

In [53, chapter 7] it is shown that the set

$$\{\psi^1_{j,k_1,k_2}, \psi^2_{j,k_1,k_2}, \psi^3_{j,k_1,k_2}\}_{(k_1,k_2)\in\mathbb{Z}^2} \tag{4.69}$$

for fixed j is an orthonormal basis of $\mathbf{W}_j^2$ and the set

$$\{\psi^1_{j,k_1,k_2}, \psi^2_{j,k_1,k_2}, \psi^3_{j,k_1,k_2}\}_{(j,k_1,k_2)\in\mathbb{Z}^3} \tag{4.70}$$

is an orthonormal basis of $\mathbf{L}_j^2$. In [56, chapter 3] this is called the *non-standard construction* of a basis.

The corresponding computation of the two-dimensional wavelet and scaling function coefficients is shown in Figure 4.7. Figure 4.8 demonstrates the Fast Wavelet Transform in two dimensions. The three different types of wavelet coefficients encode details of the image in vertical, horizontal and diagonal direction respectively.

This principle can easily be extended on higher dimensions ($n > 2$). We consider a separable multiresolution of $\mathbf{L}^2(\mathbb{R}^n)$ given by subspaces

$$\mathbf{V}_j^n = \underbrace{\mathbf{V}_j \otimes \mathbf{V}_j \otimes ... \otimes \mathbf{V}_j}_{\text{n times}}. \tag{4.71}$$

The n-dimensional scaling function is then defined by

$$\phi^n(\mathbf{x}) = \phi(x_1)\phi(x_2)...\phi(x_n). \tag{4.72}$$

Corresponding to equation (4.67) the n-dimensional wavelets are given by product functions composed from the one-dimensional wavelet and scaling functions.

It is also possible to construct non-separable wavelet bases, but these bases are not very common in image processing [53, chapter 7].

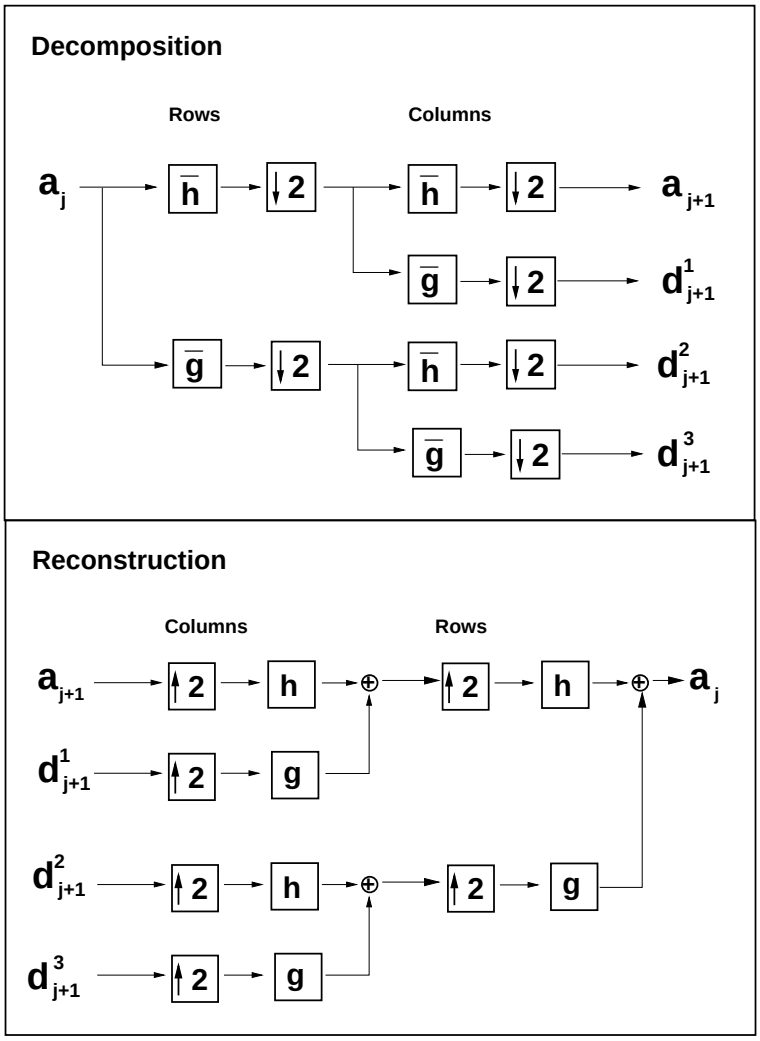

Figure 4.7.: The pyramid algorithm in two dimensions.

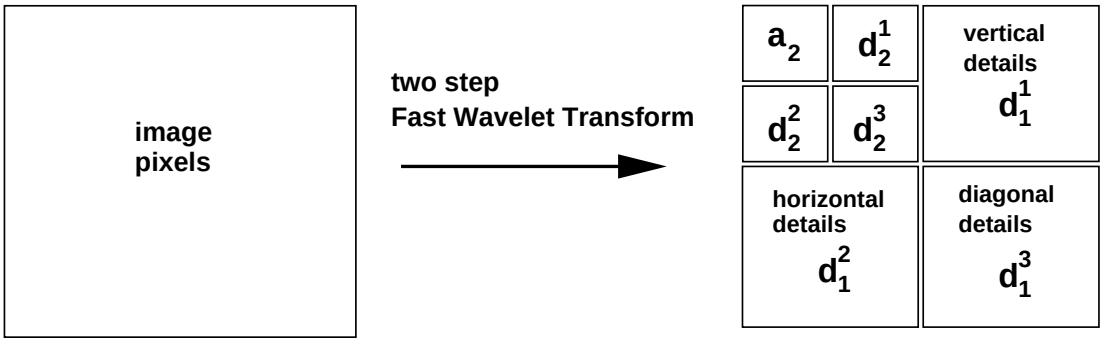

Figure 4.8.: The two-dimensional Fast Wavelet Transform. The image pixels are decomposed into the scale-dependent details (wavelet coefficients) in horizontal, vertical and diagonal direction.

4.1.6. Wavelet Bases

As mentioned above, multiresolution analysis allows to construct orthonormal wavelet bases. In the following a short overview is given regarding the construction and the properties of some important orthonormal wavelet bases. Then the generalisation of the multiresolution framework for biorthogonal Riesz bases is discussed.

Orthogonal Bases

To construct an orthonormal wavelet basis we first have to find a scaling function defining a multiresolution analysis. The Fourier Transform of equation (4.52) leads to [53, chapter 7]

$$\hat{\phi}(2\omega) = \frac{1}{\sqrt{2}} m_0(\omega)\hat{\phi}(\omega) \tag{4.73}$$

with

$$m_0(\omega) = \sum_{k=-\infty}^{+\infty} h_k e^{-ik\omega}. \tag{4.74}$$

By iteration follows

$$\hat{\phi}(\omega) = \prod_{j=1}^{\infty} \frac{1}{\sqrt{2}} m_0\left(\frac{\omega}{2^j}\right). \tag{4.75}$$

The definition of m_0 is important in defining the necessary and sufficient conditions for a scaling function ϕ. Mallat and Meyer have proven the following

theorem [53, chapter 7]. Let m_0 be a 2π-periodic function and continuously differentiable in a neighbourhood of $\omega = 0$. If m_0 satisfies

$$\forall \omega \in \mathbb{R}, \quad |m_0(\omega)|^2 + |m_0(\omega + \pi)|^2 = 2 \tag{4.76}$$

$$m_0(0) = \sqrt{2} \tag{4.77}$$

$$\inf_{\omega \in [-\frac{\pi}{2}, \frac{\pi}{2}]} |m_0(\omega)| > 0 \tag{4.78}$$

then

$$\hat{\phi}(\omega) = \prod_{j=1}^{\infty} \frac{1}{\sqrt{2}} m_0 \left(\frac{\omega}{2^j} \right) \tag{4.79}$$

is the Fourier Transform of a scaling function $\phi \in \mathbf{L}^2(\mathbb{R})$. Conversely, if $\phi \in \mathbf{L}^2(\mathbb{R})$ is an integrable scaling function, then m_0 satisfies equations 4.76 and 4.77. This theorem allows to proof whether a function ϕ is appropriate for a multiresolution analysis and thus for the construction of a wavelet. It can e.g. be shown that the function

$$\phi_{Haar} = \begin{cases} 1 & \text{if } 0 < t < 1 \\ 0 & \text{otherwise} \end{cases} \tag{4.80}$$

is the scaling function of a multiresolution analysis. Equation (4.54) gives the filter coefficients h_k as

$$h_k = \begin{cases} \frac{1}{\sqrt{2}} & \text{if } \; k = 0 \; \text{ or } \; k = 1 \\ 0 & \text{otherwise,} \end{cases} \tag{4.81}$$

which results in

$$m_0(\omega) = \frac{1}{\sqrt{2}} (1 + e^{-i\omega}) \tag{4.82}$$

that satisfies 4.76 and 4.77. The corresponding wavelet ψ_{Haar} is defined by equations 4.56 and 4.57.

$$\psi_{Haar}(t) = \sqrt{2} \frac{1}{\sqrt{2}} (\phi(2t) - \phi(2t-1)) \tag{4.83}$$

$$= \begin{cases} -1 & \text{if } 0 \leq t < \frac{1}{2} \\ 1 & \text{if } \frac{1}{2} \leq t < 1 \\ 0 & \text{otherwise} \end{cases} \tag{4.84}$$

The function ϕ_{Haar} was introduced by Haar in 1910 (long before the development of wavelet theory), who realized that the dilations and translations of this

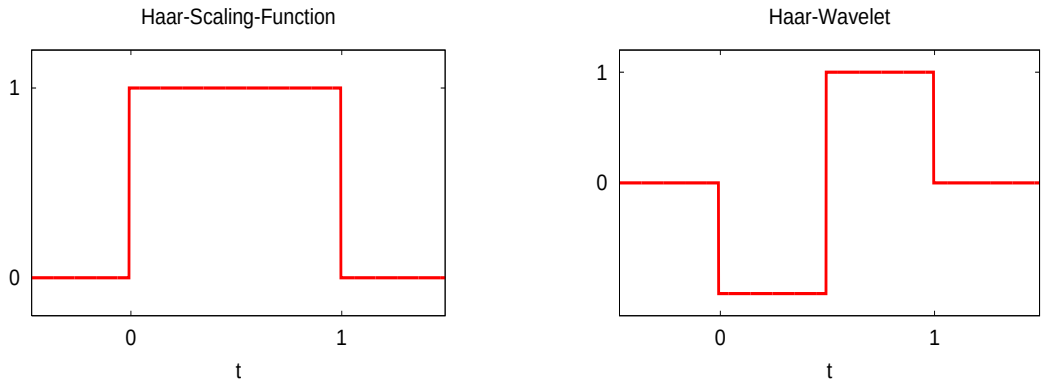

Figure 4.9.: The Haar Wavelet (right) and the corresponding scaling function (left).

function constitute an orthonormal basis in $\mathbf{L}^2(\mathbb{R})$ [55, chapter 1]. It is therefore called the *Haar-Wavelet*. The Haar-Wavelet and the Haar-Scaling-Function are shown in Figure 4.9. Further examples for the construction of wavelets from a given scaling function are the Shannon-Wavelet and the Battle-Lemarié-Wavelet. In case of the Shannon-Wavelet, the scaling function is defined by its Fourier Transform, which is given as a piece-wise constant function [53, chapter 7]. The Battle-Lemarié-Wavelets are obtained by orthogonalising spline functions [55, chapter 5]. These wavelets have in common, that the number of filter coefficients necessary for the multiresolution analysis is infinite in contrast to the case of the Haar-Wavelet. However, for practical applications one is interested in wavelets obtained using a finite number of filter coefficients. Daubechies has shown how to construct orthonormal wavelet bases with compact support and a finite number of filter coefficients. For this purpose she started with the function m_0 and assumed m_0 to be a trigonometric polynomial, i.e. constructed with a finite number of filter coefficients h_k.

$$m_0 = \sum_{k=0}^{N-1} h_k e^{-ik\omega} \tag{4.85}$$

Furthermore, she constructed wavelet bases with different numbers of vanishing moments. A wavelet ψ is said to have p vanishing moments if

$$\int_{-\infty}^{\infty} t^k \psi(t)\, \mathrm{d}t = 0 \quad \text{for } 0 < k < p. \tag{4.86}$$

In [53, chapter 7] it is shown, that the number of vanishing moments is correlated with the value of $m_0(\omega = \pi)$. To be precise, ψ has p vanishing moments,

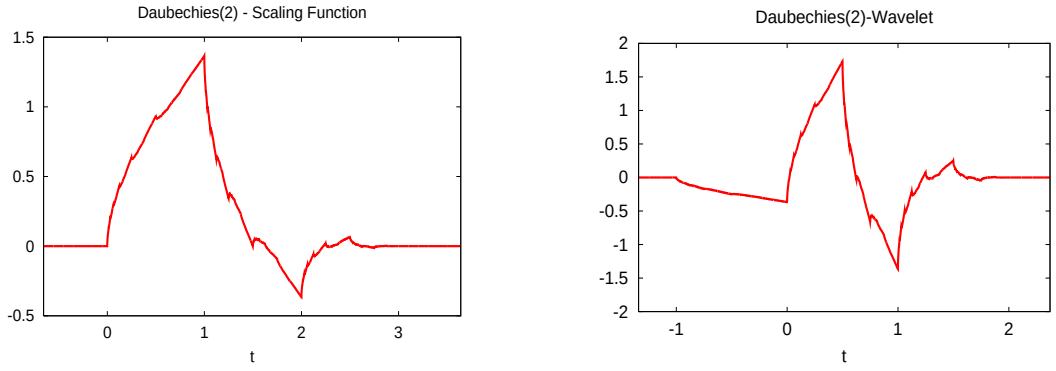

Figure 4.10.: The Daubechies wavelet providing two vanishing moments and a filter length of 4 (right) and the corresponding scaling function (left).

if $m_0(\omega)$ and the first $p-1$ derivatives of m_0 are zero at $\omega = \pi$. Therefore to construct a wavelet with compact support, a finite number of filter coefficients and a specific number of vanishing moments, we make the ansatz

$$m_0(\omega) = \sqrt{2}\left(\frac{1+e^{i\omega}}{2}\right)^p R(e^{-i\omega}) \tag{4.87}$$

with $R(e^{-i\omega})$ a trigonometric polynomial. The factor $\left(\frac{1+e^{i\omega}}{2}\right)^p$ ensures that m_0 and the first $p-1$ derivatives are zero at $\omega = \pi$. The challenge at this point is to construct $R(e^{-i\omega})$ with a minimum degree m in such a way, that m_0 satisfies the condition

$$|m_0(\omega)|^2 + |m_0(\omega+\pi)|^2 = 2. \tag{4.88}$$

Consequently, the number of non-zero filter coefficients is $N = m + p + 1$ [53, chapter 7]. Daubechies proved that the minimum degree m is $p-1$ and hence the number of non-zero filter-coefficients is $2p$. She further constructed a series of wavelet families by specifying the $R(e^{-i\omega})$ [55, chapter 6]. The Daubechies-Wavelets have a support of minimum size for any given number p of vanishing moments. In Figure 4.10 the scaling function and wavelets of the most common Daubechies-Wavelet (providing two vanishing moments) are shown. The wavelet will further be denoted as Daubechies(2)-Wavelet. Please note, that $m_0 = \sqrt{2}\left(\frac{1+e^{i\omega}}{2}\right)$ leads to the construction of the Haar-Wavelet. Therefore the Haar-Wavelet drops out as a special case of a general construction of wavelets with compact support.

Biorthogonal Bases

It is not possible to construct compactly supported orthogonal wavelet bases, which are symmetric or antisymmetric, besides the Haar-Wavelet [55, chapter 8]. However, smooth symmetric wavelets are especially desirable in image coding since symmetric artefacts are less prominent for the visual system [55, chapter 8]. The construction of symmetric or antisymmetric wavelets with compact support is possible, if the orthogonality conditions are slightly relaxed [55, chapter 8] leading to so called biorthogonal bases. Biorthogonal wavelet bases can be symmetric or antisymmetric. In case of a biorthogonal wavelet transform the wavelets utilised for decomposition and reconstruction are not identical. We will further denote this pair of wavelets with $\tilde{\psi}$ for the decomposition wavelet and ψ for the reconstruction wavelet. The corresponding scaling functions are indicated by $\tilde{\phi}$ and ϕ. The sets $\{\tilde{\psi}_{j,k}\}_{(j,k)\in\mathbb{Z}^2}$ and $\{\psi_{j,k}\}_{(j,k)\in\mathbb{Z}^2}$ are then biorthogonal Riesz bases of $\mathbf{L}^2(\mathbb{R})$. Biorthogonal wavelet bases are also related to multiresolution approximations. Compared to the descriptions presented above some modifications occur. Here two multiresolution approximations are given. The sets $\{\tilde{\phi}_{j,k}\}_{k\in\mathbb{Z}}$ and $\{\phi_k\}_{(j,k)\in\mathbb{Z}}$ are Riesz bases of the spaces $\tilde{\mathbf{V}}_j$ and $\mathbf{V}_j$ respectively. $\{\tilde{\mathbf{V}}_j\}_{j\in\mathbb{Z}}$ and $\{\mathbf{V}_j\}_{j\in\mathbb{Z}}$ are multiresolution approximation of $\mathbf{L}^2(\mathbb{R})$. The sets of wavelets $\{\tilde{\psi}_{j,k}\}_{k\in\mathbb{Z}}$ and $\{\psi_{j,k}\}_{k\in\mathbb{Z}}$ are Riesz bases of the detail spaces $\tilde{\mathbf{W}}_j$ and $\mathbf{W}_j$ such that [53, chapter 7]

$$\tilde{\mathbf{V}}_j \oplus \tilde{\mathbf{W}}_j = \tilde{\mathbf{V}}_{j-1} \quad \text{and} \quad \mathbf{V}_j \oplus \mathbf{W}_j = \mathbf{V}_{j-1} \tag{4.89}$$

The biorthogonality conditions are

$$\langle \psi_{j,k}, \tilde{\psi}_{j,k} \rangle = \delta_{j,k} \quad \text{and} \quad \langle \phi_{j,k}, \tilde{\phi}_{j,k} \rangle = \delta_{j,k}. \tag{4.90}$$

Two different types of filter coefficients are then related to the two types of multiresolution approximations.

$$\phi(t) = \sqrt{2} \sum_{k=-\infty}^{\infty} h_k \phi(2t-k), \qquad \tilde{\phi}(t) = \sqrt{2} \sum_{k=-\infty}^{\infty} \tilde{h}_k \phi(2t-k) \tag{4.91}$$

$$\psi(t) = \sqrt{2} \sum_{k=-\infty}^{\infty} g_k \phi(2t-k), \qquad \tilde{\psi}(t) = \sqrt{2} \sum_{k=-\infty}^{\infty} \tilde{g}_k \phi(2t-k) \tag{4.92}$$

In the Fourier domain equation (4.91) becomes

$$\hat{\phi}(2\omega) = \frac{1}{\sqrt{2}} m_0(\omega) \hat{\phi}(\omega), \qquad \hat{\tilde{\phi}}(2\omega) = \frac{1}{\sqrt{2}} \tilde{m}_0(\omega) \hat{\tilde{\phi}}(\omega) \tag{4.93}$$

where m_0 and $\tilde{m}_0$ have to satisfy

$$m_0^*(\omega)\tilde{m}_0(\omega) + m_0^*(\omega+\pi)\tilde{m}_0(\omega+\pi) = 2. \tag{4.94}$$

Cohen, Feauveau and Daubechies have constructed a series of compactly supported, biorthogonal wavelets. Let us consider two wavelets ψ and $\tilde{\psi}$ with p and $\tilde{p}$ vanishing moments respectively. In [53, chapter 7] it is described how to construct these wavelets by starting with

$$m_0(\omega) = \sqrt{2}e^{\frac{-i\epsilon\omega}{2}}\left(\cos\frac{\omega}{2}\right)^p L(\cos\omega) \tag{4.95}$$

$$\tilde{m}_0(\omega) = \sqrt{2}e^{\frac{-i\epsilon\omega}{2}}\left(\cos\frac{\omega}{2}\right)^{\tilde{p}} \tilde{L}(\cos\omega) \tag{4.96}$$

with $\epsilon = 1$ for p and $\tilde{p}$ even and $\epsilon = 0$ for p and $\tilde{p}$ odd. Both p and $\tilde{p}$ can be shown to have the same parity. L and $\tilde{L}$ have to satisfy

$$L(\cos\omega)\tilde{L}(\cos\omega) = P\left(\sin^2\frac{\omega}{2}\right) \tag{4.97}$$

with special requirements for the polynomial $P(\sin^2(\omega/2))$. The wavelets constructed by Cohen, Daubechies and Feauveau are sometimes called CDF-Wavelets. The different pairs of mother wavelets can be distinguished by the number of vanishing moments and the length of the filter. The simplest CDF-Wavelet-pair providing one vanishing moment for each of the two wavelets is again the Haar-Wavelet. In Figures 4.11 and 4.12 two pairs of CDF-Wavelets and the corresponding scaling functions are shown. In Figure 4.11 the CDF-Wavelet with two vanishing moments for decomposition and reconstruction is presented. This filter resulting from this pair of wavelets has been known in image processing before and is sometimes termed 5-tap/3-tap-Filter in literature [57] according to the filter length of decomposition and reconstruction wavelet. The pair of biorthogonal wavelets shown in Figure 4.12 provides four vanishing moments in decomposition and reconstruction respectively. However, to avoid confusion with another pair of spline wavelets also providing four vanishing moments, the pair of wavelets in Figure 4.12 should also be termed using its filter length of 9 and 7 respectively. Thus, we will further use the terminology $CDF_{5/3}(2,2)$ for the wavelets shown in Figure 4.11 and $CDF_{9/7}(4,4)$ for the pair shown in Figure 4.12. The $CDF_{9/7}(4,4)$ has a special property. As can be seen in Figure 4.12 the wavelets for decomposition and reconstruction are very similar. This can be interpreted in such a way, that the two wavelets are nearly orthogonal, resulting in a good numerical stability [53, chapter 7]. Both pairs of biorthogonal wavelets described are used in the JPEG-2000 Algorithm for image compression [57].

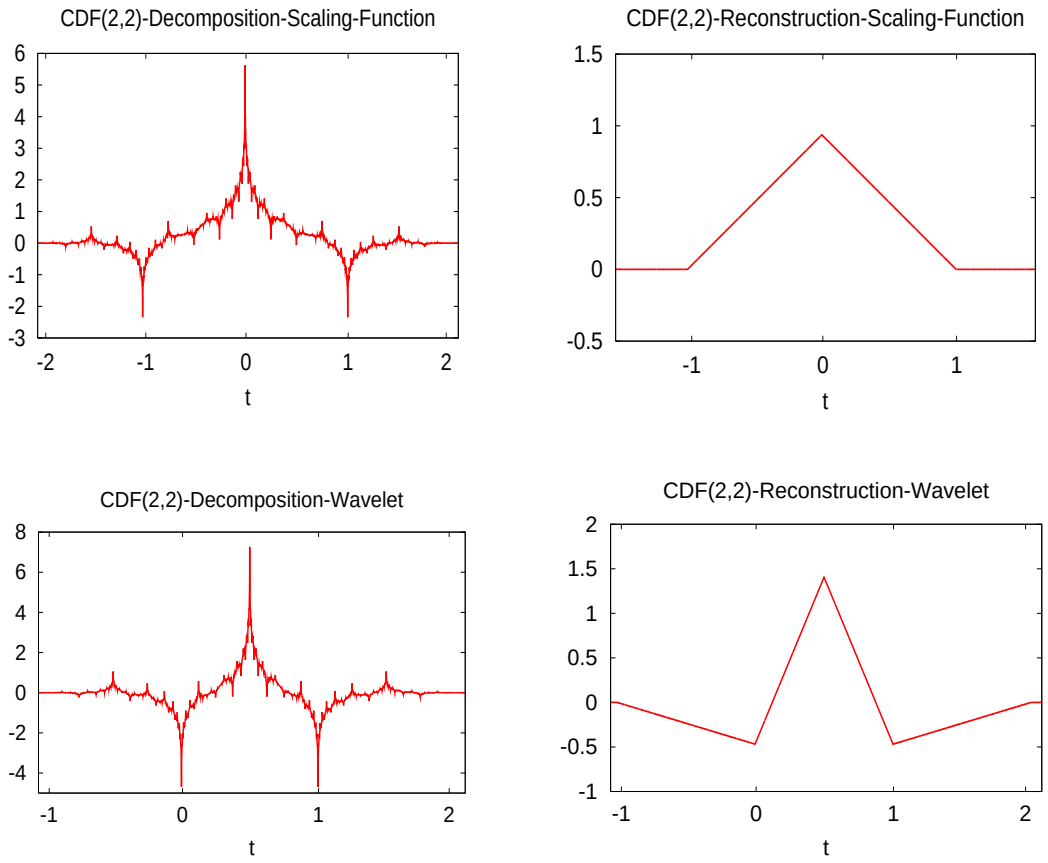

Figure 4.11.: The wavelets and scaling functions of the biorthogonal $CDF_{5/3}(2,2)$-wavelet-pair.

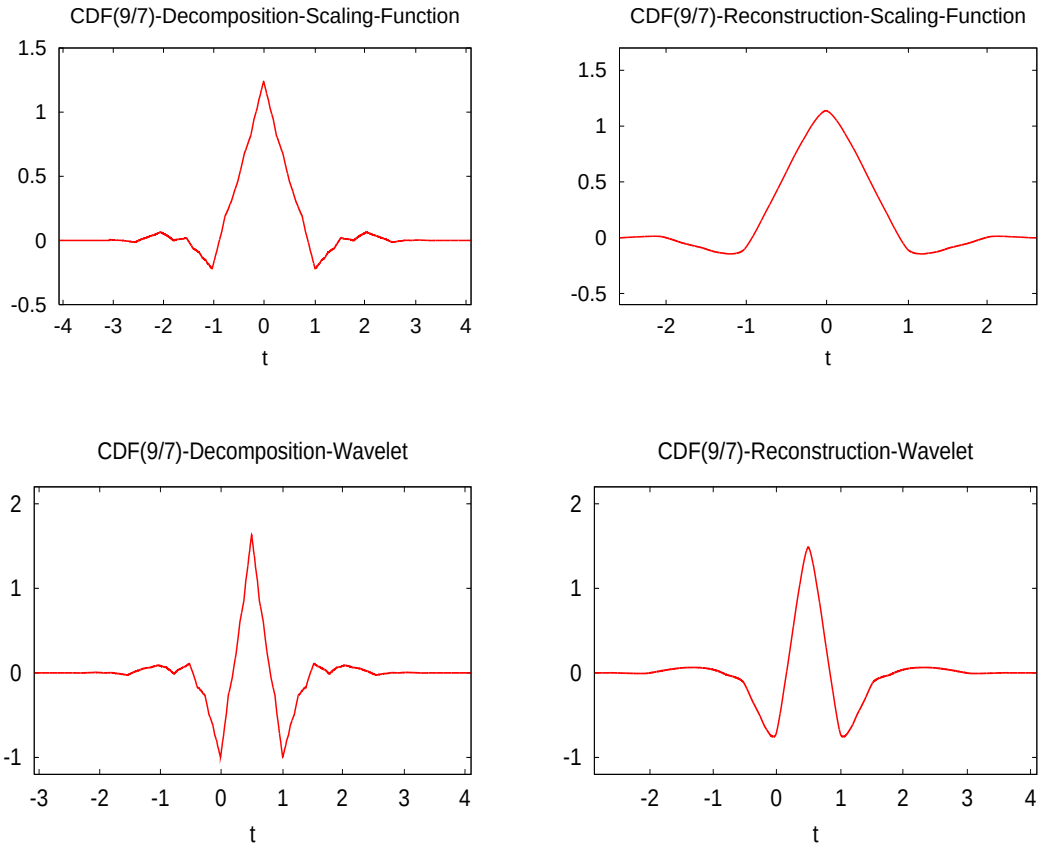

Figure 4.12.: The wavelets and scaling functions of the biorthogonal $CDF_{9/7}(4,4)$-wavelet-pair.

4.1.7. Software for Wavelet Applications

In the research presented here an Open Source Software Library (*blitzwave*) was utilised to perform the Discrete Wavelet Transform. The Library is written in the C++ computer language and provides an n-dimensional Discrete Wavelet Transform. It uses a special mathematical scheme to compute the coefficients of the Fast Wavelet Transform. This scheme is called *Lifting* and was developed by Wim Sweldens [58, 59]. The principle is also shortly introduced in [53, chapter 7] and can be described as a modification of the filterbank algorithm. The basic idea is that any biorthogonal filter can be synthesised by applying a specific modification - the *Lifting* - to a particular type of filters - so called *Lazy Filters* [53, chapter 7]. The usual filterbank algorithm is here replaced by two different steps. The first step is the so called *Lazy Transform*, i.e. the application of Lazy Filters. This is just a separation of odd and even samples. After the Lazy Transform the Lifting is applied that creates the desired coefficients starting from the results of the Lazy Transform. The principle is shown in Figure 4.13. One of the main advantages of the Lifting Scheme is a reduction of the number of necessary operations by a factor of 2 [53, chapter 7]. The Software Library utilised was developed by Oliver Schulz (Max-Planck Institute Dortmund) and is available at [60].

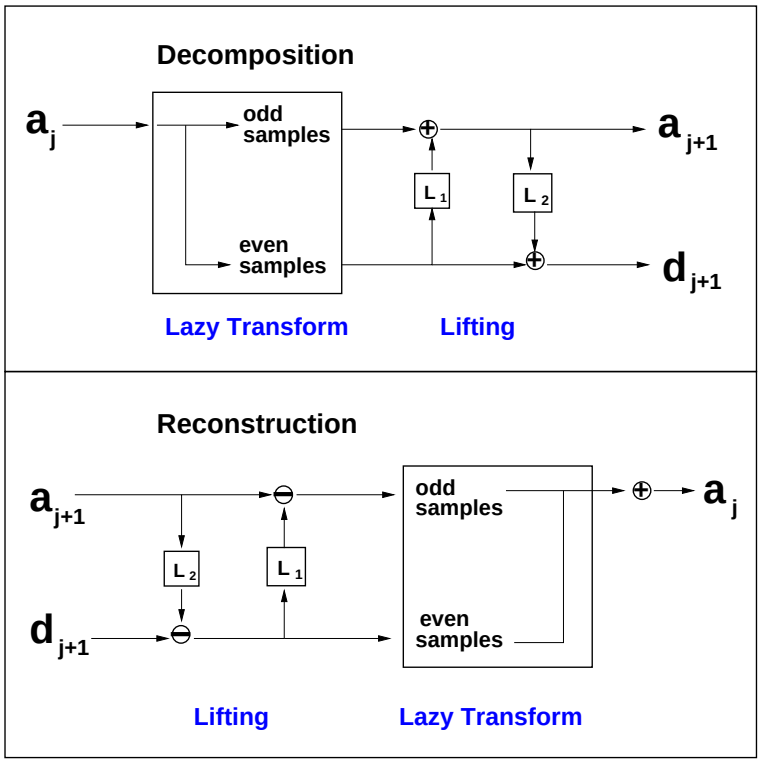

Figure 4.13.: Principle of the Lifting Scheme. The usual step of computing the wavelet coefficients is replaced by a Lazy Transform and a successive Lifting composed of the two convolutions denoted by L_1 and L_2.

4.2. Methods of Dimension Reduction

4.2.1. Principal Component Analysis

The Principal Component Analysis (PCA), also termed *Karhunen-Loève transform*, is a method suitable for dimension reduction [61, chapter 8]. The PCA is a linear transformation from a d-dimensional space to an M-dimensional space, with $M < d$. Suppose, that the input vectors $\mathbf{x}_n \in \mathbb{R}^d$ can be written using an orthonormal bases $\mathbf{e}_i$ as

$$\mathbf{x} = \sum_{i=1}^{d} z_i \mathbf{e}_i. \tag{4.98}$$

Then the coefficients z_i can be expressed as

$$z_i = \mathbf{e}_i^T \mathbf{x}. \tag{4.99}$$

An approximated vector $\tilde{\mathbf{x}}$ is defined by

$$\tilde{\mathbf{x}} = \sum_{i=1}^{M} z_i \mathbf{e}_i + \sum_{i=M+1}^{d} b_i \mathbf{e}_i. \tag{4.100}$$

Here the b_i are chosen as constant. Thus, $\tilde{\mathbf{x}}$ is a vector with M degrees of freedom, i.e reduced dimensionality. The error of the approximation of $\mathbf{x}$ by $\tilde{\mathbf{x}}$ can be written as

$$\mathbf{x} - \tilde{\mathbf{x}} = \sum_{i=M+1}^{d} (z_i - b_i). \tag{4.101}$$

Considering the whole dataset $\mathbf{x}_n \in \mathbb{R}^d$ the constant must be chosen in a way to optimise the approximation in $\mathbb{R}^M$. To define the best approximation the sum of the squares of the error has to be minimised.

$$E_M = \frac{1}{2} \sum_{n=1}^{N} \|\mathbf{x}^n - \tilde{\mathbf{x}}^n\|^2 = \frac{1}{2} \sum_{n=1}^{N} \sum_{i=M+1}^{d} (z_i^n - b_i)^2 \tag{4.102}$$

The minimisation of E_M with respect to b_i yields

$$b_i = \frac{1}{N} \sum_{n=1}^{N} z_i^n = \mathbf{e}_i^T \bar{\mathbf{x}} \tag{4.103}$$

with the mean vector $\bar{\mathbf{x}}$. Thus the sum-of-squares error can be rewritten as

$$E_M = \frac{1}{2} \sum_{i=M+1}^{d} \mathbf{e}_i^T \underbrace{(\sum_n (\mathbf{x}^n - \bar{\mathbf{x}})(\mathbf{x}^n - \bar{\mathbf{x}})^T)}_{\text{covariance matrix } \Sigma} \mathbf{e}_i. \tag{4.104}$$

It can be shown that E_M is minimal if the basis vectors satisfy [61, chapter 8]

$$\Sigma \mathbf{e}_i = \lambda_i \mathbf{e}_i \tag{4.105}$$

with the covariance matrix Σ. This means that the basis vectors have to be eigenvectors of the covariance matrix. If the eigenvalues λ_i are determined the sum-of-squares error is given by

$$E_M = \frac{1}{2} \sum_{i=M+1}^{d} \lambda_i. \tag{4.106}$$

Therefore the minimum error is obtained, if the smallest eigenvalues and corresponding eigenvectors are discarded [61, chapter 8]. The eigenvalue λ_i is proportional to the variance of the term $z_i - b_i$:

$$\begin{aligned} \frac{1}{N} \sum_n (z_i - b_i)(z_j - b_j) &= \frac{1}{N} \sum_n \mathbf{e}_i^T (\mathbf{x}^n - \bar{\mathbf{x}})(\mathbf{x}^n - \bar{\mathbf{x}})^T \mathbf{e}_j && (4.107) \\ &= \frac{1}{N} \mathbf{e}_i^T \, \Sigma \, \mathbf{e}_j && (4.108) \\ &= \frac{1}{N} \mathbf{e}_i^T \lambda_j \mathbf{e}_j && (4.109) \\ &= \frac{1}{N} \lambda_j \delta_{ij} && (4.110) \end{aligned}$$

Please note, that sometimes in literature the covariance matrix is defined including the term $\frac{1}{N}$. According to the equations above, the eigenvector related to the largest eigenvalue corresponds to the direction of largest variance within the original dataset. In Figure 4.14 the principle is demonstrated in 2D. In practice, one usually starts with computing the mean $\bar{\mathbf{x}}$ and subtracting it from all datapoints. In Figure 4.14 $\mathbf{e}_1$ is the eigenvector to the largest eigenvalue. If the dataset - shown in this Figure by dots - was represented in a reduced one-dimensional space, the best approximation would be given through the space spanned by $\mathbf{e}_1$.

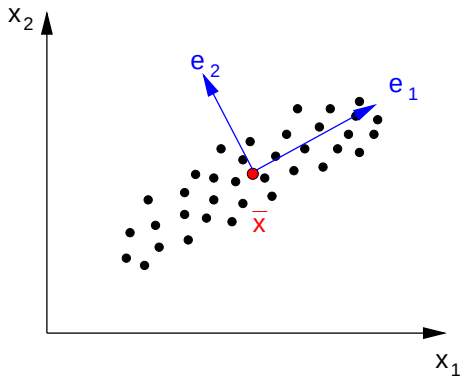

Figure 4.14.: Principal Component Analysis of a dataset denoted by dots. The vector $\bar{\mathbf{x}}$ is the mean, the vectors $\mathbf{e}_1$ and $\mathbf{e}_2$ are the eigenvectors of the covariance matrix.

4.2.2. Self Organizing Map

The Self Organizing Map (SOM) is a clustering approach from the field of artificial neural networks [62, chapter 3]. The training procedure is an example for unsupervised machine learning and defines a mapping from the input space $\mathbb{R}^n$ onto a lower dimensional array of nodes. The SOM is designed to preserve the topology of the input space and thus provides a method of dimension reduction. A reference vector $\{\mathbf{u}_i\}$ is associated to every node i in the array. The total set of reference vectors $\{\mathbf{u}_j\}_{j\in\mathbb{N}}$ is trained according to a given dataset of N feature vectors $\{\mathbf{x}_n\}_{n\in\mathbb{N},1<n<N}$. For each feature vector $\mathbf{x}_n$ the best-matching node, the so-called *winner node* c, can be determined by

$$c = argmin_j\{\|\mathbf{x}_n - \mathbf{u}_j\|\}. \tag{4.111}$$

Let t be the discrete time coordinate denoting the training step. Within each training step the reference vectors of the SOM are updated according to the feature vector $\mathbf{x}_n$ chosen as the training sample. Let $\mathbf{u}_c$ be the reference vector related to winner node c at the specific training step. The training procedure of the SOM is characterised by the fact, that $\mathbf{u}_c$ and the reference vectors $\mathbf{u}_j$, whose nodes are topographically close in the SOM grid, are updated depending on the distance of $\mathbf{x}$

$$\mathbf{u}_j(t+1) = \mathbf{u}_j(t) + h_{cj}(t)[\mathbf{x}(t) - \mathbf{u}_j(t)]. \tag{4.112}$$

Equation (4.112) indicates, that the reference vector is adapted to the training sample controlled by the function h_{cj}. This function is the so-called *neighbourhood function* and is time dependent. To ensure the convergence of the training

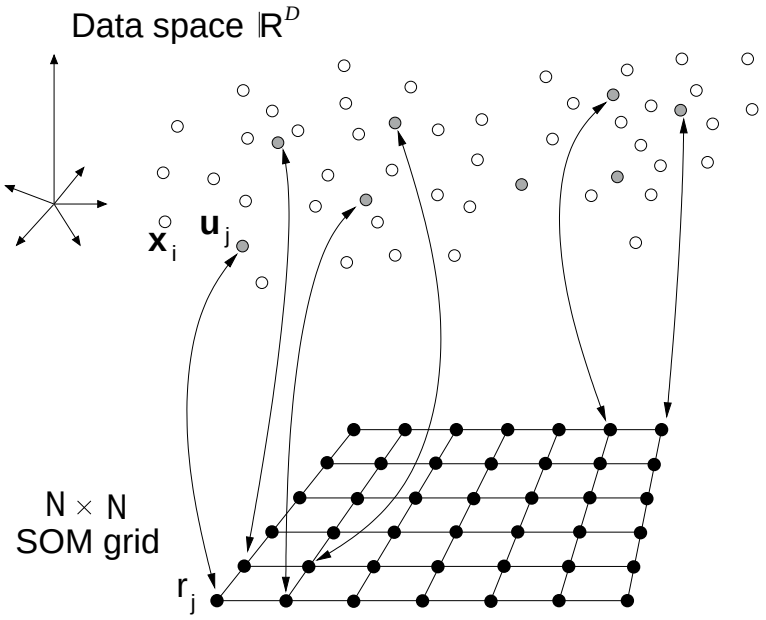

Figure 4.15.: Principle of Self Organizing Maps. The data set is represented by the white points $\mathbf{x}_1$. The reference vectors $\mathbf{u}_j$ are shown in grey and are connected with one node $\mathbf{r}_j$ in the SOM grid. Courtesy of Dr. Claudio Varini.

procedure it is necessary that h_{cj} decreases with time, i.e $h_{cj} \to 0$ if $t \to \infty$. Furthermore, h_{cj} decreases with increasing distance $\|\mathbf{r}_j - \mathbf{r}_c\|$. Here $\mathbf{r}_j$ and $\mathbf{r}_c$ are the (lower-dimensional) vectors of the nodes i and c in the SOM grid. In the literature several choices of $h_{cj}(t)$ are discussed. A very common choice is to model the neighbourhood function using a Gaussian kernel

$$h_{cj}(t) = \alpha(t) \exp\left(-\frac{\|\mathbf{r}_c - \mathbf{r}_j\|^2}{2\sigma^2(t)}\right). \tag{4.113}$$

The function $\alpha(t)$ is called *learning rate factor* and $\sigma(t)$ defines the width of the kernel. Both functions are monotonically decreasing to ensure a convergence of the training procedure [62, chapter 3].

Dimension of SOM Array The SOM array usually is low-dimensional, e.g. one- or two-dimensional. The appropriate choice depends on the application at hand and the characteristics of the provided feature space. The projection onto a two-dimensional grid is quite common and very suitable to support a visual inspection of the feature space.

Learning Rate Factor and Kernel Width As described in [62, chapter 3] the decision in favour of either linear, exponential or other behaviour of $\alpha(t)$ and $\sigma(t)$ is not very crucial. The learning rate $\alpha(t)$ should be chosen close to unity at the beginning [62, chapter 3]. In this work only a linear decreasing $\alpha(t)$ is applied. In contrast to the choice of $\alpha(t)$ the values of the kernel width $\sigma(t)$ are important and strongly influence the resulting SOM grid. As described in [62, chapter 3] the initial value must not be too small to assure a global ordering of the grid. The kernel width $\sigma(t)$ controls the neighbourhood involved in the current training step and thus the topology preservation of the SOM grid. By varying $\sigma(t)$ a controlled trade-off between the topology preservation and the local fitting of the input space can be achieved.

Number of Training Steps The number of training steps has to be large enough, to ensure a good statistical accuracy of the training result. In case of a low number of available training samples one has to use these reiteratively for training. A rule of thumb is to choose the number of training steps larger than 500 times the number of nodes in the grid [62, chapter 3].

Initialisation of the Reference Vectors The reference vectors can be initialised using different methods. Quite common is an initialisation using randomly chosen vectors of the feature space [62, chapter 3]. It is also possible to compute a PCA on the feature space and initialise the l-dimensional SOM array along the directions of the eigenvectors corresponding to the l largest eigenvalues.

Quality Measures of the Training Result As described above, two aspects have to be monitored during training. First, it is important for a clustering result, that the input space is approximated in an optimal manner. To measure this, the *average quantisation error* AQE can be determined by

$$\mathrm{AQE} = \frac{1}{N} \sum_{n=1}^{N} \|\mathbf{x}_n - \mathbf{u}_c(n)\| \tag{4.114}$$

with $\mathbf{u}_c(n)$ as the winner node related to the feature vector $\mathbf{x}_n$. Here, N is the total number of feature vectors in the dataset. This factor has been computed after training by mapping all input vectors onto the resulting SOM grid [62, chapter 3]. Secondly, the preservation of the feature space topology has to be assured. For this purpose, one can determine the best-match node c_1 and the second best-match node c_2. If both nodes are neighbours in the SOM grid,

the topology is preserved [62, chapter 3]. To define a numerical measure for topology preservation, one can compute the value *TP* by

$$TP = \frac{1}{N}\sum_{k=1}^{N} p(\mathbf{x}_k) \quad \text{with} \tag{4.115}$$

$$p(\mathbf{x}_k) = \begin{cases} 1 & \text{if 1. and 2. nearest reference vectors} \\ & \text{are not adjacent} \\ 0 & \text{otherwise} \end{cases} \tag{4.116}$$

After a successful training procedure the reference vectors depict the data distribution in the dataset, preserving the underlying topology. Thus the distance of two nodes in the SOM directly depends on the distance of the corresponding reference vectors. Due to the topology preservation the SOM is a powerful tool for the exploration of feature spaces. By varying the training parameters a trade-off between topology preservation and local feature vector approximation can be obtained. A detailed discussion of SOMs for clustering and visualisation purposes can be found in [63].

Comparison to other Methods of Clustering and Dimension Reduction Several other methods of clustering exist, usually providing better results regarding the quantisation error. In [63] various works are mentioned comparing the performance of k-Means clustering and SOMs. The clustering ability of Self Organizing Maps is reported as either equal or worse compared to k-Means clustering. However, the main benefit of SOMs is, that due to topology preservation a reduction from high-dimensional feature spaces to a significantly lower dimensional SOM array is possible, thus allowing a visual inspection of the data space. Regarding the field of dimension reduction the SOM has to be compared with the PCA. As mentioned above, PCA is a linear method and therefore fails in determining non-linear intrinsic dimensions in the data space in contrast to the SOM.

It has been shown that there is a drawback in the potential of a SOM regarding visualisation and dimension reduction due to the discretised output space [63]. However, the discretised output leads to possible visualisation methods allowing to explore the feature space in much more detail. The reference vectors of the SOM array can be visualised quite easily. This makes a linking of the single feature vector components to areas in the reduced space possible. The reduced spaces resulting from other methods of nonlinear dimensionality reduction, such as Sammon mapping [62, chapter 3] or locally

linear embedding (LLE) [64], are not similarly accessible and interpretable. The fact that the SOM algorithm allows an efficient exploration of the underlying feature space is the most important motivation for its application in this work.

4.2.3. Software

The software routines utilised for dimension reduction, especially providing the algorithms of the Principal Component Analysis and the Self Organizing Map were implemented in the working group *Applied Neuroinformatics* at the University of Bielefeld. The main authors are Axel Saalbach and Thorsten Twellmann.

5. Multiscale Analysis of Microscopy Images

5.1. Introduction

Several types of diagnostic systems working on medical images are currently under development. Examples are classification systems and content-based image retrieval systems. For classification purposes usually methods from the field of machine learning are utilised to train a system with given datasets. The system can then make a diagnosis for an unknown dataset. A content-based image retrieval system usually works according to the principle *query by example* (QBE). The medical expert provides an unknown dataset or image to the system and the system returns those cases from its database which are most similar to the provided dataset. The medical expert can now diagnose the new dataset according to the information presented by the system.

In all these cases the image content is characterised by numerical image features, i.e. numerical vectors supposed to encode the diagnostically relevant characteristics. It is challenging to decide which features are the most appropriate ones for the specific purpose considered.

In this work a dataset of pathology images is explored in order to find and interpret features of clinical relevance. The computed image features are based on the Discrete Wavelet Transform. To link local, morphological image characteristics to the space spanned by the wavelet-based features a Self Organizing Map (SOM) is employed. As a method of unsupervised learning the SOM is a powerful tool providing both the ability of clustering and data visualisation.

SOMs have been considered to serve as interactive visualisation tools e.g. for database visualisation and browsing [65], content-based image retrieval [66] or building of a texture dictionary [67]. One application of SOMs on histological datasets is the investigation of human defined image characteristics as described in [68]. In that work the features used for clustering are based on

human definition and rating, i.e. the occurrence of a specific histological characteristic (e.g. collagen fibres) has been graded on a scale of four by a human observer.

In the project presented here, the ability of SOMs to serve as an interface for the analysis of numerical features is demonstrated. The method is applied to an example database of microscopy images of benign brain tumours. The database contains histopathological images of four subtypes of meningiomas. The subtypes are classified by a medical expert into four meningioma classes depending on texture characteristics at different scales. The SOM-based visualisation of the feature space then allows to establish a correlation between single numerical features and histologically relevant image structures. Preliminary experiments have already been described in [69], which suffered from a lack of interpretability. Utilising a new colour transform it is shown, how this approach can be used to bridge the semantic gap between numerical features and histopathological terms and thus transfer clinical terms in the feature space.

The analysis of pathology images has been done e.g. in [70, 17, 71, 72]. However, these works do not focus on the analysis of image and feature spaces. They mostly address the architecture of the underlying system. In [70] a CBIR system for pathology images is described. This work mainly focuses on the development of efficient retrieval mechanisms. The features used in this work are not given in detail but only roughly described as "wavelet-based". The whole procedure requires a segmentation of image objects. In [72] a decision support system is described working on microscopy images. Here also an image segmentation is performed, the results are utilised as textural features. Again, the features utilised are presented not very detailed. The main goal is there to compare the classification performance of different features and classification algorithms. In [71] a complete retrieval system is described. The work mainly focuses on the implementation of a semantic reasoning system integrating potentially conflicting classifications based on low-level features. The visual features are shortly described as "histogram-based" and "Gabor-transform-based". A detailed analysis and interpretation of these low-level features is not presented. The work of Zheng et al. presents the prototype of a CBIR system for pathology images. The features utilised are described as based on colour histograms, texture representations, Fourier and wavelet coefficients [17]. More detailed information is not provided, especially an analysis

of the mapping between single features and clinical semantics is not included.

5.2. Image Domain

The research described in this chapter is accomplished based on the database of microscopy images from neuropathology described in chapter 3, section 3.2. As already mentioned above, the database contains histopathological images of the four most common types of meningiomas (WHO Grade I). These four classes are meningotheliomatous, fibroblastic, psammomatous and transitional meningiomas. Five cases were selected for each diagnostic group and four different photomicrographs were taken of each case, resulting in a set of 80 pictures. These pictures provide a size of 1030×1300 pixel. Further analysis was done for subimages of 256×256 pixel, therefore each original picture was truncated to 1024×1024 pixels and then subdivided in a 4×4 subset of 256×256 pixel pictures. This resulted in a database of 1280 subimages for further analysis. In Figure 5.1 example images and subimages are shown. The colour code included in this Figure is also used in the visualisation of the results obtained by the analysis. Meningotheliomatous tissue is indicated by a red frame, fibroblastic tissue by a green frame, psammomatous tissue is indicated by blue colour and the transitional class is marked with a black frame. As described in chapter 3, section 3.2 significant interclass differences exist as well as significant innerclass differences. This corresponds to an observation made in [72]. There, a different class of brain tumours was in the focus of research. In the following analysis, computed texture features will be linked to these different types of image differences, either significant or non-significant for tumour class characterisation.

5.3. Pre-Processing of Colour Channels

In many applications RGB (Red, Green, Blue) images are transformed into a colour space more suitable for human perception, i.e. the HSV (Hue, Saturation, Value) colour space [72] or the L*u*v colour space [73]. Since pathology images are limited regarding their colours the RGB values are transformed in order to enhance special image structures. In the following, two transformed images are computed from the RGB values (R(x,y), G(x,y), B(x,y)). First, an intensity value $h_1(x, y)$ is computed by averaging the three colour channels for

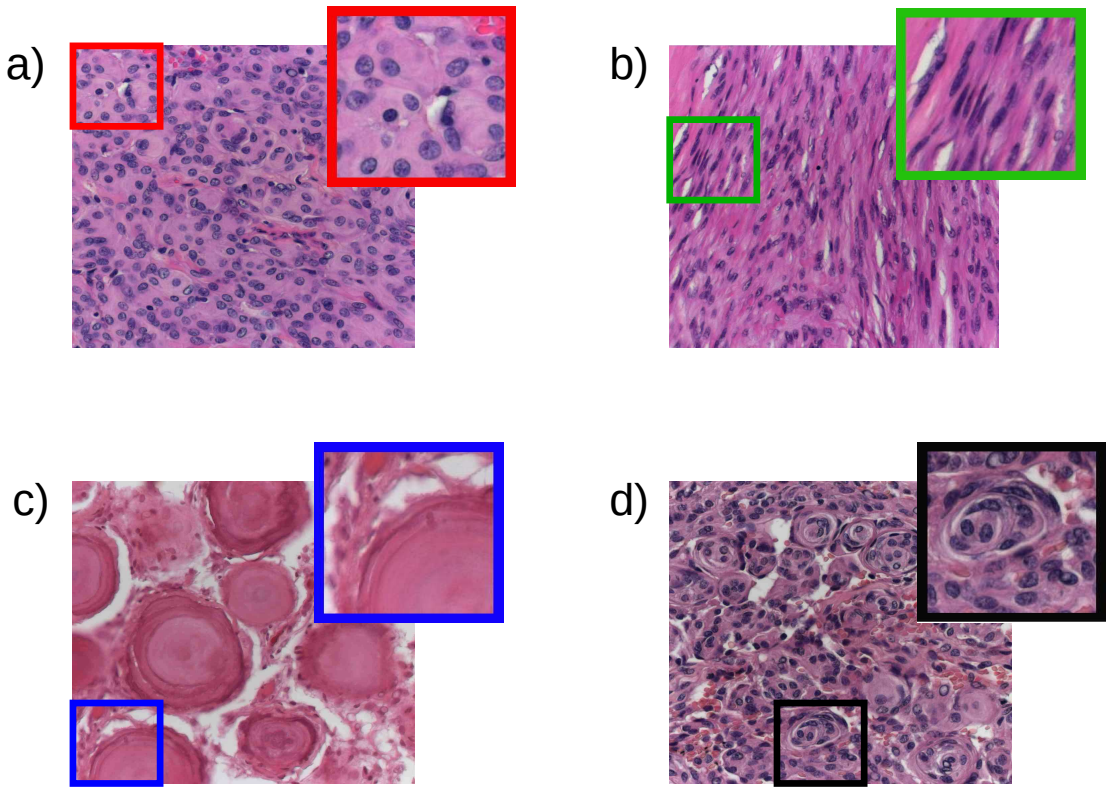

Figure 5.1.: Example subimages for the different subtypes of meningiomas: a) - meningotheliomatous, b) - fibroblastic, c) - psammomatous, d) - transitional.

each pixel and location (x, y) by

$$h_1(x, y) = \frac{1}{3} * (\mathrm{R(x, y)} + \mathrm{G(x, y)} + \mathrm{B(x, y)}). \tag{5.1}$$

The images computed according to equation 5.1 will further on be denoted as *intensity images*. Second, a transform in colour space is designed to extract the cell nuclei from the image, since they appear to exhibit significant characteristics for the distinction of the tumour classes. However, the image colour of a single stained tumour section inevitably depends to some extent on the conditions during the preparation. To reduce dependence on these colour changes, we apply a mean shift to all images and colour channels. The average colour, in the following indexed by *av*, is supposed to be very close to the colour of those structures represented by the largest areas in the image, in this case the cytoplasm or the psammoma bodies.

$$\mathrm{R_{shift}(x, y)} = \mathrm{R(x, y)} - \mathrm{R_{av}} \tag{5.2}$$
$$\mathrm{G_{shift}(x, y)} = \mathrm{G(x, y)} - \mathrm{G_{av}} \tag{5.3}$$
$$\mathrm{B_{shift}(x, y)} = \mathrm{B(x, y)} - \mathrm{B_{av}} \tag{5.4}$$

The preparation procedure described above using the routine H&E stain leads to a blue colouration of the cell nuclei in contrast to the surrounding cytoplasm usually showing a pink colour. Please note that this holds for the dataset analysed here, since it contains only WHO grade I meningiomas. Some other types of meningioma, e.g. the clear cell meningioma (WHO Grade II), result in a colouring different from the one described.

After applying the mean shift to the colour channels, those image structures, which are "bluer" than the surrounding tissue, are characterised by $\mathrm{B_{shift}(x, y)} > \mathrm{R_{shift}(x, y)}$. By computing

$$h_2(x, y) = (max_{\mathrm{RB_{shift}}}(x, y) - \mathrm{R_{shift}(x, y)}) * \mathrm{S} \tag{5.5}$$
$$\text{with} \quad \mathrm{max_{RB_{shift}}(x, y)} = max\{\mathrm{R_{shift}(x, y)}, \mathrm{B_{shift}(x, y)}\} \tag{5.6}$$

all image structures with $\mathrm{B_{shift}(x, y)} < \mathrm{R_{shift}(x, y)}$ are set to zero. The remaining structures, which are supposed to be mainly cell nuclei, are retained. The factor S is the saturation as defined in the HSV colour space [74]

$$\mathrm{S} = \frac{max_{\mathrm{RGB}}(x, y) - min_{\mathrm{RGB}}(x, y)}{max_{\mathrm{RGB}}(x, y)} \tag{5.7}$$
$$\text{with} \quad \mathrm{max_{RGB}(x, y)} = max\{\mathrm{R(x, y)}, \mathrm{G(x, y)}, \mathrm{B(x, y)}\}. \tag{5.8}$$

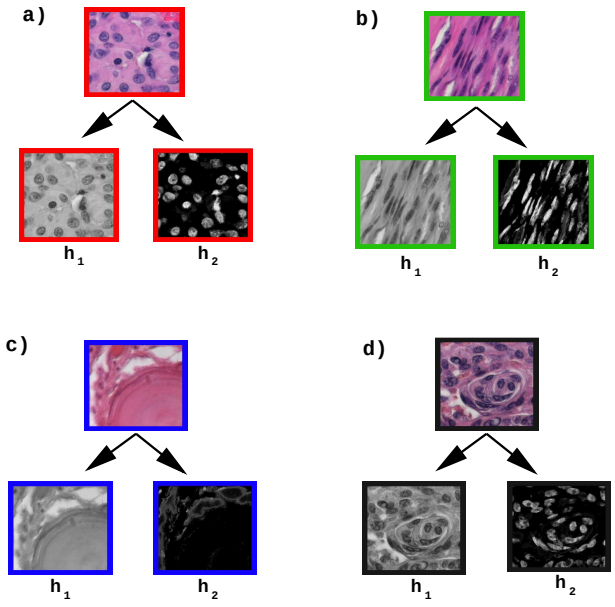

Figure 5.2.: Example subimages for the transform in colour space. Each of the subimages shown above is displayed as intensity image h_1 and with enhanced cell nuclei h_2: a) - meningotheliomatous, b) - fibroblastic, c) - psammomatous, d) - transitional.

This factor suppresses artefacts occurring from the white areas in the images. Especially in psammomatous meningiomas the white areas are due to artificial cracks resulting from the tissue preparation procedure and do not represent relevant staining properties of the tumours. The resulting images of the transform h_2 will be denoted as *cell nuclei images* in the further description. Figure 5.2 shows examples of the transform.

5.4. Texture Features

5.4.1. Texture Features for Image Analysis

Texture is probably the most important descriptor for tissue characterisation in medical textbooks. Several different texture features have been evaluated in literature, including e.g. co-occurrence matrices, line-angle-ratio statistics [75, 76], Gabor filters [76] or wavelet-based features [77]. A good overview of texture features can be found in [78], a comparative study is given in [79]. In this thesis the texture characterisation is not based on a segmentation result as

e.g. in [73] but performed on total subimages.

5.4.2. Texture Features Based on DWT

By examination of Figure 5.1 and section 3.2 it becomes clear that two main properties of the different tissues are extremely important for the tumour diagnosis considered. First, the images of tumour tissue strongly differ regarding the scale of the image structures. Especially psammomatous tissue shows very large scale structures, the so called psammoma bodies. These are reddish, large, round areas of calcification. Secondly, the directionality of the most important image structures shows important differences. Fibroblastic tissue provides parallel aligned fibres and elongated cell nuclei. Thus, there is a preferred orientation in the microscopy images of fibroblastic tissue. Consequently a type of feature is required, that encodes scale-dependent and orientation dependent image information. As described in chapter 4 the two-dimensional Discrete Wavelet Transform provides this type of information encoding. The coefficients obtained by applying the DWT are identified by a translation index, a scaling index and an orientation index. We use the pair of symmetric, biorthogonal wavelets, developed by Cohen, Daubechies and Feauveau, which is termed $CDF_{5/3}(2,2)$ in chapter 4, section 4.1.

At this point the question arises, how to construct features appropriate for characterising the images from the wavelet coefficients. The raw wavelet coefficients are numerous and translation variant. It is therefore not suitable to construct feature vectors by directly using all wavelet coefficients as feature vector components. Instead, one has to process the large number of wavelet coefficients to obtain a limited number of meaningful features.

As described in [80] and [81] the l_1 or l_2-norm of the wavelet coefficients corresponding to one scale and orientation can be used as powerful texture features. In [79] several texture features including wavelet-based ones are compared with respect to the classification performance of different textures. In that work no type of feature sticks out as a clear winner. Among the wavelet-based features wavelet packet features are considered to perform better but with the price of a significantly increased size of the feature vector. Furthermore, it was shown, that the inclusion of further subbands does not necessarily improve the classification error. Thus it seems to be of high interest to develop a methodology for a detailed exploration of the influence of single features on the discrimination of different textures. In this way it is possible to develop

powerful features with a low computational complexity as demanded in [79].

In the analysis of histopathological images wavelets have been used, e.g. in [77] for the identification of specific cell nuclei. In [17] the content of histopathological images is characterised by numerical features including wavelet-based features. In this work the l_1-norm, i.e. the mean absolute coefficient (MAC) of each scale and orientation has been computed according to

$$l_1(d_{j,o}) = \sum_{k_x,k_y} |d_{j,o}(k_x, k_y)|. \tag{5.9}$$

From these MACs two types of features vectors are constructed to encode scale dependence and orientation dependence of the image structures.

First, a mean absolute coefficient for each scale j is computed according to

$$f_1(j) = \sum_o \mathrm{MAC}(o, j), \quad j = 1..8, \quad o = o_1, o_2, o_3. \tag{5.10}$$

Here j is again the scale index, while index o indicates the orientation in the image. The indices o_1 and o_2 indicate coefficients in vertical or horizontal direction, while o_3 indicates the diagonal details.

Second, we use a feature set f_2 describing whether the image structures are anisotropic, i.e. have a preferred orientation. The derivation of this feature is explained using simple phantoms. In Figure 5.3 at left hand three phantom images are shown. Each image contains a structure, i.e. a line, orientated in vertical, horizontal or diagonal direction. At right hand the result of a two-level Discrete Wavelet Transform using the $CDF_{5/3}(2,2)$-wavelet is presented. As can be seen, horizontal or vertical structures mainly lead to wavelet coefficients in only one of the three decomposition subimages. In contrast to this, a DWT of diagonal structures results in coefficients located in all three subimages, i.e. horizontal, vertical and diagonal details.

To obtain one single feature describing structures mainly orientated in a particular direction we use the following measure f_2.

$$f_2(j) = |\mathrm{MAC}(o_1, j) - \mathrm{MAC}(o_2, j)| + c\ \mathrm{MAC}(o_3, j), \quad j = 1..8 \tag{5.11}$$

In case of image structures mainly orientated in horizontal or vertical direction, either the MAC for o_1 or o_2 should be significantly increased, while the other one is correspondingly decreased. Therefore $|MAC(o_1, j) - MAC(o_2, j)|$ reaches a high value. For image structures orientated in a diagonal direction the first part of equation 5.11 vanishes, but, at the same time, the second

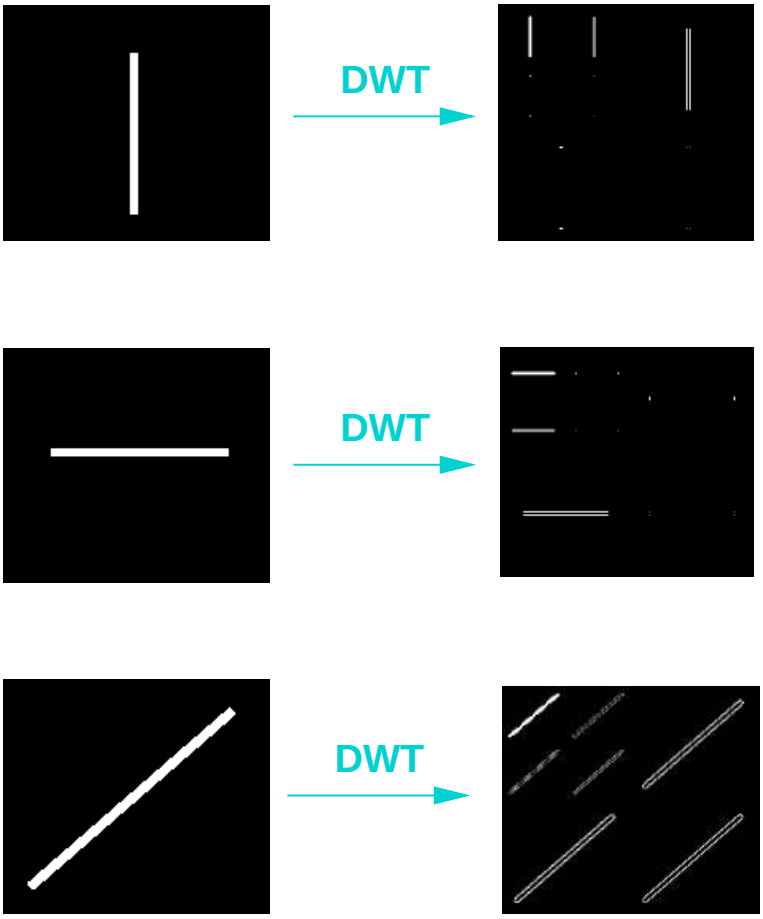

Figure 5.3.: DWT results of three phantoms depicting either vertical, horizontal or diagonal structures.

part increases. The normalisation factor c assures that the added MACs have equalised variances such that the influences of both parts of the sum are comparable. We have described this approach already in [69]. In contrast to [69] each component of the second feature set is not normalised to the corresponding component of the first set. Furthermore, the work in [69] was based on the RGB colour channels.

The suitability of these features for characterising the four types of tissue has additionally been proven in [82]. In this work the features f_1 and f_2 have been computed for the six finest scales and the RGB colour channels of each subimage. The high-dimensional feature space is projected onto two dimensions using Locally Linear Embedding (LLE). The projection result shows four groups of feature vectors. While the psammomatous group is clearly separated from the other clusters, the clusters of the remaining three classes partially overlap. However, the result is close to the visual tissue appearance.

We point out, that a similar approach to characterise images by scale- and orientation-related texture measures using wavelets has already been used for the characterisation of corrosion images [83]. However, there the computed features used differ from the ones we computed in this work. Especially the computation of orientation encoding features strongly varies from our approach.

5.5. SOM-Based Exploration of the Feature Space

5.5.1. Visualisation Techniques for SOM Results

The SOM provides various possibilities for the visualisation of the achieved results. The SOM is both a method of clustering and dimension reduction. Each node in the SOM grid is associated with a reference vector, which is a prototype for a cluster of feature vectors. Due to this properties, it is possible to visualise the spatial distribution of reference vectors and corresponding clusters in the SOM grid.

Visualisation of Reference Vectors After a successful training procedure reference vectors representing the whole data space of feature vectors are obtained. The SOM grid and the reference vectors can be displayed in two ways amongst others. First, each reference vector can be visualised by a bar plot displayed at the location of the associated node in the SOM grid (Figure 5.4, Top). Second, the components of the reference vectors can be visualised sepa-

rately. At the bottom of Figure 5.4 this method is shown. For each component of the reference vector one plot is constructed, a so called Component Plane Map. Each of these maps shows the distribution of one component of the reference vectors over the SOM grid. Black colour represents low values of the component, white correspondingly represents high values.

Visualisation of Clusters As mentioned above a Self Organizing Map is a method for clustering. Each node in the SOM is related to a cluster of feature vectors. By computing the nearest reference vector for each feature vector the cluster structure of the SOM grid is revealed. To present this structure one can simply count the feature vectors mapped to each reference vector. By visualising the number of those feature vectors at the associated node in the SOM grid the cluster structure becomes accessible (Figure 5.5).

Visualisation of the Image Domain In this work, the feature vectors encode entire images. This allows a further visualisation technique, the visualisation of the image domain. For each cluster of the training result one feature vector is determined. To be explicit, the feature vector with the smallest distance to the associated reference vector is chosen. The subimage associated with this feature vector is now displayed at the particular node. In this way, the distribution of image characteristics over the SOM grid can be shown (Figure 5.6).

The SOM is applied to visualise and explore a database content based on specific image features. Since the images have a size of 256×256 pixels, features of eight scales can be computed. The features of the coarsest two scales are neglected, since the associated coefficients encode details corresponding to the entire image or a quarter of the image, which does not seem to be reasonable. Considering the two sets of features (f_1, f_2), the two colour channels (h_1, h_2) described above and the six scales considered a total number of 24 possible features has to be taken into account.

5.5.2. Training Procedure

As described in section 4.2.2 several input parameters have to be set prior to the training procedure. The learning rate α is a monotonically decreasing function, in our case α decreases linearly from 0.9 to 0.01. The size of the SOM grid predetermines the number of clusters. However, since the main point of this

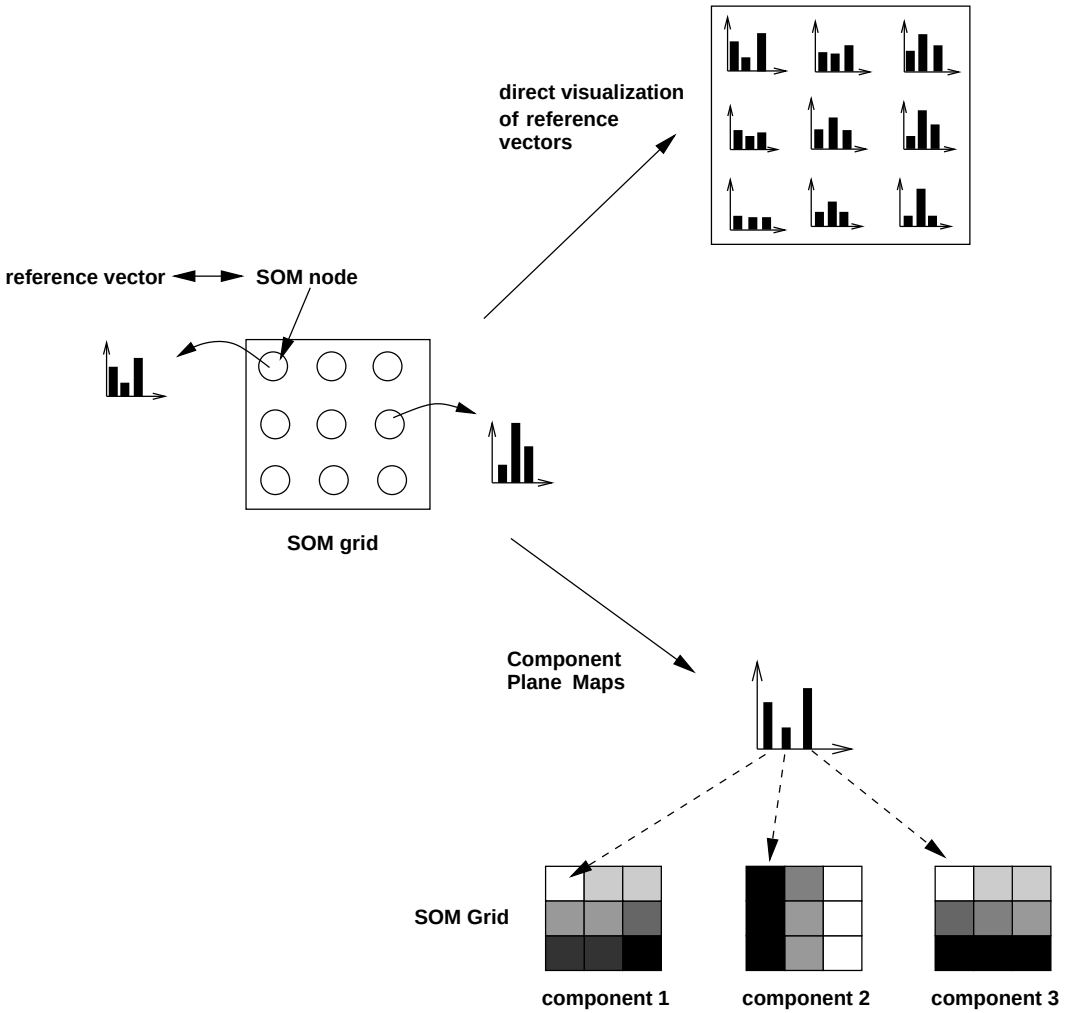

Figure 5.4.: Visualisation of reference vectors. Top: Direct visualisation utilising bar plots. Bottom: Visualisation of components utilising Component Plane Maps.

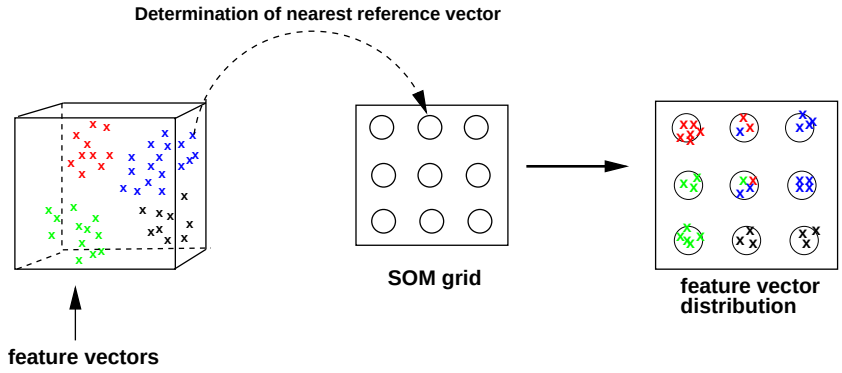

Figure 5.5.: Visualisation of cluster structure. At each node the feature vectors mapped to this node are visualised by a point of the respective colour.

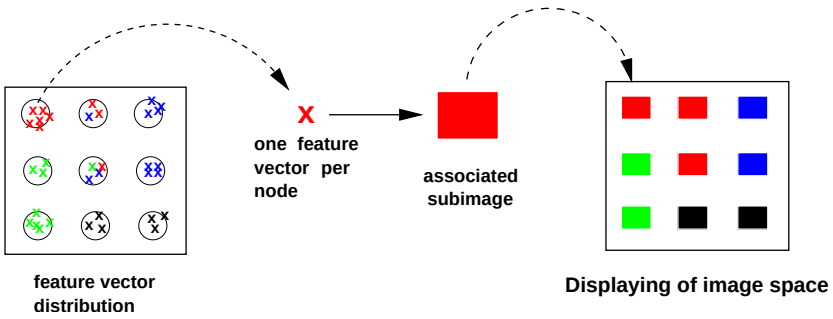

Figure 5.6.: Visualisation of the image domain. Each node in the SOM grid is represented by one subimage associated to one of the feature vectors mapped to the particular node.

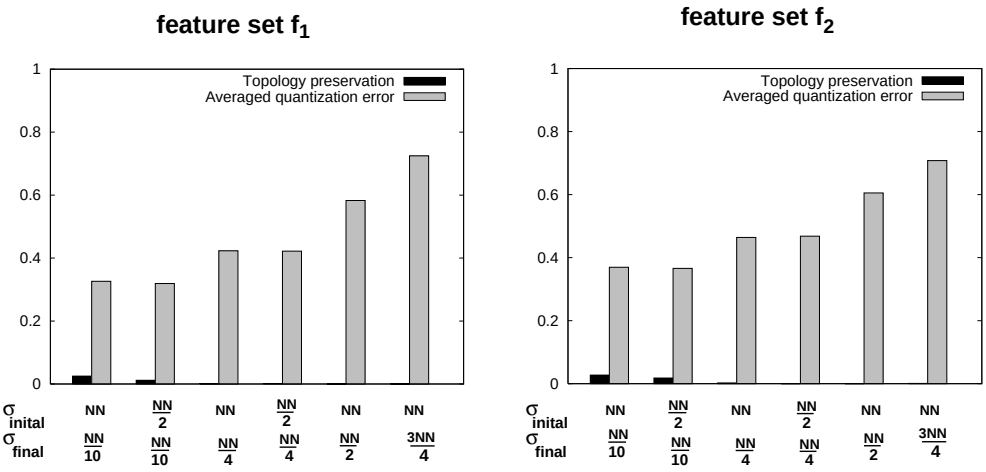

Figure 5.7.: TP and AQE values for varying parameters $\sigma_{initial}$ and σ_{final}.

work is the dimension reduction and visualisation of the database content and not the determination of a specific cluster structure, the size of the SOM grid is not regarded as a crucial point in our application. To ensure a sufficient generalisation of the results the number of nodes should not be chosen to high. In the following 8×8 SOM grids are used for visualisation purposes. The number of training steps is set to $80,000$. The training procedure has been carried out two times, using the first set of features f_1 (12 feature vector components) and the second set of features f_2 (12 feature vector components) respectively.

As described in chapter 4, section 4.2.2 the parameter σ strongly influences the properties of the resulting SOM grid and cluster structure, such as the topology preservation (TP) and the averaged quantisation error (AQE). The parameter is decreased during the training procedure linearly, i.e. an initial value σ_{intial} and a final value σ_{final} have to be chosen. To determine the optimal values the training is accomplished with varying values for σ and the results TP and AQE are compared. In Figure 5.7 the results for the two feature sets are presented. The Figure reveals that the final parameter σ_{final} plays an important role during the training procedure. On the other hand the initial value $\sigma_{initial}$ hardly influences the results for equal values of σ_{final}. In our case the topology preservation is very close to zero in all cases and thus extremely satisfying. However, the averaged quantisation error significantly increases with σ_{final}. According to these results the values $\sigma_{initial} = \frac{NN}{2}$ and $\sigma_{final} = \frac{NN}{10}$ are chosen for the further procedure with $NN = 8$.

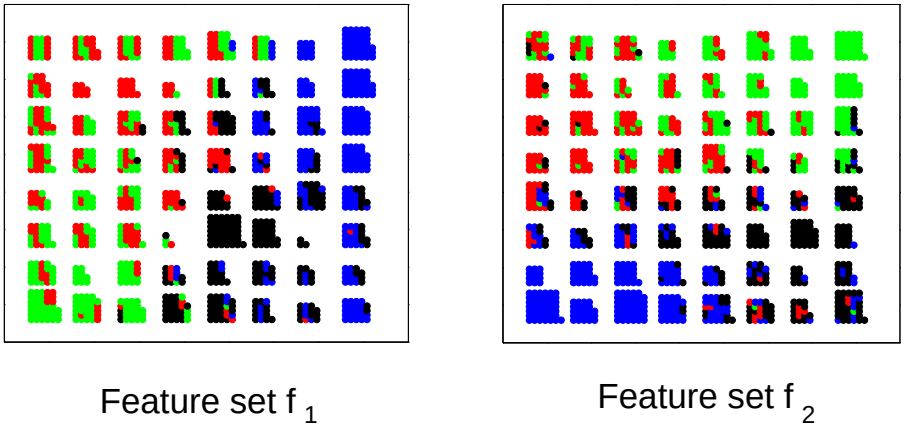

Figure 5.8.: Clustering result of both feature sets. Each feature vector is symbolised by a dot and displayed at the node of the nearest reference vector.

5.5.3. Exploration Procedure

The training results are shown in the Figures 5.8, 5.9 and 5.10 In Figure 5.8 the clustering result of both feature sets is presented according to the visualisation procedure displayed in Figure 5.5. Each subimage is symbolised by a point of the colour related to the class of tissue as shown in Figure 5.1. In the Figures 5.9 and 5.10 two further types of visualisation are shown. At the top the SOM grid is visualised in the image domain according to the method presented in Figure 5.6. In this image each node is marked with one of the subimages of the respective cluster. In this way, the distribution of histological features can be explored. At the bottom of the Figures the Component Plane Maps are shown derived as explained in Figure 5.4. Each little square is a visualisation of the SOM grid representing one component of the reference vectors. Since the reference vectors have twelve components in both cases, twelve Component Plane Maps are shown, one map for each component of the reference vector.

Feature Set f_1 Starting with the analysis of Figures 5.8 and 5.9, we can derive the following conclusions from the images. The clustering result visualised at the top shows that this set of features is appropriate to discriminate psammomatous (blue) and transitional (black) images. However, the meningotheliomatous (red) and the fibroblastic (green) classes are still strongly mixed.

By exploring the Component Plane Maps at the bottom of Figure 5.9 the correlation of this clustering result to particular components of the feature vector

- i.e. particular features - is revealed. Comparison to the visualisation of the image domain then allows a clinical interpretation of the single features.

The feature vector components $1-6$ are the scale features of the intensity image h_1. In the Component Plane Maps these components vary strongly from the top to the bottom of the SOM grid. In detail, these features increase from bottom to top. However, since there is no clear separation between meningotheliomatous and fibroblastic feature vectors in this vertical direction, this does not seem to be relevant to distinguish these two classes. The sixth component additionally introduces an innerclass separation in the psammomatous group of tissue (from top right to bottom right). By exploring the corresponding subimages it becomes clear, that from top to bottom the amount of tissue inhomogeneities increases. Regarding the psammomatous group located on the right hand side, the subimages at the bottom show large cracks in the tissue in contrast to the images located at the top. Thus, the sixth feature is linked to these large cracks. The finer scale features (scales 1-5) are quite redundant and can be linked to smaller tissue inhomogeneities in the extracellular matrix. By exploring the visualisation of the image domain, it becomes clear that the amount of these fine scale tissue inhomogeneities increases from top to bottom.

The fine scale components of colour channel h_2 (components 7-12) are especially low in those images providing a large amount of psammoma bodies. This must be due to the fact that channel h_2 mainly describes cell nuclei. The psammoma bodies do not contain any cell nuclei and therefore provide very low values in these features. The fibroblastic tissue in the lower left part of the SOM grid usually provides considerably high values in these components. This can be explained by the property of the wavelet-based features to mainly encode the contour of cell nuclei contained in the images. The amount of cell nuclei contours on the one hand increases with the amount of cell nuclei. On the other hand it can be expected, that elliptic cell nuclei as contained in fibroblastic tissue feature a longer contour than the round cell nuclei in other types of tissue and thus provide higher values regarding these features.

Feature Set f_2 As described above this set of features is constructed to describe preferred orientations in the image. As expected the separation of the fibroblastic and the meningotheliomatous class - as visualised at the top of the Figure - is significantly increased compared to feature set f_1. However, the Component Plane Maps reveal that the components 6 and 12 - associated with very coarse scale details - do not show a distribution corresponding to some histological interpretation. Furthermore, as expected all features usually take

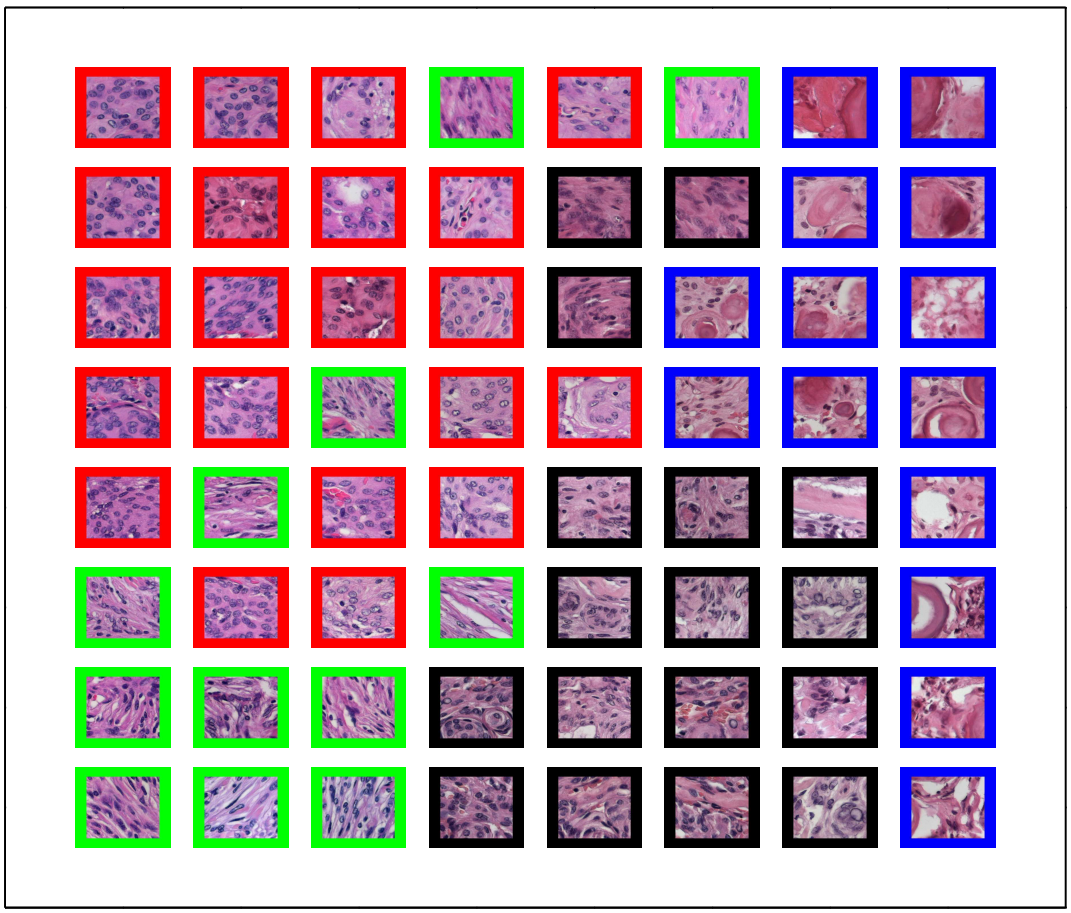

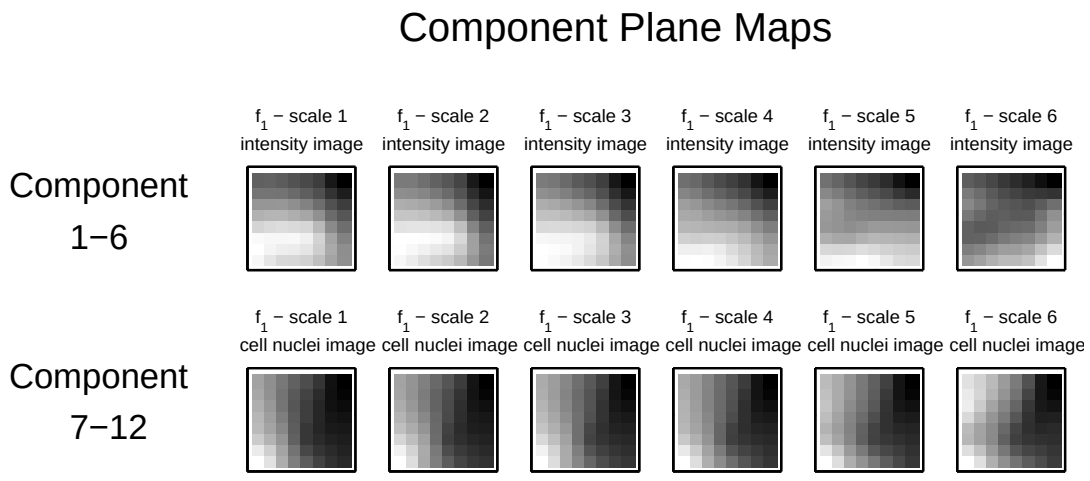

Figure 5.9.: Visualisation of the SOM training result based on feature set f_1. Top: The Visualisation of the image domain. Bottom: The Component Plane Maps.

high values in case of fibroblastic subimages since this image class possesses the strongest fascicular tissue architecture, i.e. orientated structures. The components 1-5 (corresponding to the intensity image) show their maximum at the top right of the SOM grid and decrease from top right to bottom right. The components 7-11 also have a maximum value at the right top of the grid but decrease much faster from top to bottom. By exploring the corresponding subimages, it becomes obvious that the components 7-11 (cell nuclei images) only show high values in case of elongated cell nuclei, whereas the components 1-5 (intensity images) result in high values in case of any orientated structure, either cell nuclei or characteristics of the extracellular matrix. Overall the components show a strong redundancy.

From the interpretation of both feature sets clear links between numerical feature vector components and their histological interpretation in the image domain can be derived (Table 5.1).

feature set	Component	Feature	histological interpretation
f_1	1-5	intensity image scale 1-5	amount of tissue inhomogeneities, e.g. small cracks, especially low in psammoma bodies
	6	intensity image scale 6	very large cracks in the tissue, especially high for cracked psammoma bodies
	7-12	cell nuclei image scale 1-6	amount of cell nuclei (contours), especially low in psammoma bodies
f_2	1-5	intensity image scale 1-5	parallel arranged fibres and thin parallel aligned cracks, especially high in some fibroblastic images
	6	intensity image scale 6	unclear
	7-11	cell nuclei image scale 1-5	elongated cell nuclei, especially high in fibroblastic images
	12	cell nuclei image scale 6	unclear

Table 5.1.: Histological interpretation of feature vector components.

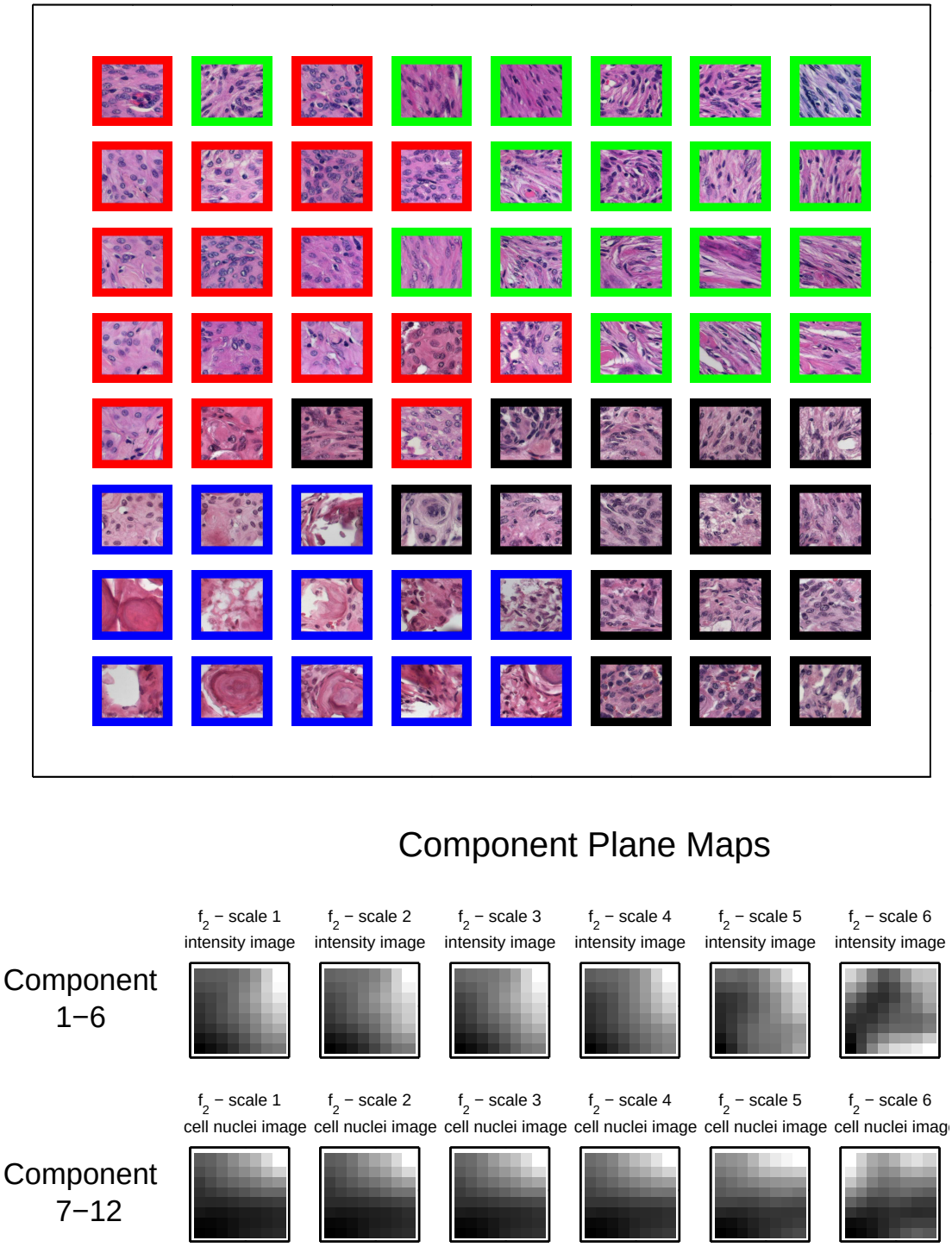

Figure 5.10.: Visualisation of the SOM training result based on feature set f_2. Top: The Visualisation of the image domain. Bottom: The Component Plane Maps.

5.6. Applications of Results

5.6.1. Feature Selection

In the foregoing section the histological characterisation of the specific feature vector components has been detailed. In this section it is described how this can be used in the process of feature selection. The selection of only a subset of features is usually desirable to increase system performance and to avoid the difficulties of large feature vectors, the so called *curse of dimensionality*. The most common method of feature selection is to evaluate the performance of a specific system, e.g. a classification or image retrieval system, based on all possible subsets of features or feature vector components. However, the results of such an approach are system dependent and may vary due to the selected method for classification or retrieval [3]. Furthermore, it is a black-box scenario, i.e. it does not provide an interpretation of the features in the image domain. While simple features such as colour histograms are easy to interpret in the image domain, features based on transforms such as the wavelet-based ones utilised here are much more difficult to understand. This is usually a crucial point of criticism from the physicians, who are interested in features or feature sets that can be interpreted to some degree at a clinical level of understanding. The analysis method just described allows a direct interpretation of even abstract features. In this way, features can be selected in correspondence to their clinical semantics.

Since the amount of cracks in the tissue varies strongly in psammomatous tissue it is not considered to be of diagnostic relevance. Therefore the component 6 of feature set f_1 will be negelcted. The components $1-5$ of feature set f_1 vary strongly within the meningotheliomatous and the fibroblastic class. Consequently, these components are also classified as encoding innerclass differences and thus negelcted.

The visualisation further reveals some redundancy in the components $7-12$ of this feature set. These components show a very similar distribution. Some of them can therefore also be neglected. Eventually only the components $9-10$ of feature set f_1 are chosen for tissue characterisation. These components correspond to the scales 3 and 4 of the cell nuclei image h_2. All others are neglected due to redundancy or due to a lack of clinical relevance.

Regarding feature set f_2 first the components 6 and 12 are discarded due to a

missing interpretability. The remaining components then provide a useful clinical interpretation (Table 5.1) but show a strong redundancy. Therefore some of them are also neglected. Only the components 3, 4 and 9.10 are retained. These components correspond to the scales three and four of both colour channels h_1 and h_2.

set of features	h_1	h_2
f_1		scale 3 & 4
f_2	scale 3 & 4	scale 3 & 4

Table 5.2.: Selected features for tissue characterisation.

In this way a subset of six features is selected from a total set of 24 features. The six selected features are presented in table 5.2.

The SOM training based on the selected features is now repeated. The result is shown in Figure 5.11. Obviously, although only six features have been selected from a group of 24 features, these six features are clearly sufficient for a good separation of the four classes of tissue. Due to a feature selection based on histological interpretation, the components of the reference vectors can clearly be linked to particular image structures at a clinical level of understanding. This is shown in Figure 5.12. This Figure shows the reference vectors associated to each node as a bar plot. Due to the visualisation in the image domain in Figure 5.11, we are able to link the characteristics of the reference vectors to the clinically relevant image structures, which is shown in the table in Figure 5.12. For instance, low values of all components of the feature vector are characteristic for psammoma bodies while high values in all components of the feature vector are typical for fibroblastic tissue, representing orientated image structures and a significant amount of cell nuclei.

To prove that the subset of features selected above is even more appropriate for class separation than the combination of all possible features, a measure rating the class separation in the feature space is computed. First, the centre of each class c in the feature space $\bar{\mathbf{x}}_c$ and the average distance of each class centre from the centres of the remaining three classes $dist(c)$ is determined. Second, the innerclass variance of each class σ_c^2 is determined. Please note that all values are normalised to the length of the feature vectors. This normalisation assures, that the results of feature vectors with different dimensions are

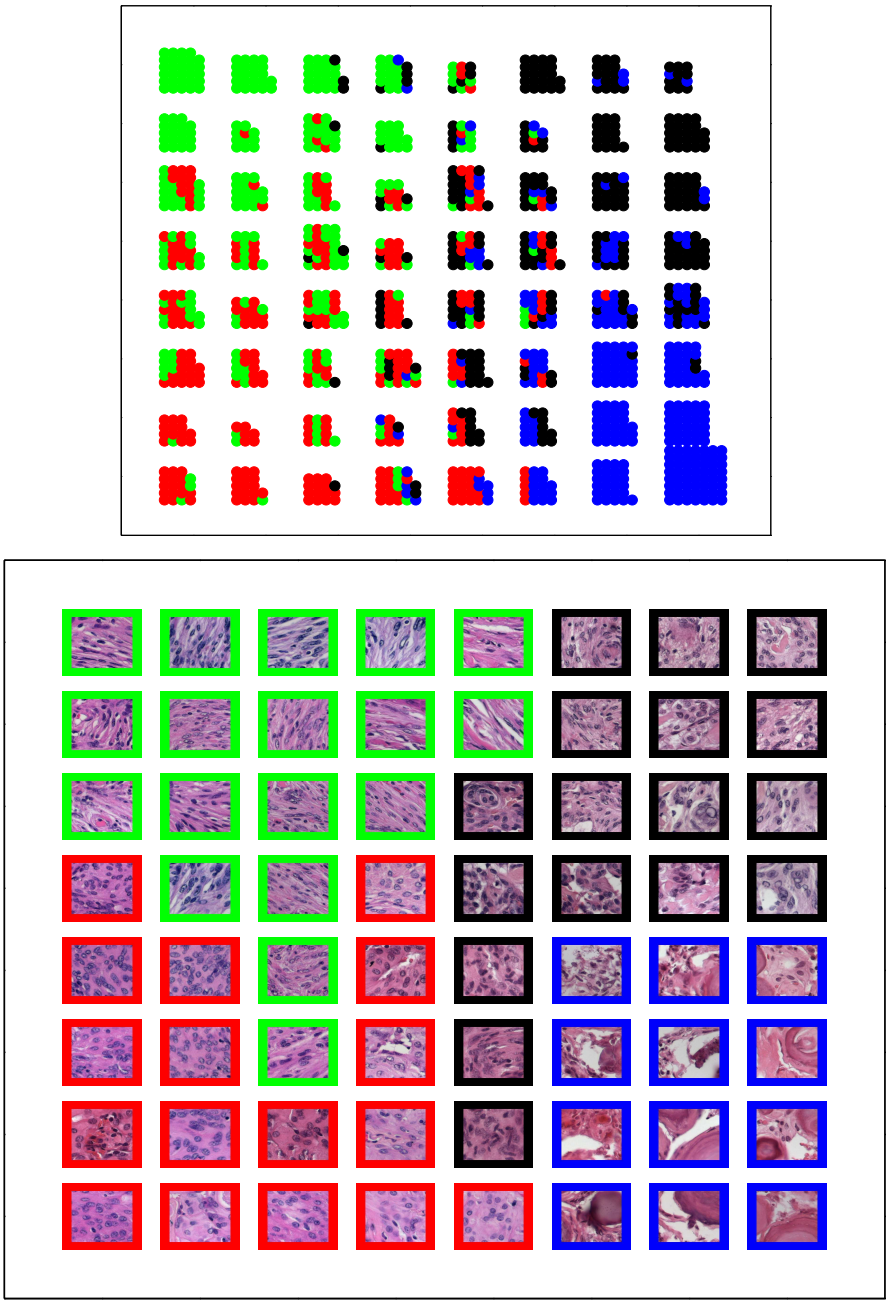

Figure 5.11.: Result of the SOM training based on the selected features. Top: Clustering result. Bottom: Visualisation of the image domain.

comparable. A good separation of one class from the others is achieved, if the distance of the class centre to the other class centres is high and the innerclass variance is small. As a measure of the separation therefore the ratio $r_c = \frac{dist(c)}{\sigma_c}$ is computed. The higher this ratio the better the class separation. In Table 5.3 the ratios r_c of the four classes based on different subsets of features are shown. Obviously, the selected subset of six features leads to the best values for r_c.

Features	r_c of tumour classes			
	meningo-theliomatous	fibro-blastic	psammo-matous	transi-tional
set f_1	1.295	1.334	1.923	1.601
set f_2	1.403	1.466	2.101	1.487
all features	1.369	1.386	1.968	1.518
selected features	**1.735**	**1.741**	**2.992**	**1.954**

Table 5.3.: Separation of tumour classes.

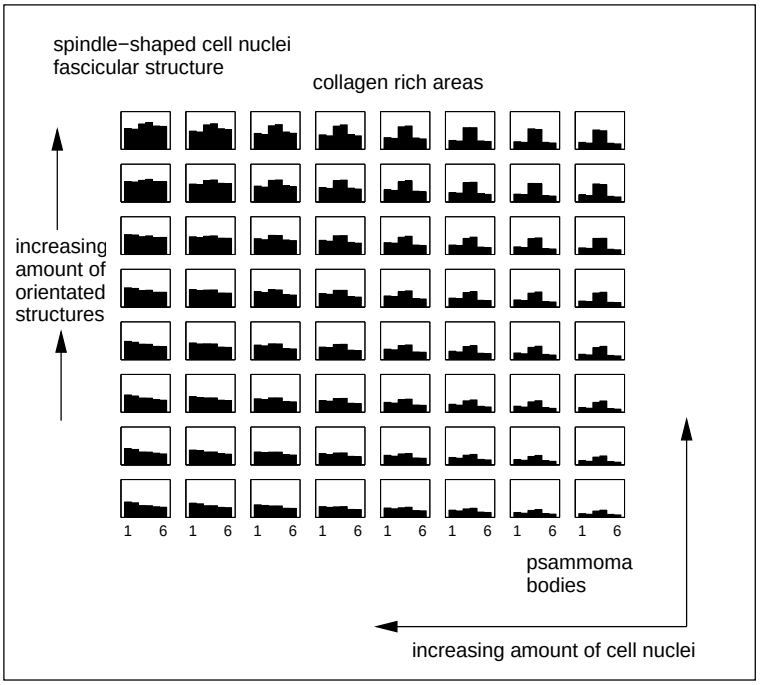

Component	histological interpretation
1+2	number of cell nuclei (contours)
	especially low values in psammoma bodies and areas of collagen
3+4	Amount of anisotropic tissue inhomogeneities
	especially high values in case of parallel aligned cracks in fibroblastic tissue
5+6	Anisotropic shaped cell nuclei
	especially high values in fibroblastic tissue

Figure 5.12.: Top: A histological feature map derived from the visualisation procedure. The map allows to clearly link numerical features to histological semantics (bottom).

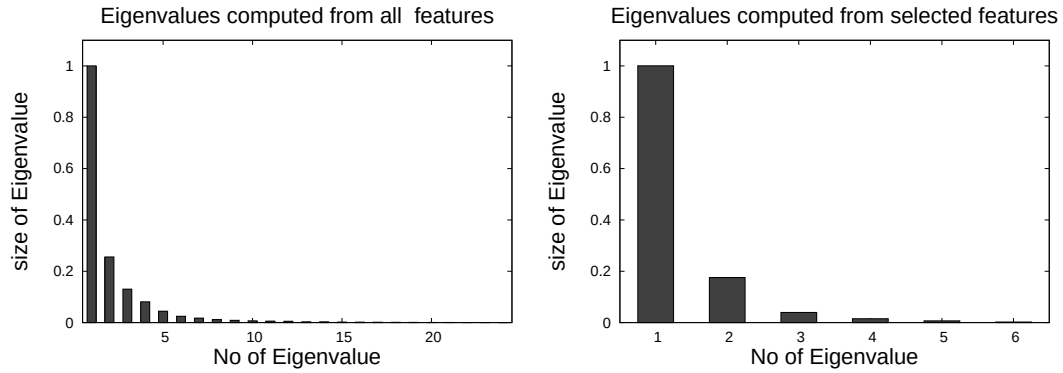

Figure 5.13.: Distribution of the eigenvalues corresponding to the different feature spaces. Left: Eigenvalues derived from all 24 features, Right: Eigenvalues derived from selected features.

Comparison to PCA

Additionally the different feature sets are compared by computing the results of a PCA. The PCA is computed for a feature set containing all possible features and for the selected subset. In Figure 5.13 the resulting eigenvalues are shown. It is clearly visible, that in the case where all 24 features are considered (left) only a few eigenvalues provide a significant value. This hints at the redundancy already observed in the result of the SOM training. In Figure 5.14 the projections of all feature vectors onto the eigenvectors corresponding to the largest two eigenvalues are shown. By comparing these two feature sets several properties of the different feature spaces become obvious. The group of psammomatous feature vectors is much more dense in the case of the selected features (right). As mentioned above, some features introducing strong innerclass differences into the psammomatous group have been discarded. As a result the cluster of psammomatous feature vectors is much more compact in the PCA projection. A second important observation is the following. In the left-hand part of Figure 5.14 the fibroblastic (green) feature vectors build two clusters, at the top and at the bottom of the meningotheliomatous cluster (red). After discarding several features encoding innerclass variations of the fibroblastic group, this separation of the fibroblastic feature vectors in two clusters is not observable anymore (right-hand side of Figure 5.14.

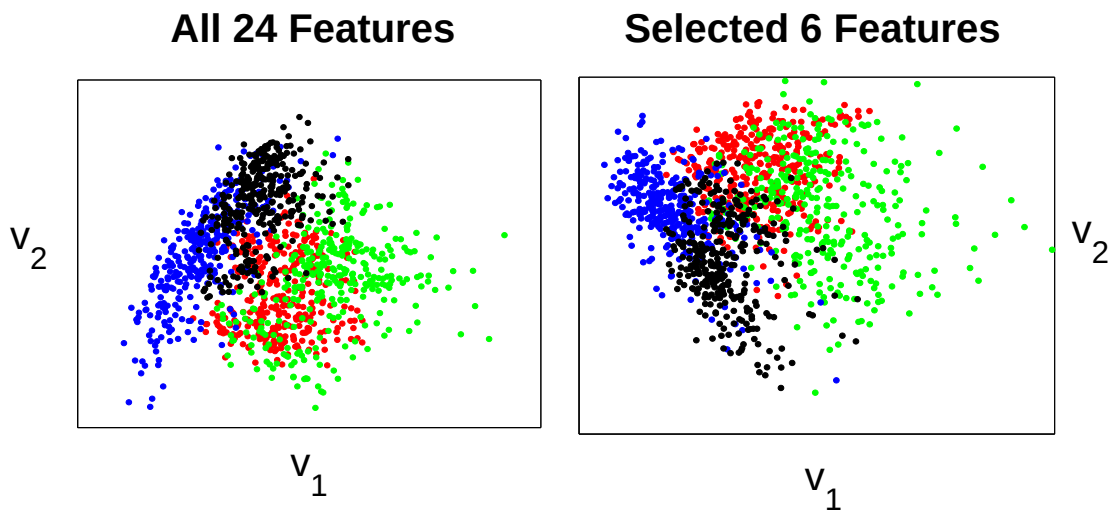

Figure 5.14.: Projections of the feature vectors onto the two eigenvectors $\mathbf{v}_1, \mathbf{v}_2$ related to the largest eigenvalues. Top: All 24 features, Bottom: Selected features.

5.6.2. Interface for CBIR Systems

In content-based image retrieval systems several types of query formulations are possible. The most common one is the query by example, i.e. the user provides an example image to the system. However, in some cases a starting image may not be available, this is called *page zero problem* [5]. One possible solution is to annotate text to the images and perform the first retrieval step based on this text. However, for this purpose all images in the database have to be annotated somehow, a very time-consuming task if done manually. Several approaches exist to annotate the images automatically, e.g. confer [6]. However, textual labels are not necessarily explicit and unambiguous. The approach described above already provides an user interface suitable for various query tasks. By providing the SOM grid visualised by example images and a histological map the user can define a query for a specific type of image just by selecting a specific example image in the SOM grid. If the user wants to perform a textual query he can select a region in the histological feature map (Figure 5.15) to define his interests. The link between a SOM region and its clinical context provides a flexible type for query support. This is a technical suggestion at this point and not already an implemented interface. However, it shows how the visualisation described above naturally contributes to various challenges in the design of systems for diagnostic support.

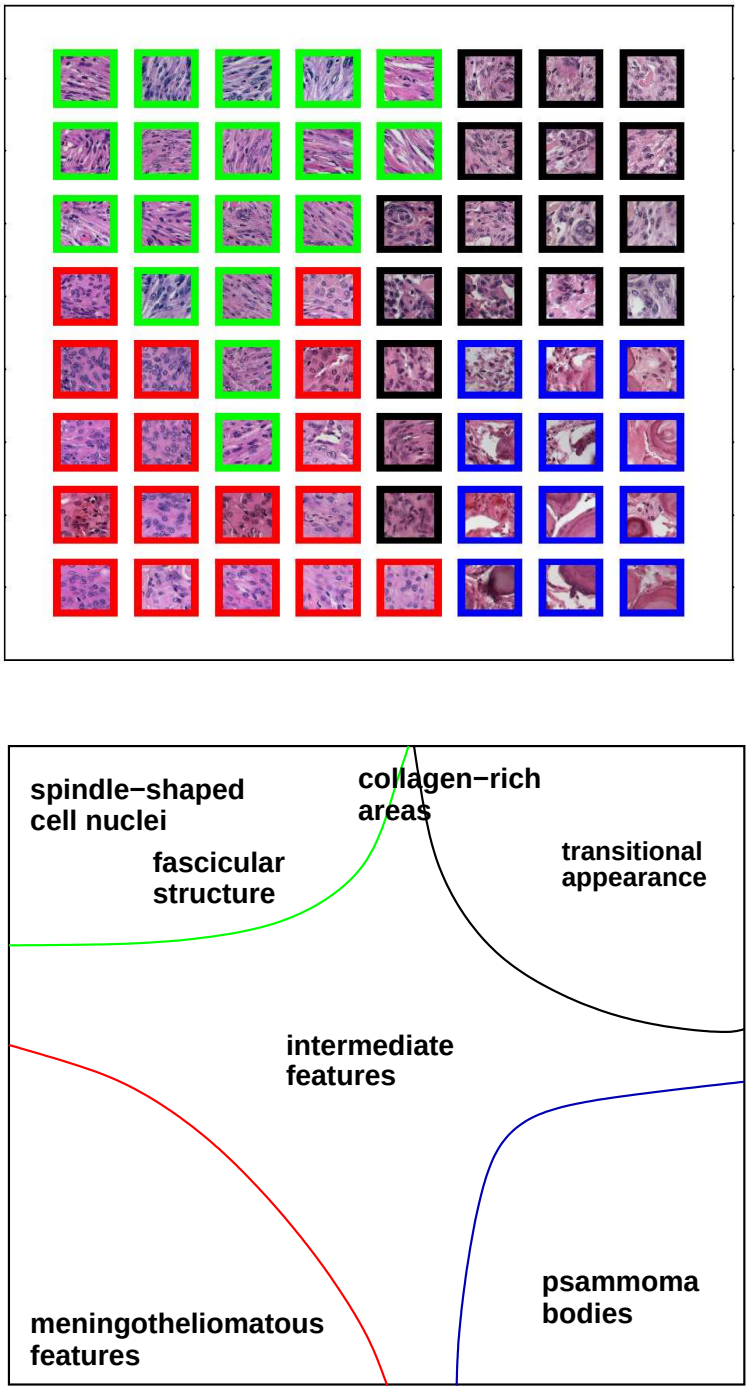

Figure 5.15.: Overview of a database by subimages (top) and by a histological map (bottom).

5.7. Choice of the Mother Wavelet

To compare the results - computed with different mother wavelets - it is not useful to rely on a SOM training, since during the training procedure randomness is introduced. Therefore in case of varying results it would not be determinable whether the changes are introduced by the change of the mother wavelet or by the randomness of the training procedure. Thus the results of a PCA are calculated and compared. Here all 24 features are involved in the computation of the eigenvalues and eigenvectors of the covariance matrix. In Figure 5.16 the projections of all feature vectors onto the two most important eigenvectors $\mathbf{v}_1, \mathbf{v}_2$ are shown. These projections are derived from features computed with four different mother wavelets, the Haar-Wavelet, the Daubechies(2)-Wavelet, the $CDF_{9/7}(4,4)$-wavelet and the $CDF_{5/3}(2,2)$, which has been used in the work described above.

As can be seen, the four mother wavelets provide very similar results regarding the PCA projection. Thus the choice of the mother wavelet does not seem to be very crucial in this particular application.

5.8. Discussion and Conclusion

In this chapter it was demonstrated how a detailed analysis of low-level texture features can be achieved. The wavelet-based features are proven to provide a powerful method for tissue discrimination in microscopy images of meningiomas. The detailed exploration of the feature space allows to interpret the low-level visual features at a clinical level of understanding. In this way features can be linked to innerclass or interclass differences.

Due to this interpretation it is possible to select a histologically meaningful subset of features, optimised for the particular set of images and its clinical context. However, a complete separation of interclass and innerclass differences cannot be achieved. This is also a general semantic problem, because some particular features are important to distinguish between two types of classes but likewise vary within a different class. One of such image characteristics is the number of cell nuclei, which is relevant to discriminate the homogeneous psammoma bodies from the other classes but also vary e.g. within the meningotheliomatous class.

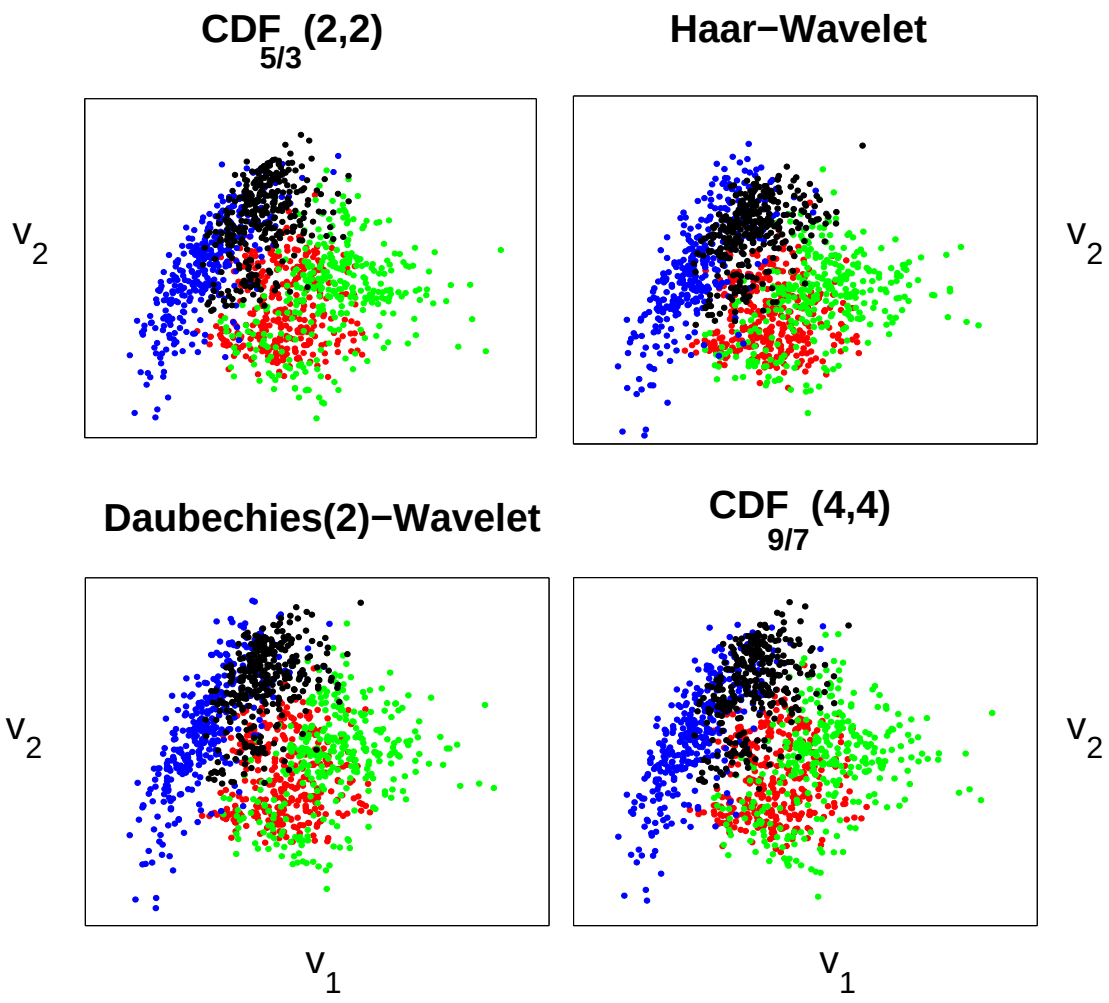

Figure 5.16.: The projections of the features vectors onto the two most important eigenvectors $\mathbf{v}_1, \mathbf{v}_2$ computed with four different mother wavelets.

6. Multiscale Analysis of DCE-MR Images

6.1. Introduction

As described in chapter 3.3 Dynamic Contrast Enhanced Magnetic Resonance Imaging (DCE-MRI) is a powerful imaging technique applied in breast cancer diagnosis. The uptake behaviour of a paramagnetic contrast medium (Gd-DTPA) in tissue is monitored over time, since enhancement of tissue can provide valuable information about the existence and the characteristics of lesions [48]. Tumour tissue often shows a significantly different vascularity and permeability compared to normal tissue. This might yield a characteristic uptake of the contrast agent. In section 3.3.5 it is described that both - the dynamics and the morphology of lesion enhancement - are important characteristics for the diagnosis of breast lesions.

In recent years several works have analysed the discriminative power of particular radiological criteria. In [84] the importance of kinetic criteria is proven for the discrimination of lesions into benign and malignant. Presence of a washout of the contrast agent is shown to be typical for malignant lesions. In [85] different kinetic and morphologic radiological criteria are compared. The most suitable criteria are proven to be the time-to-peak enhancement and the descriptor of margins. According to this work malignant lesions usually provide a short time-to-peak and an irregular margin in contrast to benign lesions. There, the dynamical features are averaged values derived from a human defined region of interest. The margin of the lesions was rated on a scale from 1 to 5 by the human observer with 1 indicating a smooth margin and 5 indicating a spiculated margin. In [86] also dynamical and morphological features were evaluated. Morphological criteria included those like mass margin and the internal lesion enhancement. There, also *inter-* and *intraobserver variability* were tested, i.e. the degree of disagreement among a group of raters of with

respect to repeated rating of the same expert. While particular features such as presence of washout provide a very low variability, the rating of other features was shown to be quite varying. In [87] the interobserver variability of carcinomas was evaluated with respect to the terminology of the Breast Imaging Reporting and Data System (BI-Rads). The authors reported moderate interobserver agreement regarding morphological criteria and also only moderate intraobserver agreement of some particular descriptors. Another work presenting moderate interobserver agreement on radiological terminology is [88]. In that work especially the terminology for those lesion descriptors expected to be very characteristic has been reported as only moderate. An additional work analysing the usefulness of morphological criteria is [89]. Also in this work a relatively high interobserver variability has been reported. Two very recent works on radiological features are [90, 91]. In [90] some lesion parameters are decided to be very characteristic in the classification of breast tumours. Especially an irregular or spiculated lesion margin and the presence of washout are reported to be specific for malignancy. In [91] dynamical features were rated qualitatively according to their shape and quantitatively by computed meta features. Morphological criteria were rated on a scale of four from present to absent. Very predictive criteria were the signal intensity and again the mass margin.

At this point it becomes obvious that methods for a derivation of objective features for lesion description are extrememly desirable. Currently several approaches to develop systems for diagnostic support are known. Computerised diagnostic systems provide information to assist the medical expert in its daily work. Especially with respect to DCE-MRI - an imaging technique resulting in large and multivariate datasets - these systems might decrease the observer variability just described. Different approaches are known in this area including systems for lesion segmentation, classification or visualisation. These approaches for automatic analysis techniques are described in the following.

Automatic Analysis of Enhancement Dynamics

As described in section 3.3.5 the signal intensity monitored over time provides information about presence and the malignancy of the lesion imaged. Regarding automatic analysis methods of enhancement kinetics those focusing on the detection or segmentation of lesions [92, 93, 94, 95] can be distinguished from those working on lesion classification [96, 97]. The work of Nattkemper et al.

[98] describes a general analysis of voxel enhancement curves. Besides this, several approaches focus on the pharmacokinetic modelling and thus visualisation of contrast agent uptake curves such as [99, 100, 101].

Most of the works mentioned above make use of neural networks or machine learning methods for the particular application. In [93, 94, 96, 97] supervised machine learning methods are applied while [92, 98, 95] are based on unsupervised learning algorithms.

In [97] kinetic meta features are derived from a human defined region of interest. In contrast to this, the other works are voxel-based, i.e. the signal intensity of each voxel is analysed separately with respect to its development over time [92, 93, 96, 94, 95, 98].

Automatic Analysis of Lesion Morphology

Due to the injected contrast agent breast tumours enhance revealing a specific morphology. As reported above, it has been shown that besides dynamical enhancement characteristics also morphological criteria are useful to distinguish benign tumours from malignant ones. To increase the comparability of morphological criteria an automatic classification of tumour morphology is important. Therefore several works focused on an automatic diagnoses of lesions based on tumour boundaries and tumour texture regarding different imaging domains either X-Ray imaging [8] or DCE-MRI [102, 103]. Shape based descriptors in tumour diagnostics usually rely on the determination of an exact tumour boundary. This may be hand-drawn [8, 9] or the result of pre-processing steps such as automated segmentation results [102, 103]. The exact boundary is then used to compute further parameters such as geometric descriptors [103, 104], Fourier-based descriptors [104], moment-based descriptors [104] or wavelet-based descriptors [8]. Besides margin descriptors also textural descriptors have been analysed. In [105] a hand-drawn region of interest was analysed utilising several texture descriptors based on co-occurrence matrices.

Simultaneous Analysis of Dynamics and Morphology

Approaches for the simultaneous analysis of lesion dynamics and morphology are rare. The usual way is here, to use human-defined meta features for enhancement kinetics and morphology and combine these in a following analysis or classification step. In [106] these meta features are used to train a neural

network in order to classify lesions into benign or malignant. A comparable approach has been made in [107] in order to evaluate the human-defined features with respect to their classification performance. In [108] several morphological and dynamical features of the lesions are computed and analysed after determining an exact lesion boundary by a human observer.

Focus of this Work

The various examples of different applications prove that kinetic and morphologic criteria are extremely important in the diagnostic process and that it is possible to implement systems providing an automatic analysis. However, some particular challenges are not addressed in the works mentioned above. For instance, some of the methods require a significant amount of human interaction such as the determination of a tumour boundary. Others only take into account a particular part of the DCE MR images and are not suited to process entire datasets. In the following, two types of analysis will be described. First, an analysis of enhancement dynamics is presented, resulting in the definition of features encoding typical enhancement patterns of tumour tissue. Second, features encoding lesion morphology are derived. The benefits of both types of features are shown by the development of solutions for particular tasks in image processing based on the derived features.

6.2. Analysis of Dynamic Characteristics

6.2.1. Motivation

In this work the focus lies on a general analysis of the DCE-MRI datasets, because a derivation of features specific for different types of tissue may naturally lead to several applications such as visualisation or segmentation of images. At this point an additional challenge arises. The MR images analysed are in the majority of cases very large, e.g. the database utilised in the research described here provides a time series of MR images, with single images containing approximately two million voxels. The lesion analysed usually constitutes about 1 % of the entire image. Therefore a large amount of data has to be processed in order to find a very small amount of diagnostically relevant information.

Additionally, the features have to provide solutions for a specific problem typical for exactly these kind of datasets. All analysis methods suffer from a

huge amount of additional contrast agent uptake, which is not related to suspicious tissue. Depending on the patient's anatomy, the region of the body imaged usually includes also a significant part of the patient's chest. The contrast agent injected intravenously thus produces a significant uptake in the region of the heart (Figure 6.1). This enhancement is not significant for the diagnosis but can be confused with contrast agent uptake in tumour tissue. An example for these similarities can be found in [99]. That work concentrates on the visualisation of tumour enhancement properties. There, several results are presented showing breast tissue enhancement by a colour code. The region of the chest containing the heart features the same colour code as the tissue of strongly enhancing breast lesions. Thus, the features derived in this thesis have to be able to distinguish contrast agent uptake in the tumour tissue from contrast agent uptake in other parts of the body such as the chest.

The segmentation approaches mentioned above usually only take into account the specific region of interest, either derived by a human observer or some pre-processing steps. However, they do not address the question how to segment or classify the lesion in presence of a large amount of interfering information such as the region of the chest. This region is usually not included in the analysis. In [93] the breast parenchyma is separated from the region of the chest - including the heart - by several pre-processing step including a median filter, thresholding and a closing operator. In [95] a region of interest has been selected manually by a human observer. In many other publication this particular aspect remains unmentioned.

In this work, the differences between diagnostically relevant enhancement related to breast lesions and irrelevant enhancement in the region of the chest are analysed in order to develop a method to process entire datasets. The aim here is to distinguish both types of contrast agent uptake without prior knowledge of lesion location, size or other types of information.

One important challenge in this analysis is the fact, that the data processed significantly increases due to the inclusion of a large region of the chest. Especially the application of machine learning methods then suffers from a huge amount of training data. Therefore a trade-off between the amount of image information and detailedness of the approach is required. This trade-off can be achieved by applying wavelet-based multiscale analysis, since this produces localised image information at several levels of detailedness.

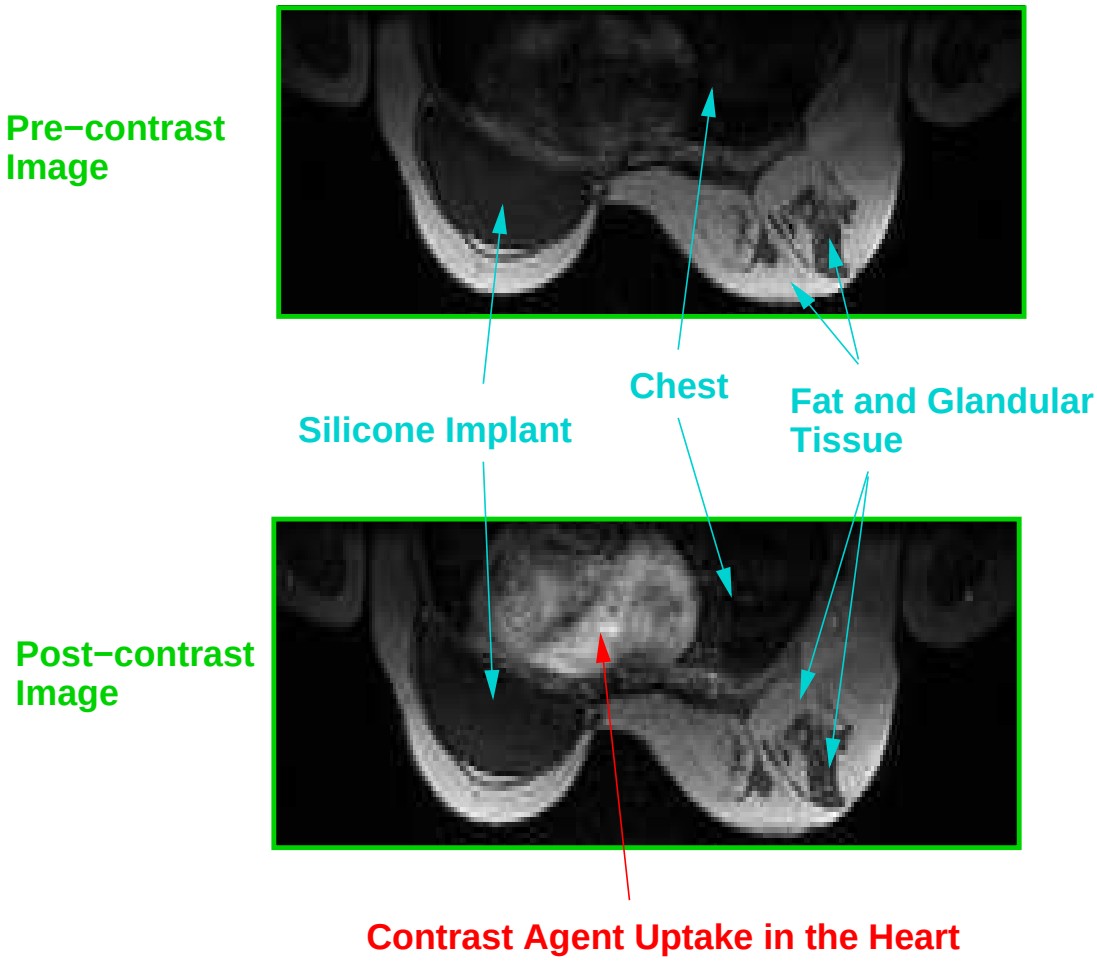

Figure 6.1.: After injection of the contrast agent, the signal intensity inside the chest increases due to contrast agent uptake in the heart.

6.2.2. Wavelet Analysis in Breast Cancer Diagnostics

Wavelet Analysis has often been applied in medical image analysis, e.g. for denoising, image enhancement or segmentation [10, 11]. Wavelet Analysis in Breast Cancer diagnostics is already known. However, most of the approaches are related to the analysis of X-Ray mammography, e.g. detection or classification of microcalcifications or masses in static X-Ray images [109, 110]. In MR mammography the use of wavelets is quite rare. One example is the use of Gabor Wavelets for texture analysis [111]. However, there have been several approaches regarding the analysis of neuroimaging results. In [112] two different acquisition methods in functional MR Imaging of the brain are compared in the wavelet domain. In [113] time-dependent MR images of the rat brain are analysed and clustered, based on a wavelet transform. In contrast to my work in [113] the wavelet transform has been applied to voxel time series and not to the spatial image information. Further voxel-based approaches can be found in [114, 115] focusing on wavelet-based statistical analysis or linear modelling of functional MRI time series.

The specific requirement in the application of the DWT on entire DCE-MRI datasets is to analyse the huge amount of wavelet coefficients. After decomposition an appropriate exploration framework is necessary to identify relevant wavelet coefficients and typical temporal patterns in the wavelet domain. Here, a method from the field of unsupervised machine learning is selected, the Self Organizing Map (SOM).

In this work a SOM is applied since it provides a favourable combination of clustering and visualisation capabilities. It allows the identification of tumour enhancement characteristics in the wavelet domain and the distinction from non-significant enhancement in the image.

6.2.3. Datasets

The database analysed has already been described in section 3.3. The analysis of collection I is presented in the following section. It contains eight datasets including ten lesions marked by a medical expert. Table 6.1 shortly resumes the content and histological diagnosis of collection I. For each volume an expert label marking the tumour is available. The first pre-contrast and all post-contrast images are included in the analysis, each one containing $256 \times 128 \times 64$ voxels with a spatial resolution of $1.33\ mm \times 1.33\ mm \times 2.5\ mm$ per voxel.

patient	diagnosis
1	multiple invasive carcinoma (ductal (NST) and lobular)
2	Sclerosing lymphocytic lobulitis
3	invasive tubular carcinoma
4	invasive carcinoma (ductal (NST))
5	Fibroadenoma, Fibrocystic changes
6	Fibroadenoma
7	invasive ductal carcinoma (ductal (NST))
8	invasive carcinoma (not assessable)

Table 6.1.: Diagnostic outcome of the patients included in the analysis.

6.2.4. Exploration of Datasets

Generation of Training Data In the following a Self Organizing Map will be used for the visualisation and thus exploration of wavelet-based image features. In this paragraph it is described how the training data is generated. To control the amount of image information analysed the Discrete Wavelet Transform is utilised. The image data is transformed spatially resulting in a huge amount of wavelet coefficients.

Due to this transform from the image domain into the wavelet domain some particular challenges arise in the generation of training data. Each dataset contains a time series of MR images. This work sets focus on the discrimination of two types of tissue enhancement, the enhancement in tumour tissue and the enhancement inside the chest. Thus, two separated sets of training data have to be generated from each single image, one for each type of enhancement.

To this end, wavelet coefficients have to be linked to specific regions inside the image. In applications based on voxel-based time series this could be done easily by utilising an expert label. Those voxels inside the labelled region belong to the training data, the voxel outside the region do not. However, after the DWT the link between a single coefficient and the region of interest in the image domain is more difficult to establish. A further question is how to value each training sample regarding its importance of the image information. In contrast to single voxels, which equally contribute to the image, the contribution of wavelet coefficients to an image depends on their size. Here, it is important to find a measure describing the contribution of each coeffcicient to the change in signal intensity due to contrast agent uptake.

To locate the wavelet coefficients derived from a specific type of enhance-

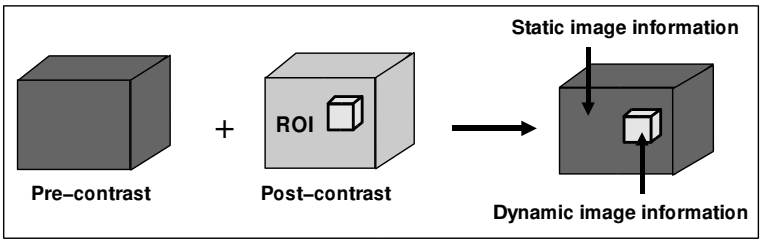

Figure 6.2.: Principle of deriving the relevant wavelet and scaling function coefficients.

ment new datasets are generated. First, the expert label is used to create a box - the region of interest (ROI) - around the tumour. Then a new time series of MR images is generated by exchanging in each image the image information outside the region of interest with the image information of the pre-contrast image (Figure 6.2). In this way artificially optimised images are created, providing only enhancement inside the region of interest considered, e.g. the tumour region or the region of the chest. A 3D Discrete Wavelet Transform is now applied to each single image of the time series. The coefficients related to the enhancement of the region of interest are now those providing the most significant change over time. This is measured in the following way.

Since the focus is on image characteristics resulting from contrast agent uptake, subtraction images are considered at this point. After subtracting the pre-contrast signal intensity from the post-contrast signal intensity, mainly the enhancing part of the breast tissue is visible and can produce significant coefficients. The DWT is a linear transform and can therefore be interchanged with the subtraction. Thus the coefficients d_i of the subtraction image computed from two images at $t = t_1$ and $t = t_2$ are equivalent to the subtraction of the coefficients of the two images

$$d_i(t_1 - t_2) = d_i(t_1) - d_i(t_2). \tag{6.1}$$

If the pre-contrast image is denoted by $t = 1$ and the five post-contrast images by $t = 2, ..., 6$ the following measure E_i related to the coefficient d_i via

$$E_i = \sum_{t=1}^{6} |d_i(t) - d_i(1)|^2 \tag{6.2}$$

describes the contribution of the coefficients with the index i to all five possible subtraction images and thus the enhancement at the five time points after contrast agent injection. This measure will be utilised for the further analysis.

scale	No of coefficients	
	per subimage	per scale
1	262,144	1,835,008
2	32,768	229,376
3	4,096	28,672
4	512	3,584
5	64	448
approximations	64	

Table 6.2.: Number of coefficients at each scale and decomposition subimage after applying a Discrete Wavelet Transform to an MR Image providing $256 \times 128 \times 64 = 2,097,152$ voxels.

The DWT performed involves five decomposition steps, resulting in wavelet coefficients of five different scales and the remaining approximation coefficients. In first heuristically derived results the $CDF_{5/3}(2,2)$ biorthogonal wavelet pair has been shown to be appropriate for this image domain [116]. Therefore the first steps of this analysis will be derived using this wavelet pair. A more detailed discussion of choosing an appropriate wavelet will be given below.

Now, the coefficients related to both types of enhancement can be computed. However, their number is still very high requiring a preselection before the analysis of coefficients. The particular properties of the DWT allow such a preselection depending on the scale and the size (or energy measure) of the coefficients.

Each MR image provides approximately two million voxels leading to the same number of wavelet coefficients after the DWT. In Table 6.2 the number of coefficients at each scale and decomposition subimage is presented. The number of coefficients at the finest scale (scale 1) is highest. The corresponding details describe signal changes between adjacent voxels, i.e. at a scale of 1.3 mm in x- or y-direction or 2.5 mm in z-direction. To reduce the amount of data analysed the coefficients of the first finest scale are neglected, since their number is very large and they are considered to be strongly influenced by noise. In this way the number of coefficients to be analysed is reduced by a factor of eight.

To perform an additional preselection based on the energy measure a histogram of this energy measure is computed. In Figure 6.3 this histogram com-

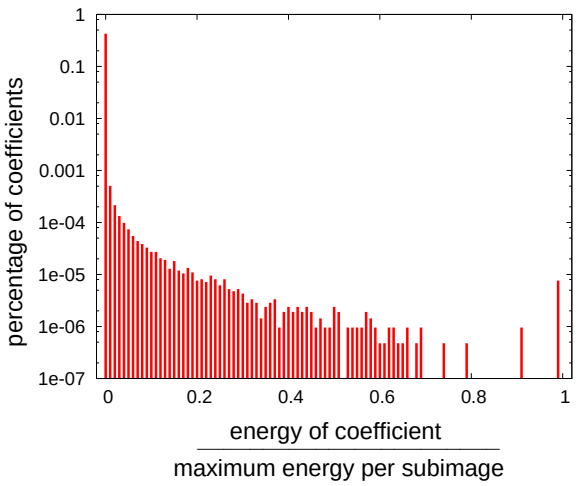

Figure 6.3.: Histogram of the energy measure. The tumour enhancement of one example dataset is shown.

scale	No of feature vectors	
	chest	tumour
2	$\approx 2 \cdot 10^5$	$\approx 10^4$
3	$\approx 3 \cdot 10^4$	$\approx 3 \cdot 10^3$
4	$\approx 5 \cdot 10^3$	$\approx 10^3$
5	$\approx 10^3$	$\approx 5 \cdot 10^2$
scaling function coefficients	$\approx 2 \cdot 10^2$	≈ 50

Table 6.3.: Number of feature vectors included in the procedure.

puted from the dataset shown in Figure 6.1 is presented. The histogram with 100 bins is calculated by including only the tumour enhancement. Since the energy measures of different scales cannot be compared, all values are normalised to the maximum energy of the particular decomposition subimage. As can be seen, by neglecting all coefficients providing a value smaller than 1% of the maximum the number of coefficients can be reduced significantly.

The total number of feature vectors included in the training procedure is presented in Table 6.3.

Exploration The coefficients with the same indices at each of the six time points are combined resulting in a six-dimensional vector, a time series of wavelet coefficients. In a first attempt these time series are used as feature vectors in the training procedure. The training procedure is then carried out utilising the feature vectors of all scales and of both tumour and chest enhancement. To eliminate dependencies on the absolute size of the coefficients, which increases significantly with increasing scale, all feature vectors are normalised with their absolute value. Thus the feature vectors are given by

$$\mathbf{x}_i = (d_i(1), ..., d_i(6))^T \cdot \frac{1}{norm_{1i}} \tag{6.3}$$

with

$$norm_{1i} = \sqrt{\sum_{t=1}^{6} d_i^2(t)}. \tag{6.4}$$

To explore the feature space a Self Organizing Map is trained and the results are visualised. The wavelet and scaling function coefficients are analysed separately. As in chapter 5, several training paramters of the SOM have to be set appropriately.

Also in this chapter the main purpose of the SOM training is a visualisation of the feature space. Thus the number of nodes is considered not to be a crucial parameter and is chosen as 10×10 to provide a suitable size for the Figure. Both α and σ are chosen to be linearly decreasing parameters. The initial and final values of the learning rate are set to $\alpha_{initial} = 0.9$ and $\alpha_{final} = 0.0001$ to provide a strong learning effect at the beginning and a convergence at the end of the training procedure. The SOM grid is initialised by randomly chosen feature vectors from the input space. The number of training steps is set to $N_{steps} = 10^6$.

As already discussed the choice of σ is a very crucial point and can strongly influence the training results. The initial value $\sigma_{initial}$ is set to $n = 10$ to ensure that the entire grid participates in the training at the beginning. As already mentioned in chapter 5 the final value σ_{final} has to be chosen very carefully, since it constitutes a trade-off between topology preservation and approximation of the input space. A training of 10×10 SOM grids with varying values for σ_{final} leads to training results showing clear differences regarding the value for TP (Topology Preservation) and AQE (Averaged Quantisation Error). In Figure

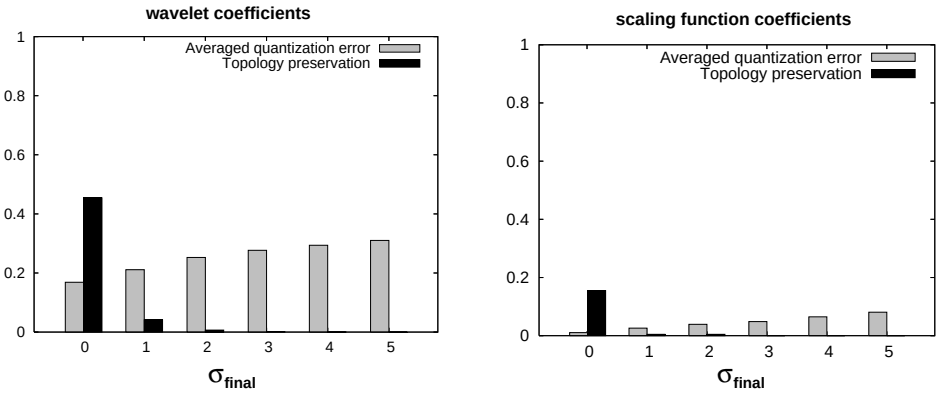

Figure 6.4.: The TP values after training a 10×10 SOM with either wavelet coefficients (left) or scaling function coefficients (right).

6.4 the results for both wavelet and scaling function coefficients are shown. The training result obtained with $\sigma_{final} \approx 0$ provides the best AQE. However, the preservation of the feature space topology is very poor. Increasing σ_{final} improves the topology preservation, but also slightly increases the AQE. For the purpose of feature space visualisation the topology preservation is important. Therefore a value of $\sigma_{final} = 2$ is chosen to explore the space of wavelet coefficients and a value of $\sigma_{final} = 1$ is chosen with respect to the scaling function coefficients.

The resulting SOM grids are visualised in Figures 6.5 and 6.6. In both figures each SOM node is shown by a little box plot representing the reference or prototype vector of this node. This visualisation method has already been described in chapter 5, section 5.5. Each feature vector now can be mapped to one of the nodes in the SOM by computing the nearest prototype vector. In contrast to the exploration procedure in chapter 5 the number of vectors mapped to each node is not a significant measure, since the contribution of the corresponding coefficients to the signal intensity differs. Thus the number of feature vectors is replaced by the energy measure introduced above. In this way each time series of coefficients $d_i(t)$ is related to one feature vector $\mathbf{x}_i$ and one energy value E_i.

Due to the generation of two separated training sets describing either contrast agent uptake in the tumour (denoted by (tu)) or in the chest (denoted by (ch)) all feature vectors can be labelled accordingly. By calculating the sums over all feature vectors mapped to one node $\mathbf{u_j}$ the energy-measures of feature vectors per SOM node for tumour and chest ($E_{(\mathrm{tu})}(\mathbf{u}_j)$ and $E_{(\mathrm{ch})}(\mathbf{u}_j)$) are

Figure 6.5.: Result of SOM training computed from the *wavelet coefficients*. The colour code indicates the energy measure at each node. Red symbolises tumour enhancement, blue indicates enhancement inside the chest.

obtained separately:

$$E_{(\mathrm{tu})}(\mathbf{u}_j) = \frac{1}{E^{(\mathrm{tu})}_{\mathrm{tot}}} \sum_{\mathbf{x}^{(\mathrm{tu})}_i \to \mathbf{u_j}} E^{(\mathrm{tu})}_i \quad \text{with} \quad E^{(\mathrm{tu})}_{\mathrm{tot}} = \sum_{\mathbf{u_j}} \sum_{\mathbf{x}^{(\mathrm{tu})}_i \to \mathbf{u_j}} E^{(\mathrm{tu})}_i, \tag{6.5}$$

and $E_{(\mathrm{ch})}(\mathbf{u}_j)$ accordingly with $E^{(\mathrm{tu})}_{\mathrm{tot}}$ and $E^{(\mathrm{ch})}_{\mathrm{tot}}$ employed as normalisation factors. In this way each node is characterised by two energy measures describing the significance of the corresponding reference vector for the signal enhancement in tumour tissue or chest respectively. In Figures 6.5 and 6.6 tumour enhancement is symbolised by red colour and enhancement in the chest by blue colour.

The exploration of these two Figures allows a deeper insight into the feature space. By the observations made in this process the suitability of the utilised features can be assessed. The first important observation is that the separa-

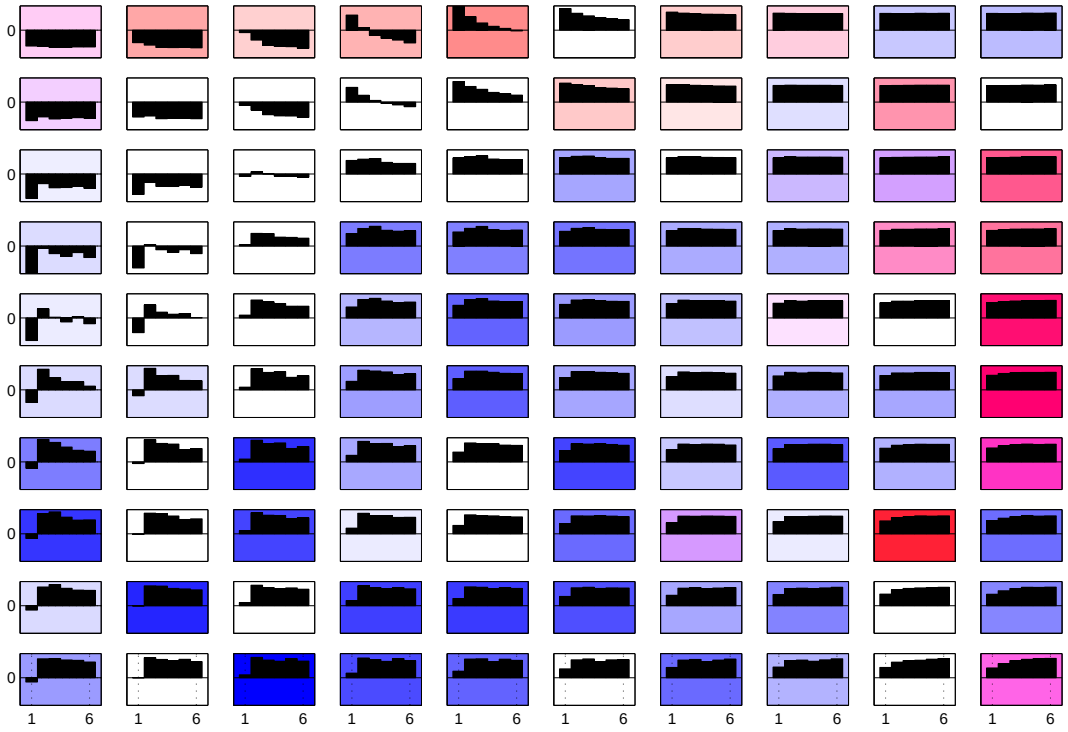

Figure 6.6.: Result of SOM training computed from the *scaling function coefficients*. The colour code indicates the energy measure at each node. Red symbolises tumour enhancement, blue indicates enhancement inside the chest.

tion of both types of contrast agent uptake is not satisfying. However, several characteristics can be found that can be utilised to optimise the feature vectors. Figure 6.5 reveals two types of feature vectors which are very similar except of the sign. They are located at the top right and the bottom left of the SOM grid respectively, Both types of reference vectors provide a mixed and quite similar enhancement classification, i.e. the violet colour reveals that they encode both types of tissue enhancement. Therefore one can draw the conclusion that the sign of the coefficient time series does not matter. (This also directly results from the mathematical properties of the DWT).

The second important observation is the following. The reference vectors described above show a more or less steady increase or steady decrease. The amount of increase or decrease can be quite equal, whereas the absolut values of the components can differ strongly. Therefore the most important property seems to be the difference between the coefficients from the pre-contrast image (component 1) and those from the post-contrast images (component 2-6). This observation also holds for the scaling function coefficients. This difference is equivalent to the coefficients derived from the subtraction images, which are usually inspected by radiologists in their daily clinical work.

Due to this observations a new type of feature vector is derived according to

$$\mathbf{x}_i = (x_i(1), x_i(2), ..., x_i(5))^T \tag{6.6}$$

$$= (d_i(2) - d_i(1), ..., d_i(6) - d_i(1))^T \cdot \frac{\text{sign}}{norm_{2i}} \tag{6.7}$$

with

$$norm_{2i} = \sqrt{\sum_{t=1}^{5} x_i^2(t)} \qquad sign = sgn(\sum_{t=1}^{5} x_i(t)). \tag{6.8}$$

In a next step the SOM-based analysis of the feature space is repeated based on these new feature vectors. Again, the optimal value for σ_{final} has to be determined. As described above, an analysis of the TP and AQE values reveals the optimal choice of σ_{final}. Due to the results shown in Figure 6.7 $\sigma_{final} = 2$ is chosen for the wavelet coefficient analysis and $\sigma_{final} = 1$ is chosen for the scaling function coefficients.

The SOM grids derived utilising these parameters are shown in Figures 6.8 and 6.9. The separation of the two types of enhancement in these SOM Grids is now significantly improved. Furthermore it is now possible to specify typical patterns encoding the two different type of tissue enhancement.

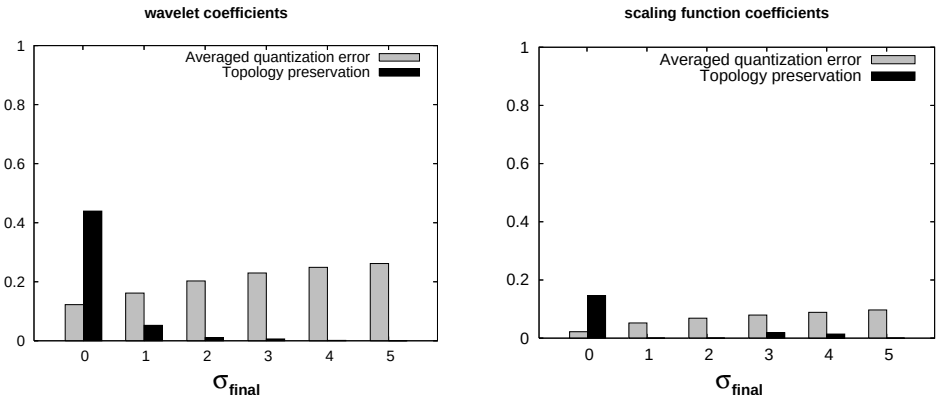

Figure 6.7.: The TP values after training a 10×10 SOM with the new feature vector. Left: Results of wavelet coefficients. Right: Results of scaling coefficients at right.

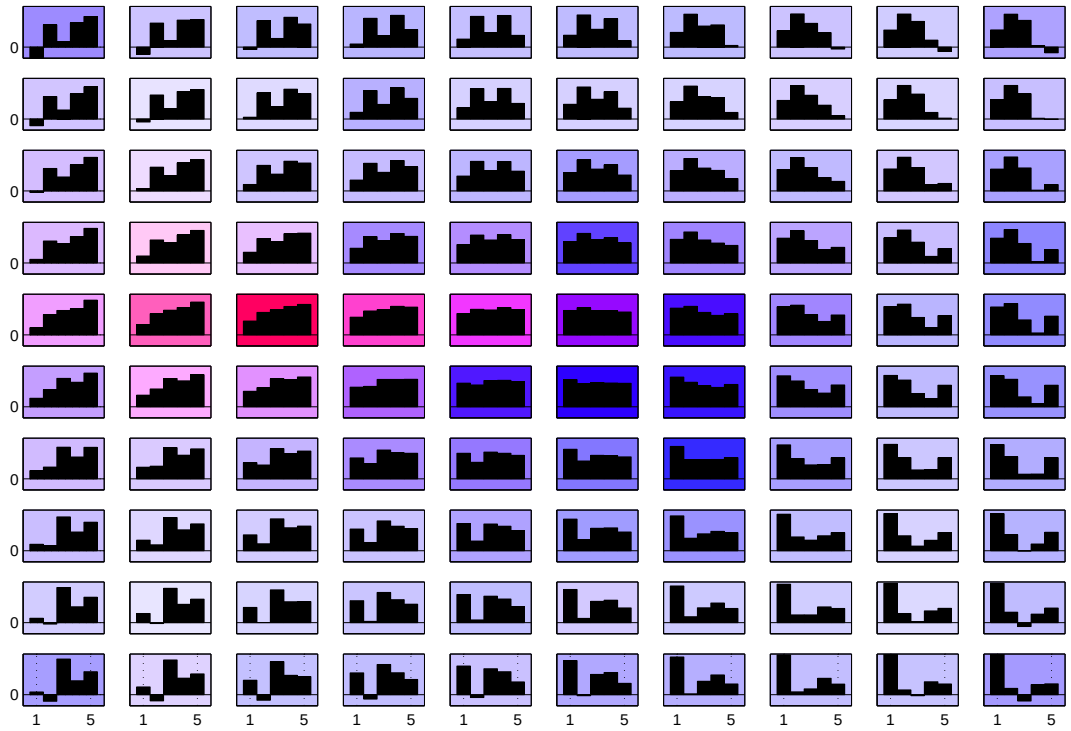

Figure 6.8.: Result of SOM training based on the new feature vectors computed from the *wavelet coefficients*. The colour code indicates the energy measure at each node. Red symbolises tumour enhancement, blue indicates enhancement inside the chest.

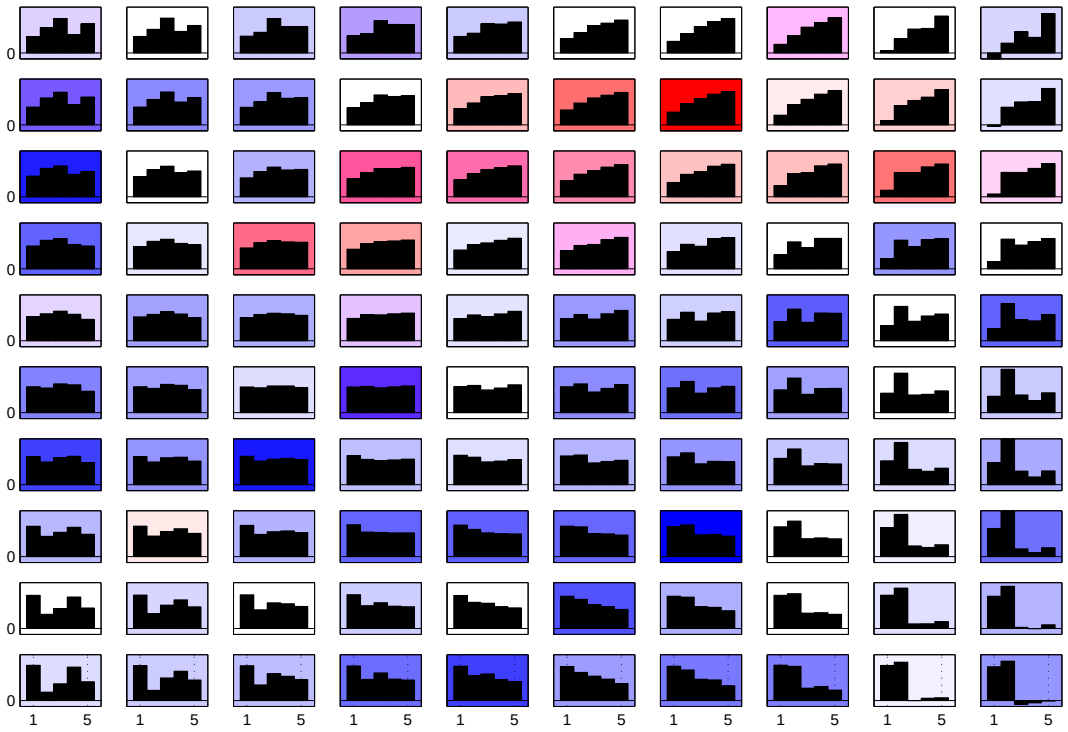

Figure 6.9.: Result of SOM training based on the new feature vectors computed from the *scaling function coefficients*. The colour code indicates the energy measure at each node. Red symbolises tumour enhancement, blue indicates enhancement inside the chest.

Tumour enhancement provides a very steadily monotonic increase of feature vector components whereas the dynamical behaviour of enhancement in the chest is either quite irregular or shows a clear decrease at the final time points.
From these results it is possible to derive simpler meta features allowing a more detailed analysis of the several scales. Up to now, the coefficients and feature vectors of all scales have been analysed together. By deriving two meta features from the presented results it becomes much easier to analyse the obtained characteristics at the different scales separately.

The first meta feature f_1 describes the difference of $x_i(6)$ and $x_i(1)$. The second meta feature f_2 is supposed to describe the observation of irregular behaviour. In case of a continuous signal higher order derivations could be used to describe strong changes of a function. In our case the following values are computed to identify strong variations in time.

$$\begin{aligned} DQ1_i(t) &= x_i(t+1) - x_i(t) && (6.9)\\ DQ2_i(t) &= DQ1_i(t+1) - DQ1_i(t) \\ &= x_i(t+2) - 2x_i(t+1) + x_i(t) && (6.10)\\ DQ3_i(t) &= DQ2_i(t+1) - DQ2_i(t) \\ &= x_i(t+3) - 3x_i(t+2) + 3x_i(t+1) - x_i(t) && (6.11) \end{aligned}$$

These values characterise the dynamical behaviour of $d_i(t)$. For $t = 1..5$ two values of $DQ3_i$ can be computed. The sum of their absolute values should be high in case of the irregular enhancement observed above. Hence, the two meta features are computed according to

$$\begin{aligned} f_{1i} &= (x_i(5) - x_i(1)) \cdot \frac{\text{sign}}{norm_{2i}} && (6.12)\\ f_{2i} &= \frac{(|DQ3_i(2)| + |DQ3_i(1)|)}{norm_{2i}}. && (6.13) \end{aligned}$$

In the next Figures these meta features are visualised by plotting f_2 in dependence on f_1 for the entire dataset and for the different scales separately. The derived plots show the meta feature of tumour enhancement in red and yellow at right hand and those for enhancement in the chest in blue and green at left hand respectively. Each circle represents one feature vector and the size of the circle indicates the energy measure related to the feature vector. Here, the relation between energy measure and size of the circle is logarithmic. To allow a discrimination of the different circles the border of each one is displayed in a different colour.

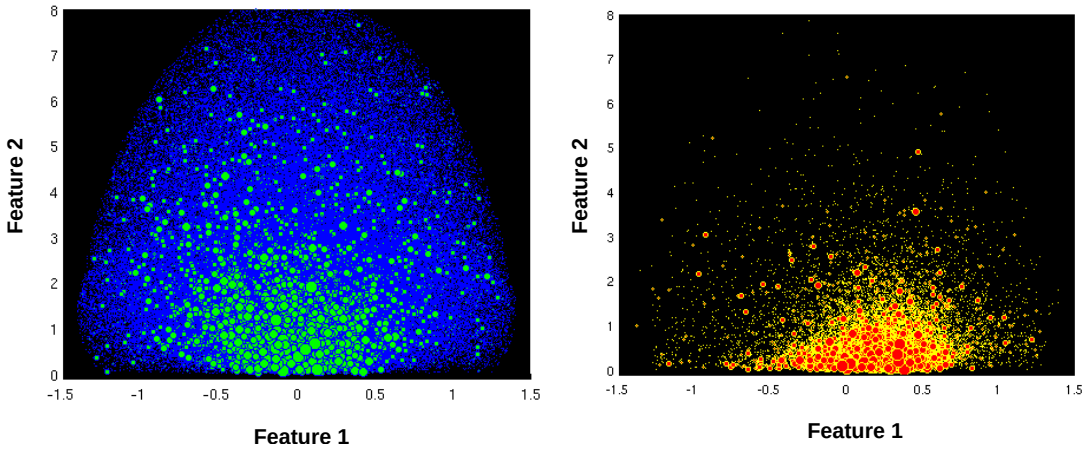

Figure 6.10.: Meta features of enhancement in the tumour (right) and enhancement in the chest (left). Wavelet coefficients of all scales are included.

Figure 6.10 shows the feature vectors of all scales. It reveals the fact, that the enhancement inside the chest results in all possible types of enhancement whereas the dynamics of tumour tissue is much more specific. The majority of feature vectors shows a regular dynamics and an increase from the first to the last component. In Figure 6.11 the meta features of the scaling function coefficients are presented. This plot is much sparser due to the low amount of coefficients. However, the observations described above can be verified in this plot nonetheless.

In Figures 6.12, 6.13, 6.14 and 6.15 the meta features are shown for each scale separately. They all share the major feature that enhancement in the tumour is much more specific and therefore restricted to a particular region in the 2D plane. The most important difference of the scales is, that both features in average show a decrease over scales for both tumour enhancement and enhancement inside the chest. However, there is always a clear difference observable with respect to contrast agent uptake in the chest and in the tumour tissue.

6.2.5. Application of Results - Segmentation

General Approach

The exploration results described above can be utilised for the development of a tumour segmentation method. The fundamental idea here is to classify

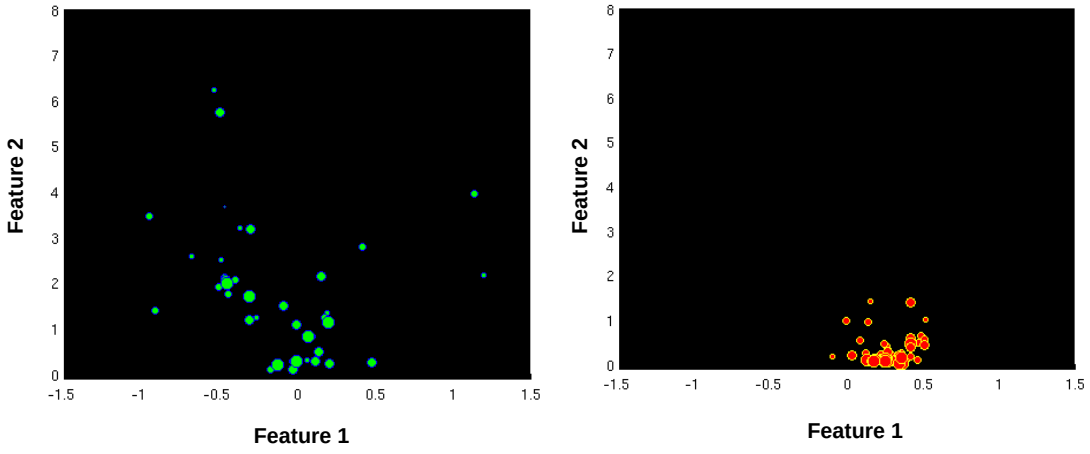

Figure 6.11.: Meta features of enhancement in the tumour (right) and enhancement in the chest (left). Only the scaling function coefficients are included.

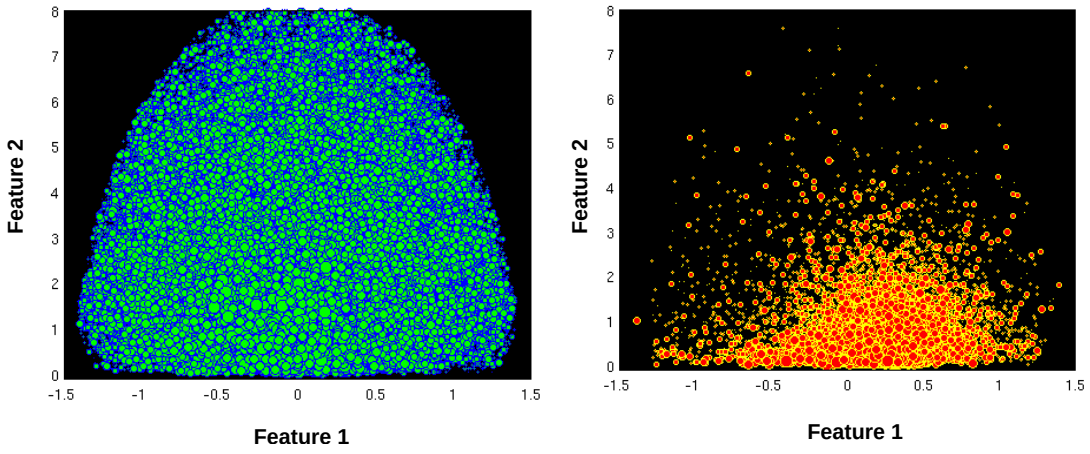

Figure 6.12.: Meta features of enhancement in the tumour (right) and enhancement in the chest (left). Wavelet coefficients of the second scale are included.

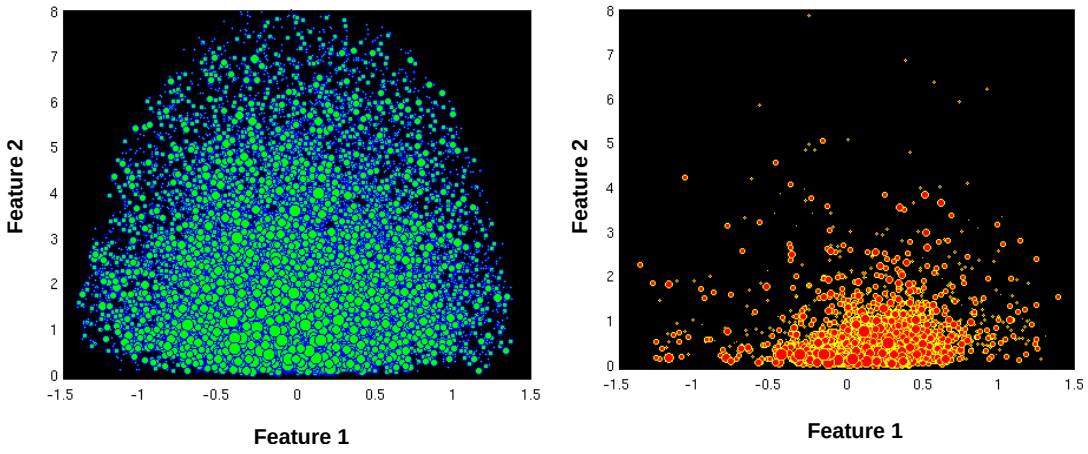

Figure 6.13.: Meta features of enhancement in the tumour (right) and enhancement in the chest (left). Wavelet coefficients of the third scale are included.

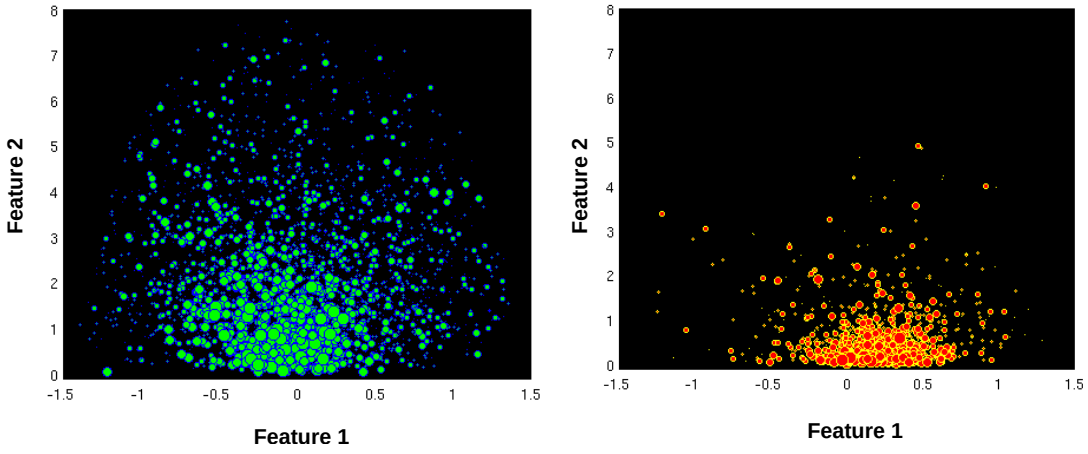

Figure 6.14.: Meta features of enhancement in the tumour (right) and enhancement in the chest (left). Wavelet coefficients of the fourth scale are included.

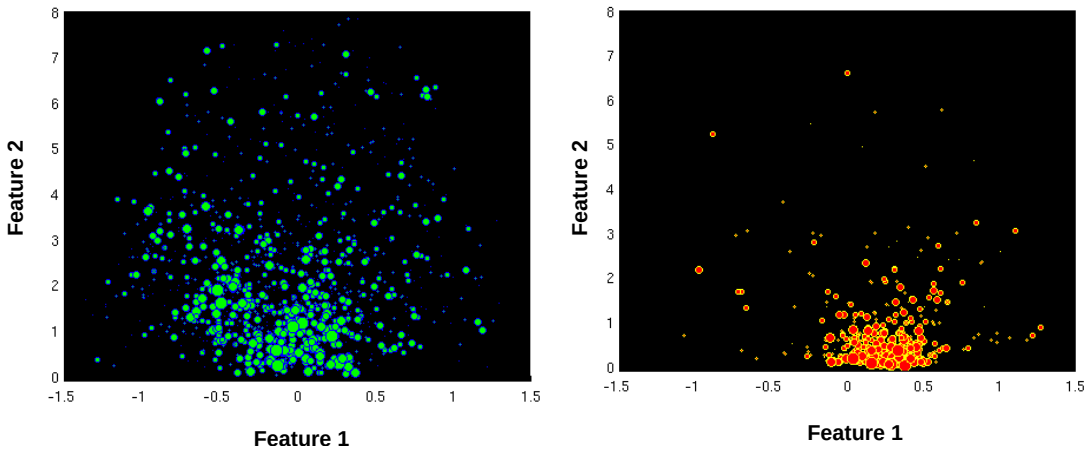

Figure 6.15.: Meta features of enhancement in the tumour (right) and enhancement in the chest (left). Wavelet coefficients of the fifth scale are included.

wavelet coefficients into tumour related and non tumour related. Due to their locality it is possible to perform a filtering in the wavelet domain. The coefficients are modified depending on their characterisation into relevant or irrelevant for tumour enhancement. From the modified wavelet coefficients images are reconstructed. In clinical practice usually subtraction images are examined, i.e. the subtraction of a pre-contrast image from a post-contrast image, chiefly to suppress the signal of fat. To evaluate the filtering result, intensity based segmentation is applied to the subtraction images. Since the aim here is to conserve all signal intensity in the tumour region and to delete all non-significant signal intensity inside the chest, the filtered images are compared to the expert labels. In this way the true and false positive as well as the true and false negative segmented voxels can be computed, depending on the chosen threshold. This procedure is termed ROC Analysis and is described in more detail in the next paragraph.

Receiver Operator Characteristic Analysis

Receiver Operator Characteristic (ROC) analysis is a useful technique to visualise and measure the performance of classifiers. In our approach the performance of the filtering procedure is measured by classifying the voxels of the images into tumour and non tumour voxels. Since our filtering approach was designed to delete the enhancement not related to tumour tissue, the intensity

of voxels in the filtered subtraction images should indicate the type of tissue. Therefore the voxels of the subtraction images are classified into tumour and non-tumour voxels depending on their intensity which is equivalent to an intensity based segmentation. All voxels above a specific threshold are classified positively (i.e. as a tumour voxel) and all others negatively. By comparing the segmentation result with the expert label - a binary mask marking the tumour region - it is possible to calculate the correctly classified voxels (true negative (tn) and true positive (tp)) and the incorrectly classified voxels, i.e. the false negative (fn) and false positive (fp) voxels. The intensity threshold for classification into tumour and non-tumour voxels is varied in this process.

Two parameters can be defined from the computed rates, the *sensitivity* and the *specificity*. The sensitivity is also termed *tp rate* and is defined as

$$\text{sensitivity} = \text{tp rate} = \frac{tp}{tp + fn}. \tag{6.14}$$

The sensitivity measures the ratio of voxels classified correctly positive and all positive voxels, i.e. in this case the sensitivity measures the amount of tumour voxels, which are correctly classified as tumour voxels. The sensitivity is 1 if all voxels of the tumour are classified positively.

The specificity is defined according to

$$\text{specificity} = \frac{tn}{fp + tn} \tag{6.15}$$

and measures the fraction of correctly classified non-tumour voxels in all non-tumour voxels. The specificity is high, if the amount of voxels falsely classified as tumour-related is low compared to the correctly classified non-tumour voxels. If no voxel is falsely classified a tumour-related ($fp = 0$), the specificity is 1.

There is always a trade-off between sensitivity and specificity, i.e. by increasing the threshold for classification the amount of fp voxels decreases leading to an increase in specificity. However, the amount of tp voxels usually decreases in the same way, leading to a decrease of sensitivity. Therefore both values are computed with a varying threshold and plotted in a so called Receiver Operator Characteristic (ROC) Graph. In this ROC graph the sensitivity is plotted against $1 - \text{specificity}$ [117]. The value the $1 - \text{specificity} = fp/(fp + tn)$ is termed $fprate$ and measures the amount of voxels falsely classified as tumour-related in all non-tumour voxels.

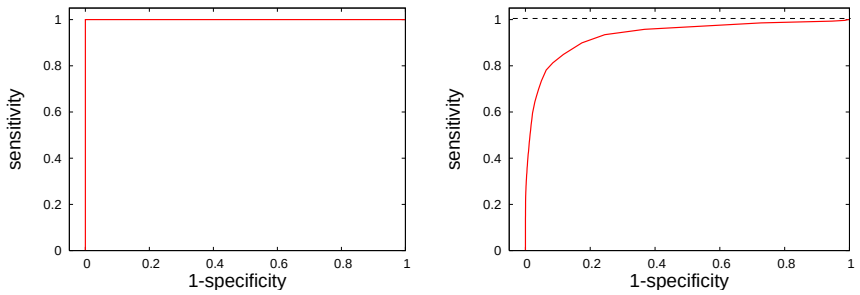

Figure 6.16.: Left hand: A perfect ROC Curve. Right hand: The ROC Curve of the first subtraction image of dataset 5.

An ideal ROC curve is shown in Figure 6.16 at right hand. There, the sensitivity is always 1 independent of the specificity. An example ROC curve for one of the subtraction images analysed is shown at left hand. To measure the quality of an ROC Curve the area under the curve (AUC) is computed. The AUC value is a number between 0 and 1, with 1 as the result for an ideal curve. Since regions of high specificity are especially interesting, the AUC value for specificity > 0.95 is computed separately. This value has been normalised to the total area 0.05, therefore these AUC also take values between 1 and 0.

SOM-Based Segmentation

Principle The first step here is the training of a SOM grid and the characterisation of the SOM nodes. As described above each of the reference vectors related to the SOM nodes can be marked as a prototype for tumour enhancement or for enhancement in the chest. This is done by computing the energy measures according to equation (6.5). From the two energy measures $E^{(\mathrm{tu})}$ and $E^{(\mathrm{ch})}$ related to each node $\mathbf{u}_j$ a value p_{tu} is computed according to

$$p_{tu}(\mathbf{u}_j) = \frac{E^{(\mathrm{tu})}(\mathbf{u}_j)}{E^{(\mathrm{tu})}(\mathbf{u}_j) + E^{(\mathrm{ch})}(\mathbf{u}_j)} \tag{6.16}$$

describing the fraction of "tumour energy" related to each node. The measure p_{tu} takes values between 1 and 0, with 1 indicating the fact that only tumour coefficients are mapped to this node.
The principle of the filtering procedure is to first compute all feature vectors of the dataset to be filtered. In a second step each feature vector $\mathbf{x}_i$ is mapped onto the SOM Grid, i.e. the nearest reference vector is determined. The measure

p_{tu} of this specific node is then multiplied with the wavelet coefficients $d_i(t)$ related to the feature vector. In this way coefficients classified as non tumour coefficients are decreased or deleted whereas coefficients mapped to tumour nodes are retained.

The computations are conducted using the leave-one-out approach, i.e. the image to be filtered is not included in the training procedure. Thus for each image a new training result is obtained using the feature vectors computed from the remaining images in the database.

Two modifications of this approach can be distinguished. First, the coefficients and feature vectors of all scales are trained together, utilising a 10×10 SOM grid. Second, for each scale one SOM is trained, i.e. the coefficients and feature vectors of the different scales are handled separately. In both cases the scaling function coefficients are processed separately utilising a 5×5 SOM grid.

As in [118] the results of the ROC analysis before and after filtering are compared in order to evaluate whether the filtering leads to a significantly increased segmentation result.

Segmentation Results Figure 6.17 shows one example of a SOM grid. The circles indicate the nodes in the SOM. The intensity of the circle's colour is the amount of wavelet-based energy related to this node. The colour code indicates the type of signal enhancement. Blue colour depicts signal enhancement inside the chest, red indicates enhancement due to contrast agent uptake in tumour tissue. A separated region representing the uptake behaviour of tumour tissue is clearly observable. The nodes of this region are the most important ones for detecting tumour enhancement. The result of this filtering procedure is additionally visualised using the subtraction image of patient 4 as an example. The green colour presents the information of the pre-contrast image. The red colour stands for the subtraction image of the first post-contrast and the first pre-contrast image, i.e. the red colour shows enhancing tissue. Due to the filtering (first method $\mathrm{SOM}_{combined}$) the enhancement in the region of the chest is nearly completely removed, whereas the image information of the tumour tissue is preserved. Intensity-based segmentation applied to the filtered images hence produces considerably improved results. This is demonstrated by ROC-analysis, the results are presented in Figure 6.18. The subtraction images of the first pre-contrast and three post-contrast images are computed. Then the AUC values for specificity > 0.95 (low amount of false positive segmented voxels) are computed. The AUC values of the original subtraction image and

the filtered subtraction images are shown. As one can observe, the AUC values of all datasets are significantly increased due to the filtering procedure. The dataset of the fifth patient provides a result overall remarkably inferior to the other cases examined, since this dataset includes a very weakly enhancing benign lesion, hardly showing any uptake at all.

An example database is presented in Figure 6.19. Different slices of the eigth dataset are shown either containing tumour enhancement of significant contrast agent uptake inside the chest. After the filtering procedure the enhancement in the heart is nearly deleted. The tumour information however, is retained. At the bottom of this Figure the corresponding ROC plots are presented. After the filtering, the ROC curve is quite near to an ideal ROC curve.

The approach presented has been published in [119]. There the size of the SOM grid differed from the one described here. A 20×20 SOM was utilised for the filtering procedure. However, since the results of both approaches are quite satisfying, the exact number of nodes does not seem to be a crucial parameter in the procedure.

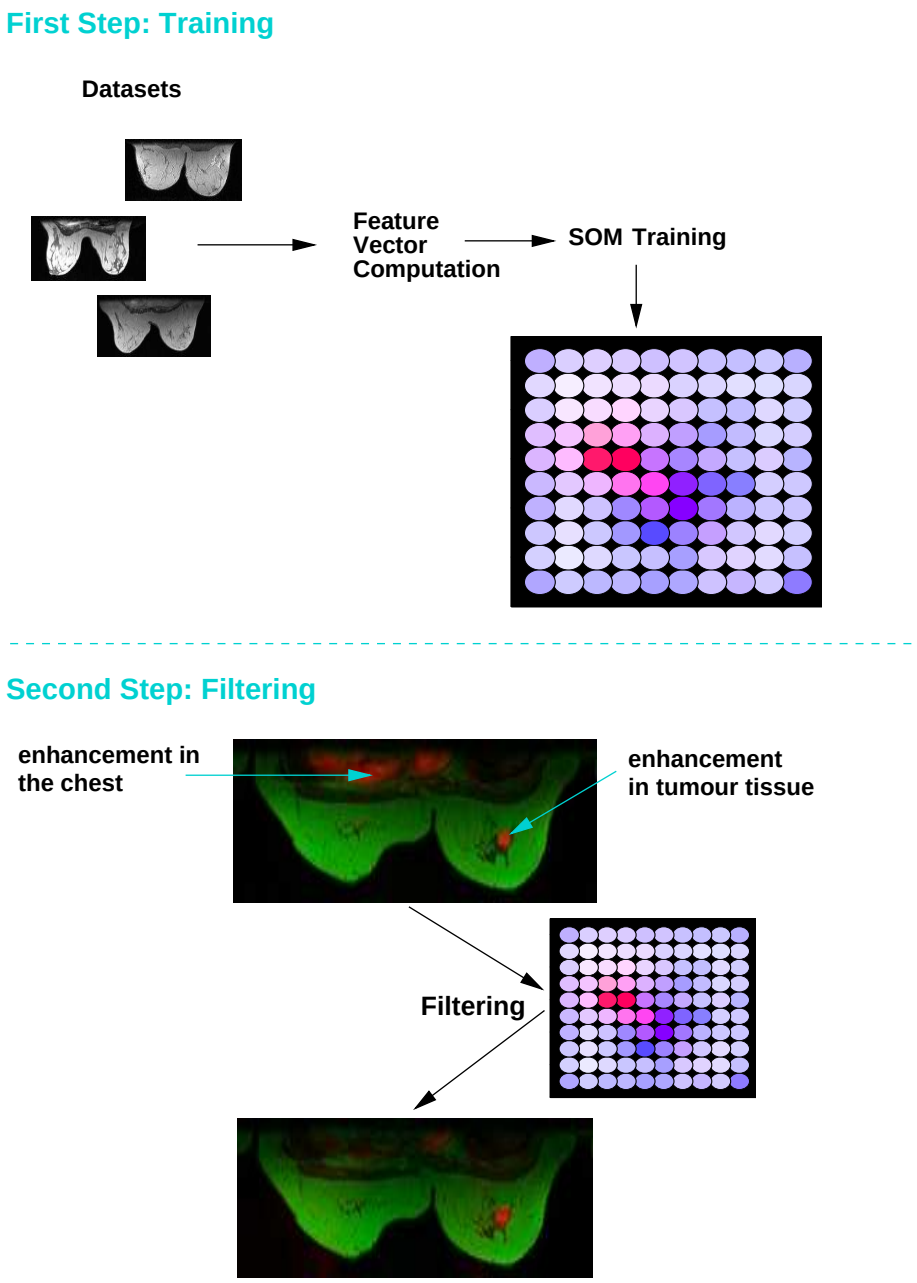

Figure 6.17.: Principle of the proposed approach. Top: SOM grid after training, the circles indicate the nodes in the SOM, representing mainly enhancement in the chest (blue) or in tumour tissue (red). Bottom: Filtering example. One slice of the dataset 4 is shown before and after filtering. The pre-contrast image is displayed in green, the enhancing tissue in red. The irrelevant enhancement in the chest is nearly completely deleted after filtering.

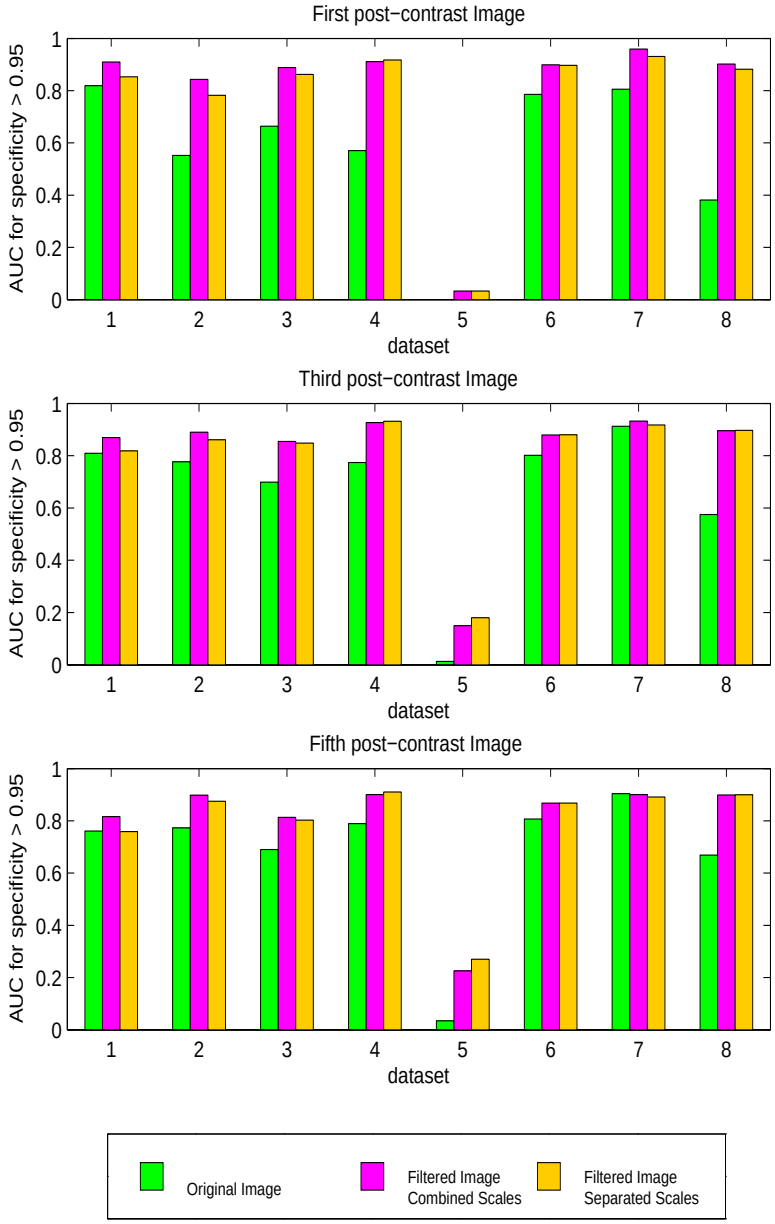

Figure 6.18.: AUC values for specificity > 0.95 for all datasets before and after SOM-filtering. Three different post-contrast images are examined. Green: AUC values for the original subtraction images. Magenta: AUC values for the filtered images. All scales have been filtered using one single SOM. Orange: AUC values for the filtered images. For the filtering of each scale a SOM has been trained separately.

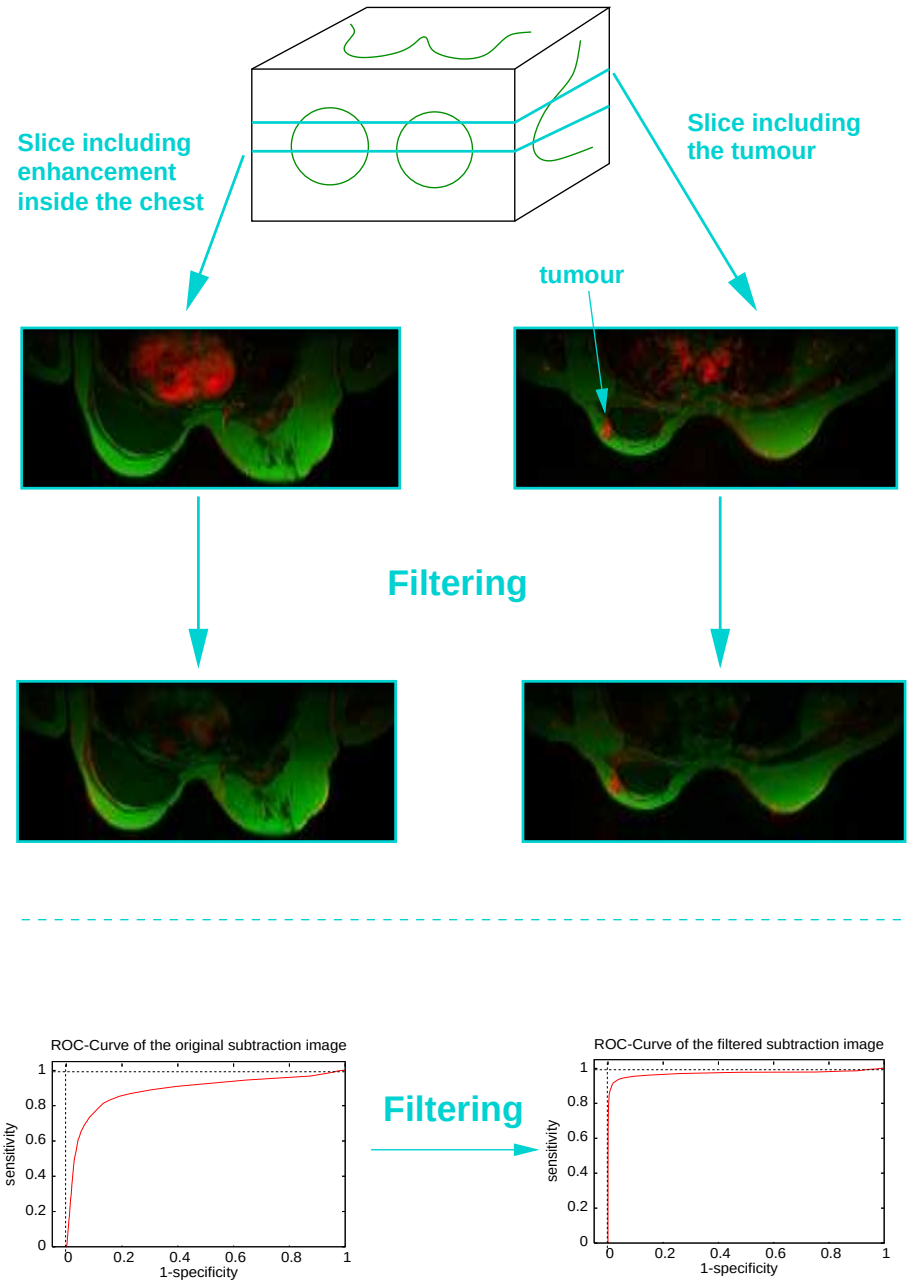

Figure 6.19.: Example filtering results. Dataset eight - providing the highest improvement of AUC values - is shown. Top: One slice mainly includes enhancement inside the chest, the other slice contains the tumour. While the contrast agent uptake inside the chest is nearly completely deleted, the tumour information is still preserved. Bottom: The ROC-Curves related to both datasets.

Segmentation Using Meta Features

Principle Now the meta features are used to perform a similar kind of filtering procedure. To use a continuous two-dimensional plot (Feature 1 vs. Feature 2) for characterising different types of coefficients, this 2D plane is discretised resulting in a number of boxes in the 2D plane. Each box is now filled with the coefficients located at the particular area of the 2D plane (Figure 6.20). As in the previous approach not the number of coefficients is determined but the total energy of coefficients in each box. After normalisation a two-dimensional histogram for both types of enhancement is available. From these two histograms multiplication factors for the filtering procedure can be computed for each box. Let $h_{k,l}^{tu}$ denote the height of the box with indices k and l in the tumour histogram. With $h_{k,l}^{ch}$ the equivalent box in the histogram describing contrast agent uptake in the chest is denoted. The multiplication coefficient $p_{tu}(k,l)$ for each box is derived by

$$p_{tu}(k,l) = \frac{h_{k,l}^{tu}}{h_{k,l}^{tu} + h_{k,l}^{ch}}. \tag{6.17}$$

It can be regarded as a kind of probability for each box describing a feature combination typical for tumour enhancement.
During the filtering procedure each time series of wavelet coefficients $d_i(t)$ is analysed by computing the two meta features f_{1i} and f_{2i}, determining the indices k and l in the discretised 2D plane and thus the value $p_{tu}(k,l)$. The coefficients are then multiplied with $p_{tu}(k,l)$ in order to retain tumour coefficients and to diminish the others. Again, the leave-one-out approach is utilised. The filtering is performed one time combining the wavelet coefficients of all scales in one histogram, the next time with separated histograms, one for each scale.

Segmentation Results The results of this segmentation procedure are shown in Figure 6.21. As in the previous section the AUC value for specificity > 0.95 is presented. The AUC is increased in all cases due to the deletion of enhancement inside the chest.

The advantage of this approach is the low number of parameters to be set prior to the filtering. Only the number of bins for the two meta features has to be chosen. By contrast, the SOM-based approach requires much more parameters to be set appropriately.

Furthermore the results of the histogram-based segmentation do not depend on any random input. In contrast to this, the training results of the SOM and

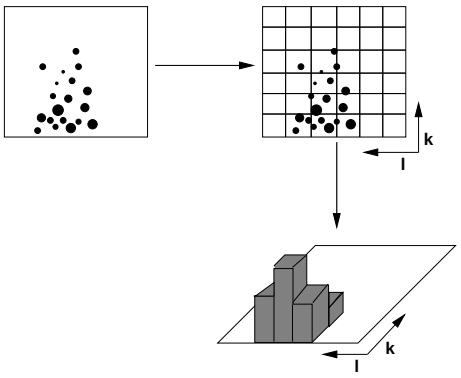

Figure 6.20.: Generation of histograms. The indices k and l describe the coordinates of the boxes in the 2D plane.

thus the outcome of the segmentation may vary depending on the initialisation of the SOM grid and the order of feature vectors during training, which are both random processes.

Therefore, the histogram-based approach is considered to be more robust whereas the segmentation results of the SOM-based approach are slightly superior (e.g. dataset 3).

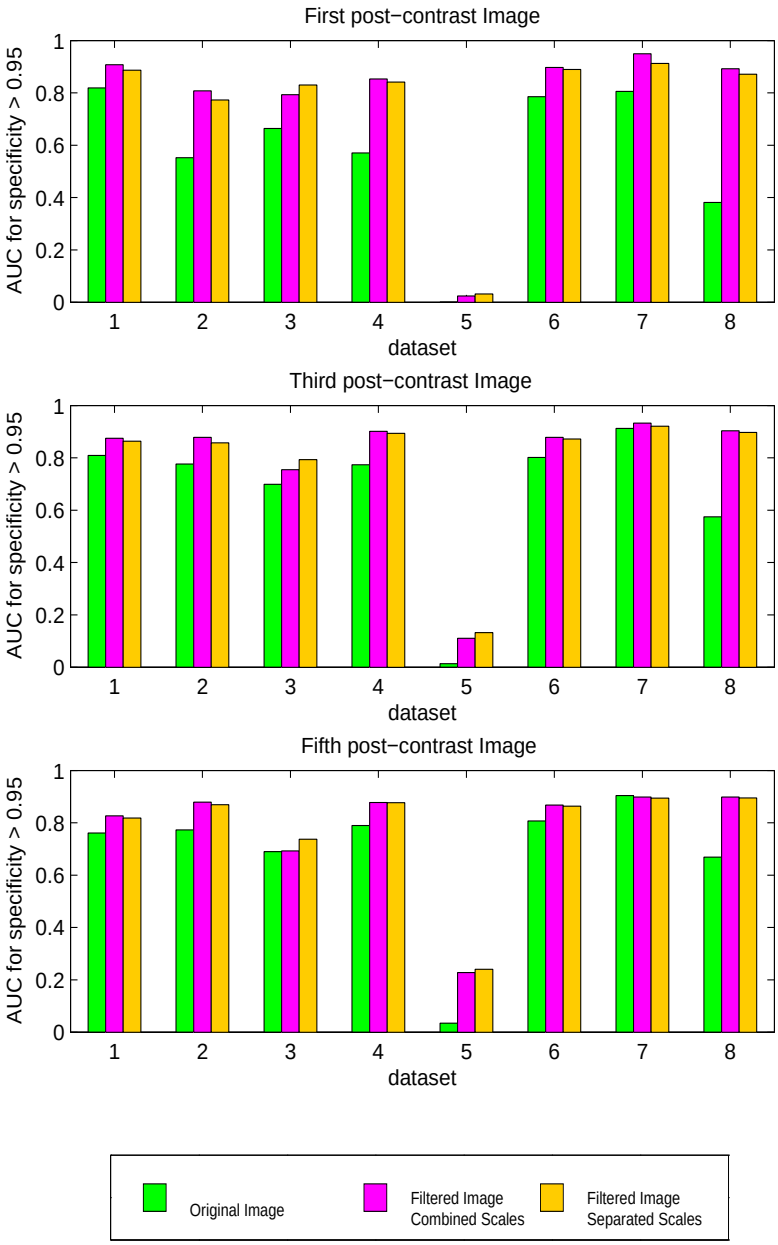

Figure 6.21.: AUC values for specificity > 0.95 for all datasets before and after filtering based on a meta feature histogram. Three different post-contrast images are examined. Green: AUC values for the original subtraction images. Magenta: AUC values for the filtered images. All scales have been filtered using one histogram. Orange: AUC values for the filtered images. For the filtering of each scale a histogram has been computed separately.

6.2.6. Choice of the Mother Wavelet

The remaining question is, whether the wavelet utilised - the biorthogonal $CDF_{5/3}(2,2)$-wavelet pair - is the most suitable one for this specific purpose. To answer this question the filtering procedure based on the meta features is repeated utilising the Haar-Wavelet, the Daubechies(2)-Wavelet and the biorthogonal $CDF_{9/7}(4,4)$ wavelet pair. The results are shown in Figure 6.22. The differences between the AUC values derived with the four mother wavelets are comparatively low. However, the $CDF_{5/3}(2,2)$ wavelet pair provides overall the best results.

6.2.7. Discussion and Conclusion

The exploration of wavelet-based feature vectors has revealed typical patterns for contrast agent uptake inside the tumour. It has been shown that this tumour-related type of enhancement offers very typical patterns in the wavelet domain in contrast to the enhancement in the region of the chest. The results of the exploration procedure lead to the definition of dynamical meta features in the wavelet domain for the detection of tumour enhancement.

In an application the discrimination potential of the derived features is proven. Two algorithms are implemented for the segmentation of tumour tissue by filtering in the wavelet domain. Both methods, one based on a trained SOM grid, the other based on the defined meta features, are clearly able to extract the relevant, i.e. tumour-related signal intensity from the image. In this way the diagnostically irrelevant enhancement inside the chest is suppressed. The tumour tissue is now detectable simply by its signal intensity. The filtering is performed without any prior knowledge such as lesion size or location. It is therefore considered to serve as a robust segmentation technique applicable in clinical practice since it requires no human interaction during the segmentation procedure.

Another possible application is the visualisation of the DCE-MR datasets by colouring the image information, i.e. the coefficients mapped to separated regions in the SOM, differently. It is also straightforward to use this method not only for the detection but also for a classification of lesions. In this case, the analysis would focus on the derivation of features able to distinguish benign from malignant tumour tissue. Due to the limited size of the database analysed this cannot be done at this point. However, it is a promising task for future research.

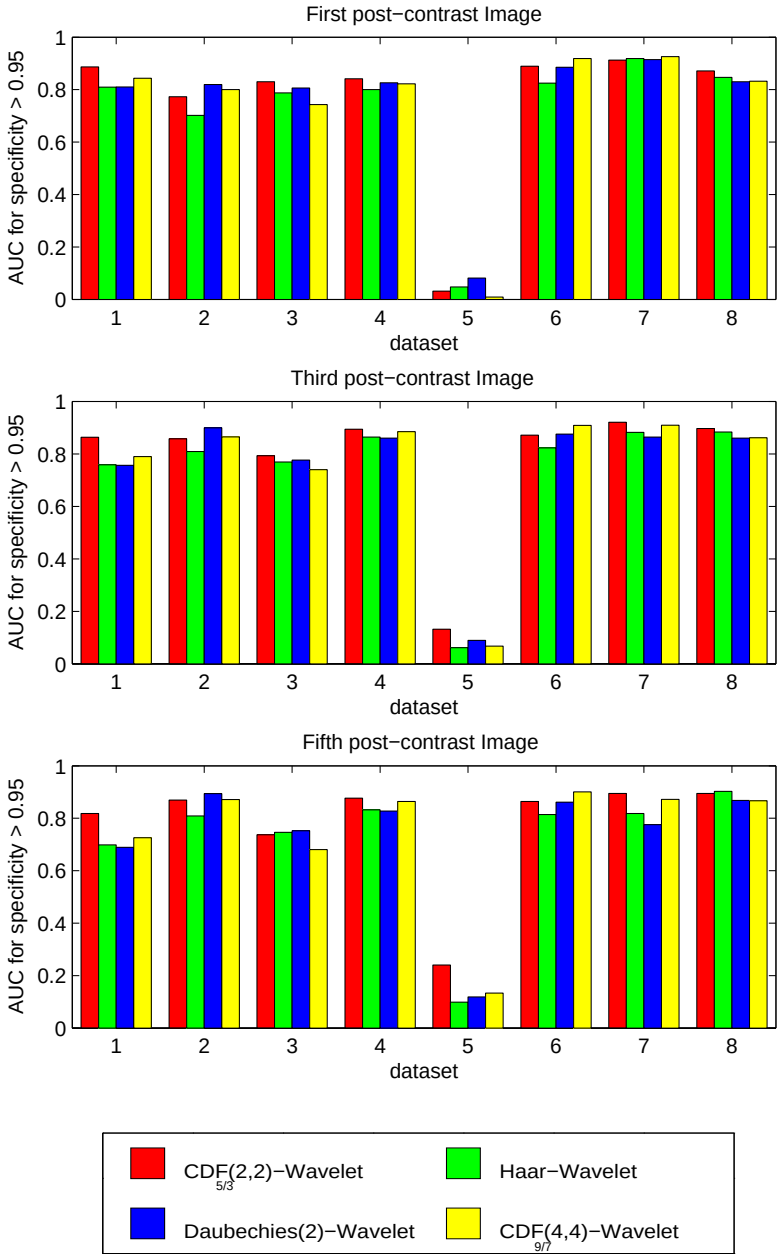

Figure 6.22.: AUC values for specificity > 0.95 after filtering with four different wavelets.

6.3. Analysis of Morphologic Characteristics

6.3.1. Motivation

As described above, morphological characteristics are essential in the diagnostic process of breast cancer detection. However, as mentioned the agreement of human experts in rating these features is only moderate and thus the definition of objective features highly desirable. Several approaches have been made to define features describing tumour morphology. However, most of these depend on an exact definition of tumour boundary. The voxels or pixels inside the boundary can then be used to compute texture information, the contour to compute shape descriptors. As mentioned in the introduction the tumour boundary is in most of the cases hand-drawn by a human expert, a very time-consuming task, which can introduce additional interobserver variability into the classification process. In some cases the boundary is defined by several pre-processing steps that strongly depend on further parameters such as segmentation thresholds and thus may introduce errors in the following process. In this work, I propose a method to obtain shape and texture descriptors, which do not rely on the prior determination of an exact boundary. An approximated region of interest with arbitrary shape is sufficient. The ROI can be derived by a human observer or by a detection process as described in the foregoing section. For this purpose the Discrete Wavelet Transform is applied using different types of mother wavelets to measure shape and texture of the tumours. The exploration of wavelet coefficients computed from different mother wavelets allows to define new features describing simultaneously the shape and the texture of a tumour. The approach is motivated using two-dimensional phantoms and then extended and specialised as an application on DCE-MR datasets.

6.3.2. Approaches for Shape and Texture Characterisation

Several descriptors for shape and texture characterisation exist. For an overview of texture and shape descriptors the reader may refer to [78, 120]. The most common ones are those used in the MPEG-7 standard [121].

In this standard three texture descriptors are defined, the homogeneous texture descriptor, the texture browsing descriptor and an edge histogram descriptor. The first one is based on a Gabor transform encoding scale and orientation dependent characteristics. The second one describes properties close to visual perception such as regularity, coarseness and dominant directions.

The last one provides a histogram of edges orientated in a specific manner. Especially in the analysis of medical images some other features are utilised. For instance in [105] texture features based on co-occurrence matrices are computed.

The shape descriptors in the MPEG-7 standard are either based on a region or a boundary. However, an exact determination of the particular object is always required.

In medical image analysis several descriptors are used, as already mentioned in the introduction. These ones as well require an exact boundary and can be characterised as geometric descriptors [103, 104], Fourier-based descriptors [104], moment-based descriptors [104] or wavelet-based descriptors [8]. These types of descriptors can be very detailed. However, in tumour diagnostic the classes of different shapes are quite limited. Thus a simpler descriptor should be appropriate for this purpose. Please note, that the focus is not on a classification into benign or malignant tumours regarding tumour morphology, since the size of the database is limited. This work addresses the question, how to derive shape and texture descriptors for tumour representation, which do not rely on an exact determination of the boundaries of the tumour. In the following at first the analysed image database is described. Then the methodology is explained utilising phantom images. Although the images considered are three-dimensional, the approach is initially explained using two-dimensional phantoms for reasons of comprehensibility. From the results of these studies morphology features for the 3D tumours can be derived and analysed in detail by utilising Self Organizing Maps.

6.3.3. Datasets

In this section a larger database is analysed. Referring to chapter 3 the two collections C_1 and C_2 are included. The total database analysed therefore overall comprises 18 datasets with a total number of 27 labelled lesions, 10 benign and 17 malignant. The lesions analysed are shortly summarised in Table 6.4. As described above the resolution of the images is given by $1.33\ mm \times 1.33\ mm \times 2.5\ mm$ for all datasets. However, the number of volumes, i.e. time points differs. The datasets 1 to 8 provide five post-contrast images, whereas the datasets 9 to 18 only contain a time series with four post-contrast volumes. For the analysis described in the following sections subtraction images are computed. The resulting time series of MR images can be regarded as a collection of voxel time series, with one time series associated to each voxel. By selecting

patient	diagnosis
1	multiple invasive carcinoma (ductal (NST) and lobular)
2	Sclerosing lymphocytic lobulitis
3	invasive tubular carcinoma
4	invasive carcinoma (ductal (NST)), two lesions
5	Fibroadenoma, Fibrocystic changes
6	Fibroadenoma
7	invasive ductal carcinoma (ductal (NST))
8	invasive carcinoma (not assessable)
9	benign - no additional information
10	invasive lobular carcinoma
11	invasive carcinoma (ductal NST), two lesions
12	Multiple papilloma, Fibroadenoma
13	invasive carcinoma (ductal NST), two lesions
14	benign - no additional information, two lesions
15	invasive carcinoma (ductal NST)
16	malignant - no additional information, three lesions
17	invasive carcinoma (ductal NST), two lesions
18	benign lesion - no additional information

Table 6.4.: Diagnostic outcome of the patients included in the analysis.

the maximum value of each voxel time series one single image is contructed. These maximum-value subtraction images are then utilised to compute the lesion descriptors.

6.3.4. Edge-Detection Using DWT

Edge-detection is a well-known problem in image-processing. Several Edge-detectors are known, either based on computing the first order derivative (e.g. Sobel, Canny, Roberts, Prewitt) or the second-order derivative (Marr-Hildreth). Using DWT one can perform a multiscale edge detection on images. In [53] it is described how to use the first and second derivatives of a gaussian function for edge-detection. In this work, the Haar-Wavelet Transform is used to compute edges of different scales and orientations. The Haar-Wavelet is an orthonormal wavelet with a shortest possible filter length of two. It has already been presented in chapter 4 and is again shown in Figure 6.23.

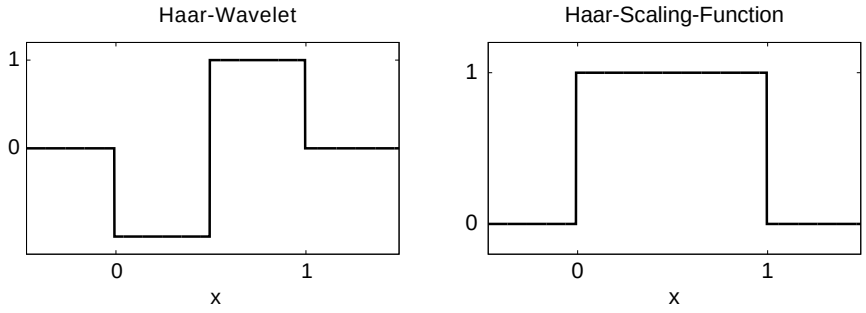

Figure 6.23.: The Haar-Wavelet and the corresponding scaling function.

Using the Haar-Wavelet the gradients of neighboured pixels - i.e. edges - at different scales are obtained. In Figure 6.24 the Discrete Haar Wavelet Transform of phantom images are shown.

In the following the diagonal details are neglected and only the vertical and the horizontal edges are further processed. Summing over positive and negative coefficients separately leads to a characteristic edge profile. In the case of vertical details (edges orientated in y-direction), all coefficients providing the same y-value and sign are summed.

$$edge_{j+}(x) \quad = \quad \sum_{k_y} d^{+}_{j,k_x,k_y}(vertical) \tag{6.18}$$

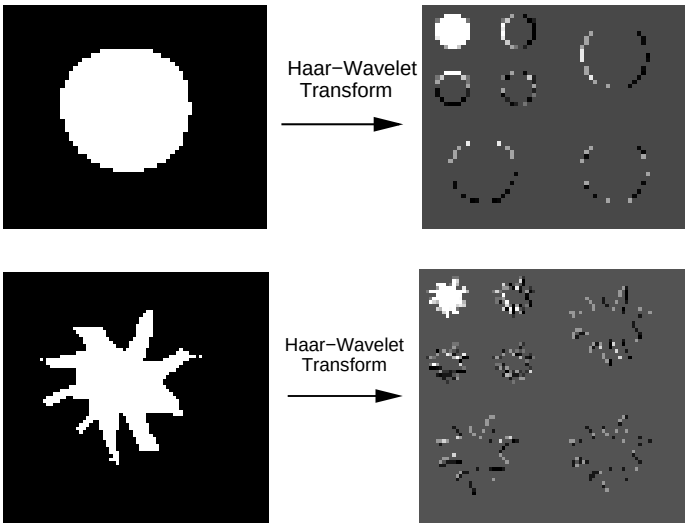

Figure 6.24.: Haar-Wavelet Transform of a circle-like and a spiculated phantom image.

$$edge_{j-}(x) = \sum_{k_y} d^{-}_{j,k_x,k_y}(vertical) \tag{6.19}$$

$$edge_{j+}(y) = \sum_{k_x} d^{+}_{j,k_x,k_y}(horizontal) \tag{6.20}$$

$$edge_{j-}(y) = \sum_{k_x} d^{-}_{j,k_x,k_y}(horizontal) \tag{6.21}$$

Here d^{+}_{j,k_x,k_y} denotes all positive coefficients and d^{-}_{j,k_x,k_y} the negative coefficients. Thus an edge-profile is derived in x- or y-direction clearly showing the ascending edges of the circle at left and the descending edges at right hand in case of the circle-like phantom. The edge-profile of the spiculated phantom varies strongly such that the ascending and descending edges are not spatially separated in the same way (Figure 6.25.

From these phantom studies it seems to be straightforward to compute a shape-descriptor describing round (symmetric and convex) and non-round (asymmetric and not convex) structures. A descriptor based on such an edge profile may not be able to distinguish between certain figures like circles or squares which are both symmetric and convex. But since the only symmetric figure occurring in tumour morphology is circle-like or ball-like this is not a problem for this specific purpose. Furthermore is is not necessary for a tumour descriptor to provide very detailed shape information. Human-defined shape or margin features in DCE-MRI are usually rated on a scale of four or five into

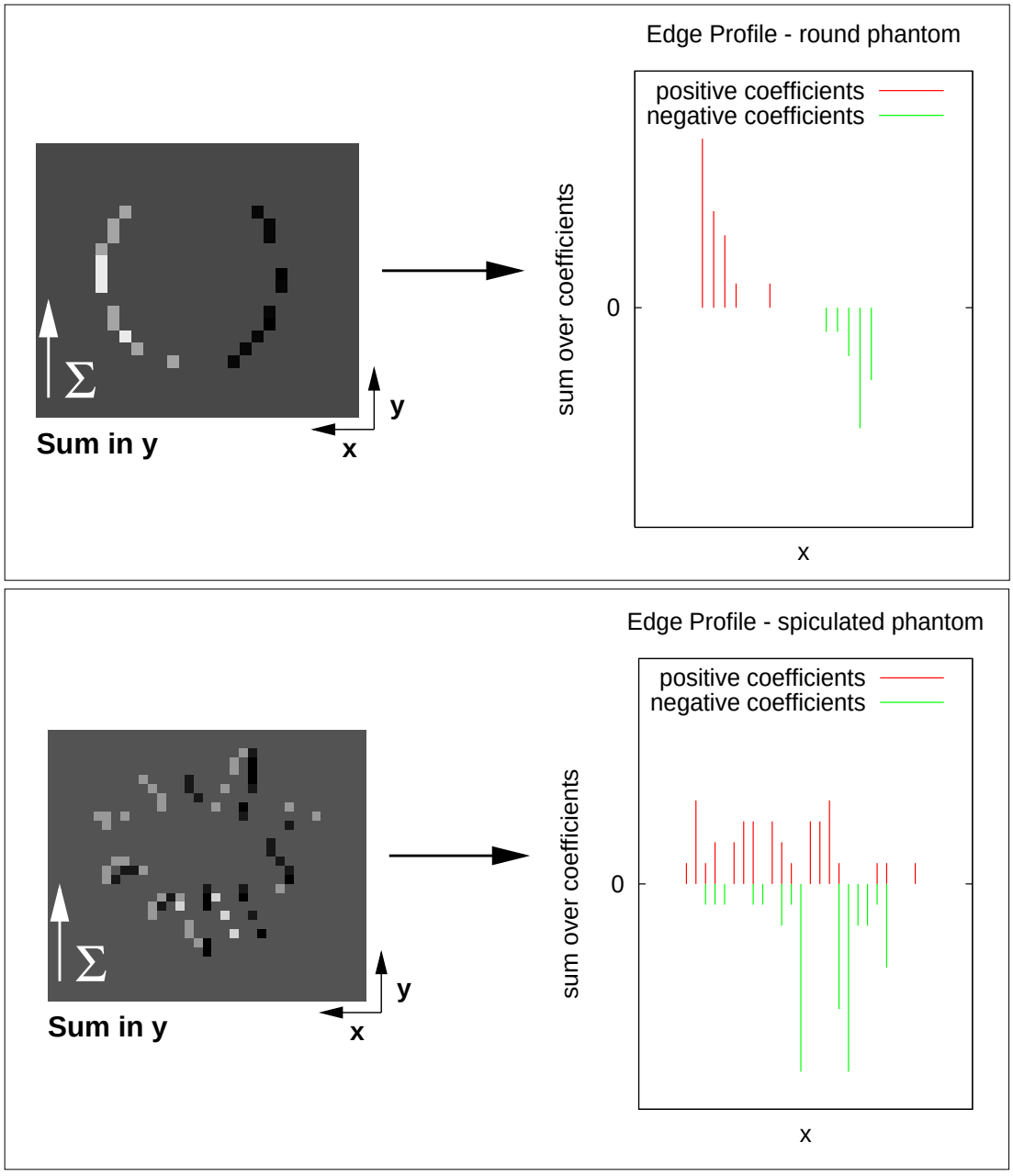

Figure 6.25.: Edge-Profiles for a round and a spiculated phantom derived from the Haar wavelet coefficients.

terms such as round or spiculated [87, 91] and consequently are also not very detailed.

One additional challenge arises at this point. In DCE-MR images the tumour may provide a significant amount of texture also producing edges in the Haar-Wavelet Transform. Thus one has to find a way to eliminate or at least reduce the texture while preserving the shape of the structure to perform the suggested analysis.

6.3.5. Texture-Filtering Using DWT

As stated above many texture features exist. However, for this specific purpose most of these features are too complicated. In DCE-MR datasets it is desirable to distinguish heterogeneous lesions from homogeneous lesions. The only interesting question here is, whether the tumour does provide a significant amount of texture or if it does not. Thus a much simpler approach can be used. In the analysed images texture is a fine scale phenomenon compared to shape. Therefore one possible approach would be to decompose the image into fine scale details, describing the texture and the remaining coarse scale image information, considered to describe the shape of the structure. However, the Haar Wavelet is not suitable for such a purpose. High-pass filtering does not preserve the shape information very well. Due to the non-continuous shape of the Haar-Wavelet a fine scale filtering creates strong block-like artefacts in the image. This is demonstrated in Figure 6.27. The Figure shows the spiculated phantom image with an artificial texture, derived by filling the area of the tumour phantom by randomly chosen grey values between 127 and 255. A DWT followed by the deletion of the wavelet coefficients of the two finest scales and image reconstruction leads to an image with a shape strongly distorted by artefacts. To preserve the shape while smoothing the texture a different wavelet has to be used. On the one hand it seems to be useful to apply a wavelet with more vanishing moments since such a wavelet is more appropriate to adapt to smooth funtions or image details. On the other hand it is desirable to use a symmetric wavelet because the encoding of the symmetry of a tumour is in the focus of research.

In image processing symmetric wavelets are quite common, since they lead in general to a decreased visible amount of artefacts. However, these symmetric wavelets of compact support cannot be orthogonal but only biorthogonal (chapter 4). In case of a biorthogonal DWT the transform and the inverse transform are performed using different types of wavelets. Biorthogonal wavelets

can be symmetric or antisymmetric. One of the biorthogonal wavelet pairs primarily used is the $CDF_{9/7}(4,4)$-wavelet already mentioned in chapter 4. It is used in the JPEG2000 algorithm for lossy compression [57] and is sometimes called 9/7-Filter. The wavelets for decomposition (analysing wavelet) and reconstruction (synthesising wavelet) of this pair are again shown in Figure 6.26 together with their corresponding scaling functions. These wavelets have four

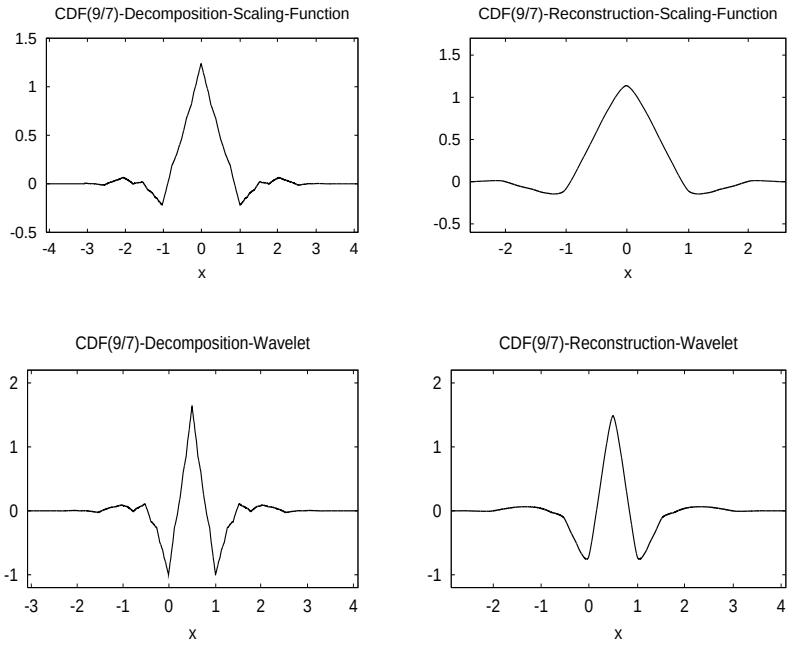

Figure 6.26.: The biorthogonal wavelet and scaling function of the $CDF_{9/7}(4,4)$-wavelet.

vanishing moments in contrast to the Haar-Wavelet providing only one. This larger number of vanishing moments is an important requirement to reconstruct smooth image structures. The filtering result of the spiculated phantom image using the $CDF_{9/7}(4,4)$-wavelet is shown in Figure 6.27. A more complicated way of separating edge from texture information is described in [122]. The approach described there is based on a detection of multiscale edges. However, the focus of the work done by Froment and Mallat was on compression. For the derivation of tumour descriptors as presented in this work a simpler texture filter is appropriate.

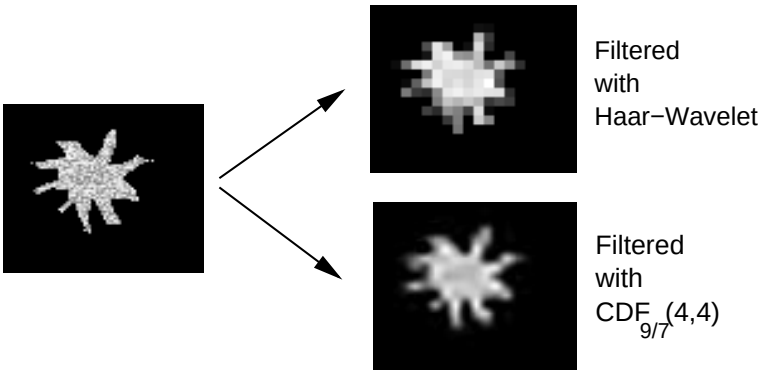

Figure 6.27.: Spiculated phantom image with texture before (left) and after (right) low-pass filtering using Haar-Wavelet and $CDF_{9/7}(4,4)$-wavelet.

6.3.6. Shape and Texture Descriptor

In the previous paragraph it was shown how to separate shape and texture in our images. The further analysed database contains three-dimensional images of the tumour. However, the approaches described in two dimensions can be easily extended to three dimensions. To derive the shape descriptor, at first the described texture filtering is applied using the $CDF_{9/7}(4,4)$-wavelet.

Since the resolution of our phantoms is comparable to the resolution of the MR images in the database, also the details of the finest two scales are considered for deletion. From the three-dimensional image an edge-profile for the different axes is computed using the Haar-Wavelet Transform, before and after texture filtering. In Figure 6.28 the edge profiles for the round phantom are shown. Please note, that not the exact label for computing the profiles is used but only a box-shaped region of interest (ROI) containing the tumour label. The filtering process in general leads to decreased edges due to the smoothing effect of the $CDF_{9/7}(4,4)$-wavelet. However, the filtered ideal phantom (top) still provides the characteristic spatially separation of ascending and descending edges, except very slight reconstruction artefacts. At the bottom the results for a phantom providing significant texture is shown. Before filtering, the edge-profile is strongly influenced by the texture and thus is quite different from the profile of the ideal phantom. After filtering, the texture is nearly deleted, leading to an edge-profile quite similar to the profile of the filtered ideal phantom.

Shape-Descriptor In the following the low-pass filtered images are used to obtain a numerical shape descriptor. The most important observation here is that round structures (in 2D) or ball-like structures (in 3D) provide a very characteristic edge-profile. Edge-profiles of irregular shaped structures do not match this characteristic pattern. It is therefore possible to define a descriptor measuring the variation from circle- or ball-like shape. One challenge here is, that the edge-profiles strongly differ in length since the tumours differ in size. Furthermore a dependence on the location of the tumour within the ROI should be avoided. Therefore the edge-profile cannot directly be used as shape descriptor. Thus a two-dimensional descriptor is computed as follows. At first the centre c of the edge-profile is determined. Since the descriptor should not depend on the length of the chosen ROI, we compute the centre of mass of the ascending and the descending edges respectively. The centre of the edge profile c is chosen as the middle between these two values. For each edge-profile the squared values of the ascending edges at left hand and the descending edges at right hand are summed ($descriptor_1$). The sum of the remaining edges is termed $descriptor_2$.

$$descriptor_1 = \sum_{x=0}^{c} edge_{j+}^2(x) + \sum_{x=c+1}^{x_{max}} edge_{j-}^2(x) \tag{6.22}$$

$$descriptor_2 = \sum_{x=c+1}^{x_{max}} edge_{j+}^2(x) + \sum_{x=0}^{c} edge_{j-}^2(x) \tag{6.23}$$

$$\tag{6.24}$$

After a normalisation with the total sum $descriptor_1 + descriptor_2$ these values can be compared for different shapes. In case of a circle or ball all ascending edges are at left hand and the descending edges at right hand. Therefore $descriptor_1$ provides the value 1 and $descriptor_2$ the value 0. An irregular shaped structure providing not spatially separated edges provides values differing from 1 and 0.

Texture-Descriptor The filtering procedure is applied to delete texture from the image. The difference between the edge-profiles before and after filtering should therefore be a measure for the amount of texture contained in the image. Thus we simply sum the absolute values of all Haar coefficients before and after filtering and compute the ration between both values. If the texture filtering has no effect the ratio is equal to 1, in case of a strong filtering effect the ratio is significantly decreased. Note here, that this value is also smaller than

1 in case of an ideal, not textured structure due to a smoothing effect working at the edges. However, in case of a strongly textured image, the distance between both profiles is significantly increased and thus the ratio is significantly smaller than 1. In order to distinguish textures at different scales, this value can be computed after deleting the first and second scale details, as described above, or after deleting only the first scale details. Both texture measures are included in the further analysis.

The features just described are derived from more or less heuristic considerations. Thus, they have to be evaluated regarding their suitability for the desired purpose. This evaluation is done in the following utilising Self Organizing Maps.

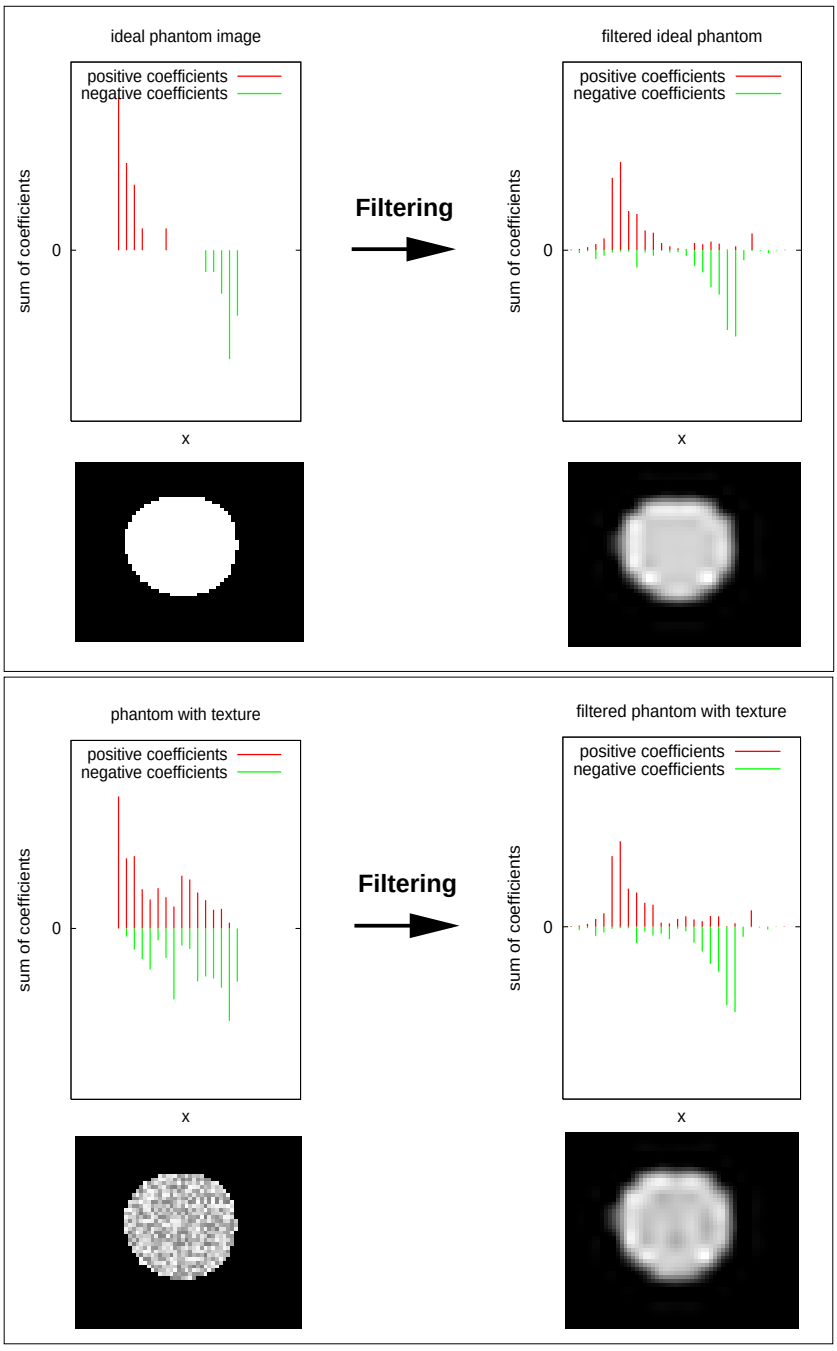

Figure 6.28.: Edge profile of the round phantom without texture (top) and with texture (bottom). In both cases the edge-profiles are shown before and after filtering

6.3.7. Exploration of the Descriptors

To evaluate the proposed features the database is visualised based on them. For this purpose a SOM is computed to establish a link between single lesions and the features describing tumour morphology. A 10×10 grid is trained, with a learning rate $\alpha(t)$ varying between $\alpha_{initial} = 0.9$ and $\alpha_{final} = 0.01$ and $5 \cdot 10^5$ training steps. The reference vectors are initialised by randomly chosen feature vectors from the input space. The parameter $\sigma_{initial}$ is set to $\sigma_{initial} = 10$. Again an appropriate value for σ_{final} has to be determined. The results for TP and AQE are computed for two values and compared:

σ_{final}	TP	AQE
1	0	0.037
3	0	0.114

As in the works before the AQE increases with increasing σ_{final}. However, the TP value is 0 in both cases, thus the parameter leading to the lower AQE is chosen.

The trained SOM grid resulting from these parameters is presented in Figure 6.29. The descriptor is computed for the finest three scales after deleting the first scale details and the first and second details utilising the 9/7-Filter. At the top of the figure the database is visualised based on the computed features. Each tumour is represented by an image of the particular lesion. At the bottom the Component Plane Maps of the reference vectors are presented. The round tumours providing regular shape are located in the lower right part of the SOM grid, whereas the irregular shaped tumours are located in the upper left part of the grid. By comparing this to the Component Plane Maps, it becomes evident, that the first scale descriptor after deleting the finest two scales corresponds best to the visual appearance of the tumours. In contrast to this the third scale shows characteristics which do not go with the visual tumour appearance. This may be due to the fact, that our resolution is very limited and thus the third scale edge-profile is not a reliable feature.

The texture descriptor is presented in Figure 6.30. Also here, the database is visualised based on a SOM training with the described feature vectors. The TP and AQE values for two different settings for σ_{final} are given below.

σ_{final}	TP	AQE
1	0	0.019
3	0	0.060

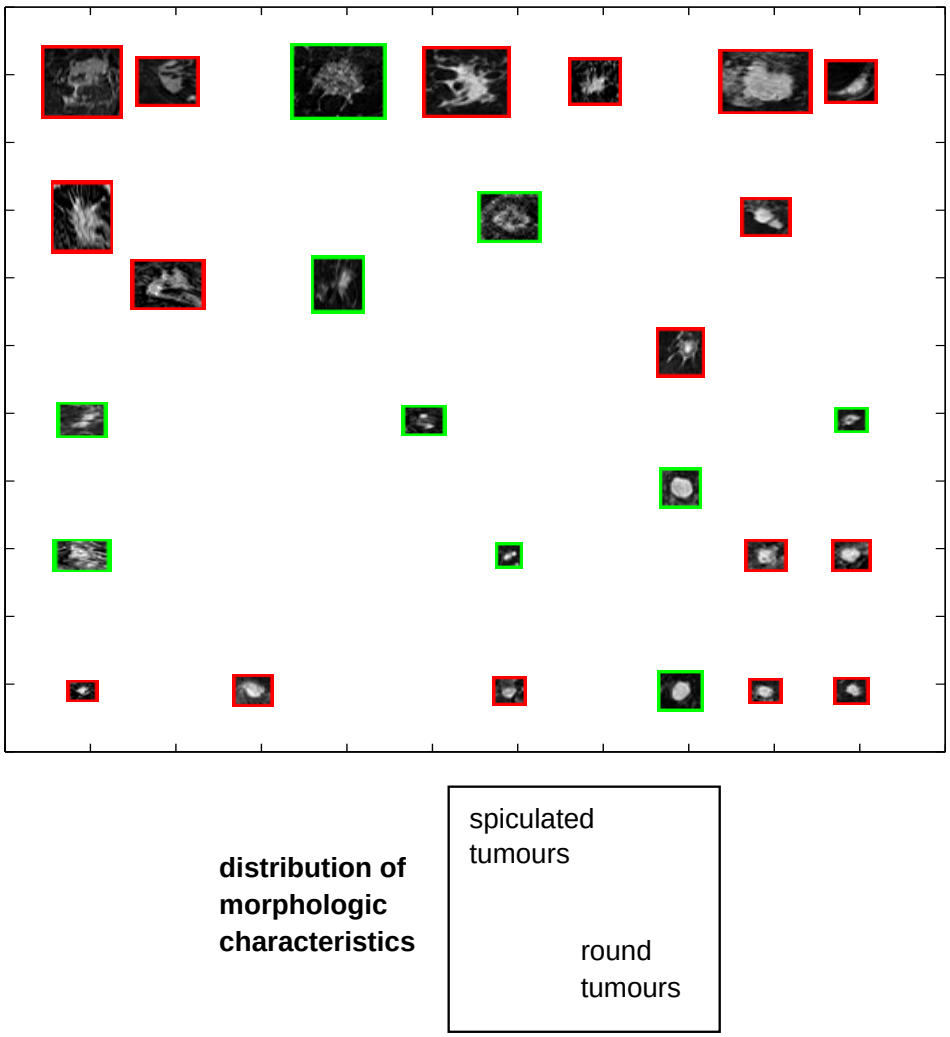

Figure 6.29.: SOM trainig results for the shape descriptor computed for three scales. Top: Visualisation of the image domain. Centre: The distribution of shape characteristics at the SOM grid. Bottom: The Component Plane Maps.

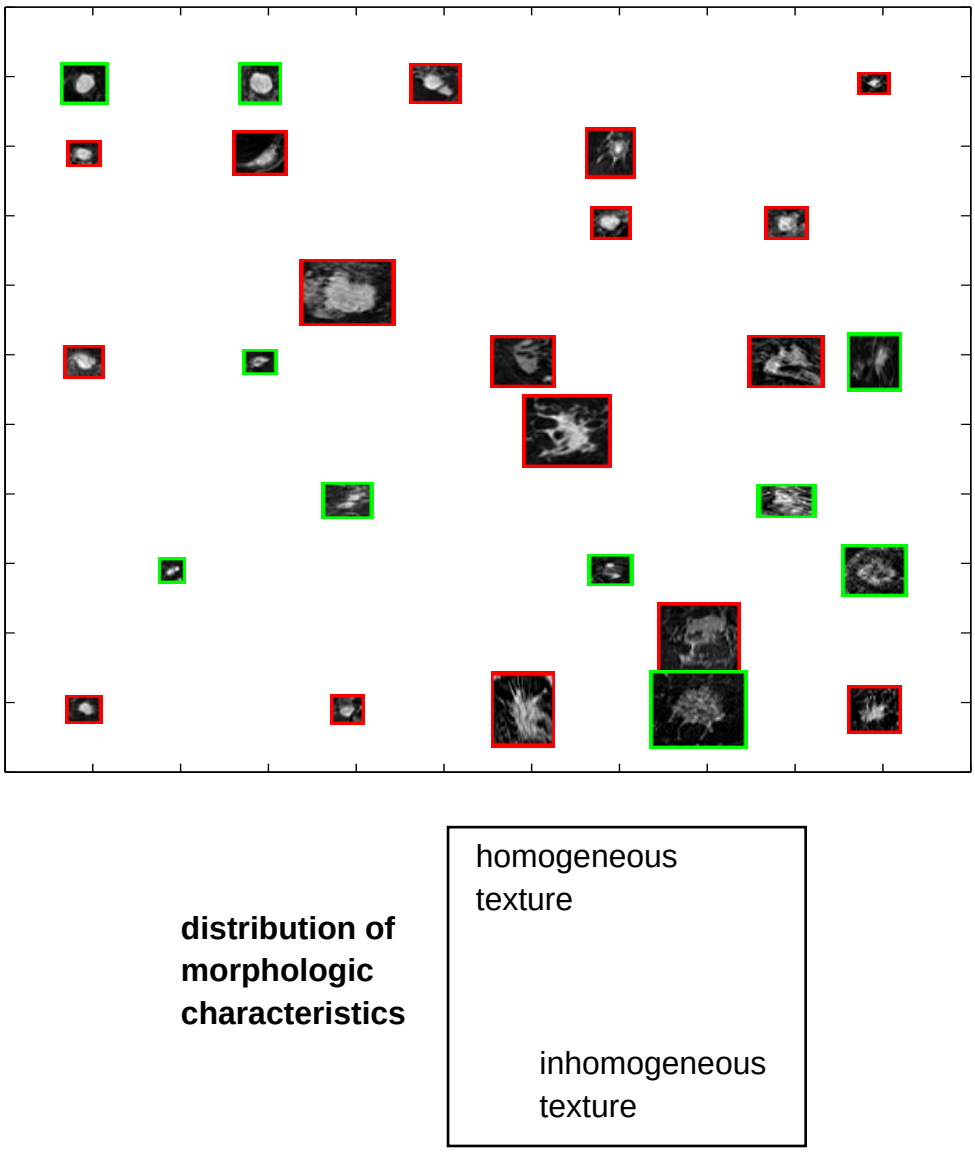

Figure 6.30.: SOM trainig results for the texture descriptor computed for three scales. Top: Visualisation of the image domain. Centre: The distribution of texture characteristics at the SOM grid. Bottom: The Component Plane Maps.

As before, $\sigma_{final} = 1$ us chosen. All other parameters of the training procedure are set as described in the previous paragraph.

The feature explored here is designed to measure the edge-profile before and after texture filtering. A homogeneous tumour should provide a very high value of the computed ratio (close to one) in contrast to strongly textured lesions. In Figure 6.30 it is visible that this expectation best holds for the descriptor computed for the first scale. Here, the homogeneous lesions at the left top of the SOM grid corresponds to high values of the related feature vector components. The other two scales do not seem to provide a reliable measure.

In the following only the descriptors computed for the first (finest) scale are utilised. The two-dimensional shape descriptor is computed after deleting the details of the finest two scales. The two-dimensional texture descriptor contains the ratios after deleting only the first scale and after deleting the finest two scales. Pleas note that the scales correspond to a particular resolution of the image. Since the length of voxels in z-direction is nearly two times the length in x- or y-direction, the first scale wavelet transform is only applied in the xy-plane. The two two-dimensional descriptors are utilised to train a one-dimensional SOM respectively for visualisation purposes. The parameter settings from above are utilised again for the 10×1 SOM. The results are shown in Figures 6.31 and 6.32.

To analyse whether the two features are independent of each other, a combined feature vector is constructed. A PCA is computed from the feature vectors of the entire database. The projections onto the two eigenvectors related to the largest eigenvalues is shown in Figure 6.33. As above each tumour is represented by a single slice image, which is displayed at the location of the corresponding feature vector in the projection plane. It is clearly visible that the features are suitable for distinguishing different morphological characteristics of tumours. At the right hand, round tumours with a homogeneous structure are located. From right to left the irregularity of tumour shape increases. The second dimension additionally leads to a vertical separation due to different texture properties. At the top left a group of tumours is located providing strongly inhomogeneous texture. At the same horizontal position at the bottom of the plane, the tumours provide a more homogeneous texture but a very irregular shape. However, the two features are not independent of each other in the analysed database. From right to left both irregularities in shape and texture increase.

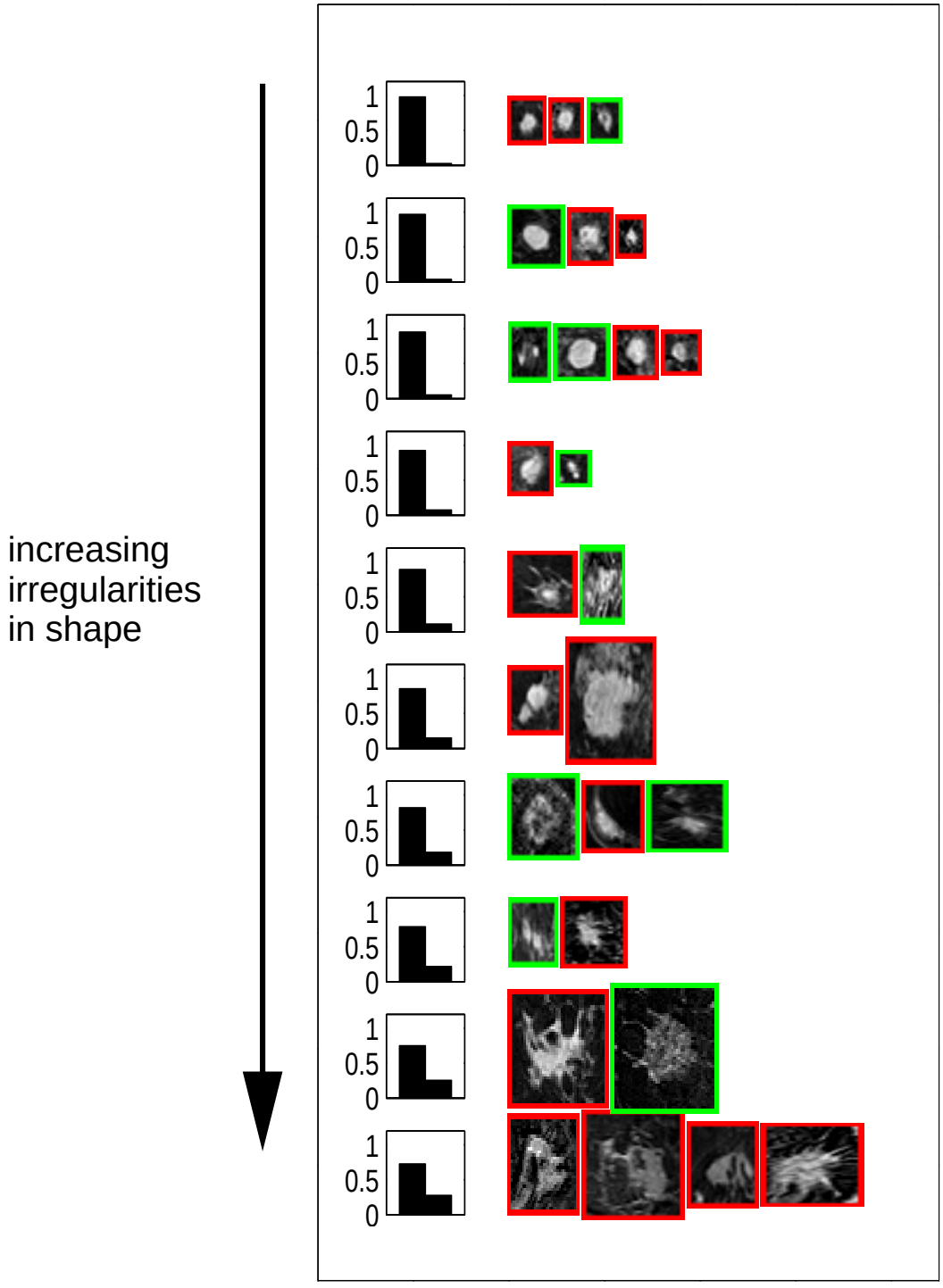

Figure 6.31.: The selected components of the shape descriptor visualised with a one-dimensional SOM grid.

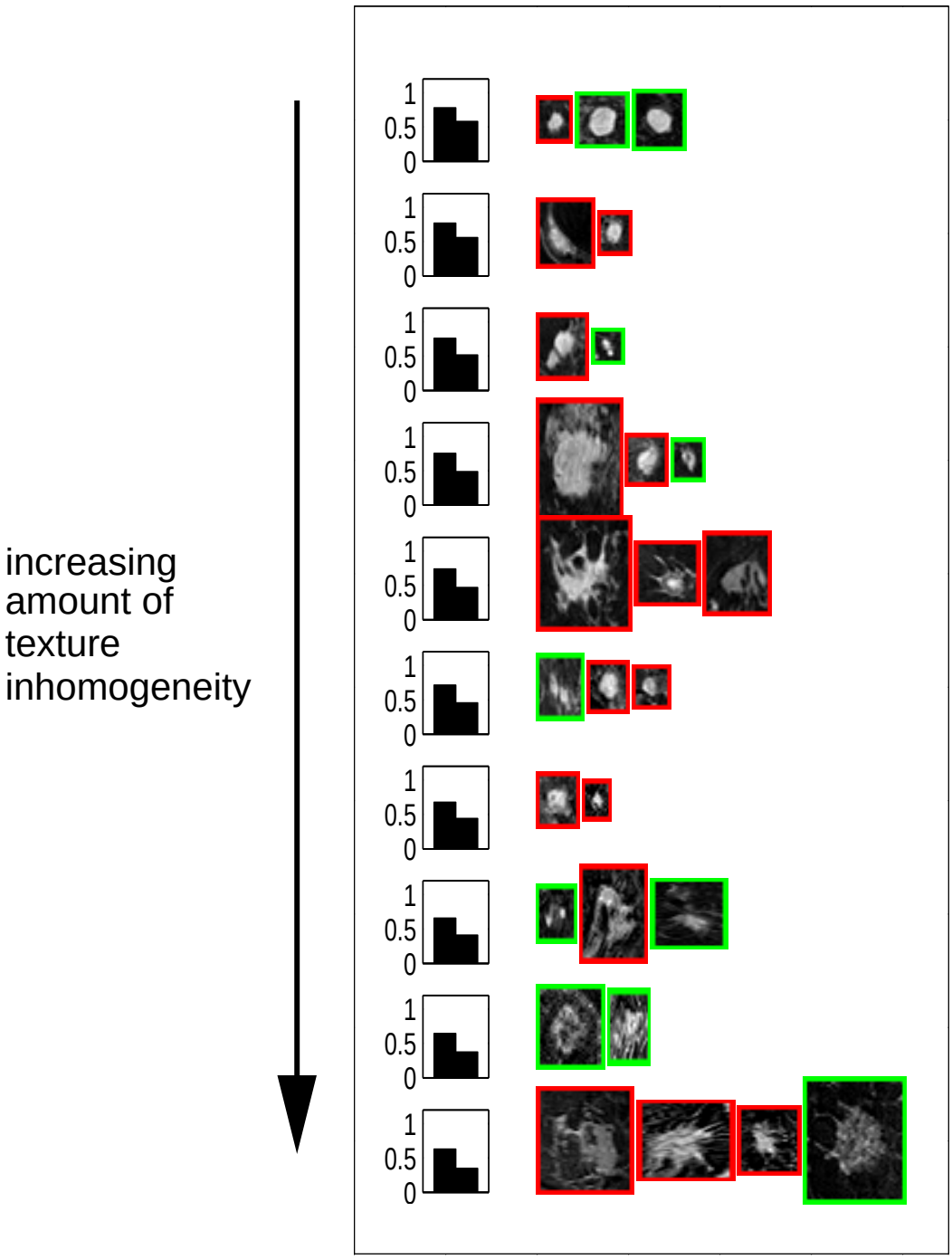

Figure 6.32.: The selected components of the texture descriptor visualised with a one-dimensional SOM grid.

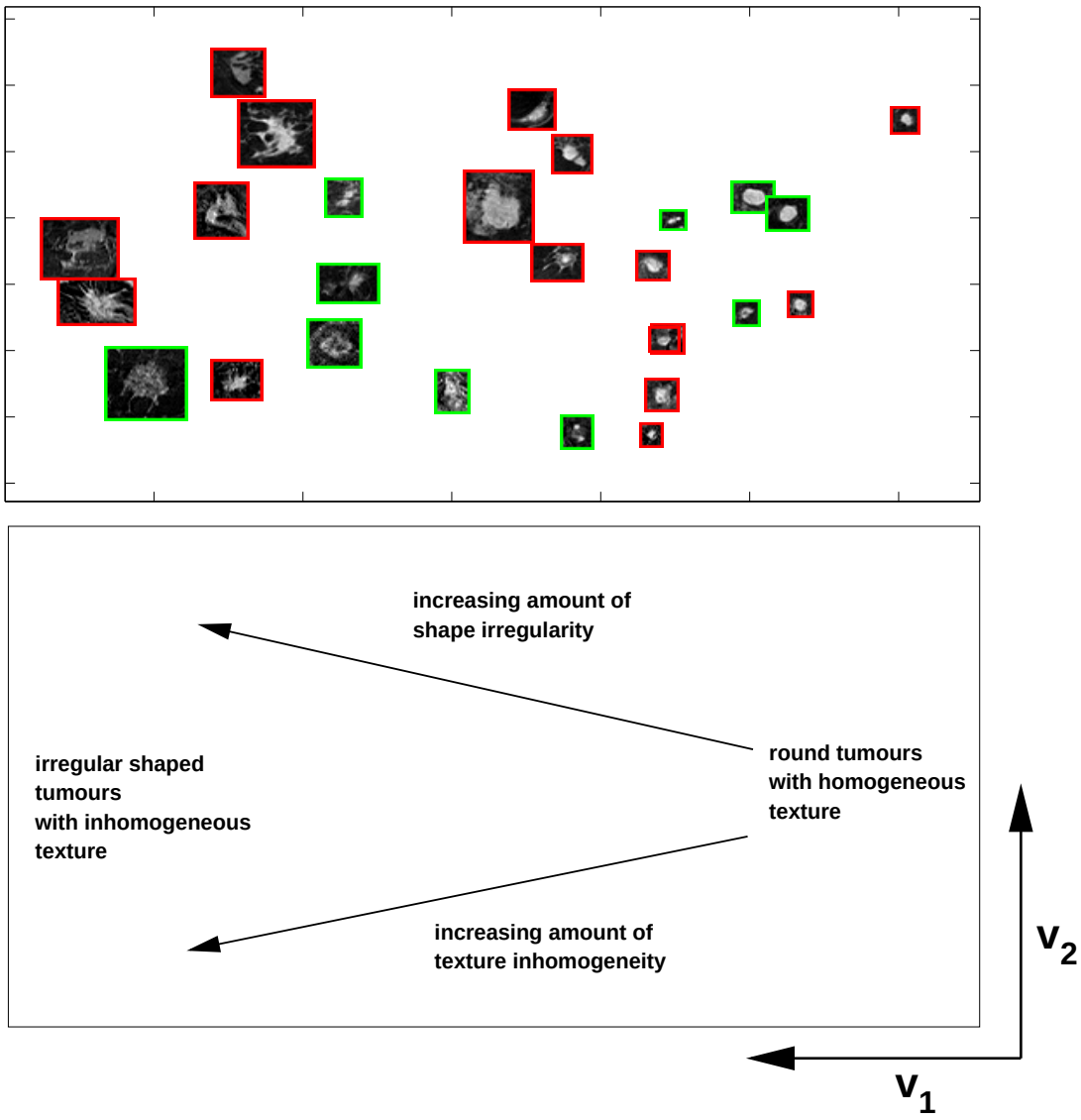

Figure 6.33.: Top: Projection of the computed feature vectors onto the eigenvectors related to the two largest eigenvalues. Each tumour is displayed at the location of the corresponding feature vector. Bottom: Variation of shape and texture in the projection plane.

To visualise the two features independently of each other the one-dimensional SOMs computed above are utilised to construct a two-dimensional grid by using the two SOM results for the x- and y-axis respectively. This visualisation is shown in Figure 6.34.

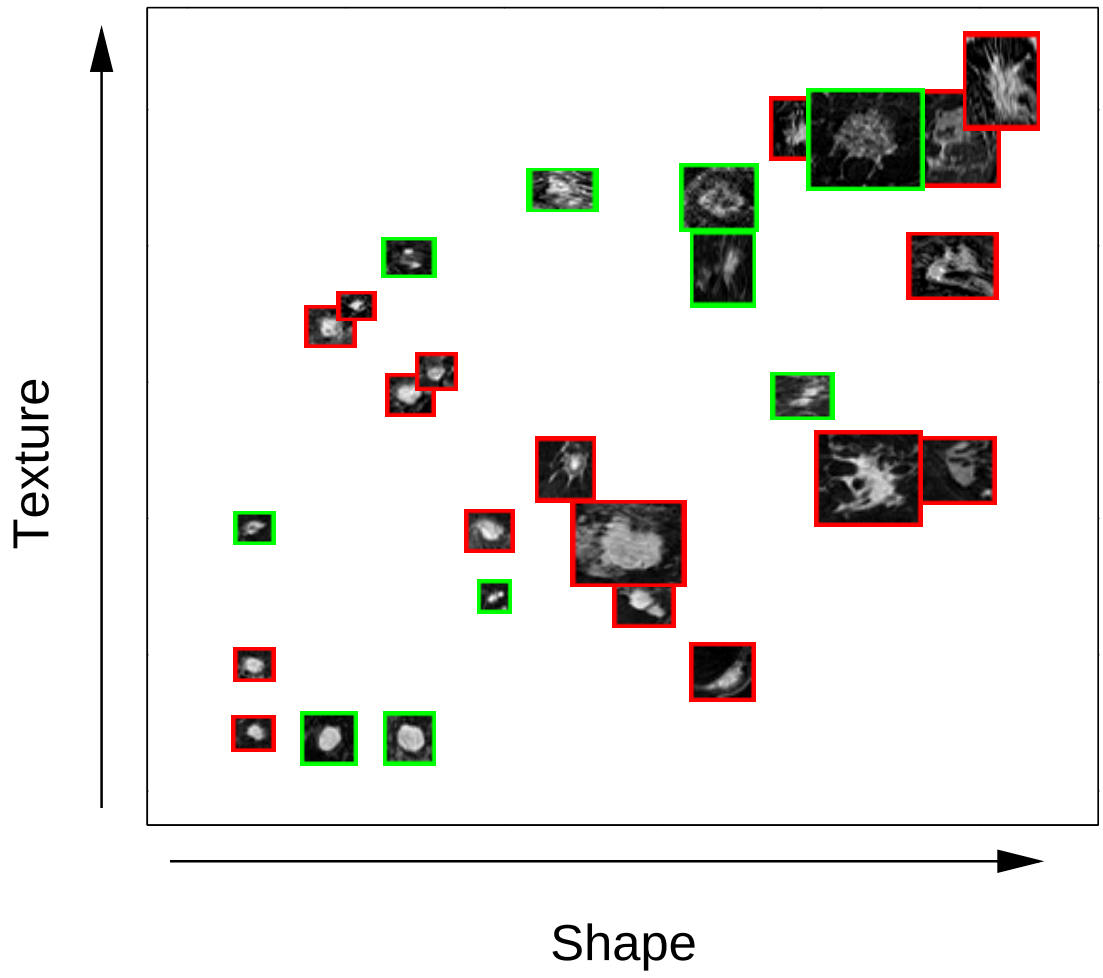

Figure 6.34.: Based on the one-dimensional SOMs shown above, the tumours are visualised in a two-dimensional plane.

6.3.8. Applications of Results

Time-Dependent Visualisation of Tumour Morphology

With the features described above it is possible to visualise the tumour morphology over time. As already mentioned the work up to now has been performed with a maximum-intensity projection of the tumour images in time. However, it is possible to compute the texture and shape descriptors for each volume at the different time points separately. Thus the change in tumour morphology over time can be visualised by utilising the visualisation described above. In Figure 6.35 the morphology of three datasets is presented. The images related to the first and the last post-contrast subtraction image are shown. The change of the location within the visualisation plane corresponds to a change of tumour morphology over time.

Tumour Encoding for Image Retrieval

In [123] an approach for content-based image retrieval for DCE-MRI datasets has been presented. There, the database entries were derived utilising a segmentation procedure, i.e. a pyramid linking pre-processing. As a result each tumour was represented by several segments. The averaged uptake curve of each segment was chosen as database entry. The subsequent analysis showed, that this type of tumour representation is insufficient for retrieval purposes. It is desirable to obtain a tumour representation that incorporates both dynamical and morphological characteristics. The approach described above encodes the tumour shape and texture properties at different time points and therefore is suitable for exactly the desired purpose. In contrast to human-defined meta features interobserver variability can be avoided. Furthermore, since the exact tumour boundary is not required, manual or semi-manual pre-processing steps are not required. A coarse definition of the region of interest is sufficient, which can be achieved by the algorithm in section 6.2. The number of tumours analysed is still insufficient to prove the retrieval performance of such a CBIR system, but this can be analysed in a future work.

6.3.9. Discussion and Conclusion

In this section the procedure of feature space exploration is utilised to derive particular descriptors for tumour morphology. Based on a DWT with different

types of wavelets a shape and a texture descriptor can be derived. The exploration procedure reveals that only the finest scale details are suitable for this particular purpose. The advantage of this type of feature set is, that it is boundary free, i.e. an exact boundary of the tumour is not required. This increases the applicability of the features in clinical practice, since no human interaction is necessary to draw a contour. The derived features can be used for applications in the field of content-based image retrieval and for the visualisation of time-dependent tumour morphology in clinical applications.

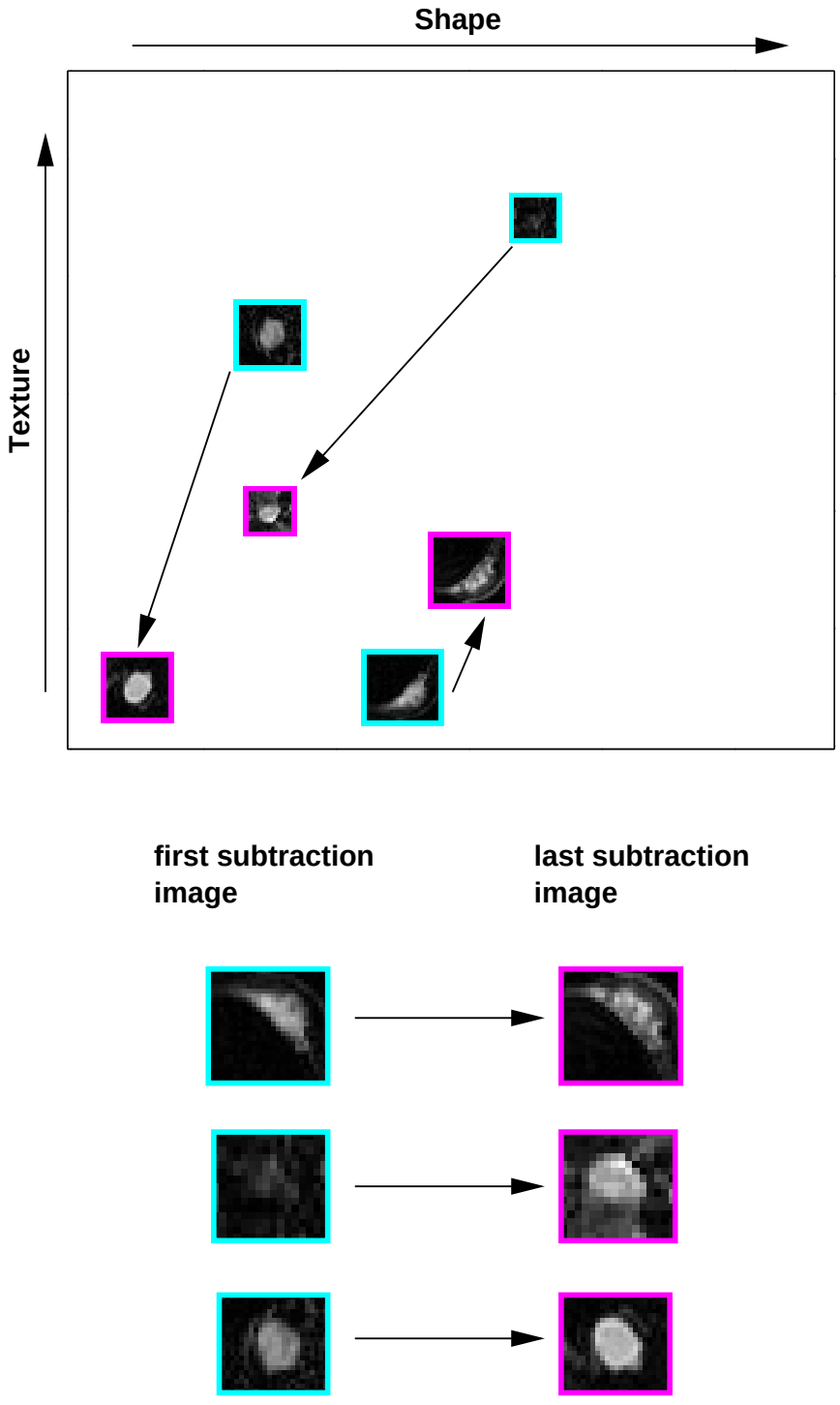

Figure 6.35.: Examples for the visualisation of lesion morphology over time. The image domain is visualised as in the previous paragraph, but for two different time points. The first (cyan) and the last (magenta) subtraction image is shown respectively.

7. Conclusion

7.1. Motivation of this Work

Nowadays the progress in medical research has become extremely fast. The more the clinical background of particular diseases is understood the more information is usually required in the diagnostic processes. One major part of such processes is the acquisition of medical images. Thus the progress in medical imaging is significant and more and more images are acquired in clinical practice. Besides the sheer number of images also the complexity of the dataset increases. This is due to monitoring of clinical characteristics, which depend on many variables, such as space and time.

The exploration of the huge amount of image information is extremely challenging for the clinical expert, generating the need for computer-based methods that assist the practitioner in his or her daily work. Strong progress has been made in the last years, however the challenge remains to develop methods which are generalisable. In the past, most of computer-based tasks in medical image analysis, that are closely related, were taken in isolation [1]. Due to the similarities of several tasks in medical imaging it is very appealing to develop methodologies, which are suited for a general analysis of structural features in medical images. Such methodologies would contribute directly to a large amount of medical image processing tasks, such as segmentation, denoising and classification. A very important aspect here is that such a method has to be very generalisable, while it should also be able to produce very specific real-world solutions in image processing.

Here, the particular approach is to represent the clinical content of images by numerical features, i.e. vectors that have potential to describe pathological characteristics. The particular challenge at this point is that these features can be quite abstract and complicated. Especially those features based on transforms such as the wavelet transform are difficult to interpret with respect to clinical characteristics. This makes handling, selection and optimisation of

these features very complicated. To overcome this lack of interpretability the set of features representing one image or image region of interest (ROI) can be regarded as a vector in a n-dimensional space. This interpretation enables the application of modern algorithms for pattern recognition and data mining and allows to answer the following questions:

Is it possible to develop a methodology that enables the user to analyse very complicated and large sets of features with respect to their relevance for the specific purpose?

How can the relation between numerical feature and clinically relevant image characteristic be assessed in order to optimise the features for the specific medical context?

Is it possible to generalise this methodology for a variety of applications on very different datasets and contexts?

In this work the development of such a methodology was described and its potential was demonstrated by developing particular image features utilisable for very different applications in medical image analysis.

7.2. Summary and Results

To obtain a highly generalisable approach the framework has to be able to process datasets, which are very different in size and complexity, clinical background or type of essential image characteristics. Current medical imaging techniques offer a wide spectrum of diagnostic images that can for instance be two- or three-dimensional. Some datasets also include time-dependent information from monitoring physiological processes. The diagnostic purposes are manifold and can require the analysis of global image information such as texture or the detection and analysis of very localised regions of interest inside the image.

The Discrete Wavelet Transform is a mathematical framework for decomposing signals or images into scale-dependent and localised information. Thus it provides the possibility of encoding both global as well as local image characteristics and the possibility of a multiscale approach in image analysis. Hence, it is a powerful method well suited as a basis for feature derivation in various applications.

The analysis of a complicated feature space and the analysis of features regarding the clinical context are enabled by utilising methods of dimension reduction. These methods, especially the Self Organizing Map, allow visualisa-

tion, exploration and thus understanding of the very abstract, wavelet-based features. Therefore, the information in the wavelet domain can be linked to the information in the image domain. The results of this exploration then allow the optimisation and selection of features clearly linked to pathological characteristics.

The effectiveness of this approach is demonstrated on two completely different image databases related to completely different diagnostic processes.

The first database contains two-dimensional RGB microscopy images taken for the diagnosis of meningiomas. The medical background of this database is well defined and understood, thus the images are chosen as a gold standard for the development of the desired methodology. Here, the four most common types of meningiomas can be distinguished and are characterised by varying texture appearance.

The images of the second database have been acquired for the purpose of breast cancer diagnostics. The time-series of three dimensional MR images are utilised to monitor the uptake of a contrast agent, since the uptake behaviour of different types of tissue provides valuable diagnostic information. Here, both the time-dependent characteristics as well as the morphology of lesions are important criteria.

The Discrete Wavelet Transform is utilised to define numerical features describing particular global or local image characteristics. One particular challenge in the definition of these features is the large number of wavelet coefficients that have to be analysed. Straight forward heuristic methods are applied to diminish the number of coefficients in a first step. These methods can be quite general such as the pre-selection of coefficients or the computation of global features of an entire image or subimage. In the case of pathology images global features based on averages of coefficients are computed for subimages to encode the scale and orientation dependent texture characteristics. For the kinetic analysis of MR images coefficients are pre-selected regarding their scale and a particular energy measure. In the development process of morphology descriptors features describing a specific region of interest are defined.

In the next step the pre-defined feature vectors are processed in different ways. Based on methods of dimension reduction the feature spaces are projected on a two-dimensional plane and thus can be visually explored. This enables the optimisation of the feature vectors and the careful adaption to the diagnostic criteria of the specific database. It is shown, that the results can be applied for very different tasks in image processing.

Regarding the microscopy images of meningiomas the four classes provide clear differences with respect to texture characteristics. However, innerclass differences are present as well and can be extremely significant. The methodology allows to explore the pre-defined features very carefully and to link the numerical features to either interclass or innerclass differences. The interpretation of the features bridges the semantic gap and allows the selection of a subset of those features which are most important in the clinical diagnostic process. Furthermore, the inherent visualisation principles directly provide an interface for sophisticated CBIR systems.

In the case of DCE-MR image processing two types of analysis are performed. Regarding the tumour kinetics the work focuses on the distinction of contrast agent uptake in the tumour from the uptake inside other parts of the body, especially the chest. To this end, the kinetic patterns in wavelet space are explored resulting in the generation of time-dependent features typical for the enhancement of tumour tissue. These features are very well adapted to the clinical purpose. The particular challenges here are the complexity and size of the datasets processed. However, due to the multiscale approach a trade-off between amount of image information analysed and level of detailedness can be achieved.

The two-dimensional visualisation of the feature space allows not only the definition and discrimination of different kinetic patterns of breast tissue but also provides the possibility of a new way of interactive filtering in wavelet space. The filtering results in a new kind of segmentation procedure. This segmentation step is able to detect the lesions inside the breast without prior knowledge regarding the tumour or any pre-processing steps. It is thus considered as very robust and also applicable in clinical practice.

Within the same framework, features for the characterisation of tumour morphology are analysed and optimised. As a result, each tumour can be represented by a specialised feature vector describing both, shape and texture of the lesion over time. This representation can be used for the visualisation of dynamical tumour morphology and the representation of tumours in CBIR systems. The descriptors encode the relevant diagnostic information, but however are short and simple.

In summary, the major advantage of the approach presented is the suitability of this analysis method for various tasks in medical image processing. The framework was utilised for feature interpretation and visualisation, feature selection and feature optimisation with respect to tissue segmentation and database representation. Thus it has been proven to be highly generalisable,

merging several related aspects of image analysis. However, it allows to define very specialised solutions strongly adapted to the underlying clinical context.

7.3. Benefits and Limitations

The usual approach to evaluate wavelet-based features is the computation of some specific parameters for each image and the following classification based on these parameters. Feature selection can then for instance be accomplished by measurement of the classification results, based on all possible combinations of features. However, this approach lacks a detailed understanding of the single features and can be highly dependent on particular properties such as size of the database, the applied classification method and so on.

By contrast, the approach described in this work aims at the visualisation of the feature space and thus the evaluation by the human observer. It is thus based on the idea that human expert knowledge can be included directly in the process of feature derivation by the medical expert.

In this way the feature spaces can be explored interactively which allows to establish a link between numerical features, the clinical semantics and the impact of different features to the discrimination of pathological characteristics.

The particular gains regarding the different datasets are manifold. Where the microscopy images are concerned, the analysis allows to select a subset of features especially suited for the discrimination of the four types of tissue. Here, the focus is on the selection of those features mainly encoding interclass differences. In the same way, the morphological descriptors for DCE-MR datasets can be optimised by selecting those scales, which are most important to discriminate specific tumour morphology.

The limitation of this approach is the missing guarantee that the numerical features only encode one specific clinical characteristic in the image. Furthermore, while it is possible to exclude features which are completely unimportant for the characterisation of different features, it is not always possible to exclude all features responsible for innerclass variances. This is for instance the case in the feature selection applied to pathology images.

A further important avail of the approach is the applicability in clinical practice. Especially the analysis of large databases and large images such as DCE-MR images suffers from applications which rely on human pre-processing steps. These steps can be for instance the drawing of a tumour contour or the manual determination of a region of interest in the image. Hand-labelling of all sin-

gle images is not possible in case of large databases. In this work it is shown, how the particular properties of wavelet analysis can be used to overcome this challenge.

Utilising the principles of multiresolution analysis our approach has generated a robust segmentation procedure that automatically extracts the tumour, i.e. the region of interest from the images. Due to this approach the processing of a large number of datasets becomes possible. The labelling of tumour regions by a human expert is a very time-consuming task and should be avoided in real-world applications. The segmentation procedure presented in this work is able to fulfil this task automatically and thus is also applicable in clinical practice.

Furthermore, by utilising the localisation properties of the DWT, a contour free morphological descriptor was defined. The main benefit of this descriptor is also the applicability in clinical practice since a hand-drawn definition of the boundary is not required to assess the morphological characteristics. A rough region of interest is sufficient and can for instance be determined by the segmentation procedure described before. Thus here as well the processing of a large number of datasets is possible.

In future applications the approach presented is supposed to be applied within further diagnostic tasks. That can e.g. be the analysis of microscopy images of neuropathological diseases, which are less well understood. Regarding further applications in the diagnostics of neuropathological diseases, we consider our framework to serve as an interface for discovering new image characteristics suitable for diagnostic purposes. In other words, databases whose image characteristics are not yet fully understood, can be analysed in order to find numerical features related to an external categorisation. The interpretation potential of our approach then allows to link these features to characteristics in the image domain, i.e. characteristics of the tissue. Besides this, the methodology is not restricted to medical image processing but can be applied in various fields of image processing task.

Another interesting application in DCE-MR imaging is the analysis of the images regarding the discrimination between benign and malignant tumours. The features described above are suited to distinguish tumour enhancement from the enhancement of other types of tissue and to encode morphological patterns, which are supposed to be of diagnostic relevance. However, the analysis whether these features are suitable for the classification of lesions into benign and malignant could not be accomplished due to the limited size of our

database. In future work these tasks can be performed on a larger database. Here, both types of features - the kinetic as well as the morphological descriptors - should be analysed. Yet another important task in future will be the extension of the features onto MR images providing a higher resolution. Especially the morphological descriptors might be improved in this way.

Bibliography

[1] J. Duncan and N. Ayache. Medical image analysis: Progress over two decades and the challenges ahead. *IEEE Transactions on Pattern Analysis and Machine Intelligence*, **22**(1):85–108, 2000.

[2] S. Wong and J. K.S. Hoo. Medical imagery. In V. Castelli and L. Bergman (editors), *Image Databases - Search and Retrieval of Digital Imagery*. John Wiley and Sons, Inc, New York, 2002.

[3] A. Jain, R. Duin and J. Mao. Statistical pattern recognition: A review. *IEEE Transactions on Pattern Analysis and Machine Intelligence*, **22**(1):4–37, 2000.

[4] A. Smeulders, M. Worring, S. Santini, A. Gupta and R. Jain. Content-based image retrieval systems at the end of the early years. *IEEE Transactions on Pattern Analysis and Machine Intelligence*, **22**(12):1349–1380, 2000.

[5] H. Müller, N. Michoux, D. Bandon and A. Geissbuhler. A review of content-based image retrieval systems in medical applications - clinical benefits and future directions. *International Journal of Medical Informatics*, **73**:1–23, 2004.

[6] H. Müller, P. Ruch and A. Geissbuhler. Enriching content-based image retrieval with automatically extracted mesh terms. In *GMDS conference*, pp. 266–269. Innsbruck, Austria, 2004.

[7] J. Stauder, J. Sirot, H. L. Borgne, E. Cooke and N. E. O'Connor. Relating visual and semantic image descriptors. In *Proceedings of the European Workshop for the Integration of Knowledge, Semantics and Digital Media Technology (EWIMT)*. London, 2004.

[8] L. Bruce and R. Adhami. Classifying mammographics mass shapes using the wavelet transform modulus-maxima method. *IEEE Transactions on Medical Imaging*, **18**(12):1170–1177, 1999.

[9] R. Rangayyan, N. Mudigonda and J. Desautels. Boundary modelling and shape analysis methods for classification of mammographic masses. *Medical Engineering & Computing*, **38**(5):487–498, 2000.

[10] M. Unser and A. Aldroubi. A review of wavelets in biomedical applications. *Proceedings of the IEEE*, **84**(4):626–638, 1996.

[11] A. Laine. Wavelets in temporal and spatial processing of biomedical images. *Annual Review of Biomedical Engineering*, **2**:511–550, 2000.

[12] D. Schomer, A. Elekes, J. Hazle, J. Huffman, S. Thompson, C. Chui and W. Murphy. Introduction to wavelet-based compression of medical images. *RadioGraphics*, **18**:469–481, 1998.

[13] M. Hilton, T. Ogden, D. Hattery, G. Eden and B. Jawerth. *Wavelet Denoising of functional MRI Data*, pp. 93–114. CRC Press, Boca Raton, FL, 1996.

[14] D. Healy and J. Weaver. *Adapted Wavelet Techniques for Encoding Magnetic Resonance Images*, pp. 298–352. CRC Press, Boca Raton, FL, 1996.

[15] E. Kolaczyk. *An Application of Wavelet Shrinkage to Tomography*, pp. 77–92. CRC Press, Boca Raton, FL, 1996.

[16] R. A. DeVore, B. Lucier and Z. Yang. *Feature Extraction in Digital Mammography*, pp. 145–161. CRC Press, Boca Raton, FL, 1996.

[17] L. Zheng, A. Wetzel, J. Gilbertson and M.J.Becich. Design and analysis of a content-based pathology image retrieval system. *IEEE Transactions on Infomation Technology in Biomedicine*, **7**(4):249–255, 2003.

[18] U. Riede, M. Werner and H. Schäfer. *Allgemeine und spezielle Pathologie*. Georg-Thieme-Verlag, Stuttgart, 2004.

[19] J. Hall and J. Knaus. *An Atlas of Breast Disease*. The Parthenon Publishing, London, New York, 2003.

[20] D. Trump and C. Robertson. Neoplasms of the prostate. In *Cancer Medicine*, pp. 1562–1586. Lea & Febiger, Philadelphia, London, 1993.

[21] S. Webb. *The Physics of Medical Imaging*. IOP Publishing Ltd, Bristol, Philadelphia, 2003.

[22] J. Bamber and M. Tristan. Diagnostic ultrasound. In *The Physics of Medical Imaging*, pp. 319–388. IOP Publishing Ltd, Bristol, Philadelphia, 2003.

[23] P. Tipler. *Physik*. Spektrum Akademischer Verlag, Berlin, Heidelberg, Oxford, 1998.

[24] D. Dance. Diagnostic radiology with x-rays. In *The Physics of Medical Imaging*, pp. 20–73. IOP Publishing Ltd, Bristol, Philadelphia, 2003.

[25] W. Swindell and S. Webb. X-ray transmission computed tomography. In *The Physics of Medical Imaging*, pp. 98–127. IOP Publishing Ltd, Bristol, Philadelphia, 2003.

[26] M. Leach. Spatially localised nuclear magnetic resonance. In *The Physics of Medical Imaging*, pp. 389–487. IOP Publishing Ltd, Bristol, Philadelphia, 2003.

[27] D. Morton. Principles of surgical oncology. In *Cancer Medicine*, pp. 523–538. Lea & Febiger, Philadelphia, London, 1993.

[28] R. Weichselbaum, D. Hallahan and G. Chen. Biological and physical basis to radiation oncology. In *Cancer Medicine*, pp. 539–565. Lea & Febiger, Philadelphia, London, 1993.

[29] L. Norton and A. Surbone. Cytokinetics. In *Cancer Medicine*, pp. 598–617. Lea & Febiger, Philadelphia, London, 1993.

[30] E. Jensen and E. DeSombre. Steroid hormone binding and hormone receptors. In *Cancer Medicine*, pp. 815–823. Lea & Febiger, Philadelphia, London, 1993.

[31] R. Bast and D. Morton. Immunostimulants. In *Cancer Medicine*, pp. 905–913. Lea & Febiger, Philadelphia, London, 1993.

[32] R. Bast, M. Zalutsky and A. Frankel. Monoclonal serotherapy. In *Cancer Medicine*, pp. 968–982. Lea & Febiger, Philadelphia, London, 1993.

[33] W. Peters. Autologous bone marrow transplantation. In *Cancer Medicine*, pp. 983–997. Lea & Febiger, Philadelphia, London, 1993.

[34] R. O'Reilly and E. Papadopoulos. Allogeneic transplantation. In *Cancer Medicine*, pp. 998–1016. Lea & Febiger, Philadelphia, London, 1993.

[35] P. Kleihues and W.K.Cavenee (editors). *World Health Organization Classification of Tumours. Pathology & Genetics. Tumours of the Nervous System.* IARC Press, Lyon, 2000.

[36] D. Louis, B. Scheithauer, H. Budka, A. von Deimling and J. Kepes. Meningiomas. In P. Kleihues and W.K.Cavenee (editors), *World Health Organization Classification of Tumours. Pathology & Genetics. Tumours of the Nervous System.*, pp. 176–184. IARC Press, Lyon, 2000.

[37] P. Brodal. *The Central Nervous System - Structure and Function*. Oxford University Press, New York, Oxford, 1992.

[38] L. Junqueira and J. Carneiro. *Histologie*. Springer, Berlin, Heidelberg, 2005.

[39] H. Burck. *Histologische Technik*. Georg-Thieme Verlag, Stuttgart, 1988.

[40] J. Peiffer, J. Schröder and W. Paulus. *Neuropathologie*. Springer-Verlag, Berlin, Heidelberg, 2002.

[41] F. Tavassoli and P. Devilee (editors). *World Health Organization Classification of Tumours. Pathology & Genetics. Tumours of the Breast and the Female Genital Organs.*, chapter 1, pp. 9–112. IARC Press, Lyon, 2003.

[42] Y. C. Kudva, C. Reynolds, T. O'Brien, C. Powell, A. L. Oberg and T. B. Crotty. "Diabetic Mastopathy" or Sclerosing Lymphocytic Lobulitis, is strongly associated with type 1 diabetes. *Diabetes Care*, **25**(1):121–126, 2002.

[43] R. Valdez, J. Thorson, W. Finn, B. Schnitzer and C. Kleer. Lymphocytic mastitis and diabetic mastopathy: a molecular, immunophenotypic, and clinicopathologic evaluation of 11 cases. *Modern Pathology*, **16**(3):223–228, 2003.

[44] B. Fisher, C. Osborne, R. Margolese and W. Bloomer. Neoplasms of the breast. In *Cancer Medicine*, pp. 1706–1774. Lea & Febiger, Philadelphia, London, 1993.

[45] P. Reuter. *Concise Medical Dictionary*. Springer, Berlin, Heidelberg, 2003.

[46] V. Kumar, R. Cotran and S. L. Robbins. *Basic Pathology*, chapter 19, pp. 607–641. W.B. Saunders Company, Philadelphia, 1992.

[47] F. Li, J. Schneider and A. Kantor. Cancer epidemiology. In *Cancer Medicine*, pp. 322–339. Lea & Febiger, Philadelphia, London, 1993.

[48] S. H. Heywang-Koebrunner and R. Beck. *Contrast-Enhanced MRI of the Breast*. Springer-Verlag, Berlin, 1996.

[49] D. Shaw. The fundamental principles of nuclear magnetic resonance imaging. In *Biomedical Magnetic Resonance Imaging*, pp. 1–46. VCH Publishers, New York, 1988.

[50] S. A. Huettel, A. W. Song and G. McCarthy. *Functional Magnetic Resonance Imaging*. Sinauer Associates, Inc, Sunderland, Massachusetts, USA, 2004.

[51] K. A. Johnson and J. A. Becker. The whole brain atlas. URL `http://www.med.harvard.edu/AANLIB/home.html`. October 2006.

[52] UK MRI Breast Screening Study Advisory Group. Magnetic resonance imaging screening in women at genetic risk of breast cancer: Imaging and analysis protocol for the uk multicentre study. *Magnetic Resonance Imaging*, **18**:765 –776, 2000.

[53] S. Mallat. *A Wavelet Tour of Signal Processing*. Academic Press, San Diego, London, 1999.

[54] G. B. Folland. *Fourier Analysis and its Applications*. Brooks/Cole Publishing Company, Pacific Grove, California, USA, 1992.

[55] I. Daubechies. *Ten Lectures on Wavelets*. Cbms-Nsf Regional Conference Series in Applied Mathematics, SIAM, 1991.

[56] E. Stollnitz, T. Derose and D. Salesin. *Wavelets for Computer Graphics*. Morgan Kaufmann Publishers, San Francisco, 1996.

[57] C. Christopoulos, A. Skodras and T. Ebrahimi. The JPEG2000 still image coding system: an overview. *IEEE Transactions on Consumer Electronics*, **46**:1103–1127, 2000.

[58] W. Sweldens. The lifting scheme: A new philosophy in biorthogonal wavelet constructions. In *Proceedings of SPIE - Wavelet Applications in Signal and Image Processing III*, pp. 68–79. 1995.

[59] W. Sweldens. The lifting scheme: A custom-design construction of biorthogonal wavelets. *Applied and Computational Harmonic Analysis*, **3**(2):186–200, 1996.

[60] O. Schulz. Blitzwave wavelet library. URL `http://blitzwave.sourceforge.net`.

[61] C. Bishop. *Neural Networks for Pattern Recognition*. Oxford, University Press, 2000.

[62] T. Kohonen. *Self Organizing Maps*. Springer, Berlin, Heidelberg, 1997.

[63] A. Flexer. On the use of self-organizing maps for clustering and visualization. *Intelligent Data Analysis*, **5**(5):373–384, 2001.

[64] S. Roweis and L. Saul. Nonlinear dimensionality reduction by locally linear embedding. *Science*, **290**:2323–2326, 2000.

[65] K. Han and S. Myaeng. Image organization and retrieval with automatically constructed feature vectors. In *Proceedings of the 19th Annual International ACM SIGIR Conference on Research and Development in Information Retrieval*, pp. 157–165. 1996.

[66] J. Laaksonen, M. Koskela, S. Laakso and E. Oja. PicSOM - content-based image retrieval with self-organizing maps. *Pattern Recognition Letters*, **22**:1199–1207, 2000.

[67] W. Y. Ma and B. S. Manjunath. Image indexing using a texture dictionary. In *SPIE conference on Image Storage and Archiving System*, volume 2606, pp. 288–298. 1995.

[68] J. Iglesias-Rozas and N. Hopf. Histological heterogeneity of human glioblastomas investigated with an unsupervised neural network (SOM). *Histology and Histopathology*, **20**:351–356, 2005.

[69] B. Lessmann, V. Hans, A. Degenhard and T. Nattkemper. Feature-space exploration of pathology images using content-based database visualization. In J. Reinhardt and J. Pluim (editors), *Proceedings of SPIE Medical Imaging*, volume 6144, 61445Z. San Diego, California, USA, 2006.

[70] J. Wang. Pathfinder: Multiresolution region-based searching of pathology images using IRM. In *Proceedings of the AMIA Annual Symposium*, pp. 883–887. Los Angeles, California, 2000.

[71] H. Tang, R. Hanka and H. Ip. Histological image retrieval based on semantic content analysis. *IEEE Transactions on Information Technology in Biomedicine*, **7**(1):26–36, 2003.

[72] J. Jelonek, K. Krawiec, R. Slowinski and J. Szymas. Intelligent decision support in pathomorphology. *Polish Journal of Pathology*, **50**(2):115–118, 1999.

[73] D. Foran, D. Comaniciu, P. Meer and L. Goodell. Computer-assisted discrimination among malignant lymphomas and leukemia using immunophenotyping, intelligent image repositories and telemicroscopy. *IEEE Transactions on Information Technology in Biomedicine*, **4**(4):265–273, 2000.

[74] D. Hearn and M. Baker. *Computer Graphics*. Prentice-Hall Intternational Inc., 1997.

[75] S. Aksoy and R. Haralick. Textural features for image database retrieval. In *Proceedings of the IEEE Workshop on Content-Based Access of Image and Video Libraries (CVPR'98)*, pp. 45–49. Santa Barbara, California, 1998.

[76] P. Howarth, A. Yavlinsky, D. Heesch and S. Rueger. Medical image retrieval using texture, locality and colour. In C. Peters, P. Clough and J. Gonzalo (editors), *5th Workshop of the Cross-Language Evaluation Forum, CLEF 2004, Bath, UK*, Lecture Notes in Computer Science, pp. 740–749. 2004.

[77] G. van de Wouwer, B. Weyn, P. Scheunders, W. Jacob, E. van Marck and D. van Dyck. Wavelets as chromatin texture descriptors for the automated identification of neoplastic nuclei. *Journal of Microscopy*, **197**:25–35, 1999.

[78] B. Manjunath and W. Ma. Texture features for image retrieval. In V. Castelli and L. Bergman (editors), *Image Databases - Search and Retrieval of Digital Imagery*. John Wiley and Sons, Inc, New York, 2002.

[79] T. Randen and J. Husoy. Filtering for texture classification: a comparative study. *IEEE Transactions on Pattern Analysis and Machine Intelligence*, **21**(4):291–310, 1999.

[80] T. Chang and C.-C. Kuo. Texture analysis and classification with tree-structured wavelet transform. *IEEE Transactions on Image Processing*, **2**(4):429–441, 1993.

[81] G. van de Wouwer, P. Scheunders and D. van Dyck. Statistical texture characterization from discrete wavelet representation. *IEEE Transactions on Image Processing*, **8**(4):592–598, 1999.

[82] C. Varini, B. Lessmann, A. Degenhard, V. Hans and T. W. Nattkemper. Visual exploration of pathology images by a discrete wavelet transform preprocessed locally linear embedding. In *Proceedings of Bildverarbeitung für die Medizin (BVM) 06*, pp. 66–70. Springer Verlag, Hamburg, Germany, 2006.

[83] S. Livens, P. Scheunders, G. van de Wouwer, D. van Dyck, H. Smets, J. Winkelmans and W. Bogaerts. A texture analysis approach to corrosion image classification. *Microscopy, Microanalysis, Microstructures*, **7**(2):1–10, 1996.

[84] C. Kuhl, P. Mielcareck, S. Klaschik, C. Leutner, E. Wardelmann, J. Gieseke and H. Schild. Dynamic breast MR imaging: Are signal intensity time course data useful for differential diagnosis of enhancing lesions? *Radiology*, **211**:101–110, 1999.

[85] B. K. Szabo, P. Aspelin, M. K. Wiberg and B. Bone. Analyis of kinetic and morphologic diagnostic criteria. *Acta Radiologica*, **44**:379–386, 2003.

[86] K. Kinkel, T. Helbich, L. Essermann, J. Barclay, E. Schwerin, E. Sickles and N. Hylton. Dynamic high-spatial resolution MR imaging of suspicious breast lesions: Diagnostic criteria and interobserver variability. *American Journal of Roentgenology*, **175**:35–43, 2000.

[87] S. Kim, E. Morris, L. Liberman, D. Ballon, L. La Trenta, O. Hadar, A. Abramson and D. Dershaw. Oberserver variability and applicability of BI-Rads terminology for breast MR imaging: Invasive carcinomas and focal masses. *American Journal of Roentgenology*, **177**:551–557, 2001.

[88] D. Ikeda, N. Hylton, K. Kinkel, M. Hochmann, C. Kuhl, W. Kaiser, J. Weinreb, S. Smazal, H. Degani, P. Viehweg, J. Barclay and M. Schnall. Development, standardization and testing of a lexicon for reporting

contrast-enhanced breast magnetic resonance imaging studies. *Journal of Magnetic Resonance Imaging*, **13**:889–895, 2001.

[89] U. Wedegärtner, U. Bick, K. Woertler, E. Rummeny and G. Bongartz. Differentiation between benign and malignant findings on MR-mammography: usefulness of morphological criteria. *European Radiology*, **11**:1645–1650, 2001.

[90] M. Tozaki, T. Igarashi, S. Matsushima and K. Fukuda. High-spatial-resolution MR imaging of focal breast masses: Interpretation model based on kinetic and morphological parameters. *Radiation Medicine*, **23**(1):43–50, 2005.

[91] M. Schnall, J. Blume, D. Bluemke, G. DeAngelis, N. DeBruhl, S. Harms, S. Heywang-Köbrunner, N. Hylton, C. Kuhl, E. Pisano, P. Causer, S. Schnitt, D. Thickman, C. Stelling, P. Weatherall, C. Lehmann and C. Gatsonis. Diagnostic architectural and dynamic features at breast MR imaging. *Radiology*, **238**(1):42–53, 2006.

[92] H. Fischer and J. Hennig. Neural network-bases analysis of MR time series. *Magnetic Resonance in Medicine*, **41**:124–131, 1999.

[93] T. Twellmann, A. Saalbach, C. Müller, T. W. Nattkemper and A. Wismüller. Detection of suspicious lesions in dynamic contrast-enhanced MRI data. In *26th International Conference of the IEEE Engineering in Medicine and Biology Society, San Francisco*. 2004.

[94] R. Lucht, S. Delorme and G. Brix. Neural network-based segmentation of dynamic MR mammographic images. *Magnetic Resonance Imaging*, **20**:147–154, 2002.

[95] W. Chen, P. Meer, B. Georgescu, W. He, L. Goodell and D. Foran. Image mining for investigative pathology using optimized feature extraction and data fusion. *Computer Methods and Programs in Biomedicine*, **79**:59–72, 2005.

[96] R. E. A. Lucht, M. V. Knopp and G. Brix. Classification of signal-time curves from dynamic MR mammography by neural networks. *Magnetic Resonance Imaging*, **19**:51–57, 2001.

[97] P. Abdolmaleki, L. Buadu and H. Naderimansh. Feature extraction and classification of breast cancer on dynamic magnetic resonance imaging using artificial neural networks. *Cancer Letters*, **171**:183–191, 2001.

[98] T. Nattkemper and A. Wismüller. Tumour feature analysis with unsupervised machine learning. *Medical Image Analysis - Special issue: Functional Imaging and Modeling of the Heart*, **9**(4):344–351, 2005.

[99] G. Hellwig, G. Brix, J. Griebel, R. Lucht, S. D. adn M. Siebert and K. Englmeier. Three dimensional real-time visualization of contrast enhancement in virtual reality. *Academic Radiology*, **9**:1255–1263, 2002.

[100] P. A. C. Behrenbruch, M. Brady and N. Moore. Extracting and visualizing physiological parameters using dynamic contrast-enhanced magnetic resonance imaging of the breast. *Medical Image Analysis*, **9**:315–329, 2005.

[101] T. Twellmann, A. Saalbach, O. Gerstung, M. O. Leach and T. W. Nattkemper. Image fusion for dynamic contrast enhanced magnetic resonance imaging. *Biomedical Engineering OnLine*, **3**(35), 2004.

[102] A. Tzacheva, K. Najarian and J. Brockway. Breast cancer detection in gadolinium-enhanced MR images by static region descriptors and neural networks. *Journal of Magnetic Resonance Imaging*, **17**:337–342, 2003.

[103] K. Shahar, M. Solaiyappan and D. Bluemke. Quantitative differentiation of breast lesion based on three-dimensional morphology from magnetic resonance imaging. *Journal of Computer Assisted Tomography*, **26**(6):1047–1053, 2002.

[104] R. Rangayyan, N. El-Faramawy, J. Desautels and O. Alim. Measure of acutance and shape for classification of breast tumours. *IEEE Transactions on Medical Imaging*, **16**(6):799–810, 1997.

[105] P. Gibbs and L. Turnbull. Textural analysis of contrast-enhanced MR images of the breast. *Magnetic Resonance in Medicine*, **50**:92–98, 2003.

[106] B. K. Szabo, M. K. Wilberg, B. Bone and P. Aspelin. Application of artificial neural networks to the analysis of dynamic MR imaging features of the breast. *European Radiology*, **14**:1217–1225, 2004.

[107] T. W. Nattkemper, B. Arnrich, O. Lichte, W. Timm, A. Degenhard, L. Pointon, C. Hayes, M. O. Leach and UK MARIBS Screening Study. Evaluation of radiological features for breast tumour classification in clinical screening with machine learning methods. *Artificial Intelligence in Medicine*, **32**(2):129–139, 2005.

[108] S. Sinha, F. Lucas-Quesada, N. DeBruhl, J. Sayre, D. Farria, D. Gorczyca and L. Basset. Multifeature analysis of Gd-enhanced MR images of breast lesions. *Journal of Magnetic Resonance Imaging*, **7**:1016–1026, 1997.

[109] T. Wang and N. Karayiannis. Detection of microcalcifications in digital mammograms using wavelets. *IEEE Transactions on Medical Imaging*, **17**(4):498–509, 1998.

[110] S. Liu, C. Babbs and E. Delp. Multiresolution detection of spiculated lesions in digital mammomgrams. *IEEE Transactions on Image Processing*, **10**(6):874–884, 2001.

[111] R. Alterson and D. B. Plewes. Bilateral symmetry analysis of breast MRI. *Physics in Medicine and Biology*, **48**:3431–3443, 2003.

[112] U. Ruttimann, M. Unser, R. Rawlings, D. Rio, N. Ramsey, V. Mattay, D. Hommer, J. Frank and D. Weinberger. Statistical analysis of functional MRI data in the wavelet domain. *IEEE Transactions on Medical Imaging*, **17**:142–154, 1998.

[113] B. Whitcher, A. Schwarz, H. Barjat, S. Smart, R. Grundy and M. James. Wavelet-based cluster analysis: Data-driven grouping of voxel time courses with application to perfusion-weighted and pharmacological MRI of the rat brain. *NeuroImage*, **24**:281–295, 2005.

[114] F. Meyer. Wavelet-based estimation of a semiparametric generalized linear model of fMRI time-series. *IEEE Transactions on Medical Imaging*, **22**:315–322, 2003.

[115] E. Bullmore, J. Fadili, M. Breakspear, R. Salvador, J. Suckling and M. Brammer. Wavelets and statistical analyis of functional magnetic resonance images of the human brain. *Statistical Methods in Medical Research*, **12**:375–399, 2003.

[116] B. Lessmann, T. Twellmann, A. Degenhard, T. Nattkemper and M. O. Leach. Wavelet features for improved tumour detection in DCE-MRI. In *Proceedings of Medical Image Understanding and Analysis (MIUA)*, pp. 93–96. BMVA, London, UK, 2004.

[117] T. Fawcett. ROC Graphs: Notes and Practical Considerations for Researchers. *HP Labs Tech Report HPL-2003-4*, 2003.

[118] B. Lessmann, T. Nattkemper, A. Degenhard, L. Pointon, P. Kessar, M. Khazen and M. Leach. Clustering approach for wavelet transformed MR image data. In *Proceedings of the 14th International Conference of Medical Physics*, pp. 1412–1413. Nürnberg, Germany, 2005.

[119] B. Lessmann, T. W. Nattkemper, P. Kessar, L. Pointon, M. Khazen, M. O. Leach and A. Degenhard. Multiscale analysis of MR mammography data. *Zeitschrift für Medizinische Physik*, **2**, 2007. Accepted.

[120] B. Kimia. Shape representation for image retrieval. In V. Castelli and L. Bergman (editors), *Image Databases - Search and Retrieval of Digital Imagery*. John Wiley and Sons, Inc, New York, 2002.

[121] P. Salembier. Overview of the MPEG-7 standard and of future challenges for visual information analysis. *EURASIP Journal on Applied Signal Processing*, **4**:343–353, 2002.

[122] J. Froment and S. Mallat. Second generation compact image coding with wavelets. In *Wavelets - A Tutorial in Theory and Applications*, pp. 655–678. Academic Press, Inc., 1992.

[123] B. Lessmann, T. W. Nattkemper, J. Huth, C. Loyek, P. Kessar, M. Khazen, L. Pointon, M. O. Leach and A. Degenhard. Content-based image retrieval for dynamic time series data. In *Proceedings of Bildverarbeitung für die Medizin (BVM) 06*, pp. 61–65. Springer Verlag, Hamburg, Germany, 2006.

[124] C. Cohen-Tannoudji, B. Diu and F. Laloë. *Quantummechanics*, chapter 4. Walter de Gruyter, Berlin, New York, 1999. German Translation.

A. Appendix

A.1. Quantum-mechanical Description of MR

The principles of Magnetic Resonance are usually described in a classical context, i.e. the behaviour of the magnetisation vector of the probe is analysed. However, the process of nuclear spin resonance is a quantum-mechanical process. In this section the quantum-mechanical principles will be detailed. Based on these descriptions it will additionally become evident, why the classical description is valid.

A.1.1. The Nuclear Spin

The nuclei of atoms, are associated with a spin. The spin can be described by the spin angular momentum $\mathbf{I}$. The magnitude of the angular momentum is given by

$$|\mathbf{I}| = \hbar\sqrt{[I(I+1)]}. \tag{A.1}$$

Here I is the spin quantum number and $\hbar = \frac{h}{2\pi}$ with Planck's constant h. The eigenvalue to the S_z-Operator is given by $\hbar m_z$ with the magnetic spin quantum number m_z which can take the values $-I, -I+1, ..., I-1, I$. The nucleus of the hydrogen atom - the proton - provides a spin angular momentum of $\frac{1}{2}$ and thus the magnetic spin quantum number can take the values $+\frac{1}{2}$ and $-\frac{1}{2}$, which are also termed "spin up" and "spin down".

In a magnetic field $\mathbf{B}(t)$ the Hamiltonian is given by

$$H(t) = -\mathbf{M}\cdot\mathbf{B}(t) \tag{A.2}$$

$$= -\gamma\mathbf{S}\cdot\mathbf{B}(t) \tag{A.3}$$

with $\mathbf{M}$ the magnetic momentum of the spin. In case of a static field $\mathbf{B} = \mathbf{B}_0$ pointing in z-direction the spin-related energy of a proton

$$E = \langle H\rangle = -\gamma\mathbf{B}_0\hbar m_z \tag{A.4}$$

can take the two values

$$E_1 = -\hbar\frac{1}{2}\gamma\mathbf{B}_0 \qquad E_2 = \hbar\frac{1}{2}\gamma\mathbf{B}_0. \tag{A.5}$$

The state corresponding to the energy E_1 is favoured due to its lower energy. The population of the two states depending on the temperature can be described by the Boltzmann distribution

$$\frac{n(+\frac{1}{2})}{n(-\frac{1}{2})} = e^{\frac{\Delta E}{kT}} \tag{A.6}$$

with the Boltzmann constant $k \approx 1.38 \cdot 10^{-23}\frac{m^2 kgK}{s^2}$, the temperature T and the energy difference between the two states

$$\Delta E = \gamma\hbar B_0. \tag{A.7}$$

In case of an additional field $\mathbf{B}_1$ rotating with frequency ω in the xy-plane the Hamiltonian $\mathbf{B}_1 = B_1(\cos\omega t, \sin\omega t, 0)$ is modified according to

$$\begin{aligned} H(t) &= -\gamma\mathbf{S}\cdot(\mathbf{B}_0 + \mathbf{B}_1) && \text{(A.8)} \\ &= -\gamma(S_z B_0 + S_x B_1\cos\omega t + S_y B_1 \sin\omega t). && \text{(A.9)} \end{aligned}$$

The general solution of the Schrödinger-Equation is a superposition of spin-up $|+\rangle$ and spin-down $|-\rangle$ with time-dependent coeffcicients $a_\pm(t)$

$$|\psi(t)\rangle = a_+(t)|+\rangle + a_-(t)|-\rangle. \tag{A.10}$$

In [124] it is shown, that using the transform

$$b_+(t) = e^{\frac{i\omega t}{2}}a_+(t) \qquad b_-(t) = e^{\frac{-i\omega t}{2}}a_-(t) \tag{A.11}$$

the Schrödinger equation can be written using a time-independent Hamiltonian $\tilde{H}$

$$i\hbar\frac{\mathrm{d}}{\mathrm{d}t}|\tilde{\psi}(t)\rangle = \tilde{H}|\tilde{\psi}(t)\rangle \tag{A.12}$$

with

$$\tilde{H} = \frac{\hbar}{2}\begin{pmatrix} -\Delta\omega & \omega_1 \\ \omega_1 & \Delta\omega \end{pmatrix}. \tag{A.13}$$

and

$$|\tilde{\psi}(t)\rangle = b_+(t)|+\rangle + b_-(t)|-\rangle. \tag{A.14}$$

Here it is $\omega_1 = \gamma B_1$, $\omega_0 = \gamma B_0$ and $\Delta\omega = \omega_0 - \omega_1$. The transform of $a_\pm(t)$ into $b_\pm(t)$ is equivalent to the application of the rotation operator

$$R(t) = e^{\frac{i\omega S_z t}{\hbar}} \tag{A.15}$$

onto $|\psi(t)\rangle$ and can be interpreted as the transform into a rotating reference frame.

A.1.2. Spin Excitation

In the classical description the rotating field $\mathbf{B}_1$ tilts the magnetisation vector out of its intial position. In the quantum-mechanical description this corresponds to a transition from the spin-up state to the spin-down state. Let us assume that at $t = 0$ the system is described by $|\psi(0)\rangle = |+\rangle$ and accordingly $|\tilde{\psi}(0)\rangle = |+\rangle$. The probability for a transition to the state $|-\rangle$ over time is described by

$$P_{+-}(t) = |\langle -|\psi(t)\rangle| = |\langle -|\tilde{\psi}(t)\rangle|. \tag{A.16}$$

In [124] it is shown that the solution is given by

$$P_{+-}(t) = \frac{\omega_1^2}{\omega_1^2 + (\Delta\omega)^2} \sin^2\left(\sqrt{\omega_1^2 + (\Delta\omega)^2}\,\frac{t}{2}\right). \tag{A.17}$$

Far from resonance $P_{+-}(t)$ is small. However, if $\omega = \omega_0$, i.e. $\Delta\omega = 0$ the probability of a transition flucuates between 0 and 1 as shown in Figure A.1. For the special cases $t = \frac{\pi}{\omega_1}$ and $t = \frac{2\pi}{\omega_1}$ the probabilities are 0.5 and 1 respectively. This corresponds to the classical description of tilting the magnetisation vector about angles $\theta = 90°$ and $\theta = 180°$. Statistically the distribution of states is balanced in the first case resulting in a zero net-magnetisation and inverted in the latter one.

A.1.3. The Magnetic Momentum

To establish a clear link between the classical and the quantum-mechanical description, we will compute the time evolution for the expectation value of the magnetic momentum $\langle\mathbf{M}\rangle$, which is given by

$$i\hbar\frac{\mathrm{d}}{\mathrm{d}t}\langle\mathbf{M}\rangle(t) = \langle[\mathbf{M}, H(t)]\rangle \tag{A.18}$$

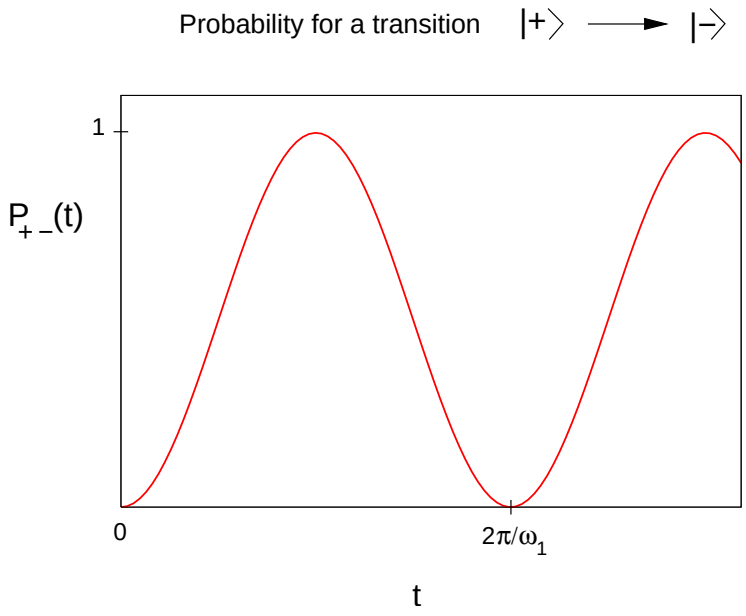

Figure A.1.: Probability for a transition from spin-up to spin-down state for the resonance case $\omega = \omega_0$.

with

$$H(t) = -\mathbf{M} \cdot \mathbf{B}(t). \tag{A.19}$$

In [124] it is demonstrated that the solution of equation A.18 is

$$\frac{\mathrm{d}}{\mathrm{d}t}\langle \mathbf{M}(t) \rangle = \gamma \langle \mathbf{M} \rangle \times \mathbf{B}(t). \tag{A.20}$$

Thus the expectation value of the magnetic momentum follows the same equation as the magnetisation vector in the classical description. In the case of a large number N of spins the total momentum $\mathcal{M}$ of a probe is given by [124]

$$\mathcal{M} = \sum_{i=1}^{N} \langle \psi^i(t) | \mathbf{M} | \psi^i(t) \rangle \tag{A.21}$$

$$= \sum_{i=1}^{N} \mathcal{M}^i(t). \tag{A.22}$$

Here the classical equation is valid for $\mathcal{M}^i(t)$ and accordingly it follows[1]

$$\frac{\mathrm{d}}{\mathrm{d}t}\mathcal{M} = \gamma \mathcal{M} \times \mathbf{B}(t) \tag{A.23}$$

[1]The assumption is that the spins do not interact with each other.